Analysis of Fracture, Fatigue, and Metallurgical Properties of Dissimilar TIG & RFW Welds: S355J2/SS316L and Ti-64/Ti-1023

A thesis

submitted in fulfilment

of the requirements for the degree

of

Master of Engineering in Materials and Processing

at

The University of Waikato

by

RAJKUMAR DAS

THE UNIVERSITY OF
WAIKATO
Te Whare Wānanga o Waikato

2024

Abstract

Weld joints comprising dissimilar metals with varying compositions are widely utilized across numerous contemporary industrial sectors such as aerospace, automotive manufacturing, shipbuilding, oil and gas, power generation, and medical device production. They offer cost efficiency, performance enhancement, weight reduction, design flexibility, and functionality. However, welding dissimilar metals with varying compositions poses complexity due to compositional gradient and differences in microstructure, leading to variations in properties across the joint. Gaining insight into the influence of parameters in welding on material properties for manufacturing defect-free welded joints is crucial. Nonetheless, there is a considerable gap in knowledge in understanding the relationship between welding parameters, microstructure, fracture toughness, and fatigue in dissimilar material joints.

This study focuses on investigating how parameters in welding influence the microstructure and fracture toughness of welds between two dissimilar materials i.e. structural steel (S355J2) and stainless steel (SS) (316L) using Rotary Friction Welding (RFW) and Tungsten Inert Gas (TIG) welding. Additionally, the study explores how parameters in welding affect the microstructure and fatigue characteristics of welds between two dissimilar titanium alloys i.e. Ti-6Al-4V (Ti-64) and Ti-10V-2Fe-3Al (Ti-1023) using RFW. To achieve the project objectives, dissimilar welding preforms of S355J2 and SS316L are meticulously prepared using corresponding pipe pup pieces and welded via RFW and TIG processes. A comprehensive series of tests are conducted, including microstructural analysis, tensile, hardness, and fracture toughness characteristics are accomplished using compact tension (CT) specimens extracted from various zones of both dissimilar weld joints. For titanium, dissimilar weld joints are fabricated using a round bar of Ti-64 and Ti-1023 via RFW, and tests, including microstructural analysis, tensile, hardness, and stress-controlled high cycle fatigue (HCF), are performed.

Results reveal significant microstructural variations in both dissimilar welding processes for the S355J2 and SS316L as well as the Ti-64 and Ti-1023 alloys. RFW joint between S355J2 and SS316L shows less instability in hardness across the weld with the highest hardness of 208 HV1 in the thermo-mechanically affected zone (TMAZ) of S355J2. Noticeable changes in hardness are observed across the TIG weld with 419 HV1 at the weld centre line (WCL) due to chromium carbide

precipitation and 284 HV1 at the TIG heat affected zone (HAZ) of S355J2 is attributed to martensite formation. Both welds exhibit superior tensile characteristics, with the RFW weld displaying ultimate tensile strength (UTS) of 540 MPa and yield strength (YS) of 367 MPa, while the TIG weld shows UTS of 526 MPa and YS of 300 MPa. Tensile failures predominantly occur on the S355J2 side, exhibiting ductile features. Both welds show nearly identical fracture toughness (K_Q) values, closely matching those of the parent metal, whereas, in terms of crack tip opening displacement (CTOD), RFW-WCL shows superior performance with 0.35 mm compared to TIG-WCL's 0.32 mm. Notably, the HAZ of S355J2 in the TIG weld exhibits the lowest CTOD of 0.31 mm. Fractography exhibits ductile failure, except for the TIG WCL, which displays cleavage fracture.

In the RFW joint between Ti-64 and Ti-1023, the highest hardness of 342 HV1 occurs at the WCL, gradually diminishing on either side of the weld, attributed to formation of hard microstructural phases and the growth of secondary alpha (α_s) phases. The weld exhibits remarkable tensile properties, comparable with those of the parent metal, with a UTS of 826 MPa and an YS of 792 MPa. Tensile failures primarily manifest on the Ti-1023 side, demonstrating ductile characteristics. The HCF test, conducted at a frequency of 40 Hz with a R value of 0.1, reveals a fatigue strength of the weld at 550 MPa, surpassing that of the Ti-64 parent metal. In all HCF specimens, crack initiates at the surface, with those under higher stress exhibiting a narrow crack propagation area characterized by coarse fatigue striation marks indicative of dominant tensile overloading, while specimens under lower stress reveal a wider crack propagation area with quasi-cleavage facets and very fine fatigue striations.

Overall, the study findings establish that the RFW process yields a robust dissimilar weld joint between different materials S355J2 / SS316l and Ti-64 / Ti-1023.

Acknowledgement

"Age is No Barrier. It’s a Limitation You Put on Your Mind," famously quoted by one of the all-time great women athletes, Jackie Joyner-Kersee, serves as a profound inspiration for individuals across all walks of life, including myself. It motivated me to make the decision to pursue a Master of Engineering, leaving behind a long career in industry.

First and foremost, I wish to extend my heartfelt gratitude to the School of Engineering at the University of Waikato for affording me the opportunity to undertake my Master of Engineering studies. The Hamilton campus exudes a welcoming atmosphere, and I am deeply appreciative of the cooperative and supportive individuals I encountered during my time here over the past year.

I am particularly indebted to my chief supervisor, Dr. Ajit Pal Singh. Not only has he been a dedicated supervisor, but he has also assumed the role of a friend and philosopher, offering invaluable guidance both in my project work and personal life. His unwavering support since my arrival at the university has been instrumental, providing essential expertise and direction throughout my academic journey. I hold in high regard his profound knowledge in material manufacturing and his exceptional ability to listen. Having him as my supervisor fills me with pride.

I extend special thanks to my co-supervisor, Dr. Giribaskar Sivaswamy, and his team at Advanced Forming Research Centre (AFRC), University of Strathclyde, Glasgow, United Kingdom (UK). Their insightful discussions and assistance in identifying suitable locations for experiments outside our university have been invaluable. I am immensely grateful for their support in manufacturing project materials and providing guidance, both academically and personally, through online interactions.

I would also like to acknowledge Dr. Himanshu Lalvani, Safran Electrical and Power, Pitstone UK for leading the project for manufacturing dissimilar weld between S355J2 and SS316L at National Manufacturing Institute Scotland (NMIS), Dr. Anas Yaghi and Dr. Pedro Santos from Manufacturing Technology Centre (MTC), Coventry, UK, for RFW process optimization, Dr. Bernd Baufeld from Pro-beam technologies GmbH, Germany for contribution towards the manufacturing of TIG welded preforms at Nuclear Advanced Manufacturing Research Centre

(NAMRC), Rotherham, UK and Dr. Amborish Banerjee, AFRC, University of Strathclyde, Glasgow, UK for manufacturing RFW titanium joint.

I would also like to express my appreciation to our research officer, Dr. Stella Raynova, for her unwavering support and guidance in experimental work, as well as for her comprehensive training on various equipment. Her expertise across various domains and her courteous demeanour are truly admirable.

The completion of this thesis would not have been possible without the invaluable assistance of our technicians: Helen Turner from the Electron Microscope Facility, Jonnathan van Harselaar for his support and training on the wire Electric Discharge Machining (EDM), Dr. Sophia Rodrigues for her continuous support and guidance on equipment utilization, and Bradley Scott from the School of Engineering workshop for timely specimen preparation. I am also grateful to the administrative officers of the School of Engineering, Mary Dalbeth and Natalie Shaw.

I extend my thanks to all members of the material research team for their assistance with experimental work, particularly to Jingnan Ma, Max Zhai, and Mengqi Jia. Additionally, I am grateful to PhD student Balakrishnan Manogar for his valuable advice, support, and engaging motivational discussions.

Finally, I express my deepest gratitude to my parents, Anil Das and Bharati Das, back home in India, for their unwavering inspiration, blessings, and support. I also extend my appreciation to my brother, Nabakumar Das, and his family, Tiyasa Das and their children Anisha Das and Sumit Das, residing in Hamilton, New Zealand, for their steadfast support throughout this journey. Their unwavering encouragement has been a guiding light. Lastly, I acknowledge my beloved wife, Mou Das, and son, Indranil Das, for their continuous encouragement, unwavering support, and positive motivation during both challenging and rewarding times.

Disclaimer

The author used an artificial intelligence (AI) language model to help with editing this thesis because he is not a native English speaker. This was done to check for and fix spelling and grammar mistakes, to preserve coherence and consistency in language, and to make case study phrasing more precise. Additionally, care was taken to make sure that when the AI made edits to fix grammatical mistakes or linguistic inconsistencies, it didn't unintentionally introduce plagiarism.

Contents

List of Tables

List of Figures

List of Abbreviations

Acronym	Abbreviations
AC	Alternating current
ACT	Actual
AI	Artificial intelligence
ASS	Austenitic Stainless Steel
BCC	Body centred cubic
BM	Base metal
CT	Compact tension
CDRFW	Continuous Drive Rotary Friction Welding
CEQ	Carbon equivalents
CMOD	Crack Mouth Opening Displacement
CMT	Cold Metal Transfer
CNC	Computer numerical control
CS	Carbon steel
CTOD	Crack tip opening displacement
CVN	Charpy V-notch
DB	Diffusion bonding
DC	Direct current
DCEN	Direct current electrode negative
DCEP	Direct current electrode positive
DCRP	Direct current reverse polarity
DCSP	Direct current straight polarity
DMW	Dissimilar metal welds
DoE	Design of experiment
EBW	Electron beam welding
EDM	Electric Discharge Machining
EDS	Energy-Dispersive Spectroscopy
EPFM	Elastic-Plastic Fracture Mechanics
ER	Electrode Rod
EWTh	Electrode Tungsten - Thoriated
FCAW	Flux-cored arc welding
FCC	Face centred cubic
FCGR	Fatigue crack growth rate
FL	Fusion Line
FSW	Friction stir welding
FT	Fracture toughness
FW	Forge welding

FZ	Fusion zone
GMAW	Gas–metal arc welding
GTAW	Gas tungsten arc welding
HAZ	Heat affected zone
HB	Brinell Hardness
HCF	High cycle fatigue
HCP	Hexagonal close packed
HCS	High Carbon Steel
HF	Hydrofluoric Acid
HRC	Hardness Rockwell C Scale
HV	Vickers Hardness
ID	Inner diameter
IFW	Inertia friction welding
IGC	Inter granular corrosion
IGC	Inter Granular Corrosion
IRFW	Inertia Rotary Friction Welding
LBW	Laser beam welding
LCF	Low cycle fatigue
LEFM	Linear Elastic Fracture Mechanics
LFW	Linear friction welding
MCH	Machined
MCS	Medium carbon steel
MIG	Metal Inert Gas
MTS	Miniaturized tensile specimen
N	Normalized
NA	Not Applicable
NDT	Non-destructive test
OAW	Oxyacetylene welding
OD	Outer diameter
PAW	Plasma arc welding
PM	Parent metal
PPM	Parts per million
PSB	Persistent Slip Band
PWHT	Post weld heat treatment
RFW	Rotary friction welding
RPM	Revolutions per minute
RPV	Reactor pressure vessel
SAW	Submerged arc welding
SCC	Stress-corrosion cracking

SEM	Scanning electron microscopy
SENB	Single edge notched bend
SENT	Single edge notch tension
SFE	Stacking fault energy
SI	System international
SMAW	Shielded metal arc welding
SS	Stainless steel
TIG	Tungsten Inert Gas
TIMETAL	Titanium Metal
TMAZ	Thermo-mechanically affected zone
TMCP	Thermomechanical controlled processing
TTT	Time temperature transformation
UK	United Kingdom
UTS	Ultimate Tensile Stress
WCL	Weld centre line
WCZ	Weld centre zone
WM	Weld metal
WZ	Weld zone
YM	Young Modulus
YS	Yield stress at 0.2% strain offset

Acronym	**Company/Organisation**
AFRC	Advanced Forming Research Centre
AISI	American Iron and Steel Institute
ASTM	American society of testing and materials
ATI	Allegheny Technologies Incorporated
AWS	American welding society
EN	European Norm
IIW	International Institute of Welding
IS	Indian standard
ISO	International organization for standardization
MTC	Manufacturing Technology Centre
NMIS	National Manufacturing Institute Scotland
NAMRC	Nuclear Advanced Manufacturing Research Centre
TIMET	Titanium Metal Corporation

Chapter 1

1 Introduction

1.1 Background

Dissimilar metal weld joints play a pivotal role in a numerous of modern industrial applications, spanning aerospace, automotive manufacturing, shipbuilding, oil and gas production, power generation, and medical device manufacturing. These joints involve the fusion of different metals with varying compositions, properties, or structures, resulting in connections endowed with unique mechanical and chemical properties. The rising popularity of dissimilar welding is driven by manufacturers' pursuit of cost optimization, performance enhancement, weight reduction, improved design flexibility and functionality, and adaptation to the complex and diverse demands of modern technology across various environments. However, welding dissimilar metals presents greater complexity compared to welding similar metals. The coalescence of two or more dissimilar parent metals introduces compositional gradients and microstructural changes, leading to significant variations in chemical, physical, and mechanical properties across the joint. Despite its challenges, dissimilar metal welding offers numerous benefits, including the flexibility to design products that effectively leverage the specific properties of each material. This approach not only fosters cost efficiency in material procurement but also drives research opportunities for advancing welding processes. To address the challenges inherent in dissimilar welding, it is essential to precisely select appropriate welding processes and electrodes and identify suitable non-destructive testing methods. Service failures attributable to factors such as fracture, fatigue, and corrosion underscore the complexities associated with dissimilar metal welding. In this thesis, our objective is to explore the intricacies of dissimilar metal weld joints while striking a balance between innovation and practical solutions to the challenges inherent in welding technology.

1.2 Statement of the Problem

Welding dissimilar materials to create defect-free welded preforms demands a thorough understanding of how welding process parameters impact microstructural characteristics and mechanical properties. Understanding this relationship is paramount for designing reliable and resilient structures. While numerous studies

have investigated the correlation between welding parameters, microstructure, and common mechanical properties such as tensile strength and hardness, a significant gap persists in comprehending the intricate relationship among welding parameters, microstructure, and critical mechanical properties like fracture toughness and fatigue in dissimilar material joints. These properties serve as pivotal considerations in dissimilar welding, ensuring joint integrity and reliability, predicting service life, optimizing welding procedures, and adhering to codes and regulations. The absence of systematic exploration into this critical relationship poses a substantial obstacle to the advancement of welding techniques for dissimilar materials.

1.3 Purpose of the Research

The present study investigates the feasibility of utilizing RFW process to create reliable dissimilar weld joints. This exploration involves two main objectives: Firstly, to evaluate the potential of RFW in creating robust connections between S355J2 and SS316L. These weld joints hold significant potential for dissimilar metal connector applications across diverse industries. Secondly, the study aims to evaluate the effectiveness of RFW in joining two distinct titanium alloys, Ti-64 and Ti-1023, to facilitate the fabrication of various components within an aero engine. Furthermore, the research focuses on a comparative analysis between RFW and TIG welding methodologies. This comparative evaluation seeks to explain the differences in outcomes between the two welding processes regarding the characterization of the dissimilar weld joints. By exploring these objectives, the research endeavours to shed light on the efficacy and potential advantages of RFW in dissimilar metal welding applications, offering valuable insights for industries reliant on such welding processes.

Objectives:

- To explore the impact of parameters in welding process on the microstructural characteristics and mechanical properties such as fracture toughness and fatigue life of welded ring preforms.
- To recommend the most suitable welding process by analyzing microstructural patterns and evaluating mechanical properties.

1.4 Research Questions or Hypotheses

The study's primary research questions, derived from the existing literature (Chapter 2), include the following:

- How do various welding processes influence the microstructural characteristics of dissimilar material joints, specifically in the welding processes involving S355J2 to SS316L and titanium alloy Ti-64 to Ti-1023?
- What are the relationships between microstructural characteristics and mechanical properties, such as fracture and fatigue, within the realm of welded ring preforms? Additionally, how do these relationships evolve with alterations in the welding process?

1.5 Significance of the Research

The significance of this research lies in addressing a critical gap in our understanding of welding dissimilar materials, particularly focusing on the feasibility of RFW processes. Welding dissimilar materials is essential for various industrial applications, including nuclear, chemical processing, oil & gas, and aerospace engineering. The success of these applications depends on defect-free welded preforms with optimal microstructural characteristics and mechanical properties.

The outcomes of this research have profound implications for the industry, as it will provide valuable insights into the optimization of dissimilar material joints. Specifically, the understanding gained from the influence of welding process parameters on microstructural characteristics and mechanical properties will contribute to the optimization of welding procedure which helps in design and fabrication of reliable and robust structures. Additionally, suggesting the best welding technique based on a comprehensive analysis will guide practitioners in selecting optimal methods for enhancing the structural integrity of dissimilar material joints.

1.6 Research Design and Methodology

This research project will utilize stock obtained from AFRC, University of Strathclyde, comprising thick steel pipes (150mm OD, 106mm ID). These pipes underwent machining to achieve 114 mm ID and 40mm thick sections,

subsequently welded together using RFW to create hybrid ring preforms. To facilitate comparative analysis, identical preforms were also fabricated using TIG welding. Titanium preforms were prepared from solid round bars (35mm diameter, 75mm length) and subsequently welded using RFW. The initial phase will involve macroscopic examination and hardness characterization for both steel and titanium alloys. The microstructural characterization will be conducted using Scanning Electron Microscopy (SEM) to assess the microstructural features resulting from the welding processes in both steel and titanium alloys. Mode-I fracture toughness tests will be performed on samples from welded hybrid transition couplings, exploring different welding processes, including RFW and TIG, for steel samples. For titanium, fatigue testing encompasses HCF will be performed on samples from welded hybrid transition titanium couplings produced through RFW. The research will conclude with a comprehensive analysis of the data obtained from microstructural characterizations, fracture toughness tests, and fatigue tests. Additionally, comparative assessments between different welding processes to discern their influence on microstructural and mechanical properties.

1.7 Scope and Limitations

The scope of this research encompasses the feasibility of RFW processes for dissimilar material welding, specifically focusing on two significant categories of materials: welding S355J2 to SS316L, and welding titanium alloys Ti-64 to Ti-1023. Conduct a comparative analysis between RFW and TIG welding on their outcomes in characterizing the dissimilar weld joints.

One limitation of this research is the restricted size of the feedstock, which has only allowed for micro-tensile testing. The small size has made it impossible to attain a plane-strain fracture toughness state, which limits the extent of mechanical property evaluations and fracture toughness testing that can be performed.

1.8 Overview of Thesis Structure

The thesis comprises five chapters structured in the following sequence: introduction, literature review, experimental methodology, results and discussions, and conclusion with future work.

Chapter 1 sets the scene for current research, providing necessary background information. It defines the scope of the thesis, articulates research questions, outlines the problem statement, and emphasizes the significance of the research. Additionally, this chapter offers an overview of the research methodology and outlines the thesis structure.

Chapter 2 conducts a comprehensive literature review supporting the research questions and objectives. It synthesizes existing literature on dissimilar welding, covering various materials such as CS, SS, Ti-64, and Ti-1023. This chapter identifies challenges in dissimilar welding, discusses the impact of welding process parameters, highlights the application of different welding processes, particularly RFW, and examines relevant material properties.

Chapter 3 provides detailed information on the materials and experimental procedures used in the thesis. It is divided into two parts. The first segment outlines the steel experiments, while the subsequent part details the titanium experiments. It includes comprehensive descriptions of specimen extraction methods, testing sample geometries and specifications, and testing equipment and methods for analysing experimental results.

Chapter 4 presents the results and discussions, again divided into two sections. The first part discusses the results of steel experiments, while the latter part focuses on titanium experiments. It presents the results of various tests such as hardness, tensile strength, microstructural analysis, fracture toughness, and fatigue testing. Additionally, this chapter provides detailed discussions of these results, highlighting correlations between outcomes and microstructure, material properties, and welding process parameters.

Chapter 5 summarizes the conclusions of the thesis and provides recommendations for future work.

Chapter 2

2 Literature Review

2.1 Introduction to Welding

Welding is a sophisticated manufacturing method that coalesces two or more components by applying heat, pressure, or a combination of both. These parts can be composed of similar or dissimilar materials, resulting in a unified part known as a weld. Figure 1 illustrates a schematic view of the various parts involved in a weld. The methods employed to execute welding are referred to as welding process [1] which encompass a diverse array of techniques. These processes are typically categorized into two primary groups: (i) Fusion welding and (ii) Solid state welding.

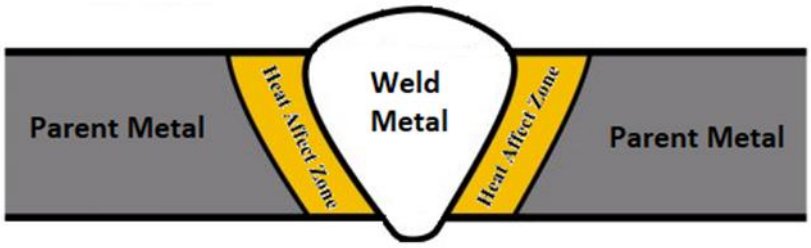

Figure 1: A schematic view of different parts of a weld.

Fusion welding is a significant method of joining that relies on the fusion or melting of the parent metal during the welding process. This approach encompasses three primary categories of fusion welding processes: (i) Gas welding, which includes Oxyacetylene welding (OAW), (ii) Arc welding, which involves Shielded metal arc welding (SMAW), Gas–tungsten arc welding (GTAW) or TIG, Plasma arc welding (PAW), Gas–metal arc welding (GMAW), Flux-cored arc welding (FCAW), and Submerged arc welding (SAW), and (iii) High-energy beam welding, which includes Electron beam welding (EBW) and Laser beam welding (LBW) [1].

Solid-state welding consists of a collection of joining methods that form welds without melting the parent metal. These methods employ a blend of heat, pressure, and duration to accomplish the welding process. The main varieties of solid-state welding include: (i) Resistance welding, (ii) Friction welding (FW), (iii) Diffusion welding (DFW), and (iv) Ultrasonic welding (USW) [1].

Within the realm of solid-state welding methods, FW emerges as highly effective, especially for welding dissimilar metals. This method encompasses a group of techniques that rely on the heat generated from friction and substantial deformation occur in plastic stage due to forging of the parent metal. It is further categorized into: (i) Rotary friction welding (RFW), which consists of: (a) Inertia friction welding (IFW) and (b) Continuous drive friction welding (CDFW), (ii) Linear friction welding (LFW), and (iii) Friction stir welding (FSW).

Welding is found to be a superior fabrication process when compared to alternatives like soldering, brazing, riveting, and bolting. It yields robust and enduring joints capable of withstanding mechanical forces, vibrations, and diverse environmental conditions. Moreover, welding is cost effective. highly productive, reliable process. As a result, it finds widespread application in joining both similar and dissimilar materials across various industries including fabrication, manufacturing, and construction.

2.1.1 Dissimilar Welding

A dissimilar weld involves the joining of two or more parent metals with differing compositions. In such welds, the parent metals exhibit compositional gradients and microstructural alterations, resulting in significant variations in chemical, physical, and mechanical properties throughout the joint. Consequently, welding dissimilar metals is considerably more intricate than welding similar metals [2].

While welding has been practiced since ancient times, the specialized field of dissimilar metal welding emerged much later, following the invention of arc welding in the late 19th century. Various arc welding processes such as SMAW, GTAW, and GMAW were subsequently developed in the early 20th century, offering new possibilities for joining dissimilar metals. The demand for joining dissimilar metals surged during World War II as industries attempted to pioneer new materials and technologies for military applications. This era and beyond witnessed substantial advancements in welding techniques and metallurgy, resulting in refined methods for welding dissimilar metals [2].

Conventional fusion welding techniques, depicted in Figure 2, are employed for welding dissimilar metal combinations. However, the fusion welding of dissimilar metals presents several challenges, foremost among them being metallurgical

incompatibility. This may lead to the formation of brittle phases and the segregation of high and low melting phases due to chemical disparities, potentially resulting in significant residual stresses from physical mismatches. Despite these difficulties, fusion welding remains one of the most prevalent methods for joining metals [3].

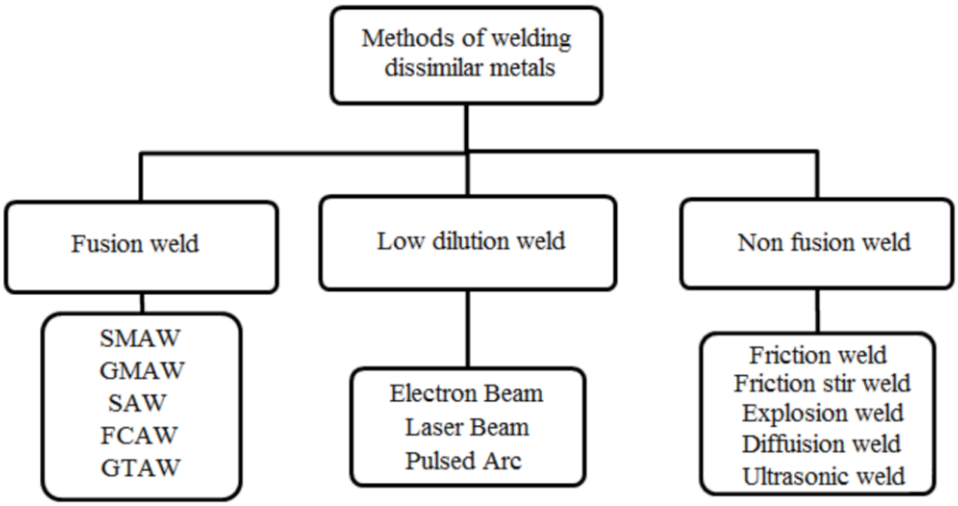

Figure 2: Common welding methods for joining dissimilar metals [3].

Dissimilar metal welding has become even more capable in the 20th and 21st centuries due to developments in laser, electron beam, and solid-state welding processes like diffusion, explosion, friction, friction stir, and ultrasonic welding as well as a greater comprehension of metallurgy and material science. One of the most useful fusion welding techniques for joining steel and aluminium is laser welding. Since the base metals (BMs) do not create intermetallic compounds during non-fusion joining, some of the issues associated with fusion welding can be resolved [3].

Modern arc welding processes, such as cold metal transfer (CMT), have been instrumental in producing satisfactory joints between aluminium and specially zinc-coated steel without the formation of intermetallic compounds [4]. One popular technique for dissimilar welding is robotic friction welding. In particular, robotic technology specifically designed for mass production applications has been developed to enable continuous welding of steel to aluminium through the integration of FSW [5]. Furthermore, dissimilar joint welding has been accomplished with the use of USW [6]. Hybrid welding techniques have been introduced for dissimilar metals by Thomy and Vollertsen [7]. In their investigation,

1.2 mm diameter filler wire (SG-AlSi12) was used to join zinc-coated steel with sheets of aluminium alloy (AA6016) in a butt joint configuration with thicknesses ranging from 1 mm using hybrid welding process combining GMAW and Laser.

2.1.2 Application of Dissimilar Welding

Dissimilar welding, which combines CS and SS, is widely used in a variety of industries, including refineries, offshore oil and gas platforms, and nuclear power plants, despite its many difficulties. Especially notable are the differentiable welded joints between CS and austenitic stainless steel (ASS), which are commonly used in a variety of structures such as spacecraft, pressure vessels, and offshore installations. S355JR and SS316L are common examples of CS and ASS, respectively, among these. In addition to meeting the requirements of the service environment, the joints that are created between S355JR and SS316L dissimilar steels also help to lower production costs. Low alloy carbon steels are commonly used in nuclear power plants' reactor pressure vessels (RPVs) because of their remarkable qualities, which include high strength, resistance to corrosion, resistance to shock and vibration, enhanced formability during manufacturing, superior mechanical and irradiation properties, and low activation capability. In this case, the RPV is made of CS. In nuclear power plants, on the other hand, SS is favoured for the main pipeline because of its exceptional creep resistance and remarkable corrosion resistance. As a result, pipelines in nuclear power plants should be made of SS. A dissimilar weld is required to make the connection between CS RPVs and SS pipelines easier, as its schematic illustrates in Figure 3 [8].

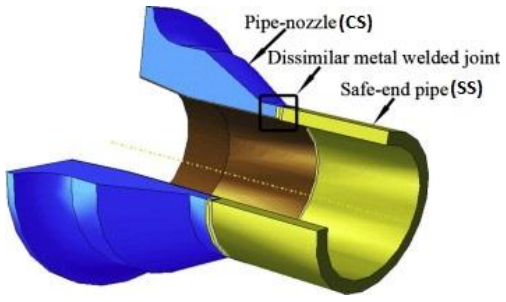

Figure 3: Schematic showing dissimilar metal weld joint between CS pipe nozzles of reactor pressure vessel and SS safe end pipe [9].

Dissimilar welding joints are essential in many industries, including refineries, oil and gas platforms, and process piping, heat exchangers, and pressure vessels. They

can be used to combine SS with CS or Inconel with CS. As the global demand for energy continues to surge, the exploration and extraction of oil and natural gas have witnessed a significant uptick in recent decades. This heightened activity has brought forth complex oil and gas fields abundant with diverse corrosive mediums, intensifying the corrosion challenges faced during drilling operations and long-distance pipeline transportation. To address these issues, materials like American Iron and Steel Institute 316 (AISI 316), a common ASS, or SS316L steel, a modified version of it, are used to ensure the safe and effective extraction and transportation of corrosive oil and gas. These materials offer enhanced resistance against corrosion, making them indispensable in harsh operational environments. Moreover, to enhance design strength and optimize cost-efficiency, the consideration of dissimilar joints between S355JR and SS316L is gaining prominence. By minimizing risks of corrosion and maintaining the integrity of vital infrastructure and equipment in the oil and gas sector, this strategic approach seeks to capitalize on the advantages of CS and ASS.

Structural parts of airplanes and aeroengine undergo rigorous cyclic loading conditions due to repeated flight cycles. Titanium alloy has emerged as a crucial material for such components in aircraft, owing to its exceptional performance, high strength, and favourable combination of ductility and fracture toughness [10]. The alloy is also used in large-scale landing gears. To improve aero engine design and reduce the fabrication cost, dissimilar joint of Ti-64 and Ti-1023 is being considered as an option.

2.2 Steels and Titanium alloys and their welding

Selection of welding process to carry out welding depends on material weldability characteristics. The characteristic of a material that indicates how easily it can be welded is called weldability. This property often determines the requirement of pre-heat, post weld heat treatment, and any other precautionary steps are required to maintain the material properties degraded by the welding operation. The weldability of steel is generally determined by carbon equivalents (CEQ). Equation 1 was developed by the International Institute of Welding (IIW) in the United States and Europe to define CEQ.

$$CEQ = C + \frac{Mn}{6} + \frac{(Cr + Mo + V)}{5} + \frac{(Ni + Cu)}{15} \qquad \text{Equation 1}$$

Because of its higher hardenability, steels with higher CEQs are more likely to cause issues during welding. Steel with high carbon equivalent is more likely to form hard, brittle microstructures during the fast heating and cooling cycles of welding processes. In case of titanium alloys, the primary challenge in the welding is the removal of atmospheric impurities, such as oxide formation. Hence, other than oxidation, weldability of titanium alloys depends on material composition which mainly influences the quality and integrity of welding joints. Large amounts of beta phase, stabilized by elements like chromium, make alloys difficult to weld; in contrast, pure titanium, alpha, and alpha-beta alloys are readily weldable.

2.2.1 Steels

Steel, often described as an iron and carbon alloy, undergoes a fundamental transformation with the addition of carbon. Pure iron, lacking sufficient strength for various applications, is strengthened by the infusion of carbon to bolster its resilience and hardness. The incorporation of carbon, in varying proportions, categorizes steel into distinct groups based on its carbon (C) content. Figure 4 Illustrates a broad classification scheme for steel, delineating its diverse compositions and properties.

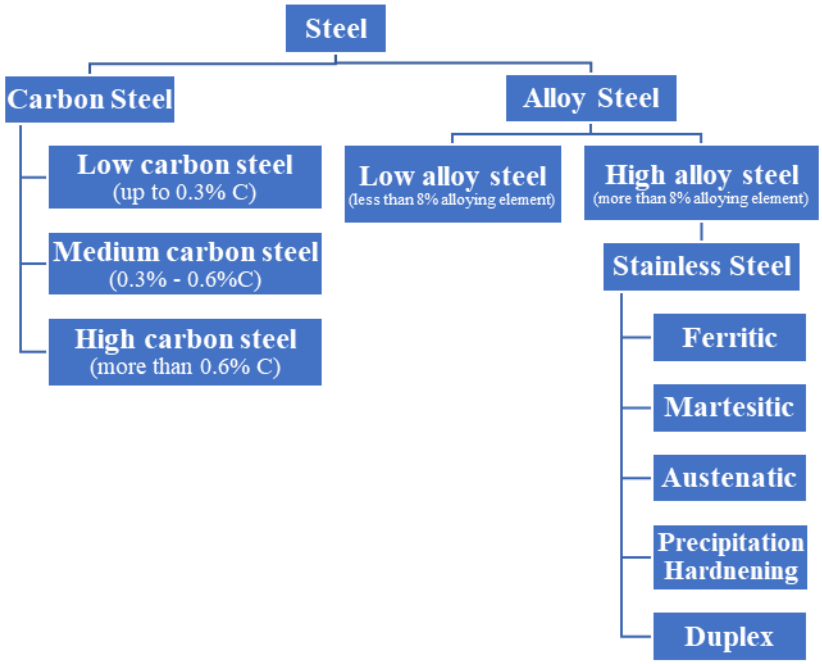

Figure 4: Classification of steel [11].

CS represents a pivotal category within the realm of steel, where the content of carbon primarily dictates its properties and characteristics. Alongside carbon, minute proportions of silicon (typically around 0.60%) and aluminium serve as deoxidizers. Additionally, manganese (usually about 1.65%) is introduced to function as a sulphide former in CS compositions. CS are typically categorized into three main groups: (i) low carbon steel (LCS) or mild steel (MS), characterized by a carbon content of up to 0.3% max., (ii) medium carbon steel (MCS), containing carbon within the range of 0.3% to 0.6% max., and (iii) high carbon steel (HCS) featuring a carbon content exceeding 0.6% [11]. Due to its affordability compared to other steel variants, CS finds widespread use across diverse applications, cementing its position as a material of choice in various industries.

Alloy steel represents a distinctive category wherein the properties and characteristics of steel are determined not by carbon but by alloying elements such as chromium, nickel, molybdenum, vanadium, boron, niobium, among others. This diverse range of alloying elements contributes significantly to shaping the performance attributes of alloy steel. The classification of alloy steel is delineated into two main categories: (i) low alloy steel, featuring a maximum total of 8% alloying elements and (ii) high alloy steel, comprising a total of a total of more than 8% alloying elements. The application range of this steel variant is expanded by the alloying elements that improve its corrosion resistance, fatigue resistance, and fracture toughness [11]. Among the diverse spectrum of steel categories, low carbon micro-alloyed steel emerges as a prevalent choice in various industrial sectors, including structural components, automobile chassis, pipelines, and other applications necessitating a balance of strength, ductility, and weldability. This steel offers a cost-effective alternative to designer instead of expensive high-strength steels while providing excellent performance and reliability. In nuclear power plants, reactor pressure vessels are fabricated with S355J2 steel. Likewise, in oil and gas industry, beams, tubular essential for fabricating offshore platforms are made of S355J2 steel, known for its remarkable strength and stiffness, making it an ideal choice for heavy-duty applications like cranes and heavy machinery. Furthermore, its exceptional resistance to abrasion and wear makes it particularly well-suited for environments where durability is paramount.

S355J2 steel: This steel is a low carbon micro-alloyed variant classified according to the European standard EN 10025. Symbol 'S' denotes structural steel, while the numerical designation '355' represents its nominal maximum yield strength in megapascals (MPa). It undergoes manufacturing processes involving either normalizing (N) or thermomechanical controlled processing (TMCP). Final steel produced in both the routes contains ferrite and pearlite microstructure as illustrated in Figure 5. According to a microstructural analysis of S355J2+N, acicular or Widmanstätten ferrite is present in trace amounts, but allotriomorphic ferrite makes up 80% of the microstructure and pearlite the remaining 20% [12]. The results of the hardness test indicate a measurement of roughly 168 HV0.1 and an average size of 15µm for equiaxed grains measured in the through-thickness direction. For reference, Table 1 lists the typical mechanical, chemical, and physical characteristics of S355J2 steel.

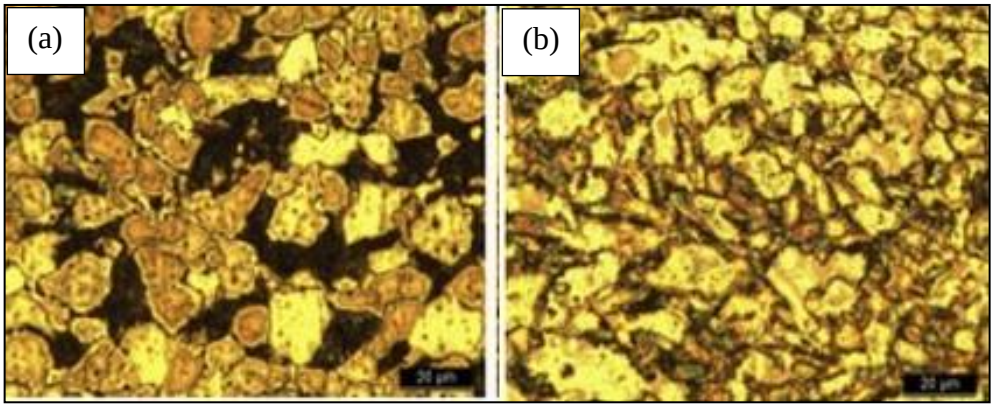

Figure 5: Typical microstructure of S355J2 steel in (a) Normalized and (b) TMCP condition [12]

Table 1: Typical chemical, mechanical and physical characteristics of S355J2 steel [13, 14]

Chemical composition

Element	Content in (%) Max.
C	0.22 – 0.24
Si	0.60
Mn	1.70
P	0.035 - 0.045
S	0.035 - 0.045
N	0.014

Mechanical Properties

Property	Value
Yield strength, MPa	275 - 355
Tensile Strength, MPa	450 - 680
Elongation (%)	17 - 22
Hardness, (HB)	140 - 190
Impact toughness, Joules (at -20°C)	27

Cu	0.60	Fracture toughness (K_{1C}), MPa√m [15]	38

Physical properties

Property	Value
Density (kg/m3)	7800
Shear Modulus (GPa)	80
Poisson's ratio	0.3
Young Modulus (GPa)	190 - 210
Coefficient of linear thermal expansion 'α' °K^{-1}	12 x 10^{-6}
Thermal conductivity, (W/m°K)	40 - 45
Electrical resistivity at ambient temperature (μΩm)	0.2 – 0.25

Stainless Steel 316L (SS 316L): SS316L is considered austenitic grade SS. Due to its austenitic grade, it is very formable, weldable, and corrosion resistant. This steel has great impact strength at low temperatures, which makes it ideal for cryogenic applications.

Table **2** provides a detailed overview of its varied properties and typical chemical composition. The non-magnetic nature of ASS is one of their distinctive qualities, which adds to their adaptability in a variety of industries. The designation 'L' in SS316L indicates that this SS contains a low carbon content, typically less than 0.04%. This characteristic is instrumental in preventing sensitization issues commonly associated with welding processes. Its exceptional resistance to corrosion highlights its importance in a variety of industrial applications and makes it a preferred option across a broad range of sectors, including nuclear, oil and gas, power plants, and the dairy industry.

The microstructure of SS316L as depicted in Figure 6, exhibits typical austenitic structure with annealing twins. Because of its low stacking fault energy (SFE), which is crucial in controlling the ease of cross-slip and allowing different deformation mechanisms to be activated at different stages of deformation, this steel notably shows a high rate of work hardening during deformation. Twinning is commonly observed subsequent to the initiation of multiple slip systems and is commonly regarded as a mechanism of deformation for SS316L. Twins manifest in two primary patterns: suspended twin and transgranular twin. [16]

Figure 6: Typical microstructure of SS316L [17]

Table 2: Typical chemical, mechanical and physical characteristics of SS316L [18, 19]

Chemical composition	
Element	Content in (%) Max.
C	0.035
Si	1.0
Mn	2.0
P	0.045
S	0.030
Cr	16 – 18
Ni	10 - 14
Mo	2 - 3

Mechanical Properties	
Property	Value
Yield strength, MPa	170 - 200
Tensile Strength, MPa	485 - 500
Elongation (%)	35 - 40
Hardness, (HB)	200 - 217
Impact toughness, Joules (at -20°C)	150
Fracture toughness, MPa√m	112 - 278

Physical properties	
Property	Value
Density (kg/m3)	8000
Shear Modulus (GPa)	74 - 82
Poisson's ratio	0.27
Young Modulus (GPa)	190 - 200
Coefficient of linear thermal expansion 'α' $°K^{-1}$	16 – 18 x 10^{-6}
Thermal conductivity, W/m^oK	13 – 17
Electrical resistivity at ambient temperature (μΩm)	0.8

2.2.1.1 Welding of S355J2 steel and SS316L

Owing to its low carbon content, S355 steel is easily weldable in both arc and solid-state welding processes, requiring minimal special precautions to avoid weld cracking. In the HAZ, faster cooling rates and the use of incorrect pre-heat temperatures for welding can result in the formation of hardened phases like martensite, which have higher hardness than the parent material and poor mechanical properties. Significant findings are revealed by Le, et al. [20] investigation into the effect of cooling rate on the HAZ microstructure of dissimilar welds between CS and SS304L that were produced using the SMAW process. Within the CS HAZ, the microstructure changes to martensitic at a cooling rate of 100°C/second; in contrast, ferrite and pearlite microstructures can form at much slower cooling rates.

SS316L's low carbon content plays a pivotal role in preventing sensitization, enhancing its weldability across a range of fusion welding processes. Nevertheless, it encounters challenges such as hot cracking, solidification cracking, and susceptibility to sensitization due to chromium carbide precipitation at grain boundaries. Additionally, post-weld heat treatment can lead to the formation of intermetallic like the sigma phase, while high interpass temperatures can generate significant residual stress due to its austenitic microstructure. To mitigate these issues, low heat input welding processes like TIG, EBW, LBW, and friction welding are preferred. Slower cooling rates and the maintenance of low interpass temperatures are crucial strategies to curb the accumulation of residual stress during SS316L welding [21].

The weld joints between S355J2 and SS316L exhibit several limitations during the welding process due to compositional differences between the two materials: (a) the formation of harmful or secondary phases in the weld metal (WM) is caused by carbon loss resulting from migration and diffusion in the S355JR HAZ, (b) alloying element dilution in the WM zone, and (c) grain growth in the HAZ, which causes a significant deterioration in the mechanical properties and resistance to corrosion of the weld seam. The choice of suitable welding processes that can preserve low heat input, maintain low interpass temperature, guarantee a narrow HAZ, and enable a slow cooling rate are crucial to prevent these issues.

Despite the numerous challenges associated with conventional arc welding in achieving a sound dissimilar weld between S355J2 and SS316L, the industry still favours the TIG welding process for fabricating dissimilar weld joints. A study on the microstructure, mechanical characteristics, and corrosion behaviour of a dissimilar welded joint made with gas tungsten arc welding in multiple passes was carried out by Huang, et al. [22]. They observed no formation of intermetallic, no sensitization issues, and high tensile strength of WM in compared to the SS316L parent metal. However, they noticed carbon depletion at the interface of S355JR/WM. In several studies, friction welding has emerged as a superior process for creating dissimilar welds between S355J2 and SS316L. In their investigation of dissimilar welding between S355J2 and SS316L. Lalvani, et al. [23] used both the EBW and the RFW processes. They discovered while the RFW process showed differences in microstructure characteristics throughout the weld, without much fluctuating in hardness, EBW resulted in a weld interface that was 2-3 mm wide, had a distinct HAZ, and displayed a significant gradient in hardness between the weld (3 times higher) and the parent. Tensile strength of the welds was higher than that of the parent SS, according to both welding processes.

2.2.2 Titanium alloys

Pure titanium possesses several remarkable characteristics: it is lightweight, strong, corrosion-resistant, and boasts a lustrous metallic colour. Titanium has comparatively low thermal conductivity (14.03 W/m°K), density (4.5 g/cm^3), and thermal expansion coefficient (8.5 x 10^{-5}/°C) at room temperature. Nonetheless, it has a moderate Young's modulus (112.5 GPa) and higher melting and boiling points (1668°C and 3287°C, respectively) [24]. The α/β phase transformation temperature, which is approximately 882°C, is the temperature at which pure titanium experiences a stable allotropic transformation. The alpha (α) phase has a hexagonal close packed (HCP) crystal structure at low temperatures, while the beta (β) phase has a body-centred cubic (BCC) crystal structure at high temperatures (above 882°C) as illustrated in Figure 7 [24].

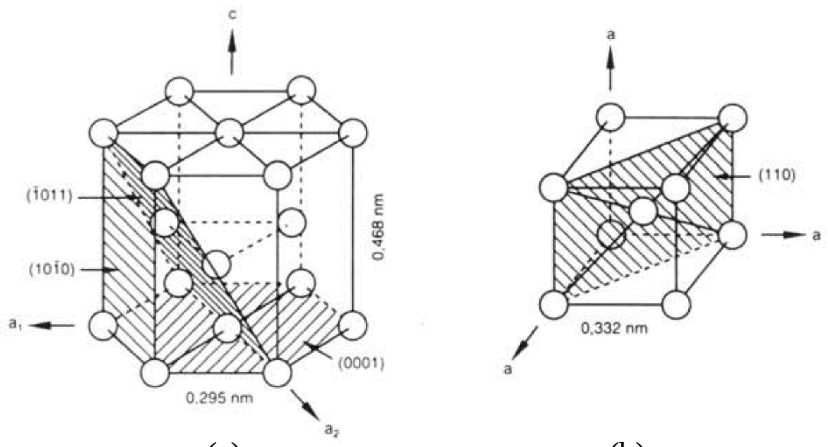

(a) (b)

Figure 7: Unit cells of titanium (a) HCP - α phase and (b) BCC- β phase [24].

Because of its remarkable blend of high structural performance and lightweight qualities, titanium alloy has become an essential material for jet engine and structural parts in aircraft. Among structural metals that are frequently used, titanium alloys have the highest corrosion resistance, which highlights their widespread use in chemical transportation [24] and potential applications in the marine industry. Furthermore, titanium alloys are the most biocompatible of all common metals, which makes them ideal for biomedical applications like dental and body implants.

There are three categories of alloying elements which are added to pure titanium to make titanium alloys. They are: α stabilizers, β stabilizers and neutral elements as depicted in Figure 8. Al and the interstitial elements (O, N, and C) make up α stabilizers, which can expand the α phase region by raising the β phase transformation temperature in response to an increase in solute concentration. Isomorphous elements (V, Mo, Nb, Ta) and eutectoid elements (Fe, Mn, Cr, Ni, Cu, Si, H) are examples of β stabilizers; by increasing the solute content, they can lower the β phase transformation temperature and expand the β phase region. Other alloying elements, such as Zr and Sn, are referred to as neutral elements since they have minimal impact on the phase transition of titanium. Titanium alloys can be broadly categorized into three groups: α titanium alloys, α+β titanium alloys, and β titanium alloys. This classification is based on the presence of final phases at room temperature [24].

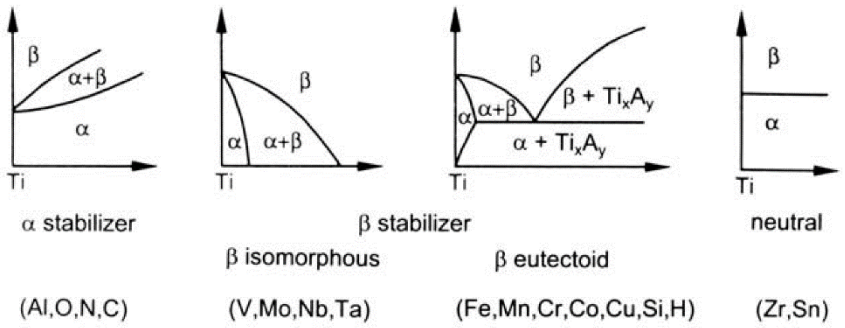

Figure 8: Schematic shows the effect of alloying addition on phase diagram of Ti-alloys [24].

Ti-6Al-4V (Ti-64): Ti-64 is a titanium alloy of great significance because of its distinct composition and characteristics. This alloy is classified as α+β because V stabilizes β and Al stabilizes α, allowing the dual phase to remain in place at room temperature refer to Figure 9 (a). Ti-64 is mostly used in the aerospace industry, but it's also used in the chemical, automotive, marine, and medical implant industries. Table 3 displays its appealing mechanical properties. It has the best weldability and good workability. This is because, as Figure 9 (b & c), illustrates, its single-phase mode of solidification protects it against solidification-related cracking which makes it resistant to solidification related cracking [25].

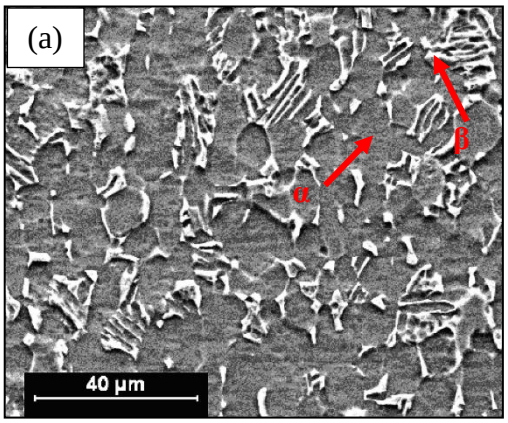

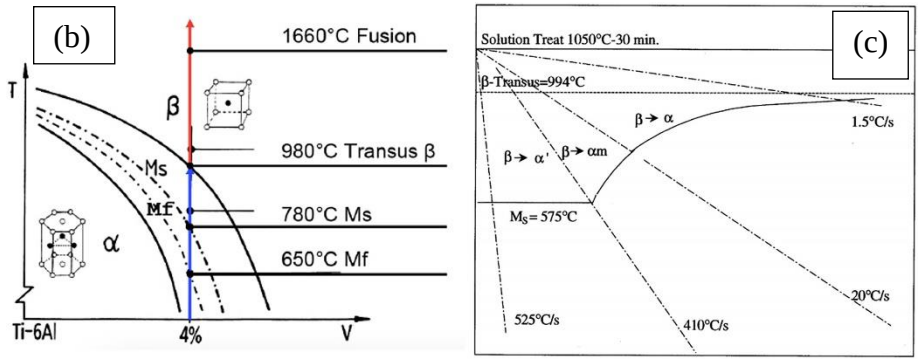

Figure 9: Image shows (a) microstructure of Ti-64, hot rolling (at 1050°C) and followed by annealing heat treatment (at 730°C) slow cooling [26], (b) phase diagram of Ti-64 and (c) phase transformation of Ti-64 as a function of cooling rate [27].

Table 3: Typical chemical, mechanical and physical characteristics of Ti-64 [28]

Chemical composition	
Element	Content in (%) Max.
Ti	90
Al	6
V	4

Mechanical Properties	
Property	Value
Yield strength, MPa	830
Tensile Strength, MPa	900
Elongation (%)	10
Hardness, (HRC)	36
Fracture toughness, (K_{1C}) MPa√m	75
Fatigue strength, MPa [10]	450 - 500

Physical properties	
Property	Value
Density (kg/m3)	4430
Shear Modulus (GPa)	44.0
Poisson's ratio	0.33
Young Modulus (GPa)	114
Coefficient of linear thermal expansion 'α' $°K^{-1}$	9.2×10^{-6}
Thermal conductivity (W/m^oK)	7.0

Ti-1023: This alloy marks a significant milestone as the first commercially available metastable β titanium alloy. The Ti–1023 alloy, created by Timet in 1970,

exhibits exceptional strength coupled with commendable ductility and fracture toughness. Because of its exceptional strength-to-weight ratio, it has been widely used as the main material for the large-scale landing gears of Boeing 777 and Airbus A380 aircraft [29]. Equation 2 and Equation 3 provide an appropriate characterization of the beta phase stability in this alloy in terms of the molybdenum equivalent [30]. This parameter serves as a crucial determinant of the alloy's performance and structural integrity.

$$[\mathrm{Mo}]_{\mathrm{eq}}\mathrm{wt\%} = 1[\mathrm{Mo}] + 2.9[\mathrm{Fe}] + 1.7[\mathrm{Mn}] + 1.7[\mathrm{Co}] + 1.6[\mathrm{Cr}] + 1.25[\mathrm{Ni}] + 0.67[\mathrm{V}] + 0.22[\mathrm{Ta}] + 0.28[\mathrm{Nb}] + 0.44[\mathrm{W}] - 1[\mathrm{Al_{eq}}]$$

Equation 2

$$\mathrm{Al_{eq}} = \mathrm{Al} + \frac{\mathrm{Zr}}{6} + \frac{\mathrm{Sn}}{3} + 10(\mathrm{O} + \mathrm{N}) \qquad \text{Equation 3}$$

For quenching processes, a $[Mo]_{eq.}$ concentration of at least 10% is thought to be required to stabilize the beta phase. To classify titanium alloys, Cotton, et al. [30] proposed distinct demarcations at 8% and 30% $[Mo]_{eq.}$ Alloys that ranged from 8% to 30% $[Mo]_{eq.}$ were classified as "metastable beta," and compositions that were less than 8% were classified as "beta-rich alpha–beta." In contrast, alloys that surpassed 30% were classified as "stable beta" alloys. As illustrated in Figure 10 (a), the phase diagram of titanium alloy delineates the region of metastable β alloys, situated between βc and βs. Within this domain, a mechanically unstable region, delineated between βc and βω exists and composition of Ti-1023 falls in between βc and βω [31, 32]. Figure 10 (b) portrays the Time-Temperature-Transformation (TTT) diagram of Ti-1023, delineating the phase changes occur during time – temperature transformation. Meanwhile, Figure 10 (c) offers insight into the typical microstructure of Ti-1023, featuring primary α embedded within a β matrix [33]. Table 4 provides a comprehensive overview of the alloy's typical chemical composition, physical attributes, and mechanical properties.

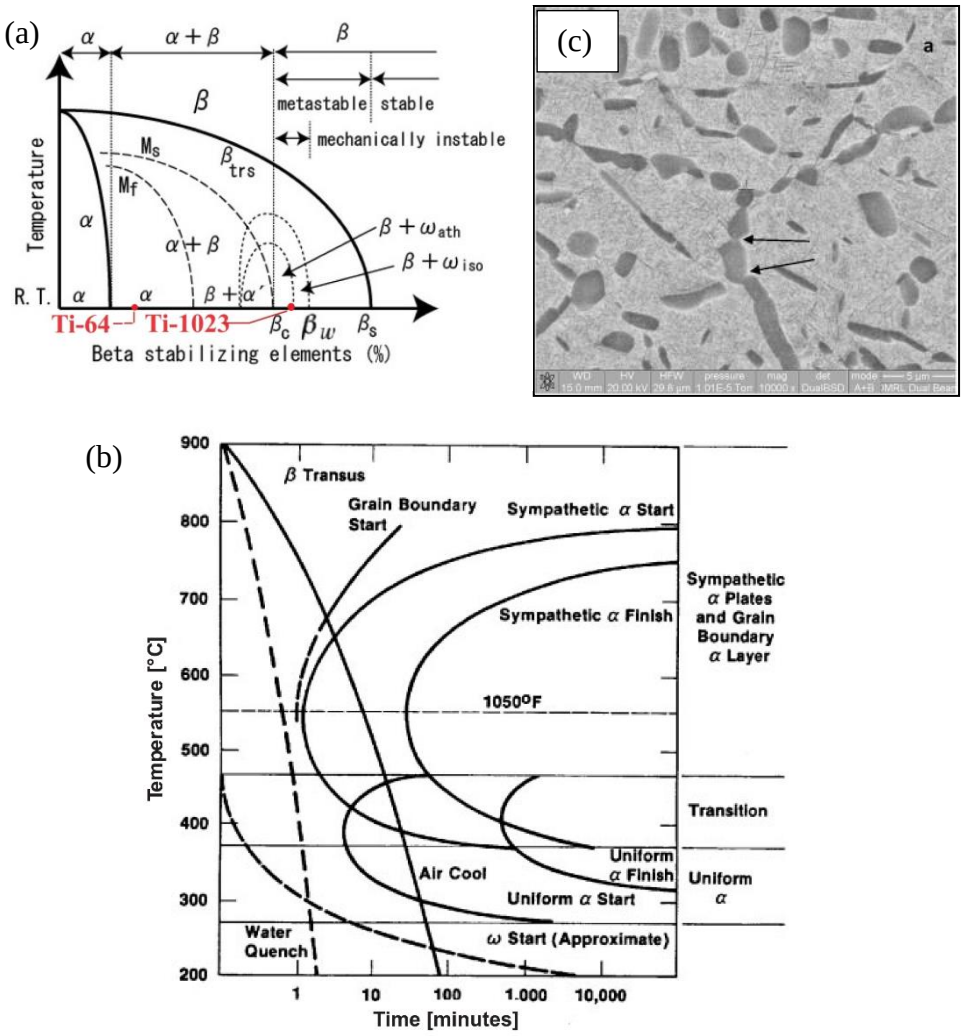

Figure 10: Image shows (a) typical phase diagram of titanium alloys, (b) TTT diagram of Ti-1023 [34] and (c) typical microstructure of solution treated Ti-1023 alloy [33].

Table 4: Typical chemical, mechanical and physical characteristics of Ti-1023, solution treated at 760°C and aged at 350°C [28]

Chemical composition	
Element	Content in (%) Max.
Ti	90
V	10
Fe	2
Al	3

Mechanical Properties	
Property	Value
Yield strength, MPa	1240
Tensile Strength, MPa	1430
Elongation (%)	3.0
Hardness, (HRC)	32
Fracture toughness, (K_{1C}) MPa√m	110

Fatigue strength, MPa [34]	700 - 800

Physical properties

Property	Value
Density (kg/m3)	4650
Shear Modulus (GPa)	41.0
Poisson's ratio	0.33
Young Modulus (GPa)	110
Coefficient of linear thermal expansion 'α' $°K^{-1}$	9.7×10^{-6}
Thermal conductivity (W/m°K)	7.8

2.2.2.1 Welding of Ti-64 and Ti-1023

Weldability remains a classic challenge with titanium and its alloys. In the molten state, the metal rapidly reacts with atmospheric gases, necessitating protective gas shielding for successful fusion welding. The low thermal conductivity of titanium prolongs weld times, especially in low energy density processes like TIG welding. These extended weld times result in slow cooling rates, demanding prolonged gas protection to safeguard the highly reactive titanium. Partial solutions are provided by high energy density techniques like laser and electron beam welding, which enable quick welding cycles by localized heat input. Nonetheless, they still require protective measures (either gas shielding for all areas above 350°C or vacuum) during the molten weld phase. Hence, solid-state welding emerges as the preferred method for titanium welding [35].

TIG welding is a conventional method of joining titanium alloys. However, TIG welding increases heat input which results in a wider HAZ, which in turn can cause softening, deformation, and contamination in WM. Titanium alloys are joined by TIG welding as well as higher energy density techniques like EBW and LBW. However, problems like porosity defects and WM cracking can be introduced by the accelerated cooling rates that are inherent in these two processes.

To address these challenges and develop successful joint between titanium alloys whether it is similar or dissimilar combinations, welding method which are classified as solid-state method such as diffusion bonding (DB), FSW, and FW are

frequently employed. Notably, broad research has been done and documented in the literature to support the potential advantages of FW maintain in producing high-quality joints in steels and alloys, both similar and dissimilar combinations [36].

2.3 Metallurgical Considerations during dissimilar metal welding

Dissimilar metal welding is the process of joining two or more parts made of various materials. Metallurgical considerations in dissimilar metal welding are decisive for ensuring the reliability and performance of the welded joint. Here are some key metallurgical factors to consider:

2.3.1 Microstructural Changes

Welding causes alterations in both the base metals' microstructure and HAZ encompassing the weld. These alterations can impact the mechanical characteristics, including strength, ductility, and toughness, of the welded connection. Adjustments to heat input, cooling rates, and post-weld heat treatment (PWHT) can be fine-tuned to regulate the microstructure and properties of the weld.

When welding dissimilar metals together through fusion, the composition and structure of the weld zone are significantly influenced by the composition of the weld and the extent of dilution. Therefore, precise management of welding parameters and corresponding dilution levels is crucial to achieve a desirable microstructure and properties for specific applications. In dissimilar metal fusion welding, the key variables controlling dilution are the rate of filler metal deposition and the power of the welding arc. Increasing the filler metal deposition rate reduces dilution, while higher arc power increases dilution. It's essential for the filler metal, when used to bond dissimilar metals, to blend with the base metals to form a WM characterized by a continuous, ductile matrix phase. Moreover, it should be capable of accepting dilution from the base metals without creating a microstructure prone to cracking [37].

2.3.2 Formation of hot cracking or solidification cracking

In fusion welding for joining dissimilar metals, the composition, and qualities of the WM stand as paramount considerations. These aspects hinge on the compositions of the base metals, any filler metal employed, the extent of their mingling or dilution, and their ability to dissolve into one another. Additionally, the

solidification traits of dissimilar welds are affected by the varying dilutions and compositional variances near each base metal. This solidification behaviour bears significance concerning the occurrence of hot cracking within the joint during the solidification process.

Sometimes during solidification of welds or casting, cracks appear at the end of solidification generally at the centre line of the weld in ASS, these are called hot cracking or solidification cracking. These cracks occur due to rejection of impurities such as sulphur and phosphorus by solid. Due to this rejection the concentration of impurities keeps on increasing in the remaining liquid also these impurities form low melting compound with other elements. At the same time due to shrinkage during solidification there will be tensile stress generated at the centre of weld joint and the weld cracks form due to synergistic effect of solidification tensile stress and formation of low melting compound [21].

According to research utilizing the ternary iron-chromium-nickel phase diagram, findings suggest that alloys solidifying primarily as ferrite demonstrate the highest resistance to hot cracking. Conversely, alloys solidifying entirely as austenite exhibit the greatest susceptibility to hot cracking. Alloys solidifying with primary austenite show lower susceptibility compared to those solidifying entirely as austenite. However, alloys solidifying fully as ferrite are more prone to hot cracking than those solidifying primarily as ferrite. Thus, from a welding perspective, the preferred sequence of solidification is primary ferrite, fully ferritic, primary austenite, and finally, fully austenitic [37].

To avoid hot cracking and to obtain preferred microstructure, in 1949, Anton Schaeffler published the well-known Schaeffler diagram as illustrated in Figure 11. This diagram provides a relationship among austenite stabilizers (nickel-equivalent elements) and ferrite stabilizers (chromium-equivalent elements). To use this diagram, first Ni equivalent and Cr-equivalent are calculated and are plotted on the diagram. The diagram contains some ferrite lines and the ferrite content for the weld composition can be found with the help of those lines to avoid hot cracking.

$$Cr_{eq}=Cr+ Mo+l.5Si+0.5Nb$$

$$Ni_{eq}= Ni+30C+ 0.5Mn$$

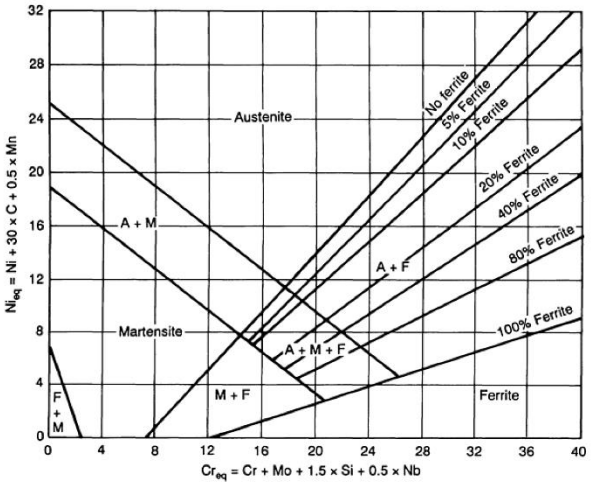

Figure 11: Schaeffler diagram [37].

2.3.3 Formation of Intermetallic

Analysing the metal's phase diagram is essential when different metals are joined by fusion welding to determine whether they are soluble to each other. Selection of filler metal depends on solubility with both dissimilar base metals. At the junction where the base metals meet each other, intermetallic compounds may develop. These compounds can have different mechanical properties compared to the base metals and may be brittle or prone to corrosion. The formation of undesirable intermetallic phases should be minimized through proper welding techniques and filler metal selection.

In case of SS, temperatures above roughly 1000°C can dissolve carbides that were originally present in ASS prior to welding. Afterwards, gradual cooling over an extended period within the temperature ranges of 400°C to 850°C facilitates to precipitate chromium- carbide ($Cr_{23}C_6$) along the grain boundaries, refer to region C as illustrated in Figure 12. Due to this carbide precipitation, the region near the borders of grain becomes depleted in chromium with Cr < 12% (region A & B). Since chromium is the main component providing corrosion resistance, grain boundary region (chrome depleted) becomes susceptible to corrosion. This phenomenon of carbide precipitation is known as sensitization and the corrosion taking place due to this phenomenon is known as inter granular corrosion (IGC). Sensitization may take place during cooling from high temperature, welding, or heat treatment. High welding interpass temperatures can contribute to sensitization [21].

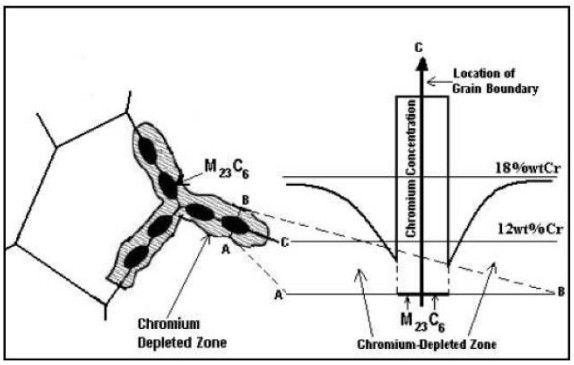

Figure 12: Schematic representation of chromium carbide formation [21].

2.3.4 Weldability issues due to variation in melting temperature

Some combinations of dissimilar metals are more difficult to weld than others due to differences in melting points. Specialized welding techniques, such as friction welding, explosion welding, or brazing, may be required for certain dissimilar metal combinations.

When welding different metals together, the melting temperature is an important consideration, especially in fusion welding situations where a lot of heat is produced. Because of their different melting points, one metal frequently melts much faster than the other at equivalent heat inputs. The lower melting temperature metal rupturing can be caused by significant differences in melting temperatures between the base metals and the filler metal. Furthermore, because the metal with the lower melting temperature is weaker and only partially solidified, stress can be caused by the solidification and contraction of the metal with the higher melting temperature. This issue of variations in base metal melting temperatures can be resolved by buttering with the filler metal, which has an intermediate melting temperature. In addition to providing a barrier layer to lessen the migration of unwanted elements from the BM to the WM under high temperature conditions, providing a layer of transition by buttering between the base metals can help with the issue of highly different coefficients of thermal expansion that must withstand the cycling temperature in service [2].

2.3.5 Formation of Sigma (σ) phase for stainless steel

The phase is usually defined as Fe-Cr and is an intermetallic compound with approximate 30wt% -50wt% Cr but it can dissolve significant amounts of nickel and other elements as well. It forms at about 538–927°C and is very hard & brittle constituent. Sigma phase is well known for having a negative impact on the mechanical characteristics of SS, including an increase in hardness and a decrease in toughness and ductility. In the region with a high concentration of Cr, δ ferrite undergoes conversion to form the sigma (σ) phase. This happens because Cr is a ferrite stabilizer and hence its concentration will be more in ferrite than in austenite also the diffusion of Cr is more in ferrite than in austenite [21].

2.3.6 Challenges due to difference in Thermal Conductivity

Dissimilar metals may have different thermal conductivities, which can affect the distribution of heat during welding. The heat source plays a crucial role in achieving proper heat equilibrium by compensating for the variation in heat distribution. Rapid dissipation of heat from the weld pool in molten stage to the base metal, particularly one with higher thermal conductivity, can impact the energy required to locally melt the base metal. Hence, to maintain heat balance, it's typically advisable to direct the heat source towards the metal with greater thermal conductivity. Preheating this metal can help manage heat loss and decrease the cooling rate of both the WM and the HAZ. This approach ultimately mitigates excessive heat input, minimizes distortion, and reduces the occurrence of metallurgical flaws in the welded joint [2].

2.3.7 Challenges due to differential Thermal Expansion

When exposed to temperature fluctuations, different metals exhibit varied rates of expansion and contraction. This may cause the welded joint to distort and experience residual stresses. During the cooling process, a significant discrepancy in the coefficient of thermal expansion between dissimilar metals causes one metal to experience tensile stress while the other undergoes compressive stress. If these stresses remain unaddressed, the metal under tensile stress may undergo hot cracking during welding or cold cracking during service. This issue becomes particularly critical in applications where joints are subjected to cyclic modes at

elevated temperatures. However, diligent selection of welding parameters and techniques can aid in alleviating these effects [2].

2.3.8 Oxidation or Heat tint

SS are preferred for a variety of applications due to their excellent mechanical qualities, strong resistance to corrosion, appealing appearance, and lack of production contamination during transportation and storage. The presence of the oxide film significantly affects stainless steels' susceptibility to the corrosion process. The properties of stainless steel's surface are significantly altered by the formation of oxide films. It is discovered that oxide film breakdown-prone areas can serve as pitting initiation sites and accelerate corrosion.

The processes of welding, brazing, annealing, and stress relieving can create conditions that lead to the formation of a surface oxide film, thereby diminishing localized corrosion resistance. When welding SS alloys, the resulting oxide scale or heat tint is primarily composed of elements selectively oxidized from the base metal, notably iron and chromium. Due to defects and stresses within the heat tint oxide layer, it becomes ineffective as a barrier against corrosive agents. Additionally, the chromium-depleted layer of the base metal beneath the heat tint exhibits significantly lower resistance to localized corrosion in specific environments, such as those containing chlorides [38].

Heat tints (refer to Figure 13) is mainly found on SS surface during welding due to presence of oxygen in case of insufficient inert gas purging [39] and maintaining high temperature due to high interpass temperature during welding.

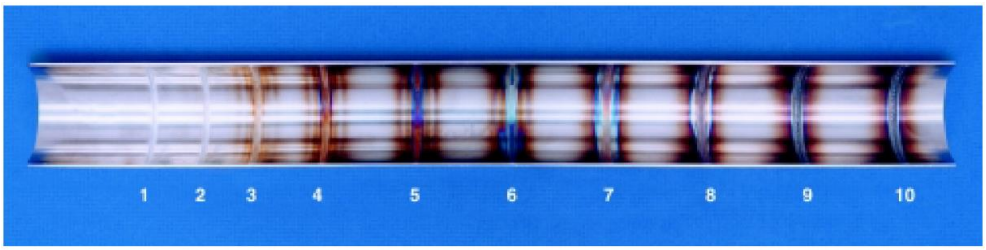

Figure 13: Guide for weld discoloration levels inside stainless steel due to various oxygen level [39].

Titanium can start absorbing oxygen from 400ºC. The metal rapidly reacts with atmospheric oxygen in the molten state, forming oxides. During heating, titanium absorbs oxygen and the grains of titanium swell, and when the joint cools, the weld becomes brittle due to the formation of a brittle phase oxide phase. As the degree of oxidation of the weld increases, the hardness of the weld also increases and makes it brittle. From the colour of weld seams, degree of oxidation can be identified: silver-white (no oxidation), gold (TiO, slight oxidation at around 250ºC), blue (Ti_2O_3, slight oxidation), gray (TiO_2, severe oxidation).

2.4 Fracture and Fatigue Characteristics

Fracture characteristics refer to the properties and behaviours of materials when they undergo fracture or failure. Understanding fracture characteristics is crucial in various fields, including materials science, engineering, and failure analysis.

Fracture refers to the separation or breaking of a material into two or more pieces due to the application of stress or force. Fracture typically occurs under three primary loading conditions: tension, shear, and tear, as depicted in Figure 14 [40].

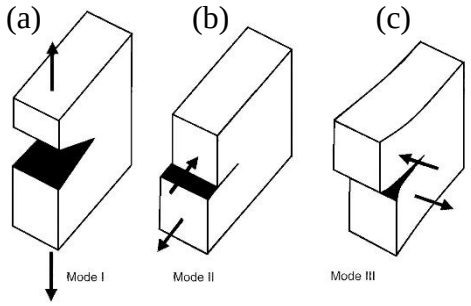

Figure 14: Image shows different mode of loading (a) Tension (Mode I), (b) Shear (Mode II) and (c) Tear (Mode III) [40].

Ductile Fracture: Ductile fracture entails significant plastic deformation prior to failure. Key characteristics of ductile fractures include substantial plastic deformation, formation of localized necking, cup and cone fracture pattern (refer to Figure 15 (a), absorption of substantial energy before fracture, shear stress surpasses shear strength, a dull and fibrous appearance of the fracture surface, indicators such as observable deformation and the occurrence of nucleation, growth, and merging of micro voids serve as warning signs (refer to Figure 15 (b & c) [40].

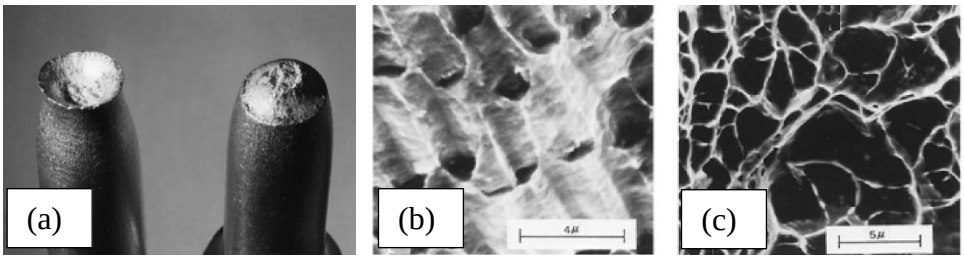

Figure 15: Image displays (a) cup and cone fracture, (b) elongated dimple due to shear, and (c) dimple [40].

Brittle fracture: Brittle fracture manifests as sudden and catastrophic material failure, without significant plastic deformation. It is common in materials with low toughness, like ceramics and certain metals at low temperatures. Key features of brittle fractures encompass minimal or no plastic deformation, surface of a brittle fracture is perpendicular to the principal tensile stress, V-shaped chevron (refer to Figure 16 (a) or herringbone marks that point toward the origin of the fracture, have radial (fanlike) ridges (refer to Figure 16 (b) emanating from fracture origin, an incapacity to absorb considerable energy before fracturing, abrupt and catastrophic material failure without warning signs or visible deformation prior to fracture, occurrence along grain boundaries or within grains leading to transgranular fractures, display of sharp, smooth, and flat fracture surfaces (refer to Figure 16 (c) with scant evidence of plastic deformation, and possession of high stiffness coupled with low ductility does not necessarily follow specific crystallographic planes [40].

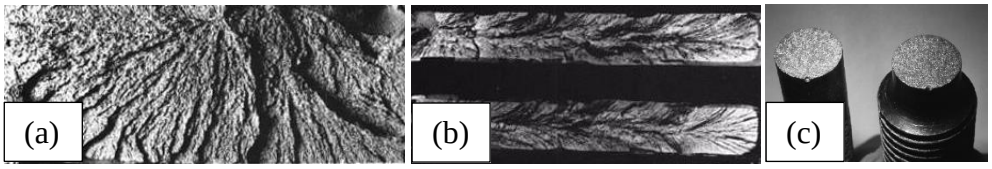

Figure 16: Image shows (a) Chevron fracture surface, (b) radiating ridge fracture surface and (c) flat fracture surface shows brittle failure [40].

Cleavage Fracture: Cleavage fracture is a type of brittle fracture characterized by the propagation of cracks along specific crystallographic planes or weak planes within the material's structure. Cleavage fractures often result in flat, shiny fracture surfaces with little to no plastic deformation. Key features of cleavage fractures include it occurring along specific crystallographic planes where the atomic bonding is weakest and shows all other features of brittle fracture [40].

Fracture mechanics: Fracture mechanics involves a quantitative examination of failure, with the objective of forecasting the load-bearing capabilities of structures and components holding cracks. It includes the connections between the materials, their characteristics, stress, defects that cause cracks, and the mechanisms that allow cracks to propagate. Designing structures to reduce the chance of structural failure is the aim of fracture mechanics. Elastic-plastic fracture mechanics (EPFM) and linear elastic fracture mechanics (LEFM) are the two primary subcategories of fracture mechanics.

LEFM: LEFM is used when there is only minor plastic deformation at or near the crack tip and the crack tip is sharp. When using LEFM, it is assumed that the component has a flaw of some kind, that the crack is located on a flat surface within a linear elastic stress field, and that the energy released during the rapid propagation of the crack is a fundamental property of the material that is independent of the component's size [40].

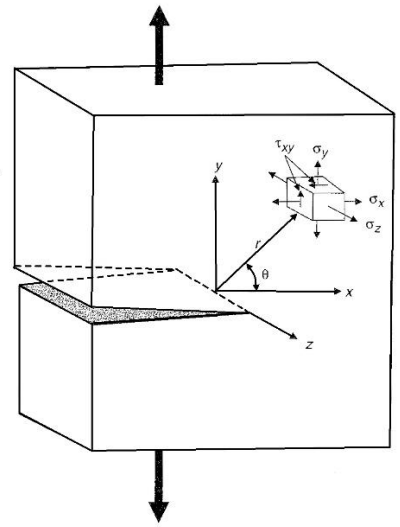

Figure 17: Stresses at crack tip in Mode I loading [40].

Based on Figure 17, if the plate is thin, then $\sigma_z = 0$ indicating a condition of plane-stress. Conversely, in case of thick plate, $\varepsilon_z = 0$ while $\sigma_z = \nu(\sigma_x + \sigma_y)$, a condition of plane-strain exists. Within these equations, the parameter K is identified as the stress-intensity factor. Generally, the stress-intensity factor is linked to the applied stress and crack length through $K = Y\sigma\sqrt{\pi a}$ where Y is a dimensionless factor contingent upon the type of crack, specimen geometry, and loading type. When the applied stress (σ) exceeds some critical value (σ_c) the crack propagation occurs,

leading to failure. Hence, K corresponds to the critical value of applied stress (σ_c) is termed as fracture toughness (K_C) and is simply $K_C = Y\sigma_c\sqrt{\pi a}$.

In the context of relatively thin specimens under plane-stress conditions, the fracture toughness parameter, K_C, is influenced by the specimen's thickness (refer to Figure 18). As the specimen gradually thickens, the state shifts from plane-stress to plane-strain and the fracture toughness (K_C) stabilizes at a consistent and reduced level, this is referred to as the plane-strain fracture toughness (K_{IC}). $K_{IC} = Y\sigma_c\sqrt{\pi a}$ The subscript "1" refers to the mode 1 crack opening [40].

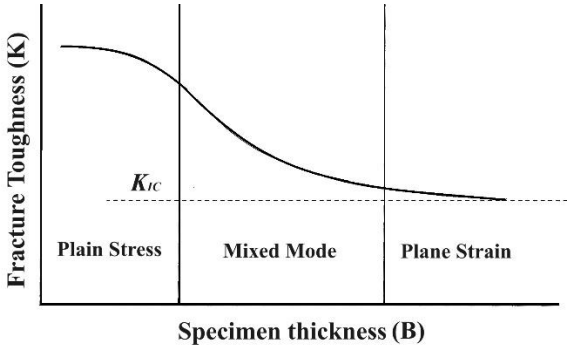

Figure 18: Variation of fracture toughness with specimen thickness [40].

The resistance of a material to crack propagation is measured by its fracture toughness. It measures the quantity of energy a material absorbs prior to breaking. High fracture toughness materials are frequently preferred in structural applications because they are more resilient to brittle fracture. Several variables, including temperature, strain rate, material processing, and the final microstructure, affect the plane-strain fracture toughness (K_{1C}). As yield strength increases and temperature drops, K's value decreases [41]. The temperature at which ferritic steels transition from brittle to ductile determines how loading or strain rates affect fracture toughness. Fracture toughness drops below this transition temperature as the loading rate increases. Fracture toughness typically rises with loading rate at higher shelf temperatures [42, 43]. Finer grain sizes typically result in an increase in it. The thickness of the specimen has no effect on the value of K_{1C} calculated for a particular material. As a result, among material properties, plane-strain fracture toughness (K_{1C}) is especially important [40].

EPFM: This is a branch of fracture mechanics dedicated to analysing materials that undergo both elastic and plastic deformation prior to failure. EPFM finds useful in

scenarios where: (a) the tip of crack is blunt, (b) there is some degree of plasticity at the tip of crack, and (c) in material designs which involve higher-toughness, lower-strength steels are subjected to impact or other mechanical stressors that can cause plastic deformation and fracture and are cyclically loaded [40].

Three primary methods underlie EPFM: The J-Integral, R-Curve, and CTOD techniques are the first three. These approaches are tailored to provide specific assessments of fracture characteristics. A thorough evaluation of fracture toughness is provided by CTOD, which is particularly appropriate for slow low loading rates. The R-Curve method assesses resistance to fracture extension within the realm of elastic-plastic fracture and slow loading rates, whereas J-Integral sheds light on fracture toughness related to elastic-plastic fracture under these circumstances. All these tests adhere to the standards outlined in American society of testing and materials (ASTM) E1820 [40].

ASS (SS308) and its weldment in different welding processes shows elastic-plastic fracture toughness response in various test temperature. Fracture toughness is found highest at room temperature and decreases with increase in test temperature. In fusion welding, TIG shows the highest fracture toughness due to absence of manganese silicide [44]. In their study, Samuel, et al. [45] examined the impact of temperature on the fracture toughness measured using J–R-curves method of modified variant of SS316L. They discovered that, for SS316L, fracture toughness peaks at room temperature and diminishes with rising test temperature. According to a study by Ghosh, et al. [46] the degree of sensitization reduces the fracture toughness of 304LN ASS. The characteristics of fracture toughness in dissimilar weld joints between SA508 Gr.3 Class 1 and SA312 Type 304LN was investigated by Kumar, et al. [47] both with and without stress-relieving treatment. It was discovered that the former reduces fracture toughness in comparison to the as-welded condition. This is explained by a rise in the microstructural heterogeneity in the HAZ and close to the DMW's fusion boundary.

Fatigue: Fatigue denotes the gradual and specific structural deterioration arising from cyclic loading on a material, resulting in failure at stress thresholds substantially below its ultimate tensile strength. Fatigue failure is especially deceptive as it transpires without evident forewarning. Typically, on a larger scale,

the fracture surface aligns perpendicularly to the principal tensile stress direction. Identifying fatigue failure is feasible through the visual characteristics of the fracture surface [40].

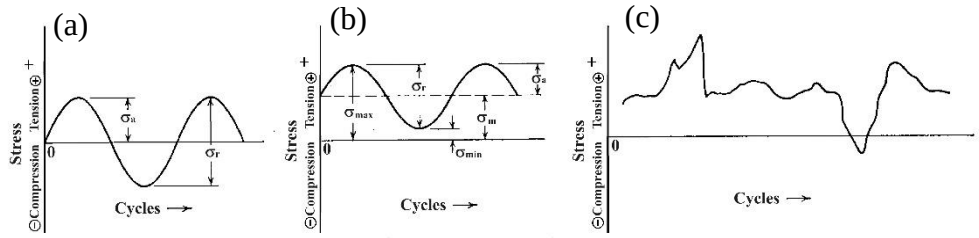

Figure 19: Typical fatigue stress cycle (a) fully reversable, (b) repeated and (c) irregular [40].

A cyclic stress cycle as shown in Figure 19 consists of different components: maximum stress (σ_{max}) , minimum stress (σ_{min}), stress amplitude (σ_a), mean stress (σ_m),stress range (σ_r), and stress ratio (R). The relation between these components is described below [48].

$$\sigma_a = \frac{\sigma_r}{2} = \frac{(\sigma_{max} - \sigma_{min})}{2} \qquad \text{Equation 4}$$

$$\sigma_m = \frac{(\sigma_{max} + \sigma_{min})}{2} \qquad \text{Equation 5}$$

$$Stress\ ratio = R = \frac{\sigma_{min}}{\sigma_{max}} \qquad \text{Equation 6}$$

A fatigue stress cycle with an R ratio of (-1) is termed fully reversible, exhibiting a consistent R value other than (-1) is referred to as a fully repeated cycle and demonstrating irregular R values is called a fully irregular cycle [48]. From a macroscopic perspective, fatigue unfolds in three distinct stages. Stage I involves the initiation of a crack, followed by Stage II characterized by the progression or propagation of the crack. Finally, Stage III marks the abrupt fracture of the balance part of the material.

Stage I: Fatigue damage usually starts with the initiation of microstructural defects or stress concentrations within the material. These defects can include inclusions, voids, surface imperfections, or changes in material properties and surface and subsurface material discontinuities. Without any surface flaws, the onset of crack initiation ultimately arises when persistent slip bands (PSBs) are developed. Fine

slip movements accumulate systematically to form slip bands. As seen in Figure 20, the slip bands' back and forth motion causes surface irregularities, termed intrusions, and extrusions to form at the surface, culminating in crack formation. Additionally, in polycrystalline materials, cracks may initiate at grain boundaries [40].

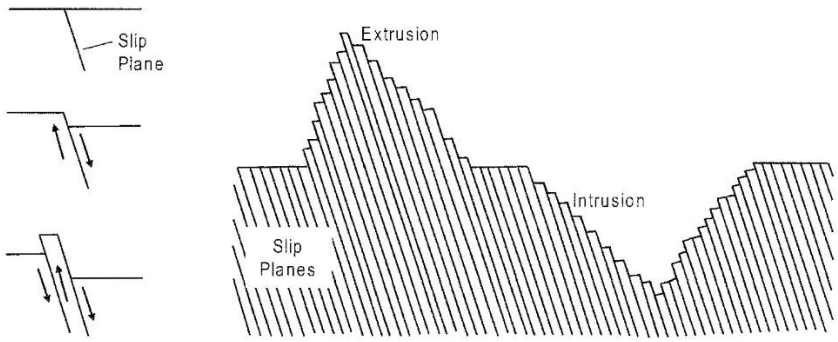

Figure 20: Growth of extrusion and intrusion during fatigue crack initiation [40].

Stage II: The advancement of crack growth transpires as the initial crack in stage I evolves and extends perpendicular to the applied stress. This progression involves a continuous cycle of crack sharpening succeeded by blunting, as depicted in Figure 21. Throughout crack growth, the propagation often generates a series of fatigue striations, with each striation symbolizing a single fatigue cycle [40].

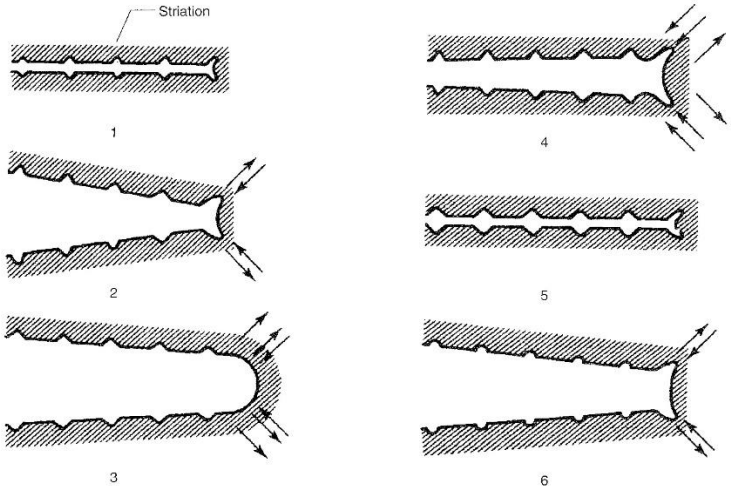

Figure 21: Image shows mechanism of fatigue crack propagation [40].

Stage III: The ultimate fracture takes place once the crack has enlarged to the critical size, resulting in failure due to overload. The extent of the final fracture region is contingent upon the applied loads' magnitude, while its configuration is

influenced by the fractured part's shape, size, and the direction of loading. The shear lip and chevron mark are two characteristics of the final fracture zone. The final fracture typically manifests in one of two distinct modes: tensile fracture, occurring in a plane strain mode and extending from the fatigue zone in the same plane, or shear fracture, happening in a plane-stress mode at a 45° angle to the part's surface adjoining the tensile fracture [40].

In addition to macroscopic features, there are several common microscopic features observed on fracture surfaces resulting from fatigue.

Beach Marks: Beach marks are concentric circular or elliptical patterns that radiate outward from the origin of fatigue crack initiation. These marks represent the progressive growth of the fatigue crack during cyclic loading cycles. The spacing between beach marks typically corresponds to the cycle frequency and the rate of crack propagation. Beach marks might also emerge due to fluctuations in load during operation, fatigue testing under varying loads, or alterations in stress intensity due to geometric characteristics of the component [40].

Striation Patterns: Striation patterns are delicate, parallel lines or ridges detected across the fracture surface, running perpendicular to the crack propagation direction. These striations arise from the recurrent expansion and contraction of the fatigue crack during each loading cycle, inducing the development of microstructural attributes like slip bands and dislocation structures [40].

Overload zone: The overload region, alternatively known as the fast fracture zone, refers to the segment of the component where the ultimate catastrophic failure transpires. The extent of the overload zone serves as an indicator of the magnitude of the load at the time of the final fracture event [40].

Ratchet marks: Ratchet marks are indicative of several origins of crack and comparatively elevated overall stresses. Ratchet marks may stem from either elevated stress exerted on the component or from High stress concentrations. Nonetheless, it is typically possible to discern whether the primary cause of the fracture was the load or the concentration of stress by examining both the ratchet marks and the dimensions of the instantaneous zone. For instance, the presence of numerous ratchet marks along with a small overload zone suggests that although

the load was light, there were elevated stress concentrations. These marks are perpendicular to crack propagation [40].

High cycle fatigue (HCF): HCF represents a type of fatigue failure evident in materials experiencing cyclic loading at stress levels considerably below the yield stress threshold but above a defined threshold termed as the fatigue limit or endurance limit. HCF typically manifests elastic deformation with minimal plastic deformation. An essential tool for illustrating the relationship between stress amplitude and the number of load cycles required for failure within the realm of HCF is the S-N curve. This curve also shows the fatigue limit, or endurance limit, which is the highest cyclic level of stress that a material can withstand indefinitely without yielding before failing due to fatigue. HCF testing is generally conducted under stress-controlled conditions [49].

HCF is characterized by cyclic loading, the capacity to endure a significant amount of fatigue cycles while operating under stress levels lower than the yield stress, reliance on the S-N curve as a fundamental representation tool, and susceptibility to environmental factors such as temperature, humidity, corrosive media, and exposure to aggressive chemicals. Usually, when subjected to HCF at low stress amplitudes, fractures occur with flat-faced (plane-strain) characteristics. Near the point where the crack initiates, where stress intensification is minimal, the fracture surface appears finely grained and lightly polished. However, as the crack advances and stress intensity rise, the surface becomes increasingly rough and fibrous. Microscopically, high cycle fatigue displays beach marks, striations, and an overload zone [40].

Low cycle fatigue (LCF): LCF refers to a form of fatigue failure observed in materials under cyclic loading at comparatively elevated stress levels, typically above yield stress and lower than UTS. Typically, components (such as turbine blades, engine mounts, and landing gear components, critical components in turbines, boilers, and other power plant equipment) subjected to high cyclic stress beyond yield stress during operation undergo LCF testing to determine their lifespan. At higher stress beyond yield stress, material shows plastic deformation and minimal elastic deformation. Typically, LCF testing is performed using a strain-controlled approach to monitor the effect of plastic strain. Strain-controlled axial

fatigue testing is preferred since it allows for the consideration of cyclic plastic deformation occurring at stress concentrations and notches within a component, even when the majority of the component experiences elastic behaviour during cyclic loading. The strain-life curve serves as a primary method for illustrating the correlation between strain amplitude and the number of cycles until failure in LCF. It provides the total strain limit corresponding to a particular cycle, as well as. transition fatigue life i.e. elastic to plastic transition point [49].

Characteristics of low cycle fatigue are existence of cyclic loading, withstand with comparatively low number of fatigue cycle, operating at plastic region i.e. beyond yield stress and less than UTS, use strain - life curve as fundamental tool to represent, affected by environmental elements like temperature and humidity, corrosive media, and exposure to aggressive chemicals. As a general principle, in high-strain situations, LCF surfaces tend to exhibit a fibrous and rough appearance, characteristic of plane-stress loading conditions, with fractures typically occurring at a 45° angle to the primary tensile load. Microscopically, LCF displays beach marks, striations, ratchet mark and an overload zone [40].

The microstructural composition of the material significantly impacts its fatigue characteristics. Elements such as size of grain, grain boundaries, distribution of phases, presence of inclusions, and material imperfections all affect the material's fatigue resilience and performance in the propagation of cracks. In case of titanium, reducing the alpha grain size in fully equiaxed structures enhances fatigue strength. Similarly, diminishing the width of alpha lamellae additionally, reducing the volume fraction of primary alpha within duplex structures, contributes to increased fatigue strength. Furthermore, reducing the size of prior-beta grains in fully lamellar microstructures improves fatigue life in both HCF and LCF [40].

In a study on the stress-induced HCF and LCF performance of LFW between two dissimilar titanium alloys i.e. Ti-64 and Ti-6Al-2Sn-4Zr-2Mo-0.1Si (Ti-6242) subjected to PWHT, Rajan, et al. [10] discovered that the weld's fatigue limit was marginally superior to base metal. Fatigue failure transpired within the Ti-64 and Ti-6242 segments, approximately 3±1 mm distant from the centre of the weld, in LCF and HCF domains, respectively. In LCF circumstances, the failure commenced at the surface (specifically on the Ti-64 side) and swiftly advanced through the zone

of small crack propagation, ultimately yielding under tensile overloading circumstances, as demonstrated by the dimples observed on the fracture surface image. In HCF conditions, the fracture, originating from the surface (specifically on the Ti-6242 side), was predominantly characterized by the crack propagation zone. This area exhibited quasi-cleavage facets accompanied by extremely fine fatigue striations. In their research, Wang, et al. [50] examined the fatigue behaviour under strain-controlled conditions of weld joints formed by EBW between dissimilar Ti–64 and Ti-17 alloys. They discovered that the fatigue resistance under strain control was similar for both the base metals and the joints. The dissimilar joint primarily experienced failure in fatigue within the HAZ of the Ti-17 side, particularly in regions showing softness. Crack initiation was noted to occur either from the surface of the specimen or near-surface flaws, while crack propagation displayed characteristic fatigue striations. Moreover, samples tested at higher strain amplitudes displayed relatively smaller fatigue crack propagation regions compared to those tested at lower strains. Impact of LFW parameters on the fatigue properties of dissimilar welds between TC-11 and near Ti–5Al–2Sn–2Zr–4Mo–4Cr (TC-17) alloys was investigated by Yang, et al. [51]. They conducted HCF tests and discovered that the fatigue characteristics were impacted by different parameters of the welding process. They observed that the fatigue limit decreased as the pressure and welding duration increased. Conversely, the fatigue limit initially increased before decreasing with higher amplitude and frequency. The rupture surface of the welds displayed a mixed pattern of rupture, including quasi-cleavage, fatigue striations, and dimples. Fatigue cracks generally originated from surface imperfections or defects near the surface, with the crack propagation area notably greater than other regions. At an amplitude of 2 mm, the crack propagation area was smaller compared to other regions, while the crack initiation site became apparent at an amplitude of 6.5 mm. Moreover, as the amplitude increased, the spacing of fatigue striations initially decreased before subsequently increasing, corresponding with the changes observed in the fatigue limit. The study carried out by Wen, et al. [52] delved into the fatigue behaviour under strain-controlled of weld joints formed by LFW between dissimilar Ti-64 and Ti–6.5Al–3.5Mo–1.5Zr–0.3Si (TC-11) alloys. Their results indicated that the fatigue performance of the welded joints was like that of the base metals, with failures mainly occurring on the Ti-64 side, located away from the weld centre line. Origination of fatigue crack typically starts either

at the surface of the specimen or near-surface flaws, whereas propagation of crack is primarily identified by fatigue striations oriented at right angles to the direction of crack growth, often accompanied by secondary cracks. Strain-controlled fatigue experiments demonstrated that the cyclic stabilization tendencies were displayed by dissimilar joint at lower strain amplitudes of up to 0.6%, while cyclic softening typically follows initial slight cyclic hardening at higher strain amplitudes. Moreover, as the amplitude of strain increases, the duration of primary cyclic hardening stage progressively diminishes.

It is concluded from above studies that during stress controlled HCF testing, origination of crack commonly arises near the specimen surface or at surface irregularities across all cyclic stress levels. The region of crack propagation typically displays fatigue striations at right angles to the direction of propagation of crack. In instances of lower stress cycles, the crack propagation area tends to be notably larger than other regions. Additionally, the spacing between fatigue striations is narrower under lower stress cycles and wider under higher stress cycles. Ultimately, the final fracture zone showcases a characteristic ductile fracture pattern characterized by numerous finely deformed dimples or micro voids distributed diffusely. During strain controlled LCF testing, failure typically commences at the surface and swiftly advances through a short area of crack propagation before fails in circumstances of tensile overload. This is indicated by the occurrence of dimples and shear lips observed on the fracture surface. Notably, the region of propagation of fatigue crack is reduced at higher amplitudes of strain compared to lower strains, and cyclic softening typically follows initial short cyclic hardening at higher amplitudes of strain.

2.5 Common Welding Techniques and Processes for Steels and Titanium Alloys

2.5.1 Rotary Friction Welding Process

RFW represents a welding method maintaining solid-state condition that coalesces metals with the help of the kinetic energy produced by the rotation of the workpiece and applying forging pressure, all without melting the parent metal. It functions through the amalgamation of heat, pressure, and duration to forge the weld joint. RFW can be categorized into two primary groups depending on the involvement of

the driving motor in the welding procedure: (i) Continuous Drive Rotary Friction Welding (CDRFW) or Direct Drive Rotary Friction Welding and (ii) Inertia Rotary Friction Welding (IRFW). These categories delineate distinct methodologies within the RFW process, each offering unique advantages and applications in various industrial settings.

Principle of RFW: The fundamental concept of RFW entails one element remaining stationary while compelled to rub against another rotating component under regular pressure.

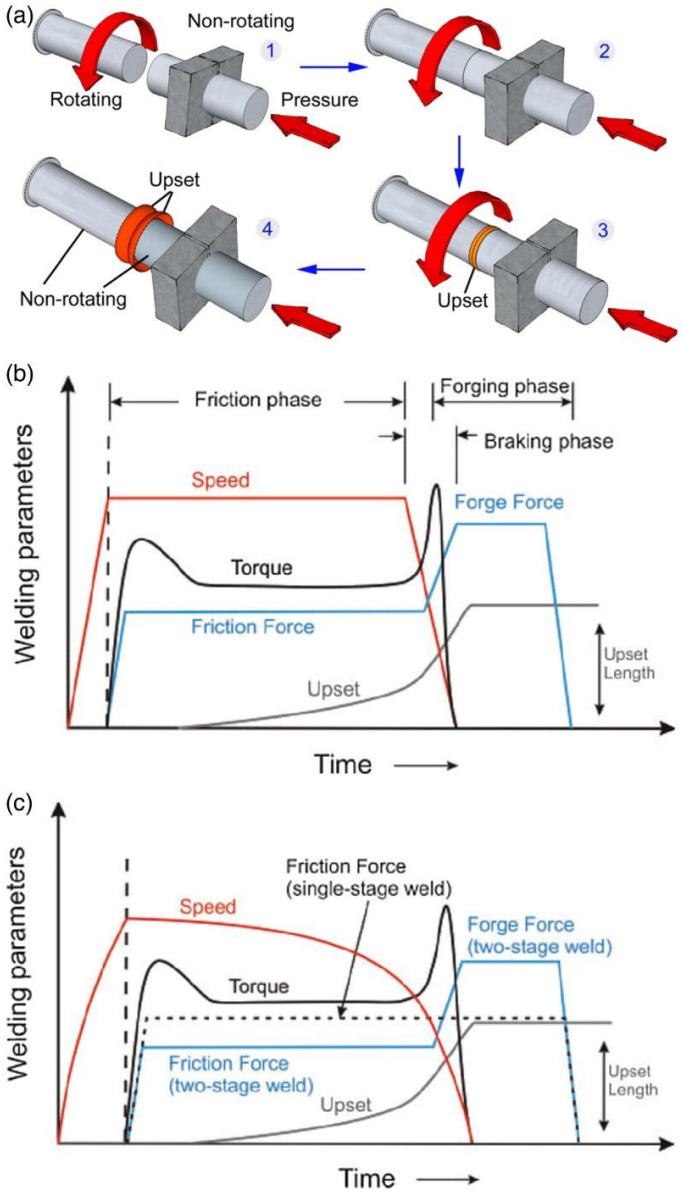

Figure 22: Schematic of (a) the RFW process, (b) the process phases of CDRFW and (c) the process phases of IRFW [53].

As shown in Figure 22 (a/1), initially, one workpiece is kept fixed while the other is kept in rotation. Once the speed of rotation touches its optimum value, the two workpieces come into contact, and axial force is employed, as illustrated in Figure 22 (a/2). When both workpieces come into contact, localized heat in the workpiece is generated by the interface friction, leading to the interface beginning to upset, as depicted in Figure 22 (a/3). Finally, after a sufficient time, when rotation of one of the workpieces stops, upsetting seems to be completed, it is considered that welding of work pieces is completed (as in Figure 22 (a/4)) [53].

Typically, RFW consists of two stages: the friction phase, where the material is heated and essential upsetting occurs, and the forging phase, which consolidates the weld. The friction pressure may remain constant during the entire process or be applied in multiple steps, as shown in Figure 22 (c).

The main distinction between the two RFW mechanisms relates to how energy is delivered to the interface of welding. In CDRFW (as shown in Figure 23 (a)), the revolving component is linked to a unit is driven by motor. This unit holds a consistent rotational speed during the friction stage or heating phases. Usually, a clutch is used to separate the drive motor from the chuck, and then a brake is applied to stop the chuck. In IRFW (refer to Figure 23 (b)), one of the components is fixed to the rotary chuck along with a flywheel of specific mass before welding. Subsequently the speed of rotation of the component is increased to store the requisite energy in the flywheel. Once the desired speed of rotation is attained, the motor is turned off, and the components are pressed together under pressure. The pressure is sustained on the workpieces even after the rotation ceases to aid in their joining [54]. The weld quality can be assessed through various criteria such as the degree of weld flash generated, the overall decrease in part length caused by flash formation, and an analysis of the metallurgical composition of the cross-section. These assessments provide valuable insights into the integrity and strength of the weld joint [23].

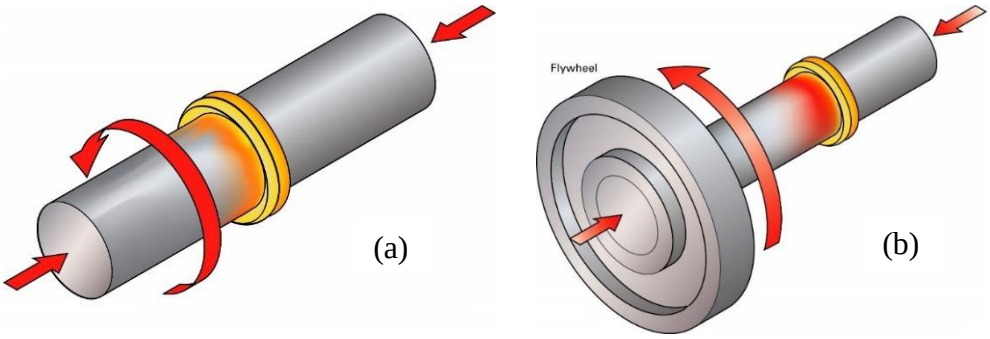

Figure 23: Schematic shows (a) Continuous drive RFW and (b) Inertia RFW [54].

Equipment of RFW: The RFW process is facilitated by equipment that is straightforward to assemble. A graphic representation of a common friction welding equipment, also known as a friction welder, is depicted in Figure 24. A friction welder can adjust to different applied load requirements, determined by the size and material of the components being welded. Usually, the maximum load capacity for metallic parts is approximately 120 kN. Generally, the motor of welder features different speed capabilities, which can be regulated via computer control. For metallic parts, a typical welder speed is around 3500 rpm. A standard welding machine comprises several essential systems, including: (i) Control system, (ii) Motor for CDRFW, (iii) Pneumatic or hydraulic pressure system, (iv) Handle, (v) Nonrotating vice, (vi) Clutch in direct-drive friction welder, (vii) Spindle, (viii) Flywheel in IRF welder, (ix) Housing, and (x) Measuring systems. These components collectively facilitate the seamless operation of the RFW process, enabling efficient and precise welding of metallic parts.

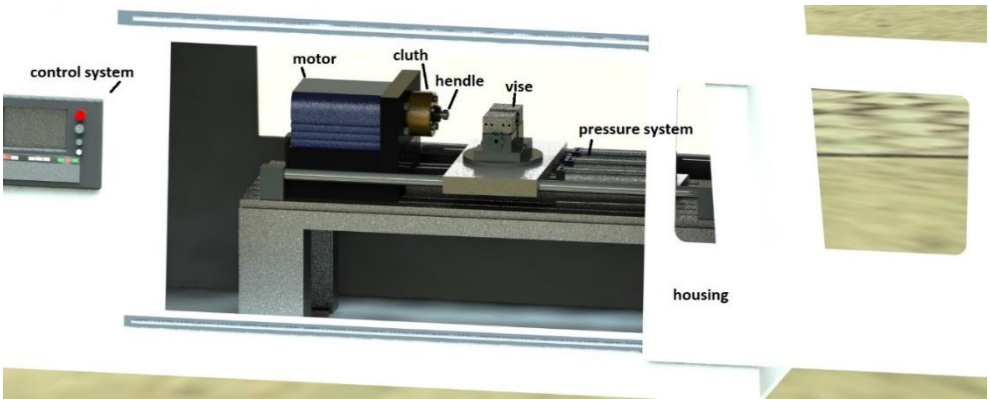

Figure 24: Schematic of Rotary Friction Welding equipment [54].

Application of RFW: With its comprehensive features characteristic of solid-state welding, RFW has appeared to be a widely adopted method for joining various

materials, including steels, superalloys, aluminium alloys, titanium alloys, copper alloys, and combinations of dissimilar materials (refer to Figure 25). Its versatility extends across a broad spectrum of manufacturing applications, ranging from everyday necessities to intricate and high-value aero-engine components.

RFW is extensively utilized in a range of manufacturing sectors and has been pivotal in creating a diverse array of products. These encompass turbine shafts, automotive parts like steel truck axles and casings, marine fixtures merging Monel with steel, piston rods, copper-aluminium electrical connections, cutting implements, and tubular transition connections that combine dissimilar metals like aluminium-titanium and aluminium-SS. Its wide-ranging applications underscore its significance and relevance across industries, facilitating the creation of robust and reliable components across varied domains.

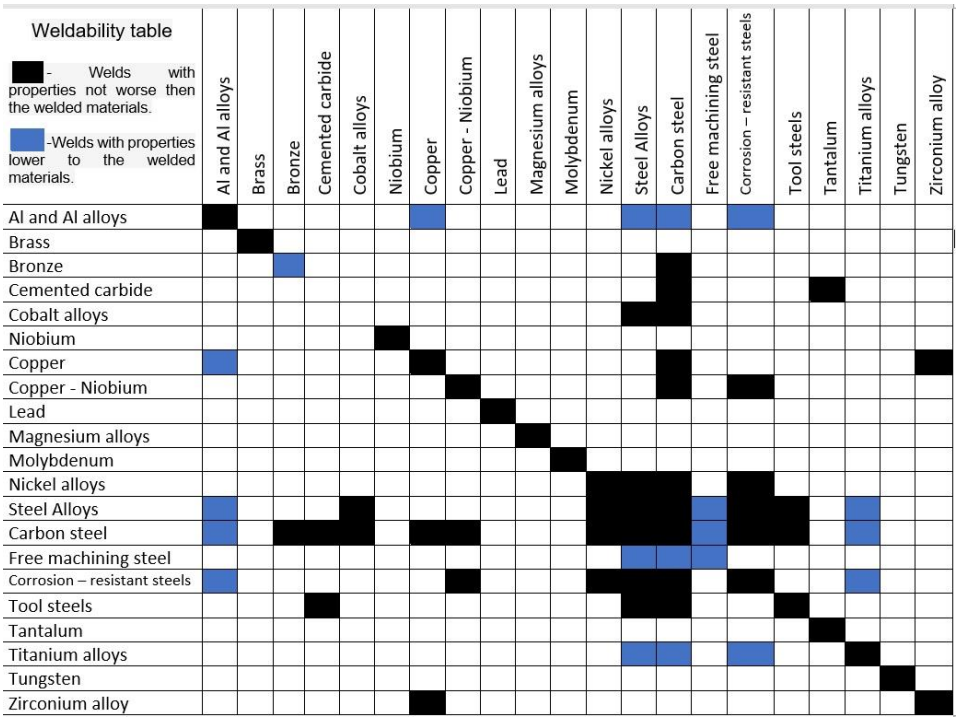

Figure 25: Image illustrates the weldability of RFW [54].

Advantages and Disadvantages of RFW: RFW processes offer numerous benefits over conventional fusion welding techniques. These include: (i) decreased likelihood of weld defects accompanying with solidification, such as hot cracking and porosity, since no molten weld pool is generated; (ii) the development of recrystallized microstructures during the process, potentially leading to enhanced tensile strength compared to other welding methods; (iii) elimination of the need

for welding consumables, resulting in cost savings; (iv) suitability for welding dissimilar materials; (v) production of welds containing only the parent materials, with interface impurities removed during the process; (vi) easy control of process parameters, minimizing operational errors; (vii) high integrity of welds, as the bonding area closely matches the interface area of the joined components; and (viii) highly repeatable processes.

As anticipated, RFW processes come with certain disadvantages: (i) they are not well-suited for welding thin-walled tubes or plates; (ii) at least one of the two components must be capable of plastic deformation to facilitate welding; (iii) the formation of flash during joining restricts component geometries, particularly when removal of the flash is necessary; and (iv) RFW techniques are constrained in that they cannot be utilized to weld components with non-circular cross-sections.

2.5.2 TIG Welding Process

TIG welding, also known as GTAW, stands out among arc welding techniques for its distinctive characteristics. The name itself encapsulates the key aspects of the process: Tungsten serves as the non-consumable electrode that initiates the welding arc, while weld pool is protected from atmospheric contamination by use of inert gas.

Principal of TIG welding: Figure 26 illustrates the complete setup of TIG welding. In this method, a welding arc is created between an electrode made of non-fusible tungsten and the base metal. Typically, the tungsten electrode contacts with a copper tube referred to as the contact tube, which is inserted within the welding torch. The welding torch is linked to a gas cylinder intended for shielding the weld pool and one terminal of the power source. To protect the tungsten electrode from overheating, the contact tube is continuously cooled either by air or water. The base metal is connected to the other terminal of the power source via a separate cable. In this method, inert gas acts as a protective agent, flowing through the torch body and being directed by a nozzle towards the weld pool to shield it from atmospheric contamination [55]. When the tungsten electrode touches the base metal, the welding arc is initiated. Notably, in TIG welding, the welding filler metal does not carry the welding current, enabling precise control of the weld pool.

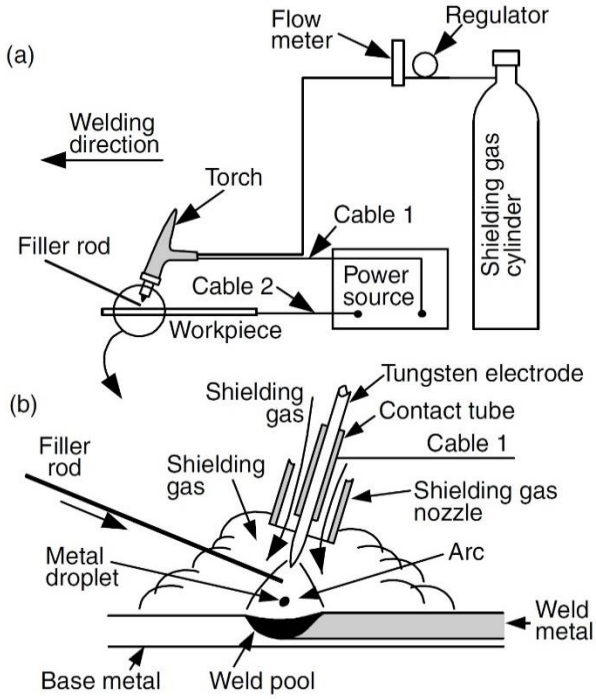

Figure 26: Gas–tungsten arc welding: (a) overall process; (b) weld zone [55]

Equipment of TIG: TIG welding equipment encompasses essential components such as (i) the welding power source, (ii) welding torch, (iii) welding cables, (iv) inert gas for shielding, and (v) the non-consumable tungsten electrode. Additionally, specific applications may require supplementary equipment including (i) hotwire setups, (ii) water coolers, (iii) high-frequency units, (iv) remote controls, and (v) camera systems. These additional tools cater to diverse needs and enhance the versatility and efficiency of TIG welding across various contexts and applications.

Application of TIG: TIG welding stands out among fusion welding processes for its ability to produce high-quality welds. The weld pool can be meticulously controlled by the operator since the filler wire does not carry the welding current. This versatility renders TIG welding applicable across a wide array of industrial sectors, including nuclear, oil, gas, thermal power plants, refineries, aerospace, dairy, piping, and pipeline industries, among others. TIG welding finds extensive use in overlay cladding and various repair works, and it can also be employed as an autogenous weld, eliminating the need for filler wire. Its adaptability extends to joints of any wall thickness, making it suitable for a diverse range of applications. Industries often utilize TIG welding for thin workpieces, particularly nonferrous

metals, and its compatibility with small diameter, thin-wall tubing makes it indispensable in bicycle manufacturing industries.

Advantage and Disadvantage of TIG: The following advantages and disadvantages of this process are noticed.

Advantages

- No chance of slag formation as it does not use flux.
- Produce high quality, clean welds.
- It is suitable for welding thin materials.
- It can be used without filler i.e. autogenous.
- It can be done in both manual and automatic.
- Welding can be performed in any welding position.
- Simple principle of this process makes it very operator friendly.

Disadvantages

- This process is very slow.
- Skilled labour is required to operate.
- Welders are exposed to high density light.

2.6 Welding Process Parameters Influencing Weld Joint Integrity

2.6.1 During RFW process

Various welding parameters such as the duration of friction, time spent in forging, pressure during friction, pressure during forging, and rotational speed influence the quality of rotary friction welds [56].

Rotational speed: The amount of heat generated at the interface increases with the rotational speed, while the duration of welding decreases. Higher rotational speeds lead to greater heat generation, causing the weld interface to reach a quasi-stable temperature more rapidly. Consequently, the material extrudes faster, significantly enhancing the upsetting rate and completing the process sooner [53].

Friction duration: Friction duration helps to generate heat at interface. Lower friction duration creates insufficient heat at joint interface which eventually affects interface diffusion and decreases joint strength. On the other hand, higher duration time generates higher heat due to which oxides are formed at interface and affects interface diffusion and decreases joint strength. Therefor optimum friction time is

required to obtain a sound welding joint. Increase in friction time increase in welding width [57].

Forging time: The forging duration impacts both the heat input and the time of plastic deformation throughout the welding process. Longer forging times can lead to better intermolecular bonding and improved joint strength. However, there is an optimal range for forging time, and excessive time may result in other issues. Longer forging times can influence the size and characteristics of the heat-affected zone. Proper forging time control is essential to minimize the impact on the material surrounding the weld and to prevent undesirable changes in microstructure, such as excessive grain growth or sensitization. It is essential to acknowledge that the ideal forging duration may differ depending on the type of materials, the size of the components, and the desired characteristics of the resulting joint.

Friction pressure: The level of friction pressure is crucial for ensuring effective coalescence between components in the joint. Insufficient friction pressure may result in unbonded regions at the interface, leading to a poor weld. On the other hand, excessive friction pressure can cause an excess of frictional heat, which may result in grain coarsening and reduced weld strength. Hence, it is vital to apply an appropriate level of friction pressure to adequately deform the material at the interface and promote the formation of a strong joint [53].

Forging pressure: The forging pressure has a notable impact on both the shape of the flash and the length of the weld joint. As the forging pressure rises, the width of the flash expands, while the length of the welded parts diminishes. Simultaneously, an increase in forging pressure enhances tensile strength but reduces impact toughness [58].

2.6.2 During TIG process

Polarity: Polarity defines the type of current which is flown through the welding torch. Three different welding polarities are used in TIG welding process. These are (i) Direct Current Electrode Negative (DCEN) or Direct Current Straight Polarity (DCSP), (ii) Direct Current Electrode Positive (DCEP) or Direct Current Reverse Polarity (DCRP) and (iii) Alternating Current (AC).

DCEN / DCSP: In this polarity, the tungsten electrode or welding torch is linked to the negative terminal of the power source. As a result, the tungsten electrode emits electrons, which accelerate as they travel through the arc.

At time of emission, electrons obtain a significant amount of energy which is finally released to the parent metal when the electron enters the parent metal. Hence, with DCEN polarity in TIG welding, most of the power (approximately two-thirds) is concentrated at the base metal side of the arc, while less (about one-third) is at the electrode side. Consequently, DCEN polarity offers greater penetration and produces a reasonably narrow and deep weld.

DCEP / DCRP: This is just opposite to DCEN; hence it is also called the reverse polarity. The tungsten electrode or welding torch is connected to the positive terminal of the power source. Electrons emit from parent metal and enter into the tungsten electrode. Hence, in DCEP polarity in TIG, more power (about two-thirds) is located at the tungsten electrode and less (about one-third) at the parent metal end. Hence, DCEP polarity has less penetrating power and produces a relatively wide and shallow weld. Positive irons which hit the parent metal bombard the surface of parent metal, hence this polarity helps to remove oxide from parent metal.

AC: In AC polarity, tungsten electrode experiences both positive and negative cycle. In positive cycle, it acts as DCEP and cleans the parent metal and in negative cycle it acts as DCEN, penetrates parent metal. As a result, AC is employed for welding materials that form strong oxides, such as aluminium and magnesium.

Current: Current helps to produce the heat in weld. Increase in current helps in melting of more filler metal as a result increase in weld deposition. Increase in current increase the width of heat affected zone. Hence the size of weld pool is manipulated by controlling the current. Normally DC and AC current are used. At present, pulsed DC current or square wave AC current is widely used to improve the process efficiency and quality of the weld.

Shielding gas: In TIG welding, inert gas is used as shielding gas which shields the weld pool from the atmosphere. Common types of inter gases used in TIG welding are Argon and Helium. The ionization potential of Argon is less than Helium. Therefore, in the same current supply, Helium shielding gas generates heat in weld pool than Argon. Hence, Helium improves the wettability compared to Argon and makes the weld bead wider and shallower compared to Argon.

Gas flow rate: The flow rate of shielding gas creates pressure on the weld pool. Therefore, more flow rate creates turbulence in weld pool because of shape of weld bead become irregular and wider. At the same time less flow rate creates insufficient

protection on weld pool as a result, weld defect such as porosity is noticed, and weld bead becomes very narrow and peaky.

Tungsten electrode: Tungsten electrodes containing 2% cerium or thorium exhibit enhanced emissivity of electron, capability of current-carrying, and contamination resistance compared to pure tungsten electrodes. Consequently, they facilitate easier arc initiation and contribute to a more stable arc. Electron emissivity is called the capability of emission of electrons by the electrode tip. A lower electron emissivity increases the temperature of electrode tip temperature which creates a greater risk of melting the tip of tungsten electrode and tungsten inclusion in the weld. As the tip of tungsten electrode emits electrons, therefore, tip preparation of tungsten electrode is very important refer Figure 27.

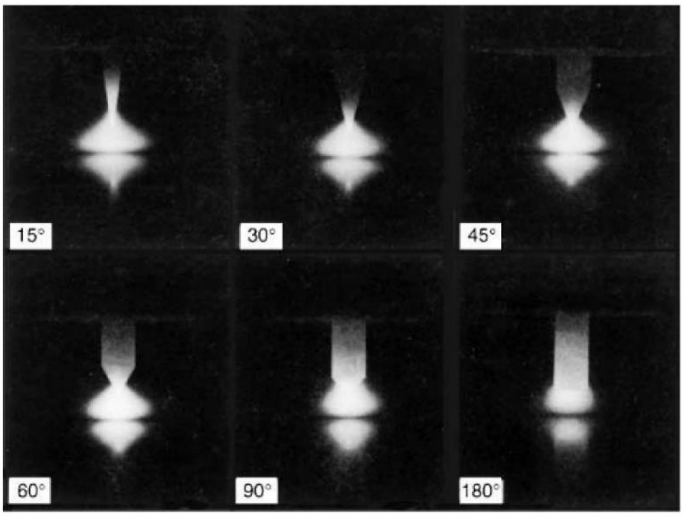

Figure 27: Effect of electrode tip angle on shape of arc in TIG welding [59].

2.7 Recent works on dissimilar welding and associated problems

One of the most popular techniques for performing dissimilar welds in industries is fusion welding. Consequently, ongoing endeavours persist in employing these techniques for joining dissimilar metal combinations, despite numerous challenges encountered [60, 61].

Fusion welding processes come in a variety of forms, including SMAW, GTAW or TIG, GMAW, and SAW. Among these conventional processes, TIG welding is commonly utilized and consistently produces high-quality dissimilar welds between ASS and LCS, typically employing ER309L filler metal [62]. Initial investigations into dissimilar metal welding using conventional methods have

shown that the mechanical properties degrade along the fusion line due to the development of localized high stresses resulting from mismatch in thermal expansion between CS and SS [63]. This issue has been identified as the primary reason for failures in dissimilar welds between CS and SS [64]. Degradation of mechanical properties shortens the lifespan of the component of nuclear plant facility and increases the risk of abrupt failures that could cause catastrophic events. Radiation leaks may be the result of structural damage at nuclear power plants. Thus, assessment of safety or evaluation of life of these kinds of structures is highly relevant and required. Many studies have been conducted recently to enhance the mechanical and microstructure characteristics of the dissimilar weld between SS and CS that is fabricated by TIG welding process with the assistance of adjusting parameters of welding process [65-68]. The distribution of hardness within the dissimilar weld between SS316L and mild steel, created using TIG welding, is observed to be uneven. The weld exhibits higher hardness levels compared to the parent metal, attributed to the formation of hard micro-constituents in the WM due to the migration of carbon from the mild steel side into the weld [68]. In another study, it is revealed that fatigue crack growth rate (FCGR) of HAZ of dissimilar weld of SS316L and IS 2062 Grade A CS using SS E309 electrode in TIG welding process is found to be the lowest [69]. In their study, Huang, et al. [22] et al. investigated the dissimilar weld joint of S355JR and SS316L manufactured using a gas tungsten arc welding multi-pass process. They observed that the WM consists of austenite and vermiform δ-ferrite microstructure. Additionally, a layer of carbon depletion is present at the interface of S355JR and the WM, although detrimental phases such as sigma (σ) and $M_{23}C_6$ (chromium carbide) are not detected in the WM due to use of appropriate parameters during welding. Electrochemical corrosion testing also revealed that the corrosion resistance of the WM is lower compared to the SS316L base material. The tensile strength of welded joint is same as parent metal. The average microhardness of the WM significantly exceeds that of the base materials and HAZs. Microhardness diminishes with increasing distance from the edge to the weld centre. Moreover, the impact toughness of the HAZs and WM is inferior to that of the base materials.

To address the primary issues linked with fusion welding, such as the creation of intergranular carbide formations due to migration of carbon, uneven hardness

distribution, residual stresses which lead to failure of the joint, it has been found that solid state welding is becoming an alternating welding process for dissimilar welding in various industries. The absence of melting in solid state welding eliminates the potential for weld flaws like porosity, slag inclusions, and solidification cracking. These techniques are capable of effectively joining dissimilar metals that conventional methods struggle with due to metallurgical incompatibilities, all without requiring filler materials. However, the difficulty in discerning a genuine metallurgical bond in the absence of solidification means that non-destructive testing methods may not always be suitable for solid-state welding processes [1].

CDRFW was employed to investigate the bonding of AISI 304 and AISI 430 ferritic SS. Findings revealed that the welds exhibited superior toughness and strength compared to the parent ferritic steel, with deformation observed exclusively within the weld [70]. Numerous research works have focused on optimizing parameters for RFW process to enhance the mechanical and metallurgical characteristics of dissimilar welds between CS and AISI SS304 [71-74]. The microstructural changes and mechanical characteristics of a dissimilar weld between 1045 CS and AISI SS304 using the RFW process were investigated. It was discovered that a carbide layer composed of CrC and $Cr_{23}C_6$ forms at the weld interface due to element diffusion, impacting the tensile properties of the weld [75]. A comparative study was carried out on dissimilar weld between AISI 304 with AISI 4140 using three different welding processes TIG, EBW and RFW and found that increase in burn off length i.e. increase in flash decrease toughness and increase hardness across the RFW welds [76]. A hybrid transition coupling composed of two dissimilar materials, S355J2 and SS316L, was fabricated using three distinct welding techniques: FW, RFW, and EBW. It was observed that all three welding methods yielded satisfactory dissimilar welds. However, the dissimilar welds generated through FW and RFW exhibited a notably thin weld interface. Furthermore, the FW and RFW demonstrated uniform micro-hardness and microstructures across the weld interface, along with consistent tensile properties [23]. Analyses of fatigue crack growth rate (FCGR) and fracture toughness (FT) were performed on dissimilar metal welds (DMW) between Inconel 718 and Nimonic 80A manufactured employing RFW. The FT and FCGR analyses employing the Single

Edge Notched Bend (SENB) specimen revealing that the base metals exhibited superior toughness compared to the DMWs. Furthermore, in the as-welded condition, the fatigue crack growth rate of DMWs was higher than that of the base metals. Results, however, varied greatly in the case of DMW with PWHT condition [77]. In a different investigation, the RFW technique was utilized to weld SS304 to MCS and LCS effectively. The tensile strength of both types of RFW joints surpassed that of the original SS materials. A metal mixing zone with an island of SS304 and CS were formed at the interface between the two metals may have formed because of a combination of deformation and heating. Diffusion of elements was noted between these islands [78]. FW was effectively employed to join SS316L and 1045 MCS. Microstructural analysis showed that the widths of the TMAZ and HAZ of 1045 MCS were greater than those of SS316L. With increasing forging pressure, hardness at the weld joint interface and tensile strength also increased.[79].

Demand of dissimilar weld of titanium alloys are increased in modern days without compromising the quality of properties. Therefore, novel design concepts necessitate validation of both HCF and LCF [10]. The fatigue behaviour, encompassing both HCF and LCF, of LFW of dissimilar titanium alloys, Ti-64 and Ti-6242, was examined. It was observed that the fatigue limit at 10^7 cycles in the HCF zone was marginally higher at 450 MPa compared to both the Ti-6242 base metal (BM) (434 MPa) and the Ti-64 BM (445 MPa). Fractures in the Ti-64 BM under LCF displayed fractographic surfaces predominantly characterized by dimples associated with a tensile overload. Conversely, HCF fractures in the Ti-6242 BM exhibited extensive crack propagation areas on the fracture surfaces along with fine fatigue striations within the quasi-cleavage facets [10]. The impact of microstructure on the strength, fatigue strength, and fracture toughness of three dissimilar LFW joints between Ti-17 and Ti-64 was investigated. The microstructural analysis revealed α-depleted β grains in the weld centre zone (WCZ) on the TMAZ of Ti17, while the TMAZ of Ti-64 exhibited acicular entangled α’ martensite with a Widmanstätten morphology. As well as a mixture of both Ti-64 and Ti-17 Island were observed in WCZ., the fatigue endurance limit of the LFW joint was 450MPa at 10^5 cycles. Fracture toughness of the LFW joint showed lower than the PM [80]. An experiment on LFW joints between dissimilar

Ti–64 and Ti–6.5Al–3.5Mo–1.5Zr–0.3Si alloys was conducted to assess the microstructure, microhardness, and low cycle fatigue characteristic. Substantial microstructural alterations were observed across the dissimilar weld joint, characterized by martensite formation in the weld zone (WZ) and finer crystallized grains in the TMAZ on the TC-4 side. An asymmetrical hardness distribution was noted across the dissimilar joint, with markedly higher hardness values in the WZ and the weld was soft zone free. According to strain-controlled fatigue tests, cyclic softening typically happens after initial mild cyclic hardening at higher strain amplitudes, whereas the dissimilar joint displays cyclic stabilization behaviour at lower strain amplitudes up to 0.6%. The fatigue life of the welded dissimilar joint was found to be essentially equivalent to that of both base metals. [50]. The microstructure and microhardness characteristics of the dissimilar weld of Ti-64 and Ti-1023 manufactured using EBW were assessed. The transformation of αs into the β phase occurred during welding, leading to a decrease in hardness values in the HAZ of Ti-1023. Conversely, in the fusion zone, hardness increased due to the formation of acicular α'' martensite within the β phase matrix is attributed to welding [81].

2.8 Critical Analysis and Gaps in Current Knowledge

The review of literature indicates that numerous research endeavours have explored the relationship between parameters in welding, microstructure, and conventional mechanical properties like tensile strength and hardness in dissimilar welds between CS and SS using RFW and TIG techniques. Similar investigations have been conducted for RFW dissimilar welds between alpha and beta titanium alloys. Among these, studies conducted particularly on RFW and TIG dissimilar welds between S355J2 and SS316L, as well as RFW dissimilar welds between Ti-64 and Ti-1023, have not adequately addressed the complex relationship between welding parameters, microstructure, and critical mechanical properties like fracture toughness and fatigue. As these properties are pivotal considerations in dissimilar welding for ensuring joint integrity and reliability, predicting service life, optimizing welding procedures, and complying with codes and regulations, therefore this project objective has been set up to explore this critical relationship to advancing welding techniques such as feasibility of RFW process to produce reliable weld joint for dissimilar materials.

2.9 Conclusion of the Literature Review:

The literature review delved into an in-depth examination of various welding processes, with a particular focus on RFW and TIG welding. This analysis provided valuable insights into the microstructural characteristics of dissimilar material joints, specifically involving S355J2 to SS316L and titanium alloys Ti-64 to Ti-1023. The comprehension of microstructural requirements for enhancing the hardness and tensile properties of dissimilar welds produced by RFW and TIG was thoroughly discussed.

The synthesis of findings emphasized the importance of understanding the relationships between welding processes, microstructure, and mechanical properties in dissimilar welds. For instance, in dissimilar welds between CS and SS, both RFW and TIG processes induced notable microstructural changes, impacting properties like hardness and tensile strength. While RFW led to microstructural adjustments throughout the weld area without the formation of intermetallic phases, TIG welding exhibited the presence of intermetallic phases, such as chromium carbide, influencing mechanical and corrosion resistance properties. Similarly, in dissimilar welds of titanium alloys, RFW induced microstructural variations with the formation of islands containing both parent metals at the WCL, affecting hardness, tensile strength, and fatigue properties.

This review identified a significant research gap in the assessment of fracture toughness and fatigue properties in dissimilar welds, urging further investigation. Specifically, there is a dearth of studies on dissimilar welds between S355J2 and SS316L using RFW and TIG methods, as well as the impact of RFW on the fatigue properties of dissimilar welds between Ti-64 and Ti-1023 alloys. Addressing this gap is crucial to advancing the understanding of dissimilar welds and optimizing their performance in various applications.

Overall, this literature review underscores the importance of future research endeavours aimed at elucidating the relationship between microstructure and mechanical properties, particularly fracture toughness and fatigue behaviour, in dissimilar weld joints. Such investigations are essential for bridging existing research gaps and enhancing the reliability and applicability of dissimilar welding processes across different material combinations.

Chapter 3

3 Experimental Procedures

This chapter outlines the methodological approach adopted to conduct the experiments, including the selection of the materials, welding processes, microstructural characterisation as well as mechanical tests carried out to calculate the mechanical properties at room temperatures, design of experimental plan and overview of equipment utilized for both experimentation and analysis. Section 3.1 delves into dissimilar weld joint between S355J2 and SS316L, while Section 3.2 elucidates the dissimilar weld joint formed between Ti64 and Ti1023, providing detailed descriptions of each testing.

3.1 Dissimilar weld between CS and SS

3.1.1 Material

For this study, S355J2 micro-alloyed LCS and SS grade 316L were selected. Initially, both S355J2 and SS316L were hot-rolled and supplied in pipe form, each measuring 3 meters in length with an outer diameter (OD) of 150 ± 1.5 mm and an inner diameter (ID) of 106 ± 1.1 mm. The chemical compositions of the initially received pipes are presented in Table 5. Following this, the pipes underwent precision-cutting into specific lengths of 40 mm for both the RFW process and TIG processes. Moreover, the ID of each cut piece was meticulously machined to 114 ± 0.1 mm, ensuring precise fitting for the subsequent joining of dissimilar metal pipe pieces.

Table 5: Chemical compositions of S355J2, SS316L and welding filler wire (ER309L) used in this study.

Alloying elements (wt%)	Material		
	S355J2	SS316L	ER309L
% C	0.22	0.01	0.013
% Si	0.55	0.39	0.43
% Mn	1.6	1.63	1.72
% P	0.03	0.03	0.02
% S	0.03	0.01	0.01

% Cu	0.4	0.27	0.17
% N	0.05	0.07	0.08
% Cr	-	16.97	23.3
% Ni	-	11.2	13.5
% Mo	-	2.1	0.14
% Cu	-	0.1	-

3.1.2 Types of welding process adopted.

3.1.2.1 Rotary friction welding (RFW) or Inertia friction welding (IFW)

The IFW method was employed to fabricate the RFW joint at AFRC, UK. Machined S355J2 and SS316L pipe pieces, each measuring 40 mm in height, were prepared for the RFW process by creating necessary key-way slots at one end to secure the parts against each other at both ends of the machine. The RFW weld joint was made using welding parameters listed in Table 6. These parameters were selected based on prior experience with joining of similar material of other steels and a design of experiment (DoE) approach for defining rotational speed and parameter of pressure. Essential variables of process monitored during RFW including inertia, pressure, and rotation speed, while machine upset, indicating the total reduction in final part length of parts to be joined, was measured as the output. Figure 28 (a) illustrates the image of the RFW joint with key-way slots. Subsequently, the RFW joint underwent proof machining to produce transition hybrid coupling demonstrator parts, as depicted in Figure 28 (b and c).

Figure 28: Image displays (a) key-way slots, (b) as welded joint after proof machining and (c) top view of RFW joint between S355J2 and SS316L.

Table 6: Input parameters of RFW joint between S355J2 and SS316L

Input parameters [23]		
Friction Pressure	Rotation speed	Forge Pressure
(bar)	(RPM)	(bar)
165	1010	293

3.1.2.2 TIG welding

TIG welding between S355J2, and SS316L pipe pup pieces was conducted at Nuclear Advanced Manufacturing Research Centre (NAMRC), UK. Prior to welding, each end of the pup piece underwent bevelling, as depicted in Figure 29 (a). Following the bevelling process, both pup pieces (one from S355J2 and the other from SS316L) were tack welded manually using TIG welding, forming a preform. Subsequently, the preform joint was welded using the parameters outlined in Table 7. Filler metal ER309L was chosen for TIG welding between S355J2 and SS316L due to its compatibility with both parent metals and its superior mechanical properties compared to the weld joint itself [82].

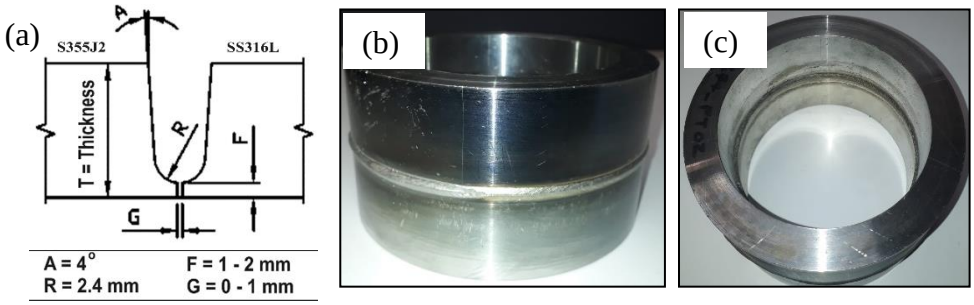

Figure 29: (a) Weld joint configuration and (b) front view of welded pipes and (c) top view of welded pipes of TIG weld joint between S355J2 and SS316L.

Table 7: Parameters of TIG welding between S355J2 and SS316L

Weld run	Root	Hotpass	Fill	Cap
Polarity	DCSP	DCSP	DCSP	DCSP
Filler wire class	American welding society (AWS) A5.9 ER309L			
Diameter of filler wire	2.4 mm			
Position	5G			
Progression	Uphill			
Torch gas	100% Argon			
Torch gas flow rate	10 – 12 lpm			
Purge gas	100% Argon	100% Argon	NA	NA
Purge gas flow rate	15 – 20 lpm	15 – 20 lpm	NA	NA
Tungsten electrode class & dia.	AWS A5.12 /EWTh-2, 2.4 mm			
Current (Amp)	60 - 75	80 - 120	140 - 150	140 - 150
Voltage (Volts)	8 - 11	9 - 12	9 - 12	9 - 12
Welding speed (mm/min)	40 - 50	80 - 100	80 - 100	80 - 100

3.1.3 Experimental Plan

To understand the impact of the welding process on mechanical characteristics, a series of mechanical tests were carried out using samples extracted as per the ASTM standard from the welded parts. Room temperature, tensile tests were done at strain rates of 0.3/min using dog-bond shaped samples. CT specimens were used to measure plane-strain fracture toughness (K_{1C}) tests, and hardness measurements were carried out. Due to constraints related to the size of the testing stock, a single CT specimen was extracted to measure fracture toughness across various orientations. For further insight into the testing procedures and plan, refer to the comprehensive details provided in Table 8.

Table 8: Testing plan of weld joints between S355J2 and SS316L

Type of Test	Standard	Type of Specimen	Test Temperature	Test Environment	Location of specimen	No. of specimen	
						TIG Weld Joint	RFW Joint
Fracture Toughness	ASTM E399 / E1820	Compact Tension	Room Temp.	Air	WCL	1	1
					HAZ-CS	1	1
					HAZ-SS	1	1
					BM-SS	1	
					BM-CS	1	
Tensile Test	ASTM E8M	Miniature Flat			Cross Weld	3	3
					BM-CS	3	
					BM-SS	3	
Micro-structural analysis					Cross Weld	3	3
Macro-structure analysis					Cross Weld	1	1
Hardness	ASTM E384-11				Cross Weld	1	1

Figure 30 illustrates the schematic representation of the sample extraction scheme for the RFW joint. This study adopts the standardized clock-based terminology commonly used in international welding standard such as Det Norske Veritas-Germanischer Lloyd (DNV-GL) standard ST-F101 [83] to streamline communication and maintain consistency. In Figure 30 (b), distinct positions corresponding to 3 o'clock, 6 o'clock, 9 o'clock, and 12 o'clock are clearly identifiable on the sample weld piece, providing convenient reference points. The macrostructure combined with hardness analysis specimen was extracted from the 8 o'clock position along the circumference of the weld joint. Microstructure analysis specimens and cross-weld tensile specimens were extracted from three distinct locations: 7 o'clock, 10 o'clock, and 2 o'clock positions. Fracture toughness test specimens namely compact tension specimens CT were obtained from the following positions: 9 o'clock (specimen with a WCL notch), 12 o'clock (specimen with a notch at the HAZ of SS), and 6 o'clock (specimen with a notch at the HAZ of CS).

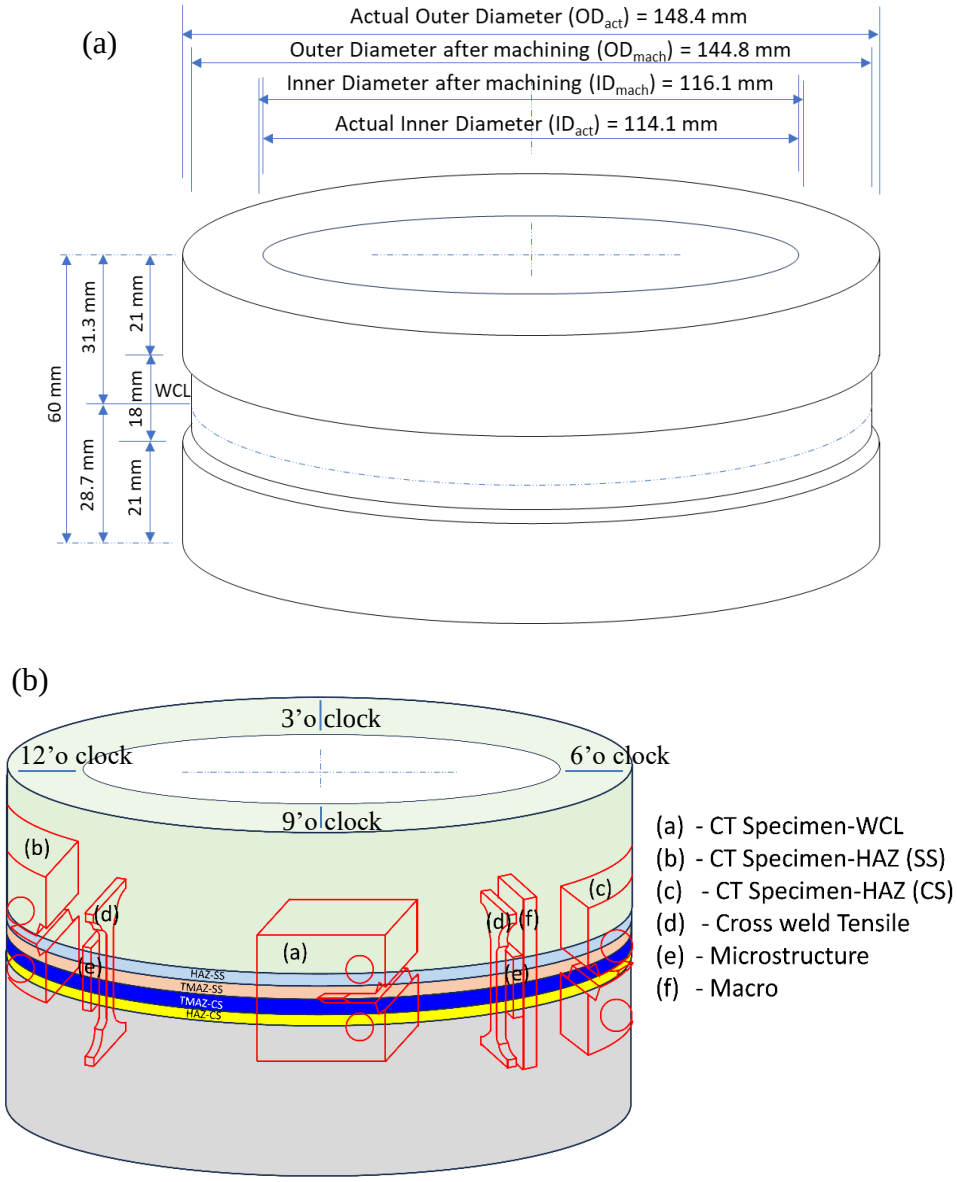

Figure 30: Schematic shows (a) RFW joint between S355J2 and SS316L with dimension and (b) locations used for extraction of samples for tensile and K_{1C} tests. Note CT specimens were positioned in such a way that the tips of notch were falling in HAZ associated with S355J2 and SS316L.

The schematic representation of the sample extraction scheme for the TIG weld joint is depicted in Figure 31. The macrostructure combined with hardness analysis specimen was extracted from the 8 o'clock position along the circumference of the weld joint. Microstructure analysis specimens and cross-weld tensile specimens were extracted from three distinct locations: 7 o'clock, 10 o'clock, and 2 o'clock positions. Tensile specimens from both base metals were extracted from the 8 o'clock locations. Fracture toughness test specimens were extracted from the

following positions: 9 o'clock (specimen with a WCL notch), 12 o'clock (specimen with a notch at the HAZ of SS), 6 o'clock (specimen with a notch at the HAZ of CS), and finally from 10 o'clock (specimens representing both base metals). The preparation of specimens was elaborately described in the respective section.

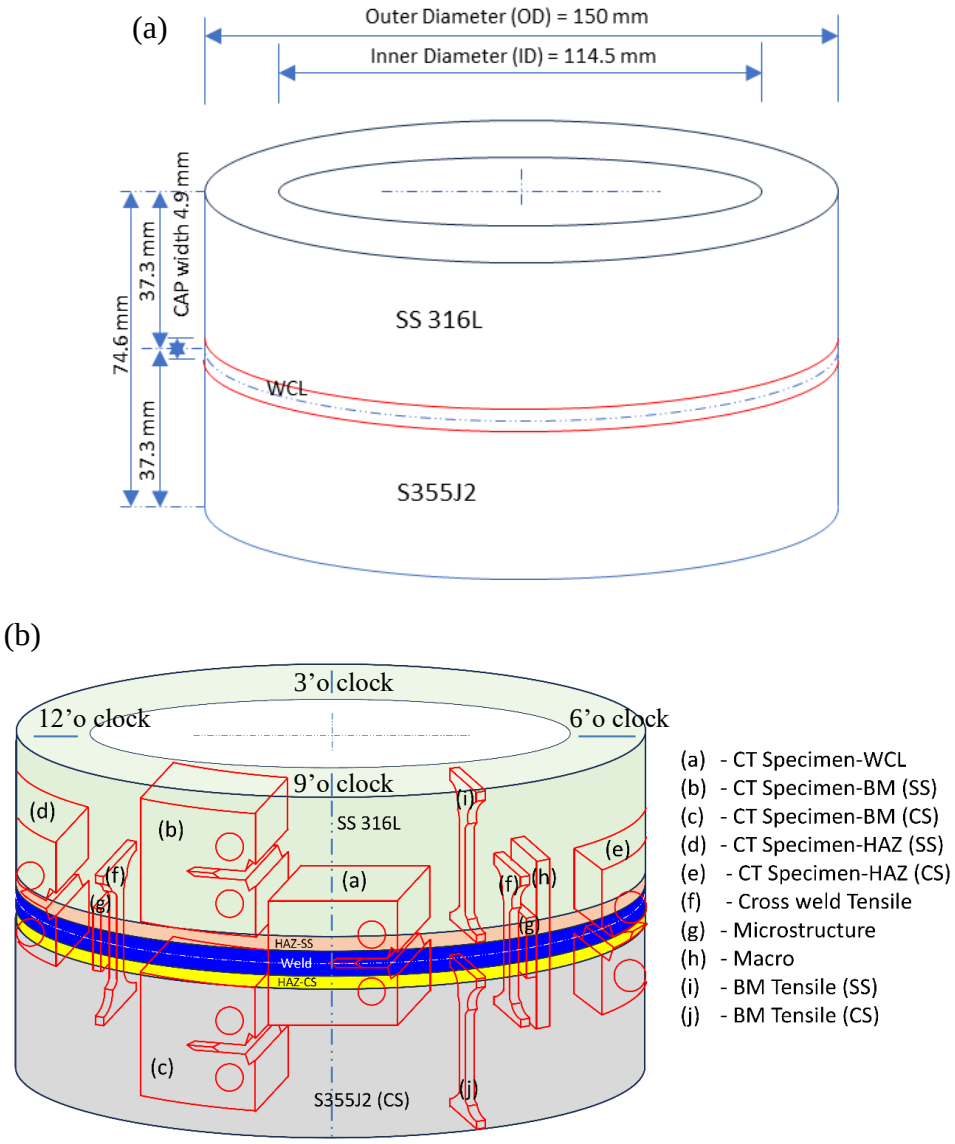

Figure 31: Schematic displays (a) TIG weld joint between S355J2 and SS316L with dimension and (b) locations selected for extracting tensile and CT samples from different key zones of the weldments.

3.1.4 Macrostructure analysis

Macrostructure observation and hardness testing were conducted on the same specimen. The macrostructure analysis aimed to assess the weld profile, including

root and cap width, weld width, and potential flaws such as porosity, lack of side wall fusion, and cold lap. Initially, a 5 mm thick section of the full-length weld joint, as depicted in Figure 32 (a & b), was extracted from the 8 o'clock circumferential using a wire EDM. Subsequently, it was cut into 40 mm lengths to facilitate polishing.

After the cutting process, the specimen underwent grinding using Struers 320, 500, 1000, and 2000 grits silicon carbide paper, followed by final polishing using two different combinations of cloths and abrasives: initial polishing on MD-Dac satin cloth with 0.3µm Diapro diamond abrasive for 4 minutes at 150 rpm, and final polishing on MD-Chem cloth with OP-S Non-dry abrasive for 3 minutes at 150 rpm.

Two different etchants were employed to etch the polished specimen: 3% Nital for the S355J2 side (a mixture of 3 ml nitric acid + 97 ml alcohol), and Aqua regia solution (a mixture of 3ml Hydrochloric acid (HCl) + 1 ml nitric acid (HNO_3)) for the SS316L side. Figure 32 (c & d) depict images of macrostructure specimens of both the RFW and TIG joints.

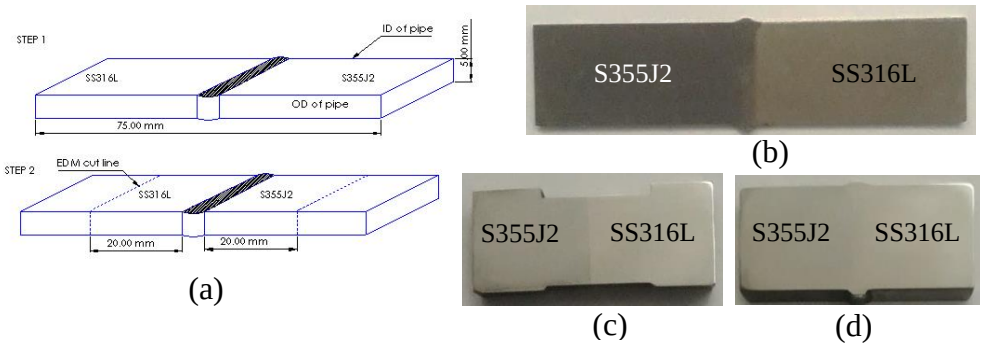

Figure 32: Schematic shows (a) extraction of macrostructure specimen, and images show (b) extracted cut piece of full-length joint, (c) macrostructure specimen for RFW joint, (d) macrostructure specimen of TIG weld joint.

3.1.5 Hardness test

The same specimen that was made for macrostructure assessments was used for hardness determination. To determine the hardness reports of the parent metals, HAZ, and the WM, Vicker Micro-indentation hardness measurements were carried out across the welds in accordance with ASTM E384-11 using a micro-hardness

tester (LM-700, Leco Ltd.) as shown in Figure 33 (a) with a load of 1 kgF (9.80 N) for 12 s dwell time at several locations with a 1.5 mm interval in through thickness direction as per indentation sketch shown in Figure 33 (b & c).

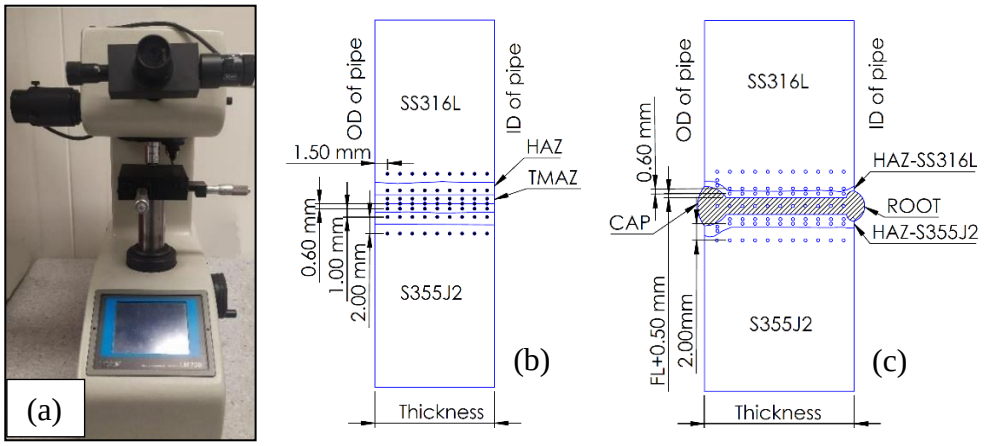

Figure 33: Image shows (a) Leco LM microhardness tester used for measuring in hardness values across the weldments, and hardness indentation sketch for (b) RFW and (c) TIG weld joint between S355J2 and SS316L.

3.1.6 Tensile test

The tensile properties of the RFW joint and TIG weld joint between S355J2 and SS316L were assessed using Miniaturized Tensile Specimens (MTS), as illustrated in Figure 34 (c) and (d). Cross-weld test specimens were obtained from three distinct circumferential locations: the 7 o'clock, 10 o'clock, and 2 o'clock positions (refer to Figure 30 and Figure 31), while tensile specimens from parent metal were machined out from the 8 o'clock position and exclusively from the TIG weld joint (refer to Figure 31) since the parent metals of both weld joints are identical. Initially, a 2 mm thick strip of the full-length weld joint was extracted using a wire EDM, from which miniature tensile specimen were extracted. Cross-weld tensile specimens were extracted to align the centre line of the specimen with the weld centre line and positioned 2 mm away from the outer diameter surface of the weld joint or pipe, as illustrated in Figure 34 (a). Similarly, tensile specimens of both parent metals were extracted according to Figure 34 (b).

The tensile test specimens underwent grinding using 320 and 500 grits Struers silicon carbide paper to eliminate the wire EDM cut marks from all external

surfaces. The ground specimen, depicted in Figure 34 (d) was then prepared for tensile testing.

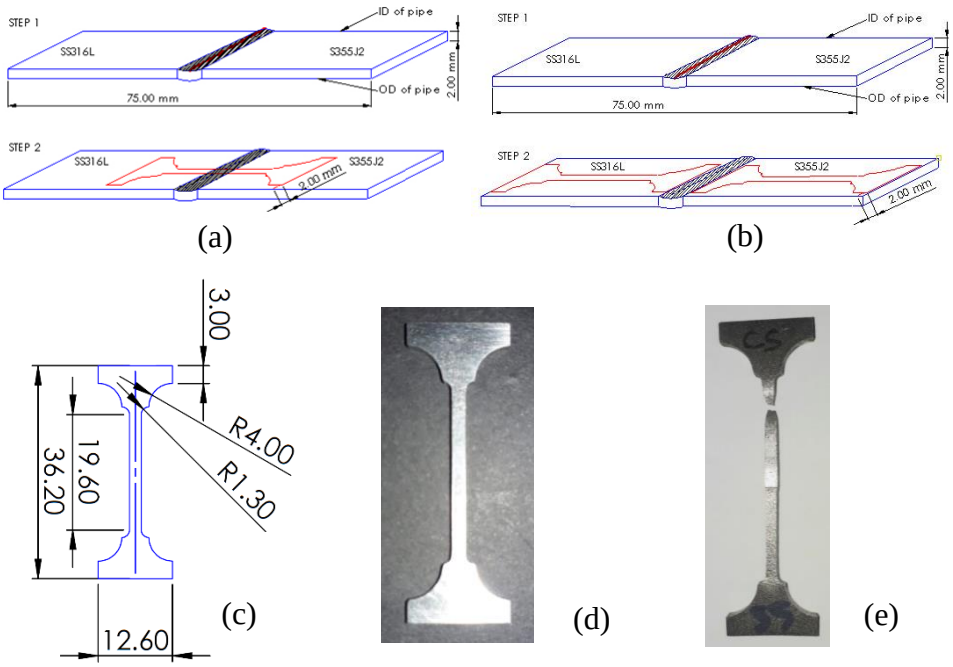

Figure 34: (a) Schematic of extraction of cross-weld tensile specimen, (b) schematic of miniature tensile specimen extracted from parent metal, (c) photograph of tensile specimen, (d) photograph of tensile specimen after polishing and (e) photograph of fractured tensile specimen.

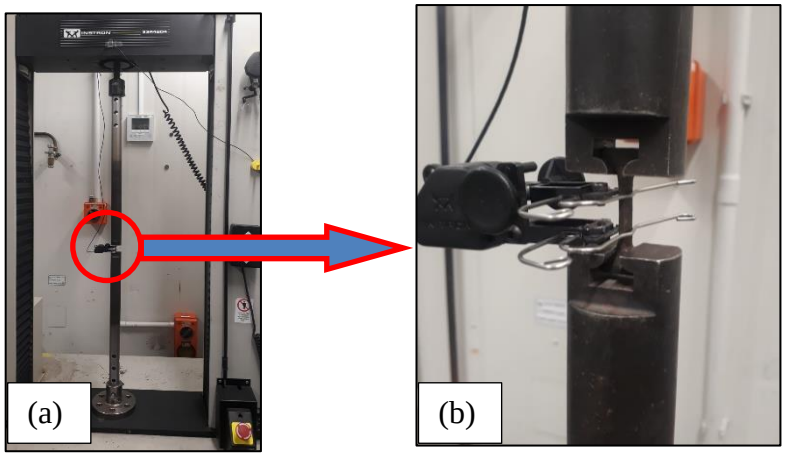

Figure 35: Image shows (a) Instron 33R4204 Tensile tester and (b) close view displays tensile specimen fitted with extensometer in tensile testing machine.

The tensile test was conducted in accordance with ASTM E8M standards, employing a strain rate of 0.3/min (equivalent to 0.015 mm/mm/min) at room

temperature. The Instron 33R4204 universal testing machine equipped with 5KN load cell, illustrated in Figure 35, was used for this purpose. An extensometer with a 10 mm gauge length was employed to record the strain during the test. It was continuously calculating engineering strain considering its extension with respect to its gauge length (10 mm) and recorded those values until test completion. Extension, load, and engineering strain data recorded by the extensometer were collected during the tensile test. Subsequently, the dataset underwent analysis using specific equations to derive parameters such as engineering stress-strain, true stress-strain, Young's modulus, strain hardening exponent, and strength coefficient.

Engineering Stress: Engineering stress or conventional stress is defined as load divided by original cross-sectional area. It is expressed as

$$S = \frac{P}{A_0} \qquad \text{Equation 7 [48]}$$

Where s = engineering stress, P = applied load, A_0 = original cross-sectional area.

Engineering Strain: Engineering strain or conventional strain is defined as change in length with respect to original gauge length. It is expressed as

$$e = \frac{\Delta L}{L_0} = \frac{1}{L_0}\int_{L_0}^{L} dL \qquad \text{Equation 8 [48]}$$

Where $e =$ engineering strain, ΔL = change in gauge length, L_0 = original gauge length.

True Stress: True stress and strain are true indication of material deformation as it considers the instantaneous cross-sectional area and length which is not provided by Engineering stress-strain. True stress-strain curve is often called flow curve as it gives the stress required to cause the material to flow plastically to any given strain.

True stress is defined as load divided by instantaneous cross-sectional area. It is expressed as

$$\sigma = \frac{P}{A} = s(e + 1) \qquad \text{Equation 9 [48]}$$

Where $\sigma =$ true stress, P = applied load and A = instantaneous cross-sectional area

True Strain: True strain is defined as change in length with respect to instantaneous gauge length. It is expressed as

$$\varepsilon = \int_{L_0}^{L} \frac{dL}{L} = \ln \frac{L}{L_0} = \ln(e + 1)$$ Equation 10 [48]

Where ε = engineering strain, L = instantaneous gauge length, L_0 = original gauge length.

Strain hardening exponent and strength coefficient: True stress-strain curve is expressed in mathematical equation as

$$\sigma = K\varepsilon^n$$ Equation 11 [48]

If log of true stress and log of true strain is plotted graphically, the slope of trend line of the log true stress- strain graph is considered as strain hardening exponent (n) and constant of trend line is considered as strength coefficient (K).

3.1.7 Microstructural analysis

The microstructure of the BMs, WMs, HAZ, and TMAZ was examined using the standard metallography procedure outlined in section 3.1.4, involving grinding, polishing, and etching. For each weld joint, three specimens measuring 15mm x 3 mm x 14 mm were cut using a wire EDM before resin mounting. Subsequently, the etched specimens were meticulously examined under an optical microscope (OM, Olympus BX 60 as depicted in Figure 36) in bright field mode at various magnifications to analyze the microstructure of the different weld areas.

Figure 36: Image of Olympus BX 60 optical microscope.

A Scanning Electron Microscope (SEM, Hitachi S4700) equipped with energy dispersive spectroscopy (EDS) and accelerating voltage of 20kV operating in both

secondary electron (SE) and backscattered electron modes (BSE) were used for comprehensive microstructural analysis. EDS analysis was conducted to assess chemical homogeneity and examine the fracture surface of broken fracture toughness and fatigue specimens. This analysis provided insights into the elemental composition and distribution within the examined specimens. The specimens prepared for optical microscopy were additionally deployed for SEM analysis.

3.1.8 Fracture Toughness Testing

Fracture Toughness Test Specimen Preparation: To conduct plane-strain fracture toughness tests in accordance with ASTM standards E399 and E1820, compact tension (CT) specimens with a width (W) equal to twice the thickness (B) of the specimen (W = 2B) were chosen. This selection was made primarily due to constraints related to weld joint geometry, which posed limitations on the extraction of single edge notch bend (SENB) or single edge notch tension (SENT) specimens as illustrated in Figure 37. In general, to determine plane-strain fracture toughness, SENB or CT specimens are utilized. SENT specimen is deployed to determine CTOD as recommended by Det Norske Veritas-Germanischer Lloyd (DNV-GL) standard ST-F101 [83].

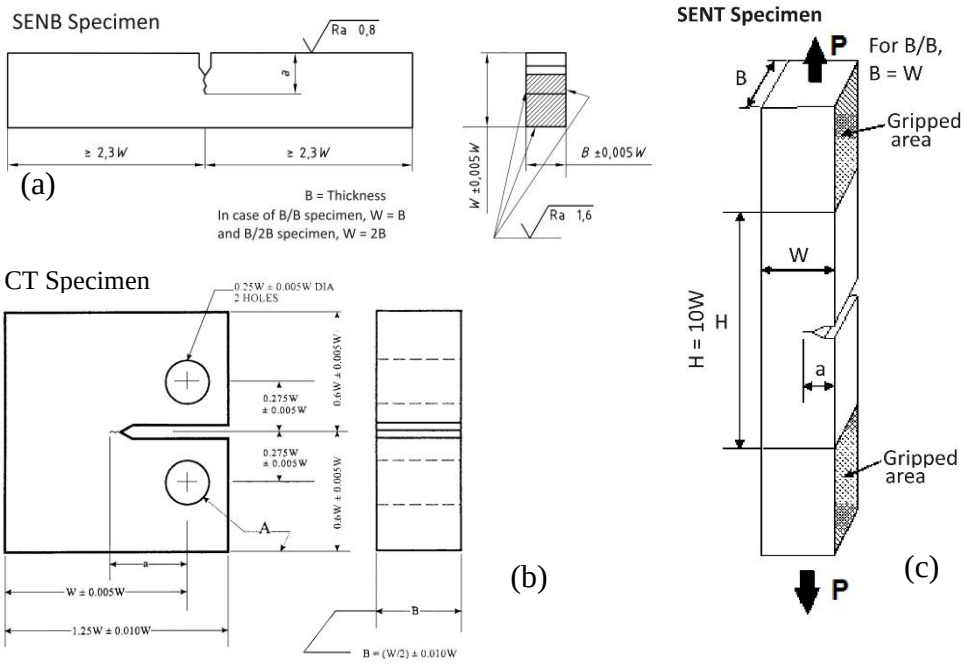

Figure 37: Image displays the schematic of (a) SENB specimen [84], (b) CT specimen [84], and (c) SENT specimen [83].

Figure 38 illustrates the schematic of the CT specimen utilized for the fracture toughness test. One specimen was extracted from each circumferential location, namely 9 o'clock, 12 o'clock, and 6 o'clock, as depicted in Figure 30 and Figure 31 and detailed in Table 8, utilizing a wire EDM. Specimen for the parent metal was extracted from the 10 o'clock circumferential location of the TIG weld joint due to the identical nature of the parent metal in both weld joints.

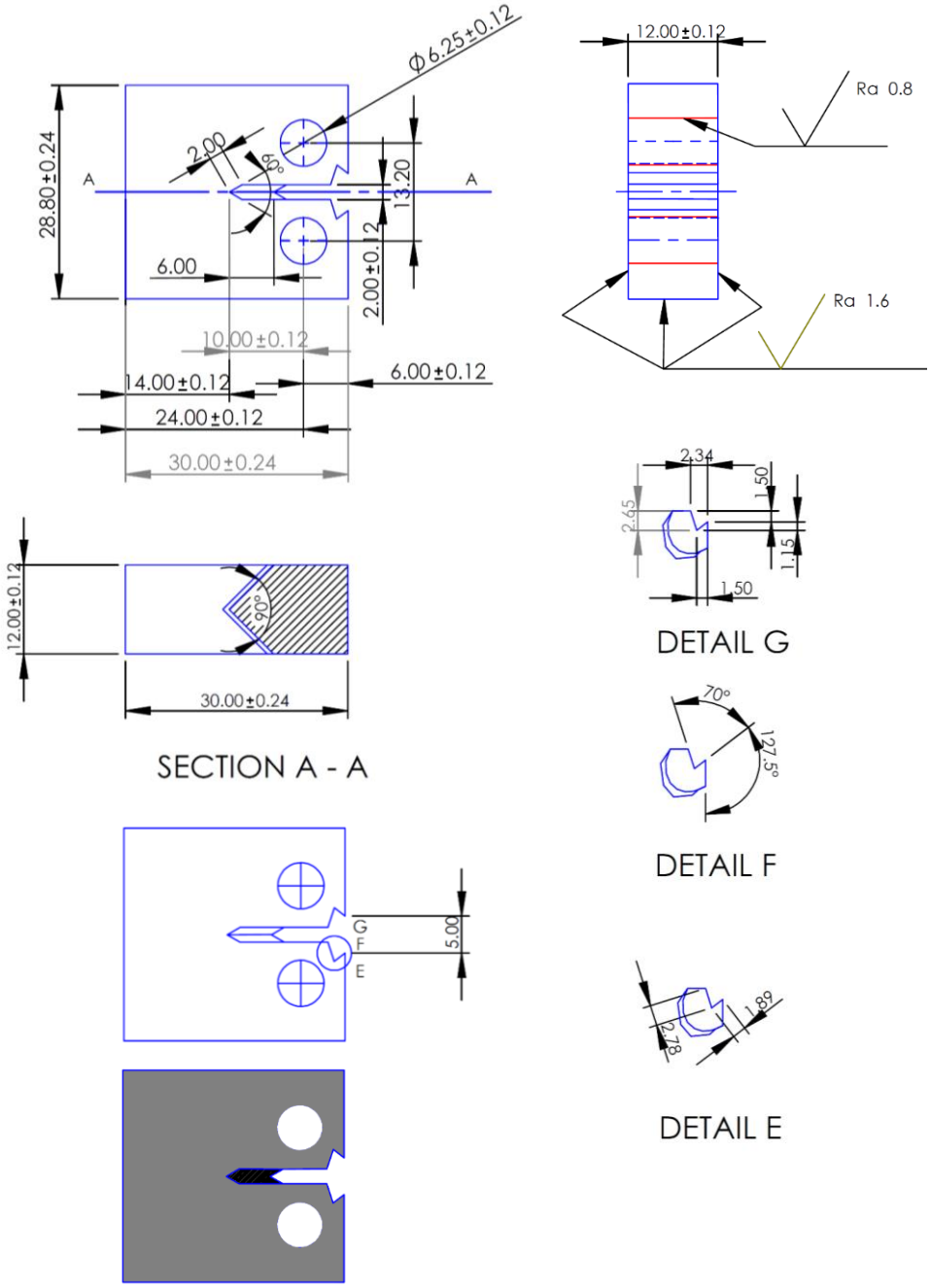

Figure 38: Schematic of fracture toughness test specimen i.e. CT specimen and details of chevron notch machined out.

Initially, rectangular blocks were extracted, as illustrated in Figure 39 (a). Following the extraction of blocks, notch locations were precisely marked on each block in accordance with the specifications outlined in Figure 30 and Figure 31. Various notches serve distinct purposes in conducting fracture toughness tests, as depicted in Figure 40. A chevron notch, renowned for its ability to easily generate fatigue pre-cracks, was selected in alignment with ASTM standards E399 and E1820. The notch orientation was set along the rolling direction or circumferential direction, parallel to the weld direction but transverse to the loading direction.

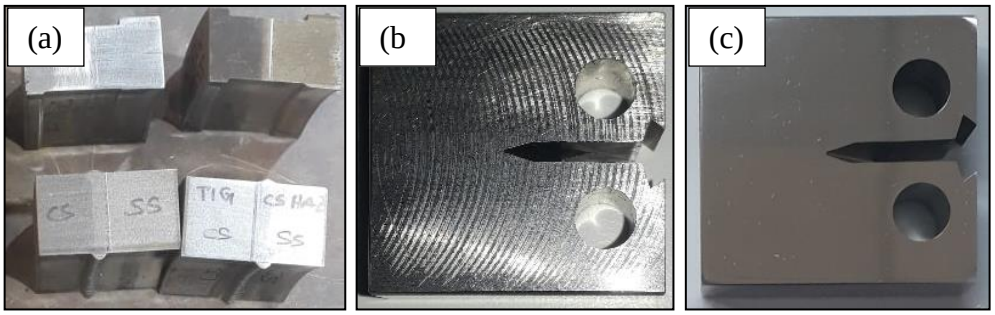

Figure 39: Photograph shows (a) extracted material for preparing CT specimen, (b) machined CT specimen and (c) polished CT specimen prepared for test.

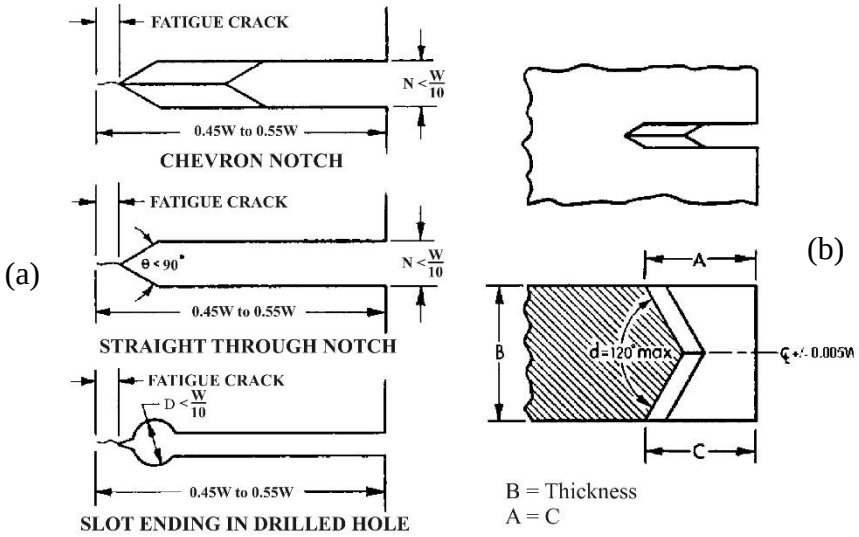

Figure 40: Image displays (a) different types of notches and (b) detail of chevron notch [85].

Following extraction, blocks underwent machining in accordance with the drawing depicted in Figure 38, employing both milling and drilling techniques, while chevron notches were precision-machined using a wire EDM. The resulting

machined specimens are illustrated in Figure 39 (b). Subsequently, to eliminate machining marks from the specimen surfaces, the grinding and polishing process outlined in section 3.1.4 was implemented. The polished specimens, showcased in Figure 39 (c), underwent examination under a Stereo microscope (HEERBRUGG WILO M38 as illustrated in Figure 41) at a magnification of 6.4X to accurately measure the initial machined notch length.

Figure 41: Image of Sterio microscope (HEERBRUGG WILO M38)

Fatigue Pre-cracking: Prior to the actual fracture toughness test, all specimens underwent pre-cracking using the Instron 8801 Servo-hydraulic dynamic testing machine. Cyclic loading in stress-controlled mode was applied with a stress ratio (R) of 0.1, a frequency of 40 Hz and a sine waveform. For all samples the number of cycles is usually maintained between about 10^4 and 10^6 based on specimen size, notch preparation, and stress intensity level.

Maintaining an initial crack length (a_0) (i.e. total length of the machined notch plus the fatigue pre-crack) between 0.45W and 0.55W was crucial to determine plane-strain fracture toughness (K_{IC}) [84, 85]. For a specimen with a thickness of 12.0 mm, (a_0) was targeted between 10.8 mm and 13.2 mm, aligning with Figure 38. To meet the specified requirements, 12.0 mm was chosen as the targeted a_0 value, ensuring the fatigue pre-crack length met the condition of being at least 5% of the initial (a_0) or 1.3 mm, whichever is greater.

According to ASTM standard E399, fatigue pre-cracking occurred in two distinct stages. Stage 1 controlled 97.5% of the initial crack length (a_0), while Stage 2 governed the remaining 2.5%. To prevent undesirably high crack growth rates in Stage 1, the maximum stress intensity factor (K) specified in Equation 13 was

limited to a maximum 80% of the assumed fracture toughness. In Stage 2, this was limited to a maximum of 60% of the assumed fracture toughness.

The range of applied load (P) for stage 1 of fatigue pre-cracking was determined by using Equation 13, where stress intensity equals to 80% of assumed fracture toughness. The maximum value of applied load was computed with the instantaneous crack length (a) set to machined notch length and minimum value of applied load was calculated with the instantaneous crack length (a) set to 97.5% of initial targeted crack size, (a_0) [i.e. 12.0 mm]. Similarly, applied load (P) range for stage 2 of fatigue pre-cracking was computed using Equation 13, where stress intensity is set to 60% of the assumed fracture toughness. The maximum value of applied load was determined with the instantaneous crack length (a) is equal to total crack length achieved after completion of stage 1, while the minimum value of applied load was calculated with the instantaneous crack length (a) set to initial targeted crack size, (a_0) [i.e. 12.0 mm].

Finally, these applied load ranges were compared with the maximum load that could be applied for fatigue pre-cracking, as determined by Equation 12. It was ensured that the load ranges remained below the maximum load obtained from Equation 12.

$$\mathrm{P_f} = \frac{0.4\mathrm{B}\mathrm{b}_0^2\sigma_\mathrm{Y}}{(2\mathrm{W} + a_0)} \qquad \text{Equation 12}$$

Where P_f = maximum load for fatigue pre-cracking for CT specimen, B = average thickness of CT specimen (for plain sided specimens, B shall be measured adjacent the notch), a_0= initial crack length (i.e. total length of the machined notch plus the fatigue pre-crack); for instance, a_0= machine notch length at start of testing, W = 2B for this CT specimen, b_0= original remaining ligament (i.e. distance from the original crack front to the back edge of the specimen, i.e. $(b_0 = W - a_0)$, σ_Y = effective yield strength = $\frac{\sigma_{YS}+\sigma_{UTS}}{2}$.

$$\mathrm{K} = \frac{\mathrm{Pf}(a/\mathrm{W})}{(\mathrm{BB_N W})^{1/2}} \qquad \text{Equation 13}$$

Where, K= stress intensity factor, P = applied load, B = average thickness of CT specimen, B_N = net thickness of side grooved specimen, for the CT specimens that are used in this project is plain sided where $B_N = B$.

$$\mathrm{f}(a/\mathrm{W}) = \left(\frac{\xi}{\zeta}\right)[\mathrm{C}_0 + \mathrm{C}_1(a/\mathrm{W}) + \mathrm{C}_2(a/\mathrm{W})^2 + \mathrm{C}_3(a/\mathrm{W})^3 + \mathrm{C}_4(a/\mathrm{W})^4]$$

The parameters for $f(a/W)$ are listed in Table 9.

Table 9: Parameters for Stress-Intensity Factors

Parameter	CT Specimen
ξ	$2 + a/W$
ζ	$(1 - a/W)^{3/2}$
C_0	0.886
C_1	4.64
C_2	-13.32
C_3	14.72
C_4	-5.6
Limits	$0.2 \leq a/W \leq 1$

Once the fatigue pre-crack parameters were established, test specimens were loaded on an Instron 8801 Servo-hydraulic dynamic testing machine as depicted in Figure 42 under load control mode to carry out fatigue pre-cracking at room temperature.

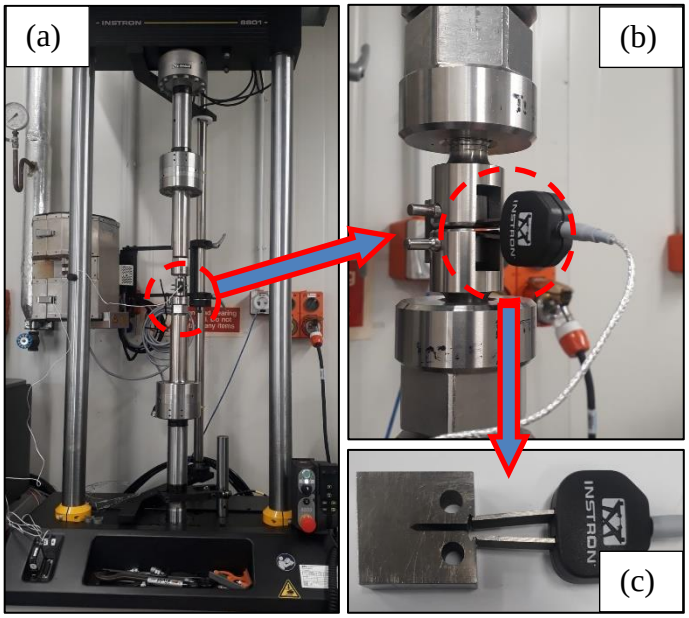

Figure 42: Image shows (a) Instron Servo-hydraulic dynamic testing machine, close view displays (b) CT specimen fitted with clip gauge loaded in testing machine, and (c) mounting of clip gauge in integral knife edge of specimen.

A 5 mm gage length extensometer or clip gauge with a 2 mm maximum extension was affixed at the mouth of the machined notch to monitor crack mouth opening displacement (CMOD), serving as an indicator of fatigue crack initiation. Specimens underwent incremental unloading, with extensions measured at intervals

of 0.2 to 0.3 mm. Optical microscopy, with magnifications of either 5X or 10X, was employed to visualize fatigue crack initiation. To ensure symmetrical behavior, the specimen end was carefully turned. Upon detection of the fatigue pre-crack under an optical microscope (refer to Figure 43) and achieving the predetermined length, the test was concluded, and the average fatigue pre-crack length was measured.

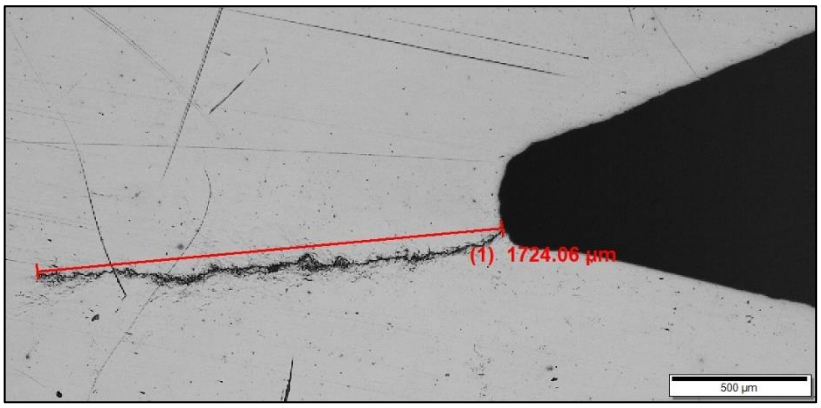

Figure 43: Optical microscopy image at high magnification displays the initiation of fatigue pre-crack from notch tip and propagated perpendicular to applied load direction.

Fracture Toughness Test: Following the completion of fatigue pre-cracking, the loading rate for the static tensile test was determined by Equation 13 considering instantaneous crack length (a) equal to machine notch length plus actual average fatigue pre-crack length.

Subsequently, specimens underwent static tensile testing on an Instron 8801 Servo-hydraulic dynamic testing machine at ambient temperature. During this static test, both load and crack mouth opening displacement were meticulously recorded using an extensometer featuring a 5 mm gauge length and 2 mm maximum extension. A loading rate of 300 N/s (i.e. stress intensity rate of 1.4 – 1.7 MPa√m/s) in compliance with ASTM E399 was employed to carry out testing.

Fracture Toughness Calculation: Following the completion of the static tensile test, load versus displacement graphs were plotted and Type-I graph generated for all the specimens as per ASTM E399 is showed in Figure 44.

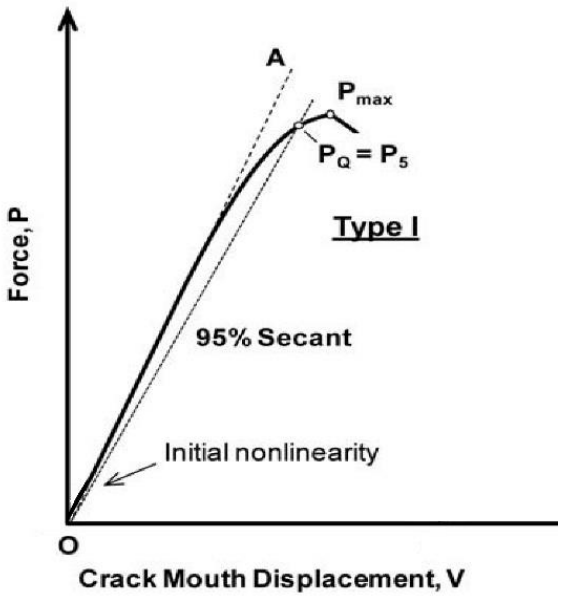

Figure 44: Typical Load or Force vs CMOD Type-I graph of ASTM E399

P_Q value for each specimen was extracted from load versus CMOD curves of respective specimen. Subsequently, K_Q value of each specimen was computed using Equation 13, where the instantaneous crack length (a) = a_0= total length of the machined notch plus the average fatigue pre-crack. K_Q represents the stress intensity corresponding to load P_Q and is commonly referred to as the fracture toughness of material.

Following the fracture of the specimen, the actual crack length up to the initial crack front was measured in nine distinct locations as illustrated in Figure 47, and the average fatigue pre-crack length was determined. This average fatigue pre-crack length was then utilized to calculate K_Q value for each specimen.

For specimen exhibiting an elastic-plastic fracture, fracture toughness was quantified in terms of CTOD (i.e. crack tip opening displacement), denoted as δ_m as per ASTM E1820 (Equation 14).

$$\delta_m = \frac{K_Q^2(1-\nu^2)}{2\sigma_{YS}E} + \frac{[r_p(W-a_0)]v_{pl}}{[r_p(W-a_0)+a_0+z]} \qquad \text{Equation 14}$$

$$r_p = \text{plastic roation factor} = 0.4\,(1+\alpha)$$

$$\alpha = 2\left[\left(\frac{a_0}{b_0}\right)^2 + \frac{a_0}{b_0} + \frac{1}{2}\right]^{1/2} - 2\left(\frac{a_0}{b_0} + \frac{1}{2}\right) \quad \text{Equation 15}$$

Where, a_0 = total length of the machined notch plus the average fatigue pre-crack after fracture; b_0 = length of uncracked ligament = $(W - a_0)$; W = width of the specimen; σ_{YS} = Yield stress at 0.2% strain offset; σ_{UTS} = Ultimate tensile stress; E = Young's Modulus; ν = Poisson's ratio; z = distance of knife-edge measurement point from the load-line on the CT specimen (refer Figure 45); K_Q can be obtained from Equation 13 considering a_0 value.

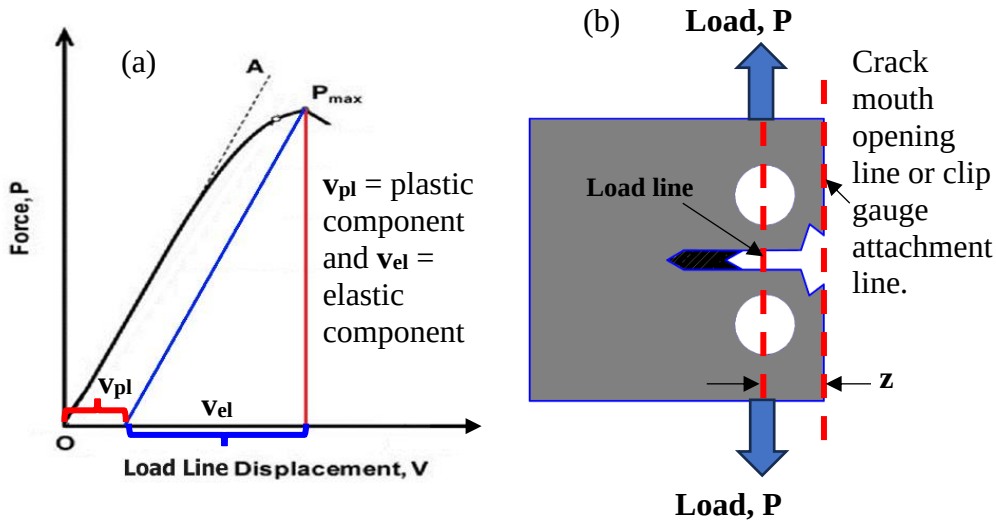

Figure 45: (a) Schematic illustrates Load Vs CMOD curves and (b) 2D CAD model showing reference lines used for clip gauge attachment.

Fracture Toughness Test Validation: To validate the test in accordance with ASTM E1820, in addition to other specified criteria, adherence to two crack length-related criteria was ensured.

$$a = \frac{1}{8}\left(\frac{a_1 + a_0}{2} + \sum_{i=2}^{8} a_i\right) \quad \text{Equation 16}$$

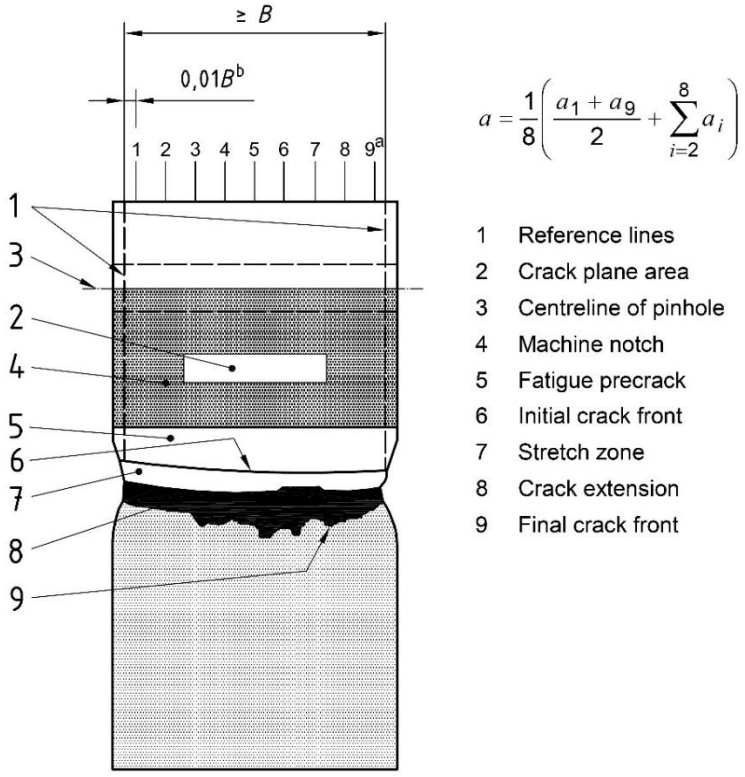

Figure 46: Schematic of measurement of initial and final crack length after breaking the specimen [86].

Specifically, none of the nine physical measurements of crack size (measured from the centerline of the pinhole up to the initial crack front in Figure 46) should deviate by more than 5% from the average initial crack size, denoted as a.

Consistency in Initial Crack Size: None of the nine physical measurements of crack size, obtained from the centerline of the pinhole up to the initial crack front as depicted in Figure 46, deviated by more than 5% from the average initial crack size.

Consistency in Final Crack Size: Similarly, none of the nine physical measurements of crack size, measured from the centerline of the pinhole up to the final crack front as depicted in Figure 46, deviated by more than 5% from the average final crack size.

Adhering to these stringent crack length criteria ensures the integrity and reliability of the test procedure as per ASTM E1820 standards.

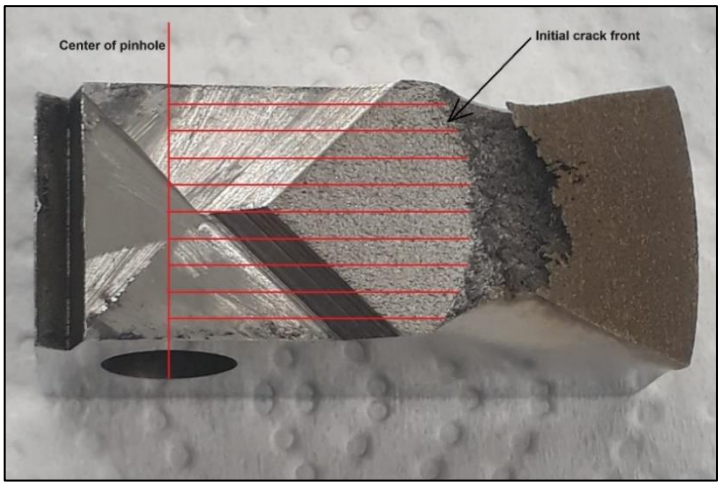

Figure 47: Measurement of crack length up to initial crack front of broken fracture toughness test specimen.

Hence, a fractured part of each specimen underwent examination using a Stereomicroscope (HEERBRUGG WILO M38). Nine measurements of both initial and final crack lengths were conducted and recorded, as shown in Figure 47. The collected crack length measurement data were then subjected to thorough analysis to validate the test results and ensure their accuracy and reliability.

Fractography and crack path analysis of fracture toughness test specimens: Fracture surface was analyzed using SEM. Two distinct types of fractographic observations were performed as depicted in Figure 48. In Type 1, the fracture surface was examined to discern the mode of failure, providing insights into the fracture mechanisms involved. In Type 2, a section was precisely extracted from the center of the fractured part. The section underwent metallographic preparation akin to microstructural analysis and was subsequently characterized using SEM to elucidate the crack path in relation to the microstructure in order to give deeper insights into the fracture behavior and its interaction with microstructure of the sample tested.

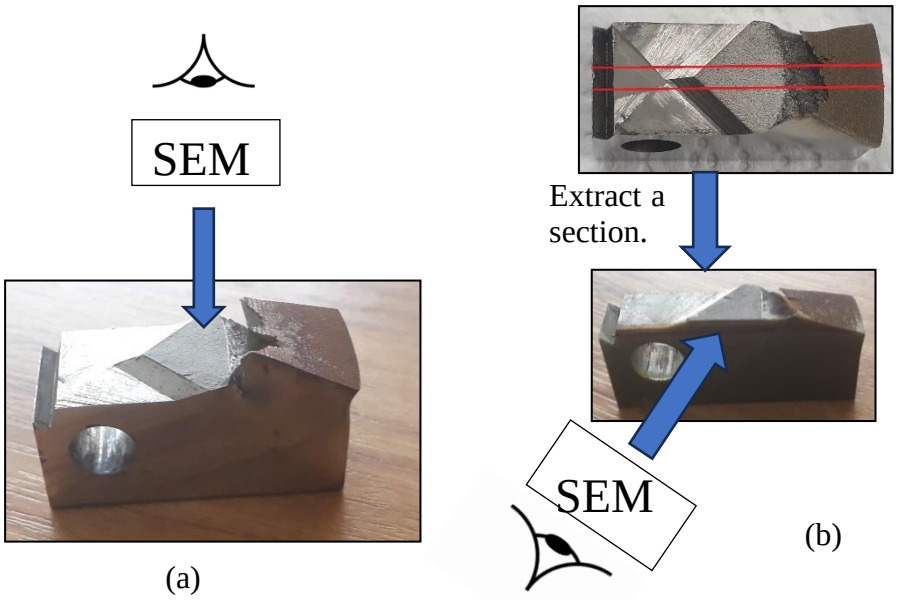

Figure 48: Types of fractographic observation (a) Type 1-fracture surface and (b) Type 2- crack path.

3.2 Dissimilar weld between Ti-64 and Ti-1023

3.2.1 Material

Ti-64, a widely used α + β titanium alloy, and Ti-1023, a common metastable β titanium alloy, were chosen for the study. Ti-64 was received in the forged annealed condition with 80 mm diameter and having various lengths (300 - 500 mm). Whereas Ti-1023 was received in the form of a forged billet of 350 mm diameter and 80 mm length, solution treated at (28°-56°C) below the beta transus temperature for a minimum of 30 minutes, then water quench followed by aged at (570°-600°C) for 8 hrs, finally air cooled. Then round bars with an outer diameter (OD) of 35 ± 0.5 mm were extracted. To facilitate the joining process in the RFW procedure, both round bars were saw-cut into several long pup pieces, each with a length of 70 mm. The chemical compositions of the initially received Ti alloys are listed in Table 10.

Table 10: Chemical compositions of Ti-64 and Ti-1023 material.

wt%	**%Ti**	**%V**	**%Fe**	**%Al**	**%N Max.**	**%C Max.**	**%O Max.**	**$[Mo]_{eq}$**
Ti-64 [87]	Balance	3.5 – 4.5	0.40 Max.	5.5 – 6.5	0.05	0.08	0.18	-4.5
Ti-1023 [88]	Balance	9 - 11	1.6 – 2.2	2.6 – 3.4	0.05	0.05	0.10	8.0

To comprehend the stability of the β phase, $[Mo]_{eq.}$ was calculated using Equation 2 and Equation 3 [30]. Based on Cotton, et al. [30] study, Ti-1023 alloy utilized in this project is classified as metastable beta titanium alloy as $[Mo]_{eq.}$ is 8 wt%.

3.2.2 Rotary friction welding (RFW)

The RFW joint was fabricated utilizing the IFW method at AFRC, UK. Round bars, 35 mm in diameter and 70 mm in length, composed of Ti-64 and Ti-1023, were made for the RFW procedure with key-way slots incorporated at one end to facilitate secure locking of the parts at both ends of the machine. Welding parameters specified in Table 11 were used for creating the RFW weld joint, chosen based on prior experiences with similar materials and employing a DoE-like approach for selecting speed and pressure parameters.

The primary variables monitored during RFW included inertia, pressure, and rotation speed, with machine upset serving as the output measurement, indicating the total reduction in the final part length. This length reduction caused by the formation of flash. The extent of weld flash formation and analysis of cross-sectional metallurgy can serve as indicators for assessing the weld's quality. Figure 49 provides a visual representation of the RFW joint and displays weld flash.

Figure 49: Image shows RFW joint between Ti-64 and Ti-1023.

Table 11: Parameters of RFW joint between Ti-64 and Ti-1023

Input parameters		
Friction Pressure	Rotation speed	Forge Pressure
(bar)	(RPM)	(bar)
10	1000	10

3.2.3 Experimental Plan

To assess the influence of the RFW on mechanical and fatigue characteristics, a set of tests was scheduled following ASTM criteria. These tests encompassed microstructure analysis, tensile assessments, fatigue properties evaluations, and hardness analyses. Due to limitations concerning the size of the test material, a micro tensile sample was selected to perform tensile test. For a thorough understanding of the testing protocols and strategy, refer the detail information presented in Table 12.

Table 12: Testing plan of RFW joints between Ti-64 and Ti-1023

Type of Test	Standard	Type of Specimen	Test Temperature	Test Environment	Location of specimen	No. of specimen
High Cycle Fatigue	ASTM E466	Uniform gauge	Room Temp.	Air	Cross Weld	8
Tensile Test	ASTM E8M	Miniature Flat			Cross Weld	3
Micro-structural analysis					Cross Weld	3
Macro					Cross Weld	1
Hardness	ASTM E384-11				Cross Weld	1

Figure 50 (a) displays the dimensions of all the RFW joints of Ti-64 and Ti-1023. The schematic representation of the RFW joint's sample extraction scheme is presented in Figure 50 (b). Four 13 mm diameter cylinders, each encompassing the full weld joint length, were extracted from four different quadrants of each round bar to prepare HCF specimens. A total of 16 cylinders (4 from each joint) were obtained. The macrostructure combined with hardness analysis specimen was obtained from the remaining material at the centre of the round bar. Additionally, each microstructure analysis and cross-weld tensile specimen were extracted from the remaining material at the centre of each round bar. The preparation of specimens was thoroughly detailed in the respective section.

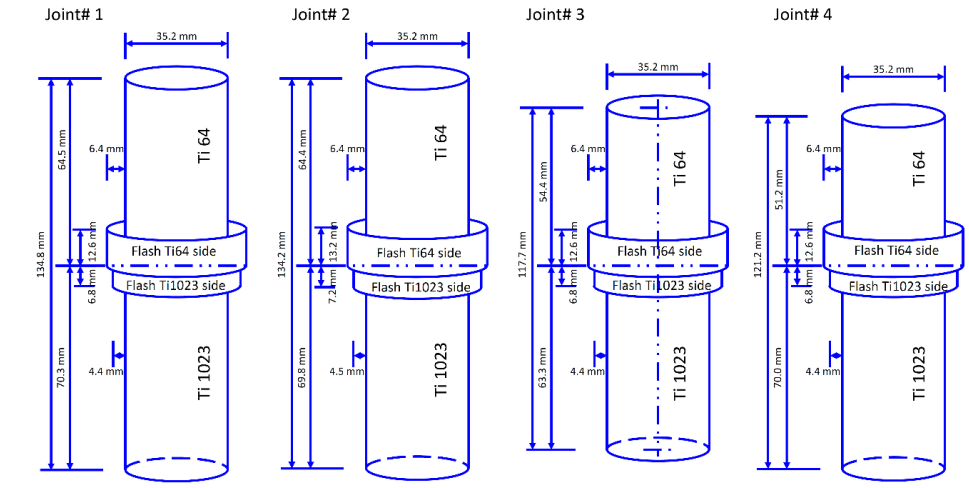

(a)

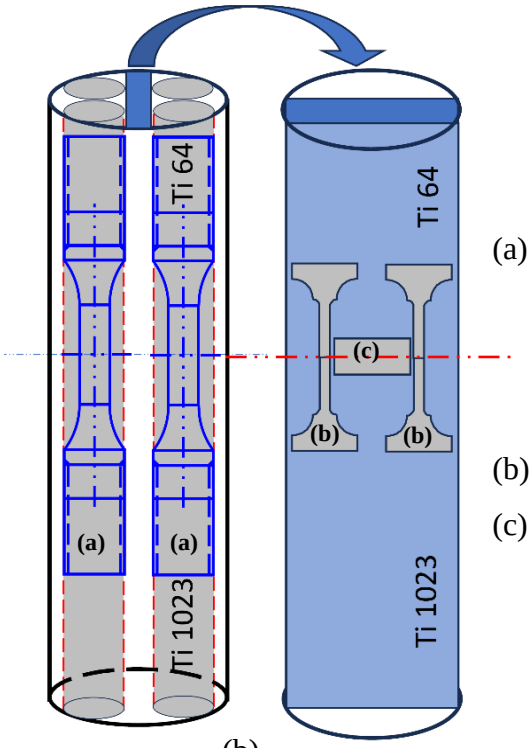

(a) – HCF test specimen
NOTE: Total 16 nos (4 nos from each joint) specimens were extracted
(b) – Tensile test specimen
(c) – Microstructure / Macrostructure analysis

(b)

Figure 50: Schematic illustrates (a) RFW joint between Ti-64 and ti-1023 with dimension, (b) locations of sample extraction.

3.2.4 Macrostructure analysis

The macrostructure specimen underwent extraction and preparation according to the guidelines outlined in section 3.1.4. For etching the polished specimen, a Kroll's reagent comprising 3 vol.% HF, 5 vol.% HNO_3 in H_2O was employed, with

exposure times ranging from 15 to 30 seconds. Figure 51 displays image of macrostructure specimen of RFW joint.

Figure 51: Image of macro specimen for RFW joint between Ti64 and Ti-1023.

3.2.5 Hardness test

Vicker Micro-indention hardness measurement was performed according to the guidelines outlined in section 3.1.5 in various locations with 1.5 mm interval from OD to centre direction as per indentation sketch shown in Figure 52.

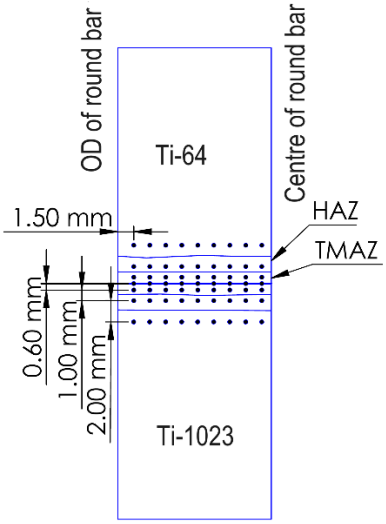

Figure 52: Hardness indentation sketch for RFW joint between Ti-64 and Ti-1023.

3.2.6 Tensile test

Miniaturized tensile specimens, as illustrated in Figure 34 (c and d), were employed to conduct tensile tests for characterizing the mechanical properties of the RFW

joint between Ti-64 and Ti-1023. Cross weld tensile specimens were extracted from the central region of the cylindrical weld joint, as depicted in Figure 50 (b) with one specimen extracted from each weld joint. Initially, a 2 mm thick strip was extracted from the centre of the full-length weld joint using a wire EDM. Subsequently, a miniature tensile specimen was extracted from the 2 mm strip in such a manner that the centreline of the specimen aligned with the weld centreline, as indicated in Figure 50 (b).

Following extraction, the tensile test specimen was prepared and tested in accordance with the procedure outlined in section 3.1.6. Test was conducted with a strain rate of 0.1/min to comply with ASTM requirements at room temperature utilizing Instron 33R4204 universal testing machine.

3.2.7 Microstructural analysis

Microstructural analysis was performed according to the guidelines outlined in section 3.1.7 to study the microstructure of different areas of RFW joint. The etching process described in section 3.2.4 previously was deployed to etch the polished specimen.

3.2.8 Fatigue Test

Fatigue Test Specimen Preparation: To prepare fatigue specimens featuring a 12 mm machine thread, as illustrated in Figure 53, 13 mm diameter cylinders (including 1 mm machine allowances) were extracted, covering the entire length of the weld joint. A total of 16 cylinders (4 from each joint) were obtained. All the specimens were machined into a uniform gauge shape, for performing the high cycle fatigue test according to Figure 53.

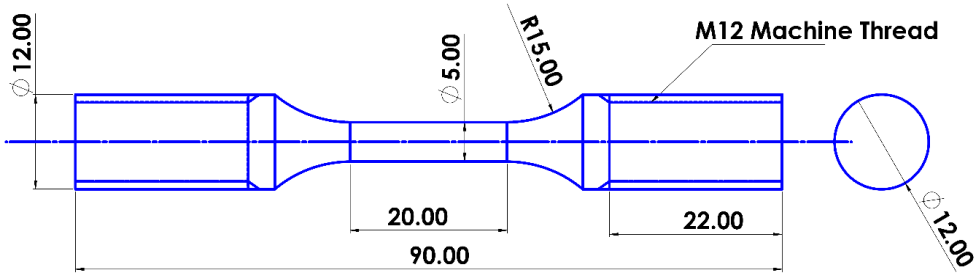

Figure 53: Schematic of high cycle fatigue test specimen.

Achieving a low surface roughness is crucial for accurate fatigue test results. Computer numerical control (CNC) machining with Carbide inserts was employed to ensure precision in machining dimensions and attain a high surface finish. To control surface roughness (R_a), the material removal rate (depth of cut) began at 0.5 mm/rev and reduced to 0.1 mm/rev during near-surface machining. A low feed rate was maintained to prevent internal stress build-up and achieve a lower surface roughness (R_a) value.

After machining, specimens underwent uniform polishing in the gauge portion along the longitudinal direction to eliminate circular machining marks and achieve a smooth surface finish. The grinding and polishing process, as detailed in section 3.1.4, was applied. Subsequently, the gauge length portion was examined by optical microscopy (OM, Olympus BX 60) at 20X magnification to ensure the absence of circular lines or scratches. Figure 54 (a) showcases a representative final prepared fatigue specimen.

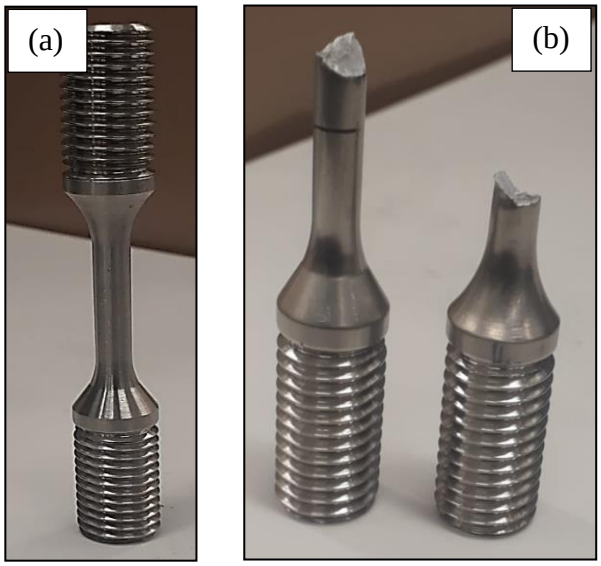

Figure 54: Photographs showing (a) a final prepared fatigue test specimen before testing and (b) the broken fatigue specimen after test.

3.2.8.1 High Cycle Fatigue Test

A high cycle fatigue test, conducted in compliance with ASTM E466 standards, adopted a load or stress-controlled approach. Polished uniform gauge length specimens were loaded onto the Instron 8801 Servo-hydraulic dynamic testing machine, employing a stress ratio (R) of 0.1 and a frequency of 40 Hz. The test was

run up to 10^7 cycles, with variations in the maximum stress levels: 500 MPa, 550 MPa, 600 MPa, 650 MPa, 700 MPa, and 800 MPa.

Upon completion of the test, an S-N curve was constructed, illustrating the relationship between maximum stress and the number of cycles (in logarithmic scale). This curve provided a comprehensive depiction of the fatigue behaviour under diverse stress conditions, enabling a thorough analysis of the material's fatigue characteristics.

Fractography and crack path analysis of fatigue test specimens: Fractographic analysis was performed on the fractured surfaces using SEM. Two types of fractographic observations were conducted, as illustrated in Figure 55. In Type 1, the fracture surface was examined to discern the mode of failure. In Type 2, the broken specimen was bisected along its longitudinal axis, and one-half section underwent metallographic preparation akin to microstructural analysis. Subsequently, it was observed using the SEM to elucidate the crack path in relation to the microstructure.

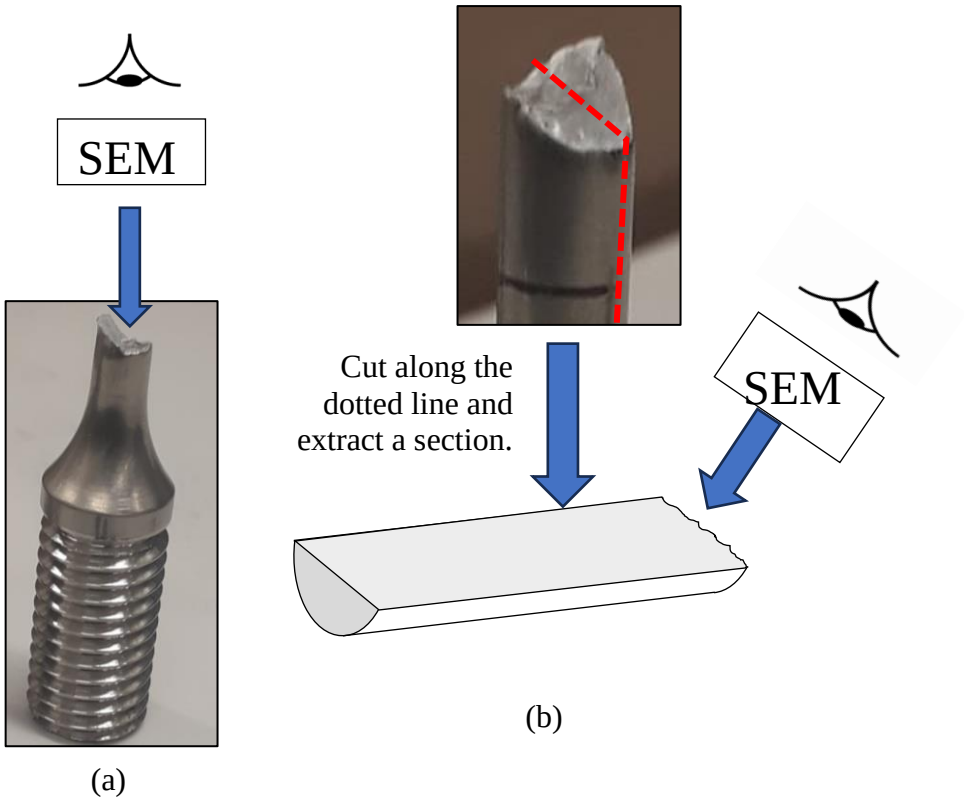

Figure 55: Types of fractographic observation (a) Type 1-fracture surface and (b) Type 2- crack path.

Chapter 4

4 Results and Discussions

This chapter serves the core of the research, presenting the findings of microstructural analysis and tests carried to evaluate the performance and structural integrity of different types of weld joints. The findings are discussed and correlated with existing literature, theoretical frameworks, and research hypotheses in detail in two sections. In Section 4.1, covers the dissimilar weld joint between S355J2 and SS316L (made by RFW and TIG), while in Section 4.2, covers the weld made between Ti-64 and Ti-1023 alloys. The main objective of this chapter is to provide the correlation between the microstructural variations and mechanical properties of the above-mentioned welded joints.

4.1 Dissimilar weld between CS and SS

4.1.1 Macroscopic observations

The purpose of macroscopic observation is to provide a visual assessment of the weld joint including its dimensions, shape, and surface characteristics. This visual inspection helps to identify any visible defects such as cracks, lack of fusion, porosity, or incomplete penetration, which may compromise the structural integrity and performance of the welded component. Furthermore, macroscopic observation allows to evaluate the weld bead geometry, including bead size, reinforcement, and penetration depth, which are critical factors in determining the weld's strength and suitability of weldments for its intended application.

Macroscopic examination of the RFW joint, as depicted in Figure 56 (a & b), unveils characteristics essential for its structural integrity and quality assessment. Notably, a discernible fusion line, portraying the bond between the adjoining materials. On the S355J2 side of the joint, a distinct HAZ is apparent, extending approximately 2.5 mm distance from the fusion line. The presence of such a HAZ signifies the thermal influence of the welding process, essential for understanding the kinetics of phase transformation and its influence on mechanical properties. Notably, macroscopic examination reveals the absence of common weld flaws such as lack of side wall fusion, porosity, or cold lap, featuring the weld joint's exceptional quality and integrity.

Macroscopic examination of the TIG weld, as illustrated in Figure 56 (c & d), offers detailed insights crucial for assessing its structural integrity and weld process parameters. Notably, it reveals a maximum excess penetration at the root of 2.0 mm, ensuring a robust bond between the welded materials while maintaining dimensional stability. With a CAP (is defined as the final cover weld pass as shown in Figure 56 (d) height measuring 1.0 mm and a weld width of 2.0 mm, the weld exhibits precise dimensions indicative of better welding technique and control. Maintaining a narrow gap bevel for welding and adherence to specific welding procedures, are contributing to the weld joint's reliability and performance. Furthermore, a distinct HAZ is evident on the S355J2 side of the joint, extending approximately 2.0 mm distance from the fusion line. This observation elucidates the thermal effects of the welding process. Notably, macroscopic inspection highlights the absence of common weld flaws. Moreover, the CAP height to width ratio (H1/W1 = 0.23) indicates a smooth weld toe. This aspect not only enhances the aesthetic appeal of the weld but also contributes to its mechanical properties and resistance to stress concentrations.

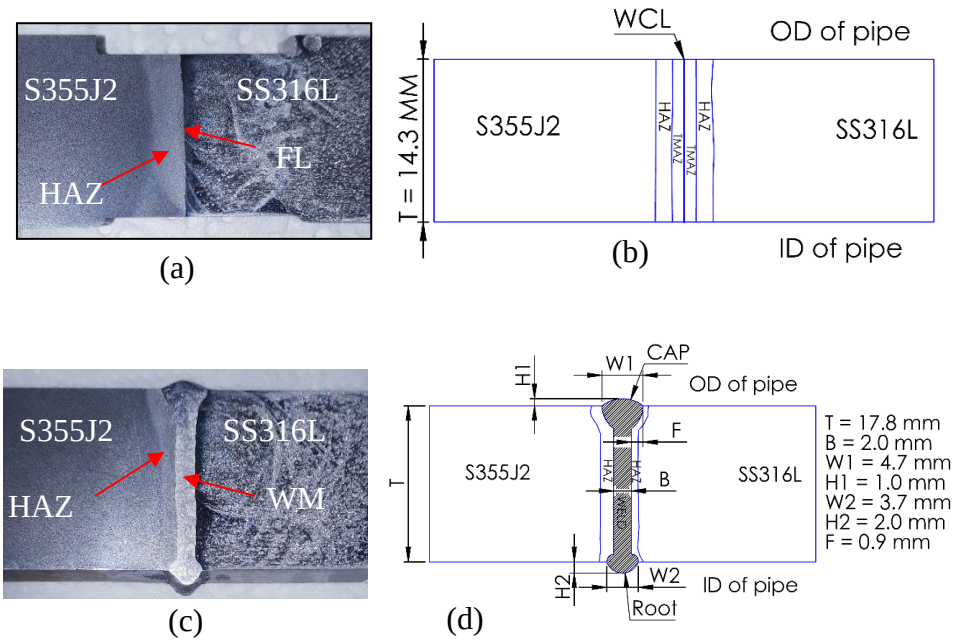

Figure 56: (a) Macro image of RFW joint, (b) schematic of macro graph of RFW joint, (c) macro image of TIG weld joint and (d) schematic of macro graph of TIG weld joint between S355J2 and SS316L.

4.1.2 Microstructure study

Microstructural study offers crucial information about the metallurgical phases, intermetallic and defects within the various zones of a weld. It helps to assess the quality of the weld, effectiveness of the welding process, and the extent of metallurgical changes induced by various welding parameters. It also provides essential information to correlate with mechanical properties, such as hardness, strength, toughness, and ductility.

4.1.2.1 Microstructure of RFW joint

Optical microscope image illustrates in Figure 57 a complete RFW dissimilar joint developed between S355J2 and SS316L. To facilitate a comprehensive examination of the microstructural alterations across distinct regions of the weld joint, the structure is delineated into six zones. Zones A and D depict the microstructure of the parent metal. Zones B and E delineate the HAZ, capturing segments influenced by thermal changes during the welding process. Zones C and F describe the microstructure of TMAZ, where the material experiences both heat and forging pressure, leading to distinctive microstructural modifications.

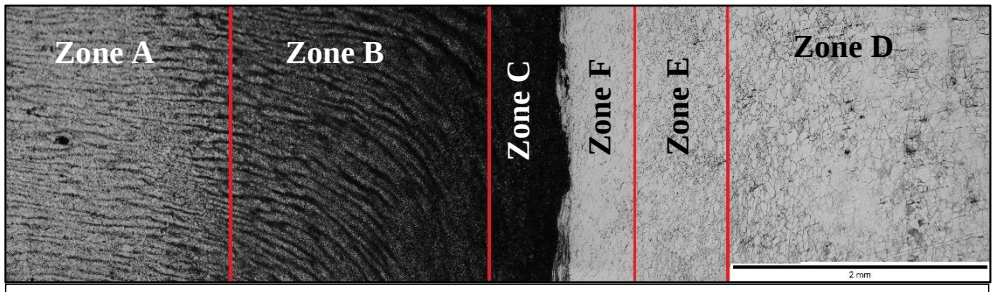

Zone A – S355J2 parent metal, Zone B – HAZ of S355J2, Zone C – TMAZ of S355J2, Zone D – SS316L parent metal, Zone E – HAZ of SS316L and Zone F – TMAZ of SS316L

Figure 57: Image of the microstructure of RFW joint between S355J2 and SS316L showing various zones.

Microstructural characteristics of parent metal S355J2 (Zone A)

Figure 58 illustrates the microstructure of the Zone A characterizes a banded microstructure. It comprises of alternating bands of ferrite (white in optical

microscope and dark in SEM) and pearlite (dark in optical microscope and white in SEM), aligned parallel to the rolling direction of the plate.

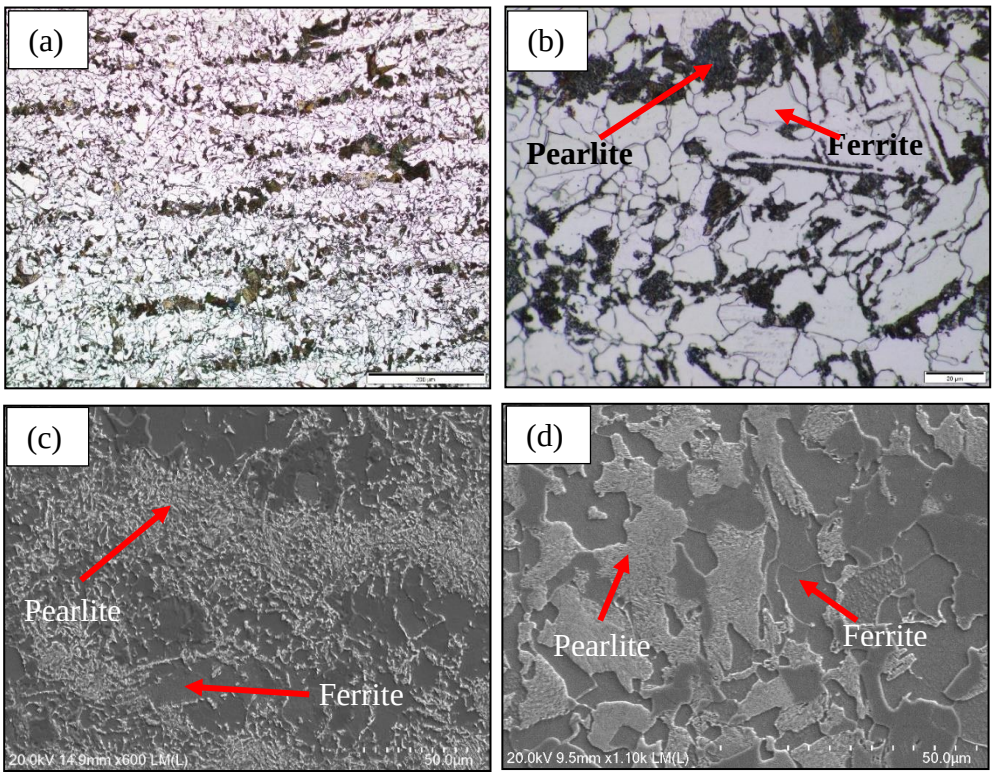

Figure 58: Optical images (a) at low, (b) at high magnification and SEM images (c) at low, (d) at high magnification of the microstructure of Zone A in the RFW joint.

A similar banded microstructure, comprising alternating bands of ferrite and pearlite distributed in the rolling direction, was also observed by Nagode, et al. [89] in their study on the microstructure of S355J2 steel under various heat treatment conditions. Their findings, illustrated in Figure 59, further corroborate the observed pattern in the Zone A sample.

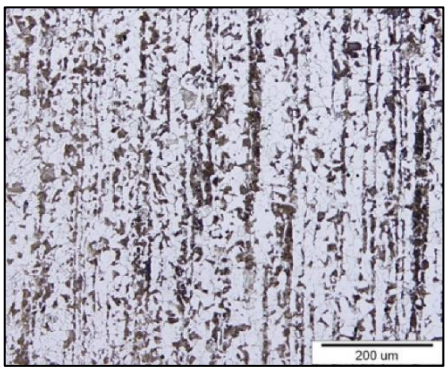

Figure 59: Optical images of the microstructure of S335J2 steel observed by Nagode, et al. [89]

Banded microstructures are frequently observed in rolled-steel products, exemplified by S355J2 steel, which typically undergoes a normalized hot rolling process, displaying a distinctive ferrite-pearlite banded pattern aligned with the rolling direction. The presence of chemical inhomogeneities within the microstructure due to inter-dendritic (micro) segregations of alloying elements, is the primary mechanism underlying the formation of such banded structures. In the case of S355J2 steel, manganese and chromium serve as significant alloying elements, exerting a pronounced influence on the distribution of carbon within the austenite phase. Consequently, regions enriched with manganese and chromium also exhibit higher carbon content. Conversely, areas of austenite depleted in alloying elements demonstrate lower carbon levels. During the cooling process from the austenite phase, regions with lower carbon content and reduced alloying elements transform into ferrite, while those with higher carbon content and positive segregations of alloying elements subsequently evolve into pearlite.[89].

Microstructural characteristics of HAZ of S355J2 (Zone B)

The microstructural analysis of Zone B as illustrated in Figure 60, analysed using both optical microscopy and SEM, reveals the presence of fine ferrite and pearlite grains arranged in banded structure. These bands exhibit deformation compared to Zone A but maintain their original alignment.

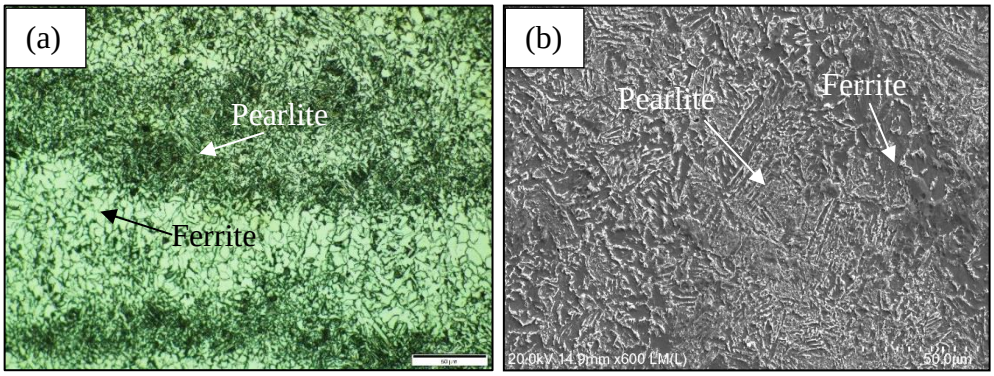

Figure 60: (a) Optical image and (b) SEM image of microstructure of Zone B in the RFW joint between S355J2 and SS316L.

Similar microstructural changes were observed by Ma, et al. [75] in the HAZ of dissimilar welds between SS304 and CS 1045, manufactured using continuous drive friction welding processes.

In RFW, the HAZ represents the region between the parent metal and the TMAZ, where the material experiences only thermal influence from the welding process but no mechanical deformation. Temperatures in the HAZ typically fall between those of the TMAZ and the unaffected base metal. Geng, et al. [90] conducted a comprehensive study involving numerical and experimental investigations on continuous drive friction welding of SS304 and CS 1045. Their findings indicated a temperature gradient across various regions of the weld, with the HAZ experiencing temperatures ranging from 300°C to 800°C depending on the welding parameters utilized, as depicted in Figure 61. Due to this thermal influence, metallurgical changes such as grain refinement and partial recrystallization are observed in the HAZ. These changes contribute to the formation of a fine-grained structure.

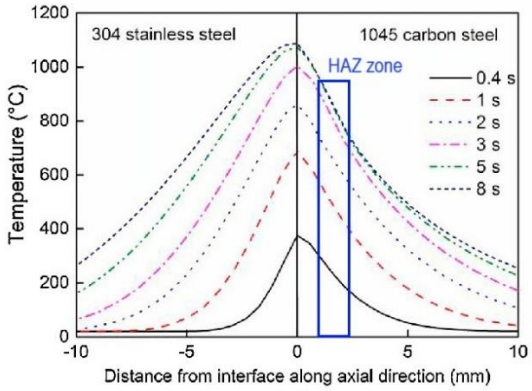

Figure 61: Evolution of temperature distribution during the welding process along the axial direction (Friction pressure = 130 MPa, rotation speed = 2200 rpm, and Forge pressure = 170 MPa) [90].

Microstructural characteristics of TMAZ adjacent to S355J2 (Zone C)

The microstructure of Zone C, depicted in Figure 62, reveals the formation of an acicular bainite, resulting from the combined thermal and mechanical stresses inherent in the welding process. In the TMAZ, positioned adjacent to the weld interface, the material undergoes significant deformation and experiences temperatures around 1100°C (refer to Figure 61). Similar observations of these phenomena and microstructure were documented by Lalvani, et al. [23] in their investigation of RFW for manufacturing transition joints between S355J2 and SS316L, particularly for high-integrity applications. The TMAZ typically shows

the formation of a refined grain structure compared to the base metal which is attributed to the recrystallization and grain growth phenomena activated by the heat generated during frictional welding [75]. Concurrently, localized plastic deformation and strain accumulation occur in the TMAZ due to the mechanical forces applied during welding process [23]. Higher thermal conductivity of S355J2 (40–45 W/m°K) [14] in compared to SS316L (13–17 W/m°K) [19] establishes a higher cooling rate in this zone. These combined thermal and mechanical effects as well as higher cooling rate gives rise to a distinctive microstructure (bainite) characterized by a blend of recrystallized grains, strain-induced features, and potential variations in alloying element distribution. The microstructural evolution within the TMAZ is pivotal in shaping the mechanical properties, integrity, and performance of rotary friction welds.

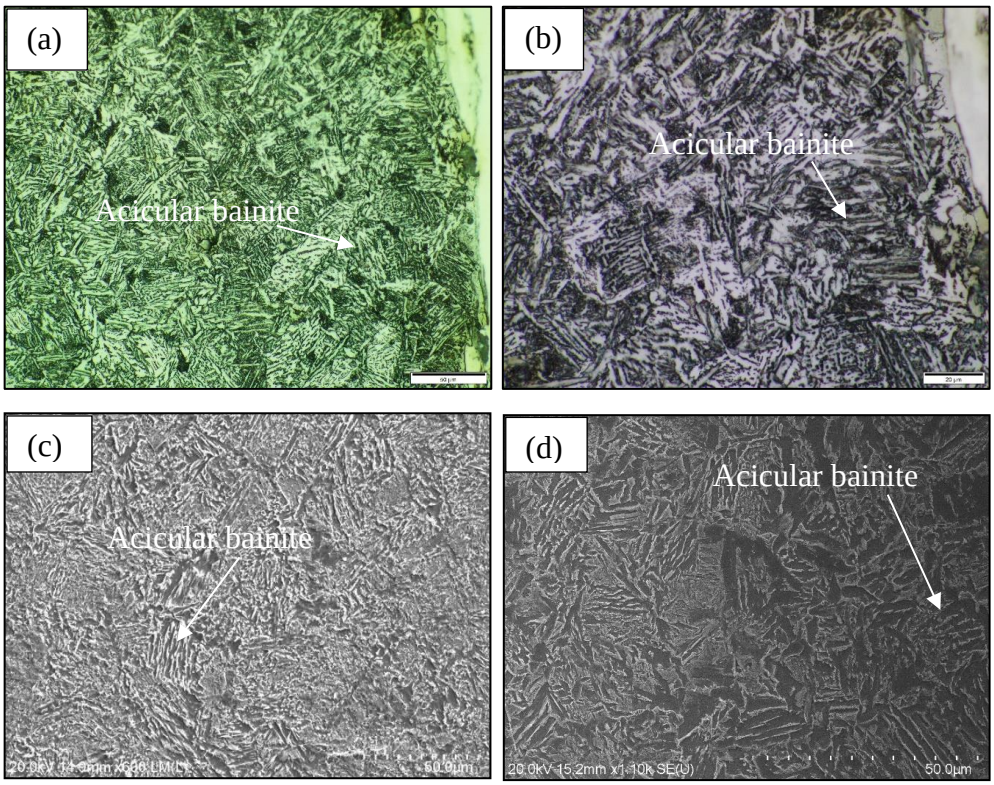

Figure 62: Micrographs recorded using OM and SEM from the Zone C in the RFW joint between S355J2 and SS316Lat different magnification.

Microstructural characteristics of parent metal SS316L (Zone D)

The microstructure of Zone D confirms the typical austenitic stainless-steel microstructure predominantly composed of austenite grains, characterized by a face-

centred cubic (FCC) crystal structure, as highlighted in Figure 63. Notably, twins are observed within the austenite grains, specifically categorized as transgranular twins. Comprising four distinct parts, these twins feature coherent twin planes on both sides and grain boundaries at both ends. The formation of these transgranular twins is attributed to the activation of multiple slip systems during the deformation of SS316L.

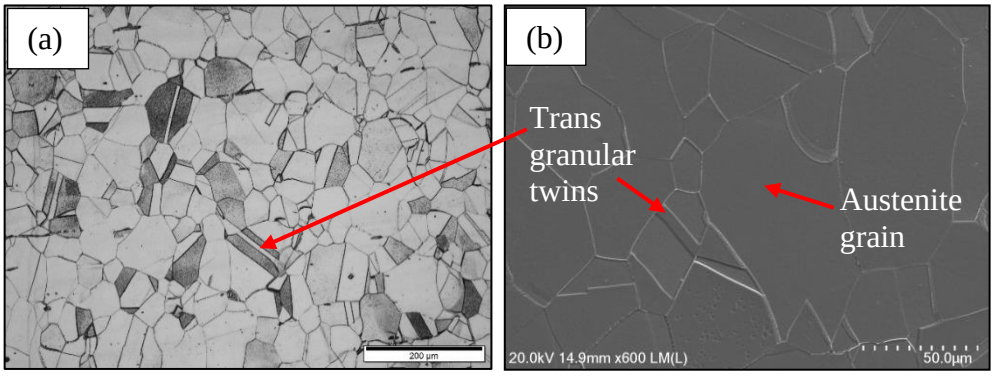

Figure 63: Microstructure characteristics of Zone D in the RFW joint between S355J2 and SS316L showing the evidence for presence of equiaxed austenite grains and twins formed with in the grain interior (a) Optical microscopy image and (b) SE-SEM image.

Microstructural characteristics of HAZ of SS316L (Zone E)

The microstructure of Zone E exhibits fine austenite grains, as observed through both optical microscopy and SEM, as shown in Figure 64. This observation is similar to the findings of Hasçalik, et al. [91], who similarly noted comparable microstructural alterations in their investigation. Like Zone B, Zone E undergoes solely thermal influence from the welding process, without any mechanical deformation. In a study by Geng, et al. [90], it was unveiled that the HAZ of SS encounters temperatures spanning from 200°C to 600°C, contingent upon the welding parameters employed, as illustrated in Figure 61. Furthermore, this zone undergoes a slower cooling rate in contrast to Zone B due to the lower thermal conductivity of SS316L (13–17 W/m°K) [19] compared to CS S355J2 (40–45 W/m°K) [14]. These thermal cycles induce metallurgical modifications such as grain refinement and partial recrystallization within the HAZ, ultimately leading to the formation of a fine-grained structure.

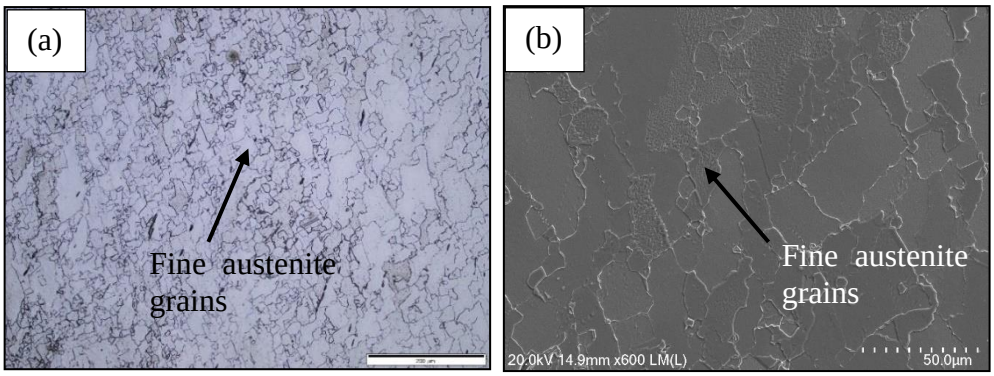

Figure 64: (a) Optical image and (b) SEM image of the microstructure of Zone E in the RFW joint between S355J2 and SS316L.

Microstructural characteristics of TMAZ of SS316L (Zone F)

Coarse austenite grains as depicted in Figure 65 are observed in Zone E, resulting from the combined thermal and mechanical stresses inherent in the welding process. The material undergoes substantial plastic deformation and reaches temperatures of approximately 1100°C (as shown in Figure 61). Hasçalik, et al. [91] documented similar observations and microstructural phenomena during their examination of fatigue behaviour of friction welding between AISI 304 and AISI 4340 steel. The TMAZ typically exhibits a refined austenite grain structure in contrast to the base metal, owing to the recrystallization and grain growth mechanisms triggered by the heat generated during frictional welding [75]. Concurrently, localized plastic deformation and strain accumulation occur within the TMAZ due to the mechanical forces applied during welding [23]. The relatively low thermal conductivity (13 – 17 W/m°K) [19] of SS316L compared to CS S355J2 (40–45 W/m°K) [14] leads to a slow cooling rate in this zone. The combined effects of thermal and mechanical stresses, along with the slow cooling rate, facilitate the retention of austenite and contribute to the formation of coarse austenite grain structure in this region.

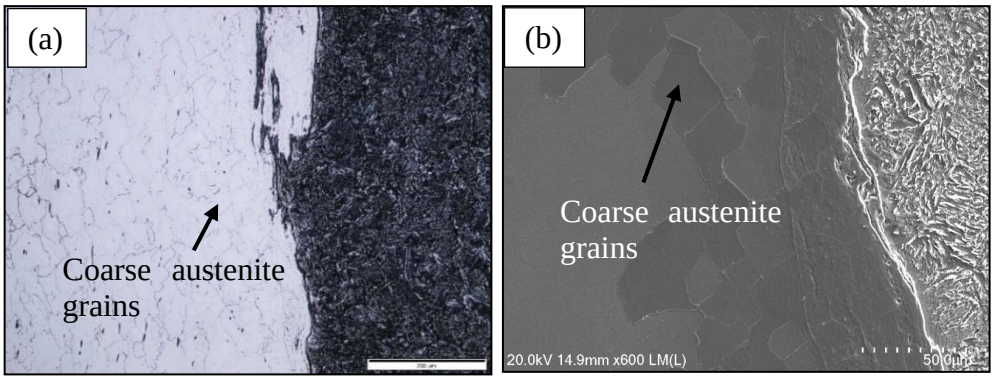

Figure 65: (a) Optical image and (b) SEM image of the microstructure of Zone F in the RFW joint between S355J2 and SS316L.

Microstructural characteristics of weld interface

The microstructure analysis of the weld interface in RFW joints between S355J2 and SS316L reveals a fascinating mixing zone comprising CS and SS, as illustrated in Figure 66. Within this metal mixing zone, distinct islands of S355J2 and SS316L are discernible. Notably, the diffusion of alloying elements between these phases in the solid state contributes significantly to the joint's enhanced strength. This phenomenon confirms findings from previous studies, such as those conducted by Firmanto, et al. [74], Purwanto [92] and Kantumuchu and Cheepu [93] exploring RFW joints between CS and SS. The welding interface undergoes severe plastic deformation [74] and intense heating during the welding process as depicted in Figure 61, leading to the formation of islands, and facilitating mixing, thereby establishing a robust interlock between the materials to be welded. The application of axial force resulting from the forge pressure induces excessive deformation, compelling the materials to intermix. Prior research has confirmed that the angular velocity during the friction [93] prompts the softened metals to disperse from the centre. However, certain materials remain at the centre and blend with the opposing metal, resulting in the creation of an intermixing zone at the joint, as also evident in the present investigation.

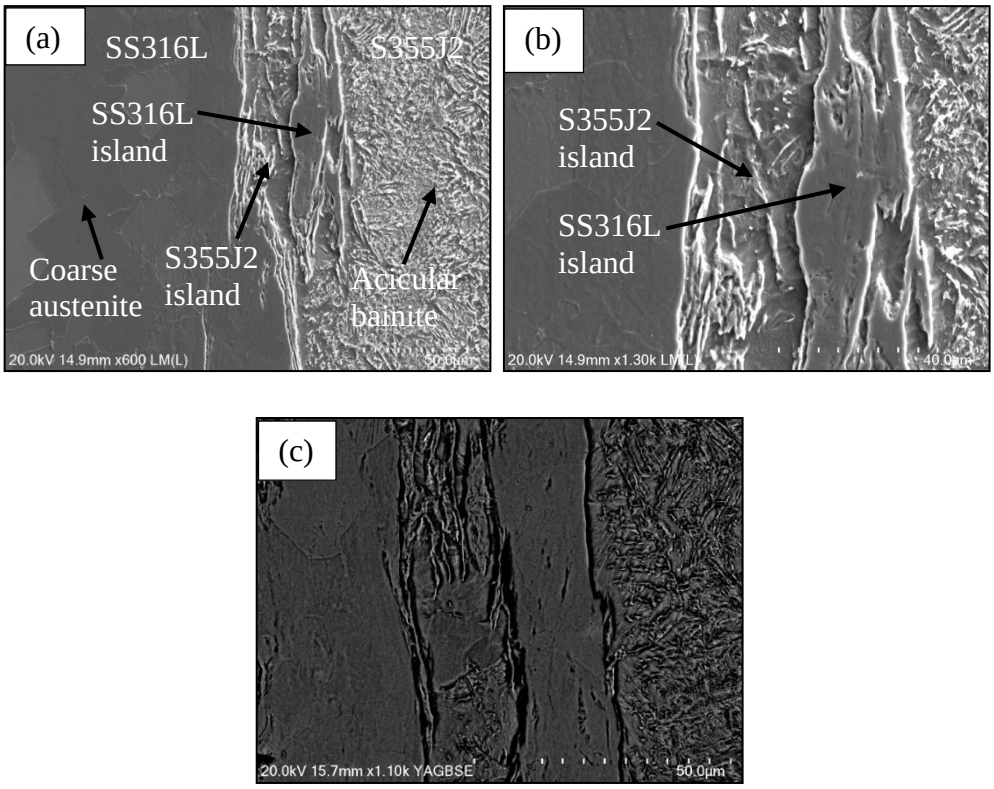

Figure 66: Images of the microstructure of weld interface in the RFW joint between S355J2 and SS316L (a) at low magnification SEM, (b) at high magnification SEM and (c) at high magnification back scattered electron mode.

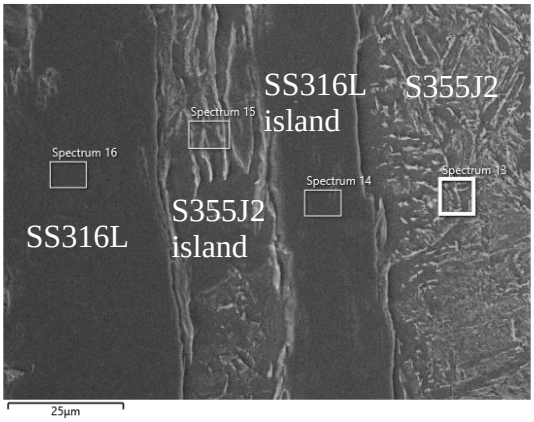

Figure 67: SEM image of the weld interface in the RFW joint between S355J2 and SS316L reflecting different areas of EDS analysis.

Energy Dispersive Spectroscopy (EDS) technique is conducted across the weld interface, as illustrated in Figure 67. The EDS spectrum unveils the dominant elemental composition of the SS316L base metal, featuring Fe, Mn, C, N, Cr, and Ni. Conversely, the S355J2 base metal showcases dominant elements of Fe, Mn,

and C. Notably, the EDS analysis proves elemental diffusion occurring between CS and SS within this interface region. The EDS examination elucidates the migration of carbon from S335J2 (Spectrum 13) to the SS316L island (Spectrum 14), while conversely, chromium and nickel diffuse out from SS316L (Spectrum 16) to the S355J2 island (Spectrum 15) forms at the weld interface, as depicted in Figure 68. This observation resonates with the findings reported by Chander, et al. [94], which documented the migration of Cr and Ni from AISI 304 to AISI 4140 SS within the welding zone. The occurrence of high shear forces and localized heating due to friction significantly contributes to elemental diffusion and metallurgical bonding between S355J2 and SS316L.

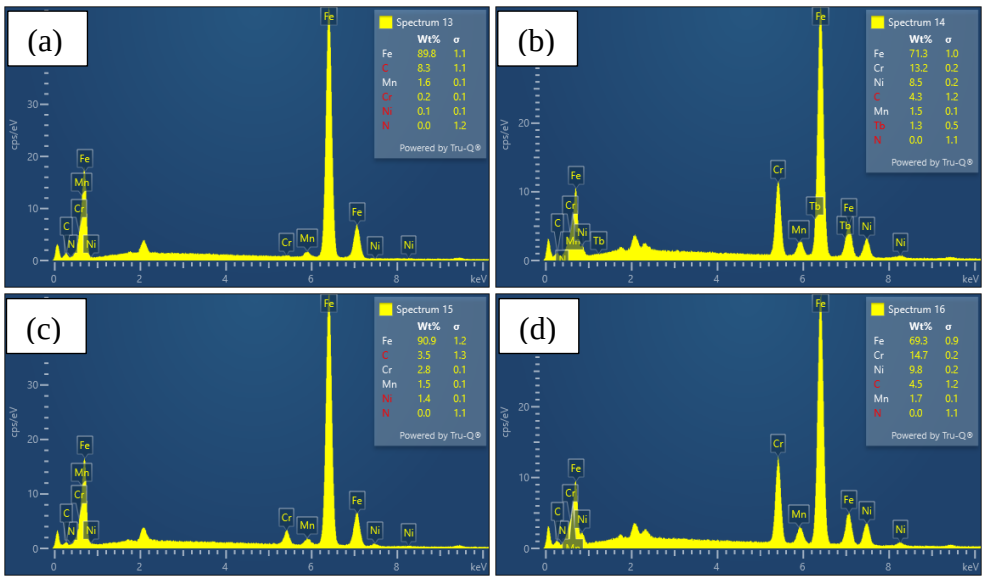

Figure 68: Results of the EDS area analysis conducted (a) at S355J2 (Spectrum 13), (b) at SS316L island (Spectrum 14), (c) at S355J2 island (Spectrum 15), and (d) at SS316L (Spectrum 16) in the weld interface of RFW joint.

4.1.2.2 Microstructure analysis of TIG weld joint

An optical microscope image of a complete dissimilar TIG weld joint formed between S355J2 and SS316L is illustrated in Figure 69. To facilitate a comprehensive examination of the microstructural changes across distinct regions of the weld joint, the structure is divided into six zones. Zones 1 and 4 depict the microstructure of the parent metal, providing insight into its original material characteristics. Zones 2, 3 and 5 delineate the HAZ, capturing segments influenced by thermal changes during the welding process. Zone 2 and Zone 3 both represent

HAZ of S355J2. They are distinguished by the formation of distinct microstructures; similar observation was noticed by Huang, et al. [22] and Wu, et al. [95] in their experiments. Zone 2 is situated farther from the fusion line (FL) and is adjacent to Zone 1, whereas Zone 3 is located farther from Zone 1 but is adjacent to FL. Zones 6 encapsulate the WM, where molten filler metal solidifies and leading to distinctive microstructural modifications. This division enables a systematic analysis of microstructural changes within different zones of the weld joint.

Zone 1 – S355J2 parent metal, Zone 2 – HAZ of S355J2-adjacent to S355J2, Zone 3 –HAZ of S355J2 adjacent to FL, Zone 4 – SS316L parent metal, Zone 5 –HAZ of SS316L, Zone 6 – Weld metal.

Figure 69: Image is showing various zones of TIG dissimilar weld joint between S355J2 and SS316L.

Microstructural characteristics of parent metal S355J2 (Zone 1)

Like Zone A of RFW joint, Zone 1 of TIG weld joint exhibits a distinct ferrite and pearlite banded microstructure along the rolling direction, as illustrated in Figure 70.

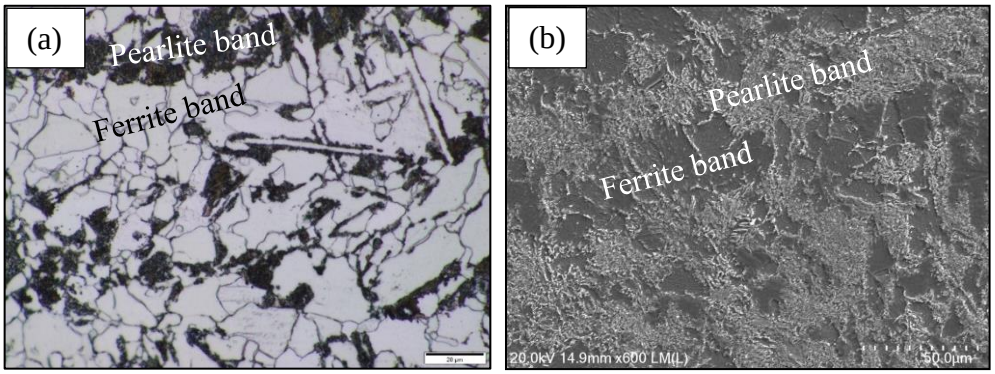

Figure 70: Microstructure of Zone 1 in the TIG weld joint between S355J2 and SS316L (a) Optical image and (b) SEM image.

Microstructural characteristics of HAZ of S355J2 (Zone 2)

The microstructure of Zone 2 reveals a fine ferrite-pearlite composition, a finding consistent with the observations made by Huang, et al. [22] and Wu, et al. [95] in their research. Throughout the welding process, Zone 2 encounters temperature variation attributed to the thermal cycle inherent in the welding process. Consequently, microstructural alterations develop. The presence of a fine ferrite-pearlite microstructure, as depicted in Figure 71, is attributed to a relatively slow cooling rate and comparatively lower peak temperature. This zone situated further away from the fusion line undergoes less intense peak temperatures, leading to recrystallization and refinement, resulting in the formation of fine ferrite and pearlite grains. The expanded width of this finely refined grain area can be attributed to a slower welding speed [95].

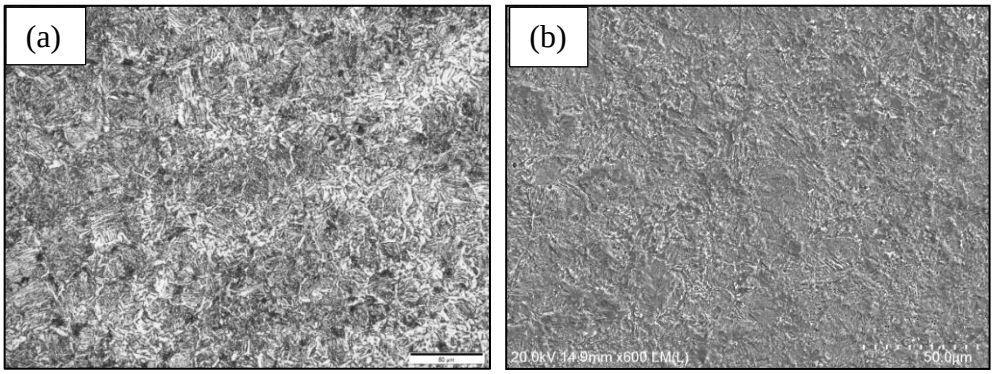

Figure 71: Microstructure of Zone 2 in the TIG weld joint between S355J2 and SS316L (a) Optical image and (b) SEM image.

Microstructural characteristics of HAZ of S355J2 (Zone 3)

The microstructure of Zone 3 reveals the presence of the hard martensite phase, along with the formation of a coarse grain structure and a narrow width as illustrates in Figure 72, findings consistent with observations reported by Huang, et al. [22] and Wu, et al. [95] in their research. Throughout the welding process, Zone 3 experiences significant temperature variations attributed to the inherent thermal cycle of welding. Being situated adjacent to the fusion line, this zone is subjected to intense peak temperatures, which facilitate grain growth. The relatively high cooling rate, resulting from the comparatively higher thermal conductivity of S355J2 (40–45 W/m°K) [14] and the elevated peak temperatures, ultimately leads to the formation of lath martensite. Similar lath martensitic structure was observed

by Le, et al. [20] in HAZ of carbon steel in their study on finding relationship between cooling rate on HAZ microstructure of dissimilar weld between CS and SS.

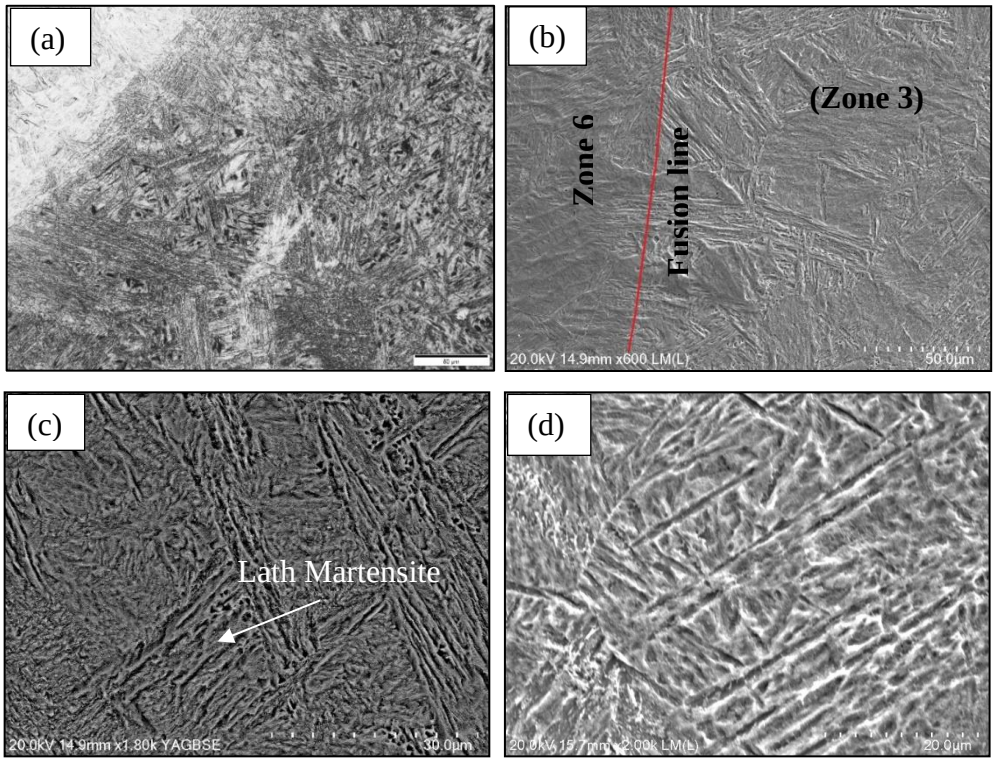

Figure 72: Images of the microstructure of Zone 3 in the TIG weld joint between S355J2 and SS316L under (a) Optical microscope at low magnification, (b) SEM at low magnification, (c) the back scattered electron at high magnification and (d) SEM at high magnification.

An area analysis, as depicted in Figure 73, utilizing the Energy Dispersive Spectroscopy (EDS) technique, is conducted across the weld fusion line between Zone 3 and Zone 6. This analysis aims to ascertain whether carbon diffusion occurs from the Zone 3 to Zone 6 i.e. the WM. Corresponds to a location, Spectrum 7 is within Zone 3, situated away from the fusion line (FL). Meanwhile, Spectrum 9 also resides within Zone 3, although closer to the FL compared to Spectrum 7. Spectrum 11 is positioned on the fusion line, while Spectrum 12 is located within Zone 6, representing the weld metal.

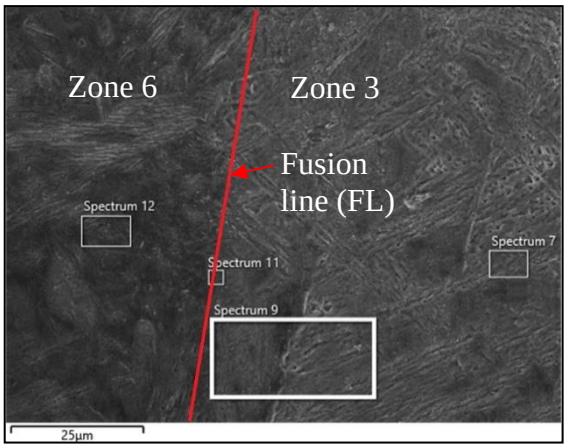

Figure 73: SEM image of the weld fusion line between Zone 3 and Zone 6 in the TIG weld joint reflecting different areas of EDS analysis.

EDS spectrum unveils the dominant elemental composition of the SS316L base metal, featuring Fe, Mn, C, N, Cr, and Ni. Conversely, the S355J2 base metal showcases dominant elements of Fe, Mn, and C. EDS area analyses reveal the migration of carbon from Zone 3 to Zone 6, as indicated in Figure 74. This phenomenon is evidenced by the gradual decrease in carbon concentration from Zone 3 towards the fusion line, as observed in Spectrum 9 and 11 in comparison to Spectrum 7. Conversely, there is an increase in carbon concentration within Zone 6, as illustrated in Spectrum 12. The decrease in carbon concentration observed in Zone 3 near the fusion line, coupled with an increase in Zone 6 close to the fusion boundary, serves as evidence of carbon diffusion. This phenomenon aligns with observations made by Huang, et al. [22] in their study.

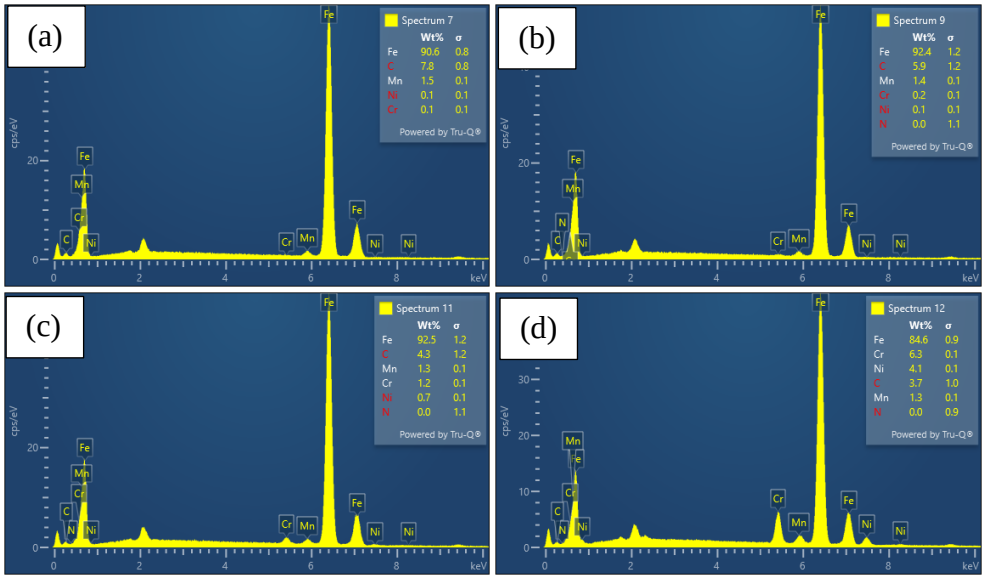

Figure 74: Results of the EDS area analysis performed: (a) at Zone 3 far from FL (Spectrum 7), (b) at Zone 3 near to FL, (Spectrum 9), (c) at FL (Spectrum 11), and (d) at Zone 6 i.e. weld metal (Spectrum 12) in the TIG weld joint between S355J2 and SS316L.

Microstructural characteristics of parent metal SS316L (Zone 4)

Like Zone D of RFW joint, the microstructure of Zone 4 exhibits typical austenitic structure with transgranular annealing twins refer to Figure 75.

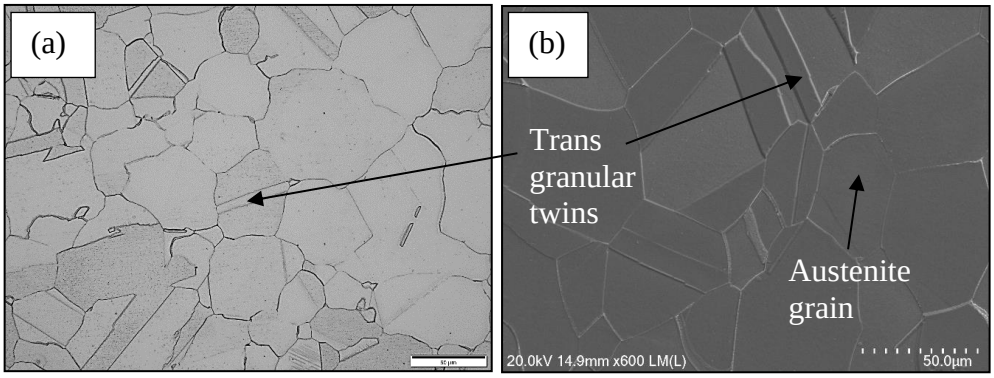

Figure 75: Microstructure of Zone 4 in the TIG weld joint between S355J2 and SS316L under (a) optical and (b) SEM.

Microstructural characteristics of HAZ of SS316L (Zone 5)

The microstructure of Zone 5 reveals the presence of clumpy austenite grains, with the width of this zone appearing narrow, as depicted in Figure 76, findings

consistent with observations reported by Huang, et al. [22] and Wu, et al. [95] in their research. This characteristic can be attributed to the poor heat dissipation properties inherent in SS. SS316L typically exhibits comparatively lower thermal conductivity levels (around 13–17 W/m-K) [19]. Consequently, the heat generated during welding tends to remain localized within the SS316L material, resulting in a narrower HAZ. Within this zone, fine ferrite is dispersed throughout the austenite matrix. Notably, SS316L shares similar alloying elements, such as chromium and nickel, with the WM composed of ER309L. The distribution of these alloying elements plays a pivotal role in determining the microstructural phases present. While minimal elemental diffusion is observed refer to Figure 81, microstructural changes within the Zone 5 are characterized by the distribution of fine ferrite along the austenite grain boundaries [22]. This phenomenon results in the formation of one-directional columnar austenite grains, with higher concentrations of chromium evident at the austenite grain boundaries as illustrated in Figure 78.

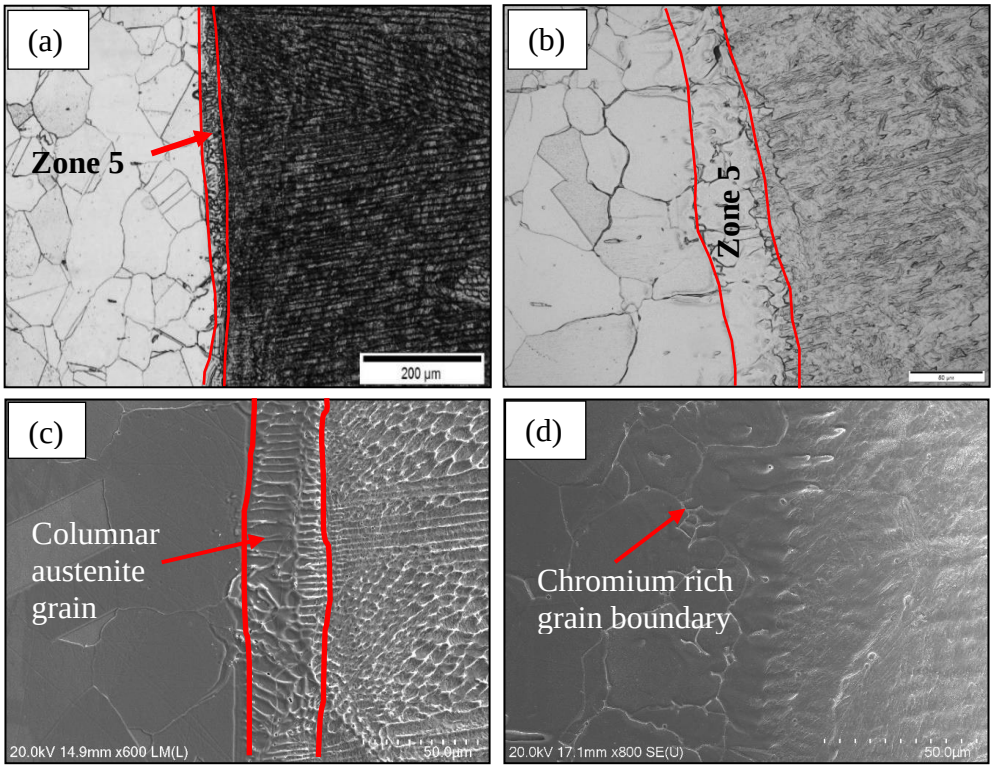

Figure 76: Microstructures of Zone 5 in the TIG weld joint between S355J2 and SS316L (a & b) optical microscopy images and (c & d) SEM images, at two different magnifications.

An area analysis, as depicted in Figure 77, utilizing the Energy Dispersive Spectroscopy (EDS) technique, is performed in both the grain boundary and columnar austenite grain. This analysis aims to ascertain whether elemental diffusion occurs to columnar austenite grain boundaries. Corresponds to a location, Spectrum 33 is situated in the grain boundary and Spectrum 34 is located inside the columnar austenite grain.

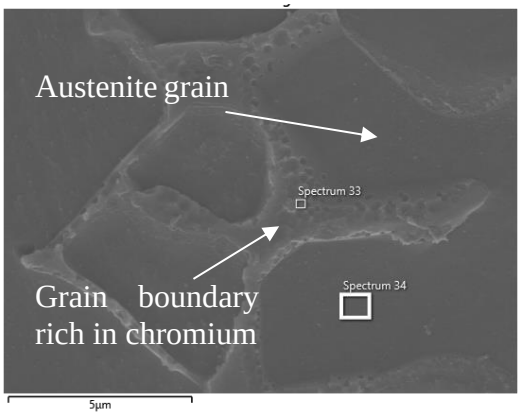

Figure 77: SEM image displays the location of area analysis in both grain boundary and grain of SS316l in Zone5 of TIG weld joint between S355J2 and SS316L.

EDS spectrum unveils the dominant elemental composition of the SS316L, featuring Fe, C, Cr, and Ni. EDS area analyses reveal the chromium concentration is notably higher in the grain boundary (as indicated by Spectrum 33 in Figure 78) in compared to the chromium concentration within the austenite grain (as indicated by Spectrum 34).

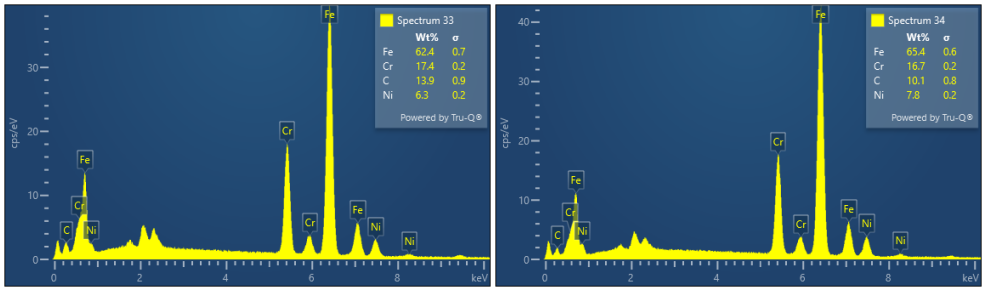

Figure 78: Results of EDS area analysis conducted (a) at grain boundary (Spectrum 33), and (b) within the grain (Spectrum 34) of Zone 5 in the TIG weld joint between S355J2 and SS316L.

Microstructural characteristics of weld metal (Zone 4)

Given the utilization of ER309L filler wire for WM deposition, Zone 6 exhibits a microstructure characterized by a blend of δ-ferrite and austenite phases. Within this microstructure, austenite is found predominantly within the grains, while δ-ferrite tends to occupy the grain boundaries as illustrated in Figure 79 (b & c). This observation resonates with findings reported by Huang, et al. [22]. The formation of equiaxed columnar grains is evident, with directional grain growth observed towards the direction of heat flow, as illustrated in Figure 79 (a). Since fusion welding method is employed and substantial chemical compositional differences exist between S355J2 and SS316L, an EDS analysis is conducted to ascertain the presence of any intermetallic compounds, such as chromium carbide, in the weld interface.

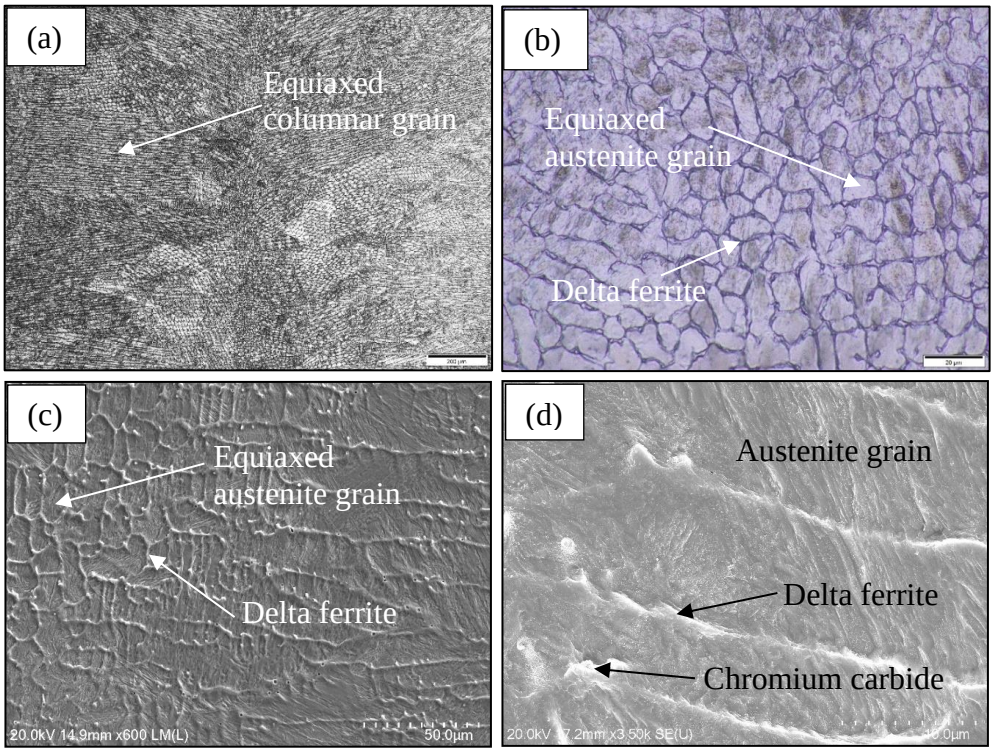

Figure 79: Images of the microstructure of WM in the TIG weld joint between S355J2 and SS316L (a & b) under Optical microscope and (c & d) under SEM.

An enhanced line analysis employing the EDS technique is conducted along the columnar grains within Zone 6, as illustrated in Figure 80 (a). This comprehensive line analysis encompasses both the grain boundary and columnar grain regions. Its primary objective is to determine the concentrations of carbon and chromium within

the grain and along the grain boundary, thereby facilitating the identification of chromium carbide precipitates along the grain boundary.

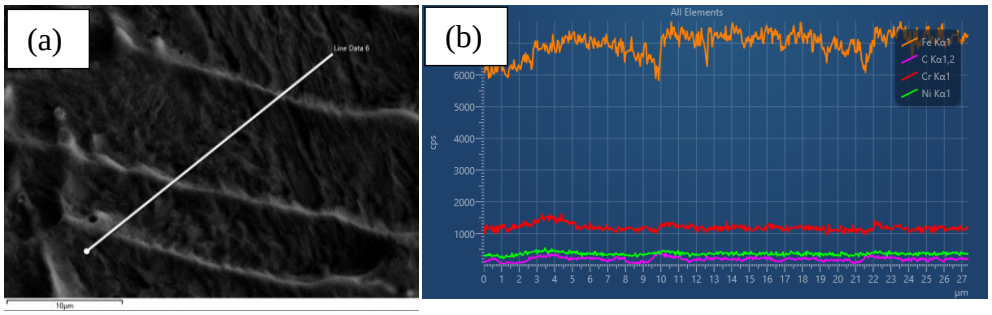

Figure 80: (a) SEM image of the EDS line analysis across the grains of WM of TIG weld joint between S355J2 and SS316L and (b) the results of EDS line analysis.

EDS line analysis unveils the dominant elemental composition of the SS316L, featuring Fe, C, Cr, and Ni. Analyses reveal the concentration of carbon and chromium are notably higher in the grain boundary in compared to within the grain as indicated in Figure 80 (b).

Furthermore, an additional EDS area analysis is conducted, focusing on a white spot area within the grain boundary (Spectrum 2) and another area situated inside the grain (Spectrum 3), as illustrated in Figure 81.

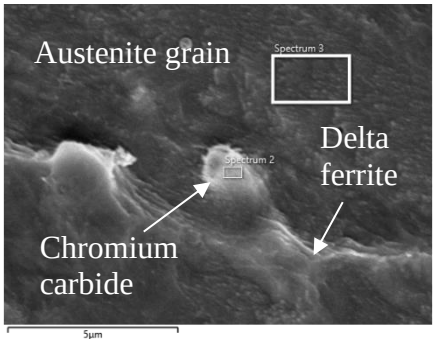

Figure 81: SEM image displays the location of area analysis both in the grain boundary and within the grain of weld metal of TIG weld joint.

EDS spectrum discloses the dominant elemental composition of the SS316L, featuring Fe, C, Cr, and Ni. EDS area analyses reveal the deposition of carbon and chromium in Spectrum 2 are much higher compared to Spectrum 3 refer to Figure 82. Based on these results of analyses, it is concluded that chromium carbide deposition occurs in grain boundary. Chromium carbide is a hard intermetallic phase. Due to high weld inter pass temperature, the WM maintains a temperature

ranges between (400°C - 850°C) for long time which helps on precipitation of chromium rich carbide along the grain boundaries [21].

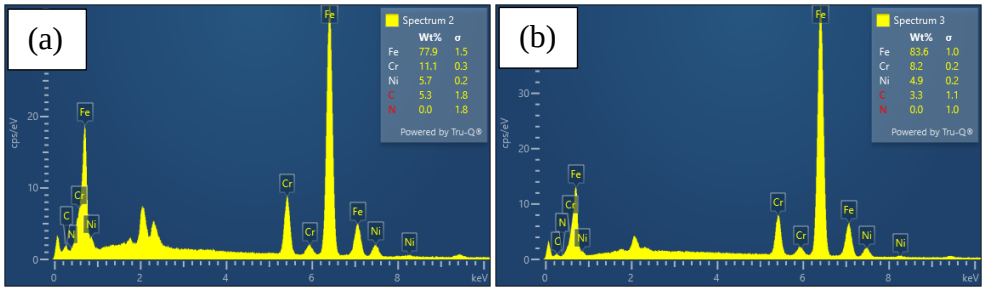

Figure 82: Results of the EDS area analysis conducted (a) at grain boundary (Spectrum 2), and (b) within the grain (Spectrum 3) of Zone 6 in the TIG weld joint between S355J2 and SS316L.

4.1.3 Hardness Testing

The assessment of material hardness is fundamental in understanding the mechanical properties and performance of materials across diverse industrial applications. Hardness testing serves as a critical tool for evaluating a material's resistance to deformation, indentation, and wear. The comprehensive analysis of hardness test results aims to elucidate the mechanical behaviour and performance characteristics of the materials under consideration. Additionally, it endeavours to furnish concrete evidence in supporting microstructural findings.

Figure 83 illustrates the variation in Vickers micro-indentation hardness test results across different zones of both the RFW and TIG weld joints. The average hardness of Zone D in the RFW joint measures 189 HV1. This finding consistent with hardness test results of SS316L reported by Huang, et al. [22]. In compared to Zone D, Zone 4 of the TIG weld joint exhibits a slightly lower hardness of 164 HV1, consistent with hardness test results of SS316L reported by Lalvani, et al. [23]. Conversely, Zone A of the RFW joint and Zone 1 of the TIG weld joint demonstrate comparable average hardness values, with measurements of 167 HV1 and 169 HV1, respectively, findings consistent with hardness test results of S355J2 steel reported by Huang, et al. [22]. Notably, the average hardness of Zone D surpasses that of Zone 4, primarily attributable to differences in austenite grain size. Zone D exhibits a finer grain size in comparison to Zone 4, as indicated by the microstructure displayed in Figure 63 (a) and Figure 75 (a).

In the RFW joint, Zone E (i.e., the hardness indentation line at 1.6 mm from the WCL) and Zone F (i.e., the hardness indentation line at 0.6 mm from WCL) exhibit an average hardness of 188 HV1 and 182 HV1, respectively. The slight variation in hardness between these zones is attributed to changes in austenite grain size within the Zone E and Zone F, as depicted in Figure 64 and Figure 65 respectively. These hardness values closely align with those of Zone D due to their similar microstructural characteristics. Similar results were reported by test results of SS316L reported by Lalvani, et al. [23]. In the TIG weld joint, Zone 5 demonstrates an average hardness of 172 HV1 at both 0.5 mm and 1.1 mm from the fusion line. This hardness level mirrors that of Zone 4, indicating identical austenite microstructures, as evidenced in Figure 75 and Figure 76.

In the RFW joint, Zone B (i.e., the indentation at 1.6 mm from WCL) displays an average hardness of 186 HV1. This hardness is attributable to the presence of a ferrite and pearlite microstructure, as depicted in Figure 60. Similar hardness characteristics were reported by Lalvani, et al. [23] in their study, confirming current observations. Conversely, in the TIG weld joint, Zone 2 (i.e., the indentation at 2.1 mm from WCL) showcases an average hardness of 215 HV1. This higher hardness can be attributed to the formation of a fine ferrite-pearlite microstructure within this zone, as illustrated in Figure 71. Comparable hardness levels were also observed in Huang, et al. [22] study, further validating present findings.

The average hardness of Zone C (i.e., located at 0.6 mm from the WCL) within the RFW joint measures 208 HV1. This increase in hardness is attributed to the formation of a bainitic microstructure in this zone as illustrated in Figure 62. Similar hardness trends have been observed in RFW joints by Lalvani, et al. [23] in their study, lending credibility to our findings. Noteworthy changes in hardness values are observed in Zone 3 of the TIG weld joint. At 1.5 mm from the WCL (or 0.5 mm from the FL), the average hardness is recorded at 284 HV1, with a single maximum value reaching 347 HV1. This notable rise in hardness values is attributed to the development of a hard martensitic structure, as illustrated in Figure 72.

The WCL of the RFW joint exhibits an average hardness of 206 HV1, attributed to the presence of a combination of bainite and austenite microstructure as illustrated in Figure 66. In contrast, the TIG weld joint exhibits the highest hardness at the

WCL, indicating an average hardness of 419 HV1. This increased hardness is attributed to the presence of an austenite grain blended with δ-ferrite and the precipitation of chromium carbide in the grain boundaries as described in Figure 79.

In Figure 83 (c), a comparative analysis of the average hardness across the different zones of both the weld joints is depicted. Notably, all regions of the RFW weld joint exhibit nearly identical peaks in average hardness. Conversely, the TIG weld joint does not display a similar trend. Zone 3 and Zone 6 of the TIG weld joint demonstrate notably higher peaks in average hardness compared to all other zones in both weld joints. This difference can be attributed to microstructural alterations and the formation of hard phases such as martensite and chromium carbide within these specific zones.

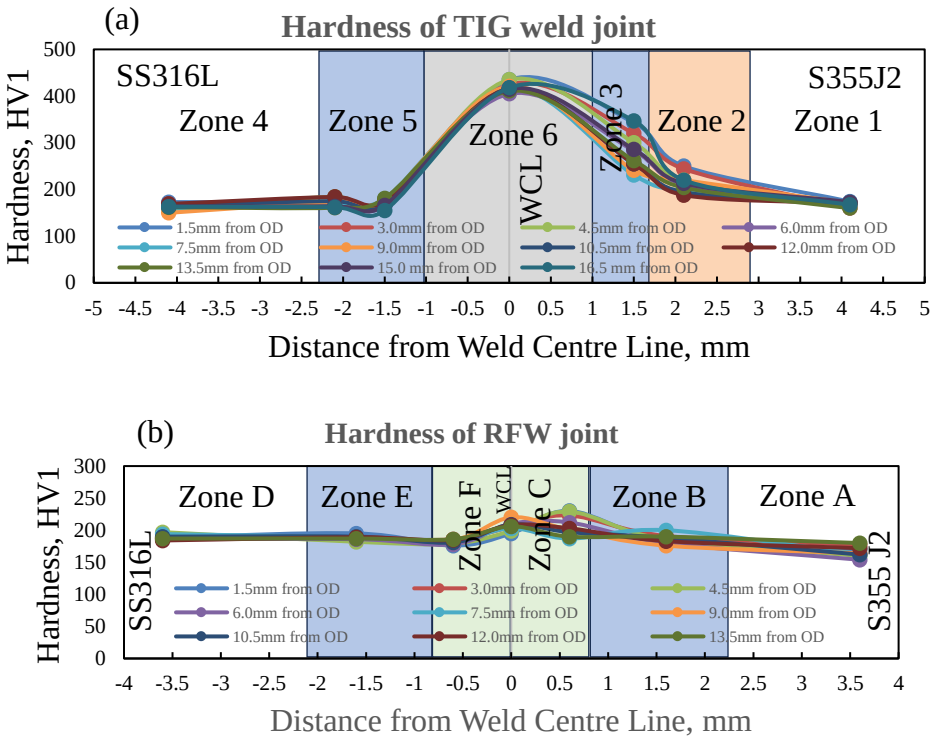

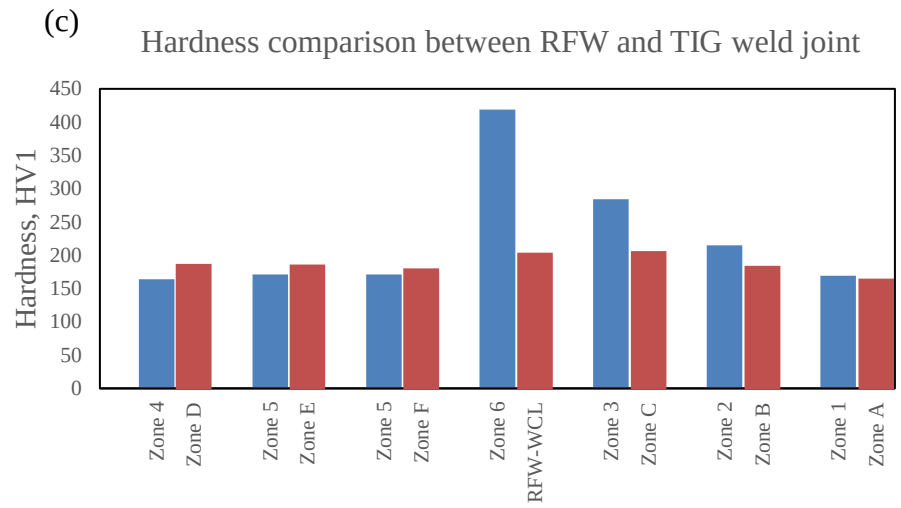

Figure 83: (a) Graphical presentation of variation in micro-hardness values at different locations in the TIG weld joint, (b) graphical presentation of the result of micro-hardness indentation in the various locations in the RFW joint, and (c) comparison of the average micro-hardness of the various locations in the TIG weld and RFW joint between S355J2 and SS316L.

4.1.4 Tensile properties

Tensile properties refer to the behaviour of materials under tensile loading, revealing their ability to withstand the tensile forces before experiencing deformation or failure. Investigating tensile properties ultimately provides crucial insights into material behaviour to failure and mechanical characteristics. Comprehensive comprehension of tensile properties is essential for designing reliable structures, optimizing manufacturing processes, and ensuring the safety and efficiency of engineered components across diverse industries.

The tensile test results from both TIG and RFW dissimilar welded joints between S355J2 and SS316L, along with the base materials on both sides of the weld joint at room temperature, are presented in Table 13. The true UTS of both RFW and TIG weld joints is notably impressive, measuring 623 MPa and 609 MPa, respectively, higher than the true UTS of the S355J2 parent metal (584 MPa). Additionally, the yield strength (YS) of both RFW (367 MPa) and TIG weld joints (300 MPa) exceeds the YS of the SS316L parent metal (255 MPa). This observation underscores the superior quality of the weld joint, as its strength surpasses that of any parent metal.

However, it's noteworthy that the average UTS of the RFW joint is 6% lower than that reported by Lalvani, et al. [23], a discrepancy attributed to the use of miniature tensile specimens. The study by Zhang, et al. [96] suggests that non-standard specimen designs can yield repeatable results for YS, UTS, and uniform elongation (eU), with differences up to 14.03%. Zheng, et al. [97] further elaborate on the 'size effect,' indicating that while MTS results may estimate mechanical properties accurately within a certain range, they may deviate significantly as thickness of specimen decreases.

Regarding yield stress, the average YS of the RFW joint (367 MPa) exceeds that reported in Lalvani, et al. [23] study by 36%. This disparity arises possibly due to differences in data recording methods. Lalvani, et al. [23] might have computed strain using cross head extension, resulting in a lower recorded yield strength compared to the actual value derived from extensometer data. These insights shed light on the complexities of tensile testing and underscore the importance of methodology in measuring load-displacement data.

Table 13: Summary of tensile properties of weld joint between CS and SS

Specimen ID	**$YS_{0.2\%}$**	**UTS**	**Young's Modulus**	**Strain at Fracture**	**True UTS**	**Strain Hardening Exponent**	**Strength coefficient**
	(MPa)	(MPa)	(GPa)		(MPa)		(MPa)
RFW Specimen 1	357	542	198.552	0.14	614	0.237	1052
RFW Specimen 2	375	535	201.974	0.22	604	0.253	1106
RFW Specimen 3	368	544	156.736	0.27	650	0.274	1117
Average of RFW	**367**	**540**	**185.754**	**0.21**	**623**	**0.254**	**1092**
TIG Specimen 1	317	528	226.762	0.12	592	0.233	1008
TIG Specimen 2	283	532	178.299	0.21	639	0.265	1010
TIG Specimen 3	301	518	169.283	0.16	596	0.256	1014

Average of TIG	**300**	**526**	**191.448**	**0.16**	**609**	**0.251**	**1010**
S355 J2 Specimen 1	389	528	173.532	0.10	578	0.270	1016
S355 J2 Specimen 2	376	513	213.519	0.11	567	0.253	1200
S355 J2 Specimen 3	363	524	218.556	0.17	608	0.262	1091
Average of S355J2	**376**	**522**	**201.869**	**0.13**	**584**	**0.262**	**1102**
SS316L Specimen 1	316	522	209.277	0.42	722	0.314	1019
SS316L Specimen 2	225	538	124.328	0.60	837	0.383	1096
SS316L Specimen 3	224	547	174.322	0.72	914	0.382	1115
Average of SS316L	**255**	**536**	**169.309**	**0.58**	**824**	**0.360**	**1077**

Comparison study of tensile properties between RFW and TIG weld joint: The RFW joint exhibits superior mechanical properties compared to the TIG weld joint, as evidenced by its higher average yield strength (367 MPa) and true ultimate tensile stress (623 MPa) as illustrated in Figure 84 in contrast to the TIG weld joint's average yield strength (300 MPa) and true ultimate tensile strength (609 MPa) respectively as depicted in Figure 85. Additionally, the RFW joint demonstrates greater ductility to failure (average 21%) compared to the TIG weld joint (average 16%). This discrepancy can be attributed to the distinct microstructural characteristics observed in each joint. In the case of samples belonging to TIG weld joint, the presence of hard phases such as martensite in Zone 3 and chromium carbide precipitation along grain boundaries in Zone 6 contributes to its relatively lower ductility. Conversely, the RFW joint exhibits softer microstructures, primarily comprising bainite and fine ferrite-pearlite phases in the WCL and Zones C & B respectively, which enhances its ductility and overall mechanical performance. Significantly, each tensile specimen of respective material exhibits varying strain to failure due to differences in their cross-sectional areas. It is observed that specimens with larger cross-sectional areas tend to manifest comparatively higher strain at failure. Similar conclusions were drawn by Kumar, et al. [98] in their study assessing tensile properties through the utilization of miniature tensile specimens.

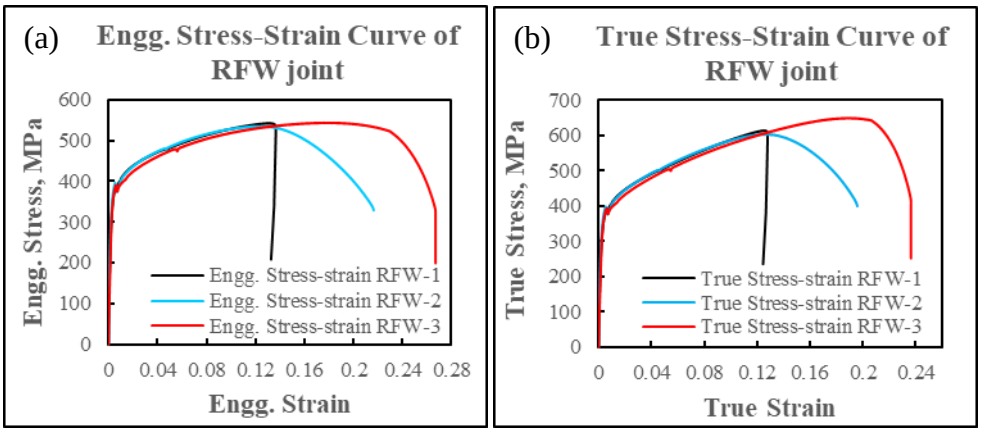

Figure 84: (a) Engineering and (b) true stress strain curve of three tensile specimens of RFW joint between S355J2 and SS316L.

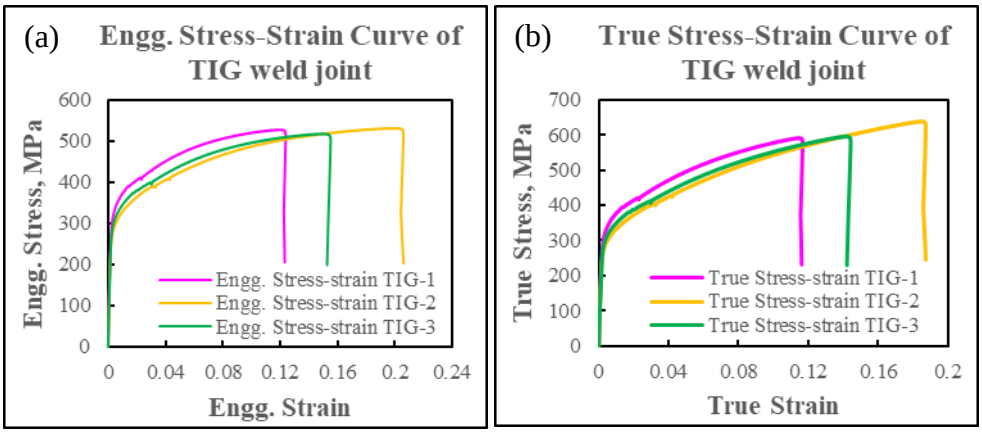

Figure 85: (a) Engineering and (b) true stress strain curve of three tensile specimens of TIG weld joint between S355J2 and SS316L.

Comparison study of tensile properties between S355J2 and SS316L: S355J2 steel demonstrates a tensile strength of 522 MPa and yield strength (YS) of 376 MPa, aligning with specifications outlined in EN 10025-2:2019. Conversely, SS316L showcases a true UTS of 536 MPa and YS of 255 MPa, adhering to ASTM A312/A312M-22a standards. Noteworthy, while SS316L demonstrates superior ductility, depicted in Figure 87, S355J2 steel exhibits relatively lower ductility, as evidenced in Figure 86. All the tensile specimens of S355J2 parent metal show yield point elongation with clear indications of upper and lower yield points. This comparative analysis not only highlights mechanical disparities between the materials but also provides valuable insights into the justification of tensile failure observed in S355J2 material. This failure became evident during the tensile testing of the dissimilar weld between these two materials.,

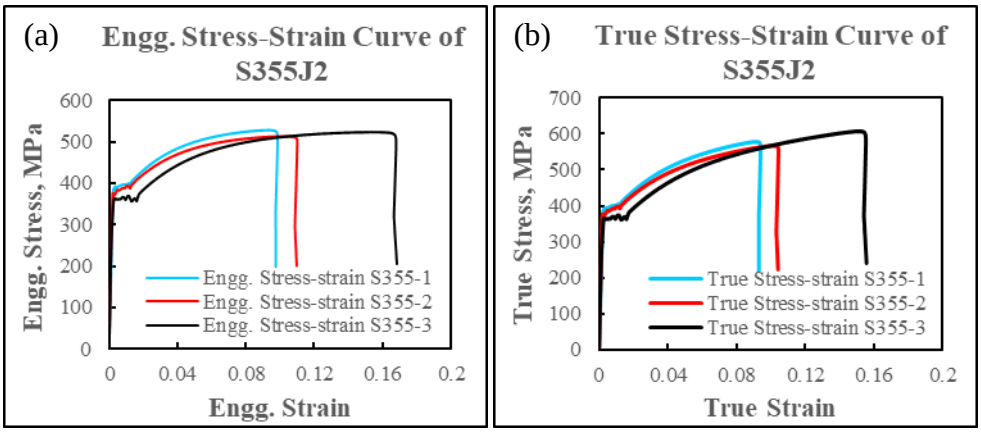

Figure 86: (a) Engineering and (b) true stress strain curve of S355J2 parent metal.

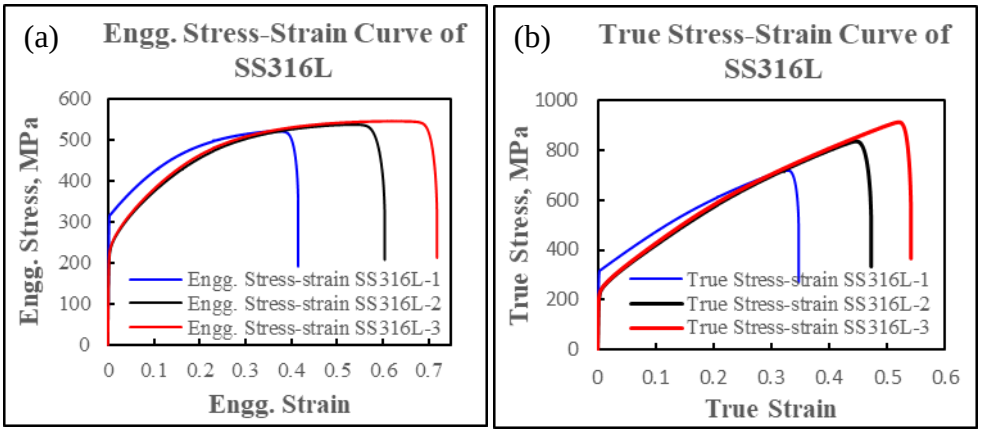

Figure 87: (a) Engineering and (b) true stress strain curve of SS316L parent metal.

Fracture behaviour of tensile specimen: The failure analysis of all cross-weld tensile specimens of both weld joints reveal that fractures predominantly occur on the S355 J2 parent metal side. This incidence is attributed to the lower ductility of S355J2 compared to SS316L, as demonstrated in Figure 86 and Figure 87. The fracture surfaces of broken tensile specimens of both the RFW and TIG weld joints reveal ductile failure characteristics. These characteristics include the presence of cup and cone features with shear lips as illustrates in Figure 88 (b & d). Notably, transgranular tensile crack propagation was observed in the tensile specimens of both weld joints (refer to Figure 88 (a & c), indicating a consistent failure mechanism across the S355J2 material.

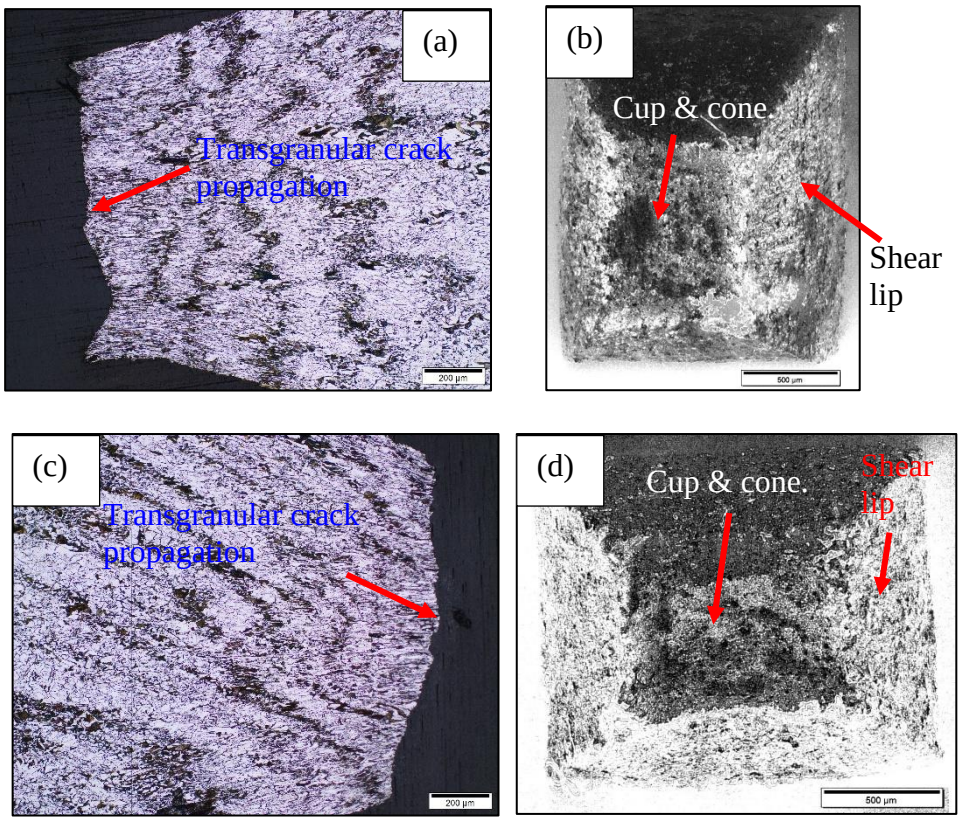

Figure 88: Optical image of (a) the crack path, and (b) the fracture surface of tensile specimen RFW-3 and optical image of (c) the crack path, and (d) the fracture surface of tensile specimen TIG-3.

4.2 Fracture toughness

Fracture toughness serves as a pivotal measure of a material's ability to withstand crack propagation and resist sudden failure under stress. It quantifies the energy required to propagate a pre-existing flaw or crack within the material. Fracture toughness testing and analysis play indispensable roles across diverse engineering disciplines, where assessing existing flaws within materials or structures is crucial for ensuring reliability and safety of structural components. This parameter is often expressed as plane-strain fracture toughness denoted by K_{1C} and as elastic-plastic fracture toughness in terms of CTOD or J integral, providing engineers with standardized metrics for evaluating material performance.

The summary of fracture toughness properties detailed in terms of K_Q is presented in Table 14. Although the fracture toughness test was conducted in accordance with ASTM E399 standards and deemed valid, the fracture toughness values obtained

for all specimens from this test do not adhere to the plane-strain fracture toughness (K_{1C}) criterion. This deviation is attributed to two primary factors: Firstly, the ratio P_{max}/P_Q (refer to Figure 44) exceeds 1.10 for all specimens. Secondly, the value of 2.5 x $(K_Q/\sigma_{YS})^2$ surpasses the specimen ligament size (i.e., W–a) for all specimens.

It is found that all specimens exhibit elastic-plastic fracture behaviour. Therefore, alongside K_Q, an elastic-plastic fracture toughness in the form of CTOD, denoted as δ_m, is determined using Equation 14. The CTOD values are documented in Table 14 with measurements taken at a 1.5% crack mouth extension, considering the limitations imposed by the extensometer utilized in the testing process. Detailed calculation and test validation are documented in Appendix.

Table 14: Summary of fracture toughness properties of weld between CS and SS.

	Parent Metal		**RFW joint**			**TIG weld Joint**		
Notch Location	S355J2	SS316L	WCL	HAZ-SS	HAZ-CS	WCL	HAZ-SS	HAZ-CS
Specimen ID	FT-3	FT-4	FT-1	FT-6	FT-7	FT-9	FT-5	FT-8
K_Q, MPa√m	**41.8**	**31.2**	**40.9**	**41.5**	**42.9**	**42.1**	**36.8**	**40.0**
$\delta_{m\ at\ 1.5\%\ extn.}$ mm	**0.34**	**0.37**	**0.35**	**0.32**	**0.32**	**0.32**	**0.34**	**0.31**

The CT specimen FT-3, representing S355J2 parent metal, exhibits a K_Q value of 41.8 MPa√m and a δ_m value of 0.34 mm. Although this K_Q value does not indicate the plane-strain fracture toughness, it closely matches with plane-strain fracture toughness (38.0 MPa√m) of S355 steel was determined by Bozkurt and Schmidová [15] in their study. Alternatively, the obtained δ_m value (0.34 mm) appears relatively lower compared to the value (0.736 mm) determined by Bannister and Trail [99] for S355J2 steel in their study. This variance is directly linked to impose a maximum crack mouth opening of 1.5 mm in present study due to constraints associated with the extensometer or clip gauge. FT-3 specimen experiences both linear elastic and elastic-plastic crack growth behaviour with linear elastic crack growth prevailing due to its ferrite-pearlite microstructure.

On the other hand, the CT specimen of SS316L parent metal (FT-4) displays the lowest K_Q value of 31.2 MPa√m. It closely matches with K_Q value (31.6 MPa√m)

of SS316L was determined by Senthil, et al. [100] in their study on Inconel 825–SS316L functionally graded wall fabricated by wire arc additive manufacturing. However, it demonstrates the highest δ_m value of 0.37 mm, indicating significant plastic deformation owing to its fully austenitic microstructure. Consequently, elastic-plastic crack growth dominates over linear elastic crack growth in FT-4. Khor, et al. [101] investigated various methods for estimating and predicting CTOD in ASS. Their findings revealed that for SS316, a CTOD (δ_m) of 0.4 mm occurred at a crack mouth opening displacement (CMOD) of 2 mm, while a δ_m of 2.0 mm was observed at a CMOD of 7.4 mm. Remarkably, the δ_m values obtained for SS316L in our present study (i.e. 0.37 mm at a CMOD of 1.5 mm) closely align with those reported in their research.

FT-1 specimen, representing WCL of RFW joint, demonstrates a K_Q value of 40.9 MPa√m and a CTOD value of 0.35 mm. This specimen exhibits both linear elastic and elastic-plastic crack growth, a result attributed to the complex microstructure present at the WCL of the RFW joint. This microstructure comprises islands of both S355J2 and SS316L materials as depicted in Figure 66, formed due to the thermomechanical behaviour of the welding process and elemental dilution.

FT-6 specimen displays a fracture toughness of 41.5 MPa√m, and a δ_m value of 0.32 mm. It also experiences both linear elastic and elastic-plastic crack growth, with linear elastic crack growth predominating in crack propagation. This dominance can be attributed to the presence of a fine austenitic grain microstructure as illustrated in Figure 64. In the case of SS316L, the fine grain structure enhances the plane-strain region of fracture, thereby improving plane-strain fracture toughness. Conversely, a large grain size enhances fracture toughness in plane-stress conditions [102].

FT-7 specimen exhibits a K_Q value of 42.9 MPa√m and a δ_m value of 0.32 mm. Like FT-6, it experiences both linear elastic and elastic-plastic crack growth, with linear elastic crack growth dominating crack propagation. This dominance is due to the presence of a fine ferrite-pearlite microstructure as shown in Figure 60.

Specimen FT-9 (WCL of TIG weld joint) demonstrates K_Q value 42.1 MPa√m in whereas it shows the lowest CTOD value of 0.32 mm as it experiences only linear

elastic crack growth due to presence of delta ferrite and precipitation of hard chromium carbide in grain boundary as illustrated in Figure 79.

The FT-5 specimen demonstrates a fracture toughness (K_Q) of 36.8 MPa√m. Additionally, it exhibits a CTOD value of 0.34 mm. During fracture, the specimen undergoes a combination of linear elastic and elastic-plastic crack growth mechanisms. However, the dominance of linear elastic-plastic crack growth is evident in the propagation of cracks. This dominance is attributed to the presence of an austenitic microstructure, as illustrated in Figure 76.

The FT-8 specimen showcases a K_Q value of 40.0 MPa√m, accompanied by a δ_m value of 0.31 mm. It undergoes a fracture process involving both linear elastic and elastic-plastic crack growth mechanisms. However, the predominant mode of crack propagation is linear elastic, attributed to the presence of martensitic structures as depicted in Figure 72, alongside a fine ferrite-pearlite microstructure shown in Figure 71. It's noteworthy that the properties of the FT-8 specimen are comparatively lower than those of FT-7, primarily due to the formation of hard martensite within this zone. This difference underscores the influence of microstructural variations on the mechanical behaviour of the material.

A comparative analysis of fracture toughness and CTOD results between FT1 and FT9 reveals similar K_Q values but FT1 exhibits a higher CTOD value of 0.35 mm compared to FT9's 0.31 mm. This discrepancy is primarily attributed to microstructural distinctions observed between the two specimens. FT1 unveils a microstructure characterized by islands comprising both S355J2 and SS316L materials, as depicted in Figure 66. These islands are formed due to the thermomechanical behaviour of the welding process and elemental dilution. Conversely, FT9 showcases hard chromium carbide deposition and delta ferrite grain boundaries alongside columnar austenite grains, as illustrated in Figure 79.

4.2.1 Fractography study

Fractography delves into the examination and interpretation of fractured surfaces to unveil insights into the mechanisms and conditions of material failure. By scrutinizing the morphology, and features of fracture surfaces, fractography offers valuable clues about the stresses, forces, and environmental factors that precipitated the failure. With its interdisciplinary relevance and analytical depth, fractography

serves as a cornerstone in understanding the behaviour and performance of materials under diverse loading conditions and environments.

The fracture surface of the broken FT-3 specimen clearly demonstrates a complete ductile failure, as depicted in Figure 89. Micro voids appear across the surface, with void coalescence significantly contributing to crack propagation perpendicular to the axial force, as shown in Figure 89 (b). Moreover, the fatigue fracture surface exhibits distinctive striation marks, as illustrated in Figure 89 (c). Dimple sizes are smaller which encourages plane-strain fracture or linear elastic fracture. Therefore, linear elastic crack growth prevailing for specimen FT-3. Li, et al. [102] found that dimple size has a distinct impact on fracture toughness depending on the stress state it creates at crack tip. Smaller dimples tend to encourage plane-strain or linear elastic fracture, whereas larger dimples foster plane-stress or elastic-plastic fracture.

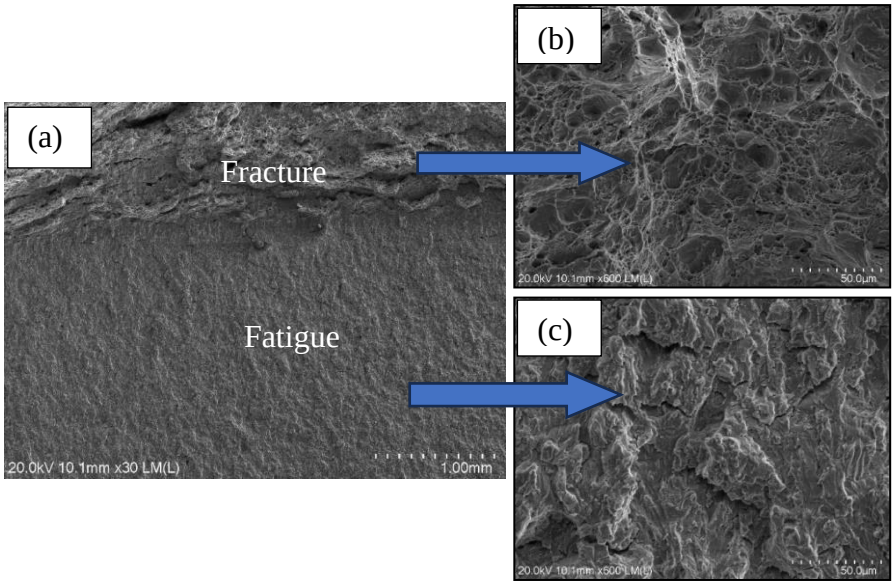

Figure 89: SEM image shows (a) the complete failure surface, (b) the fracture surface and (c) the fatigue surface of specimen FT-3.

Crack path study discloses that crack propagates through transgranular path in both fatigue and fracture mechanism as displayed in Figure 90.

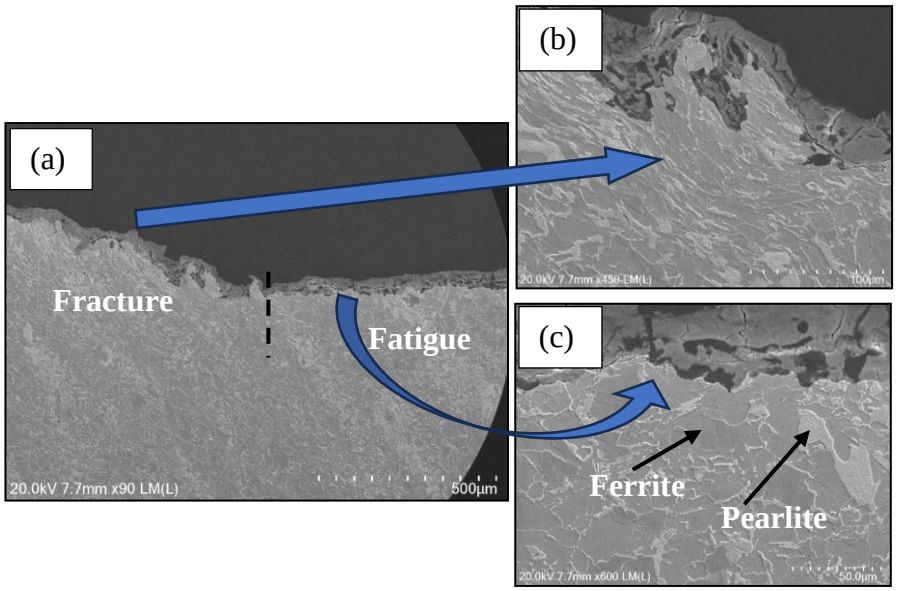

Figure 90: SEM image shows (a) the complete crack path, (b) the crack path in fracture and (c) the crack path in fatigue of specimen FT-3.

Upon analysing the fracture surface of the FT-4 specimen, becomes evident that it succumbs to a complete ductile failure, as depicted in Figure 91. Micro voids emerge, facilitating crack propagation perpendicular to the axial force, as illustrated in Figure 91 (b). Conversely, the fatigue fracture surface exhibits distinct striation marks, showcased in Figure 91 (c). Notably, the presence of larger dimples suggests a tendency towards plane-stress fracture or elastic-plastic fracture [102]. Therefore, elastic-plastic crack growth prevails for the FT-4 specimen.

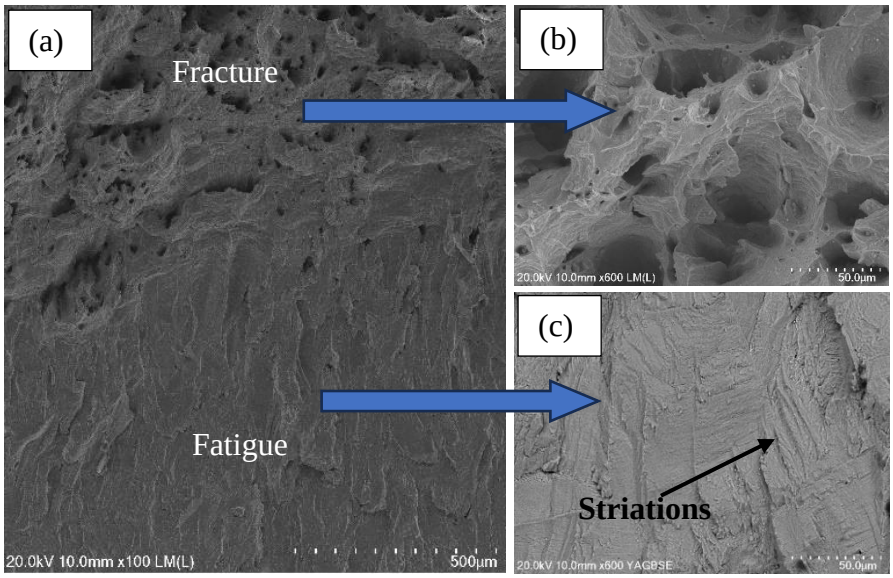

Figure 91: SEM image shows (a) the complete failure surface, (b) the fracture surface and (c) the fatigue surface of specimen FT-4.

Crack path study discloses that crack propagates through transgranular path in both fatigue and fracture mechanism as illustrated in Figure 92.

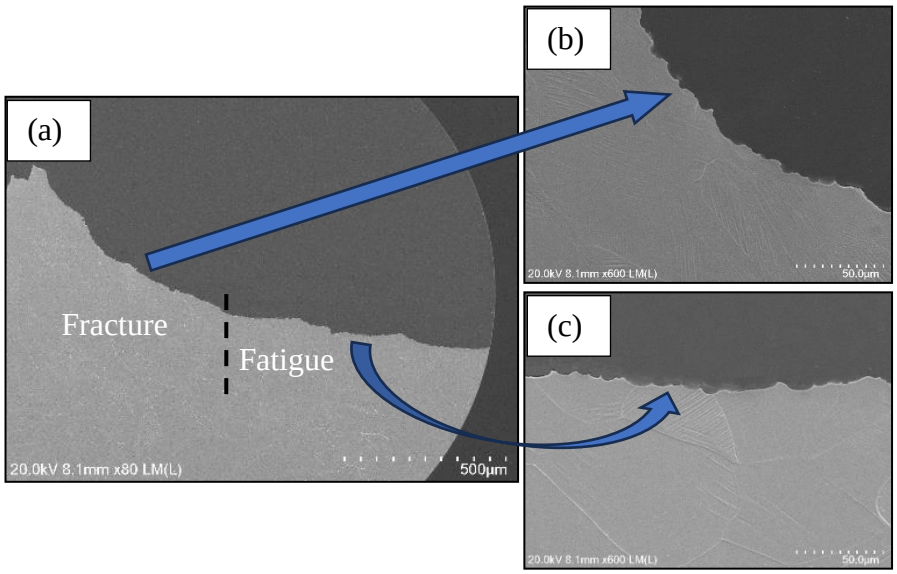

Figure 92: SEM image shows (a) the complete crack path, (b) the crack path in fracture and (c) the crack path in fatigue of specimen FT-4.

Fractographic analysis of broken surface FT-1 specimen unveils a fully ductile failure, as evidenced in Figure 93.

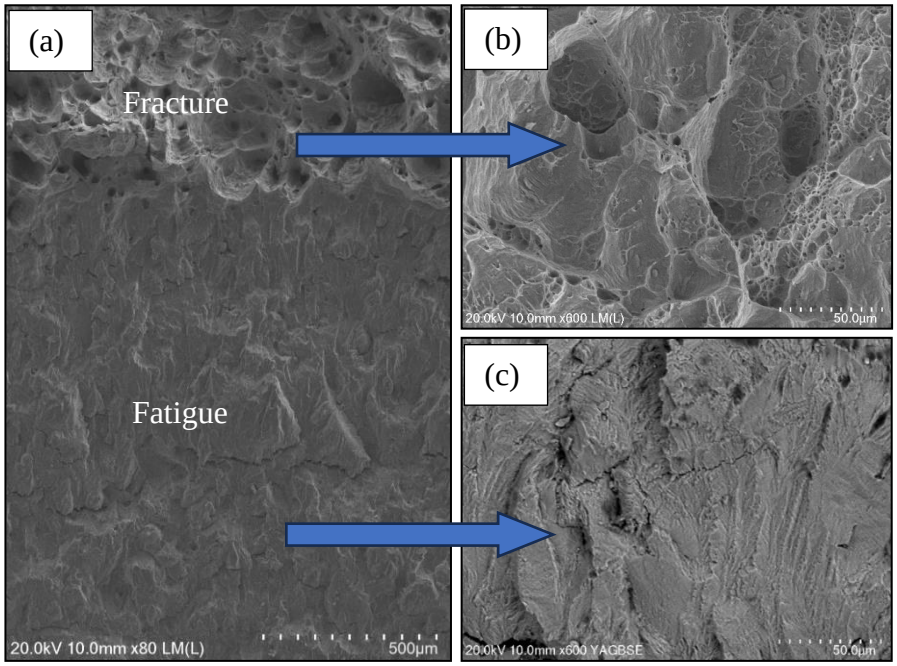

Figure 93: SEM image shows (a) the complete failure surface, (b) the fracture surface and (c) the fatigue surface of specimen FT-1 specimen.

Micro voids coalescence, facilitating crack propagation perpendicular to the axial force, as depicted in Figure 93 (b). Furthermore, the fatigue fracture surface exhibits discernible striation marks, highlighted in Figure 93 (c). Notably, the presence of larger dimples suggests an inclination towards plane-stress fracture or elastic-plastic fracture. Therefore, elastic-plastic crack growth prevails for the FT-1 specimen. These larger dimples are formed because the weld interface of RFW displays a mixture of austenite and bainite phases from both the parent metal, which is evident through the formation of distinct material islands as shown in Figure 66. Crack path study discloses that crack propagates through transgranular path in both fatigue and fracture mechanism as displayed in Figure 94.

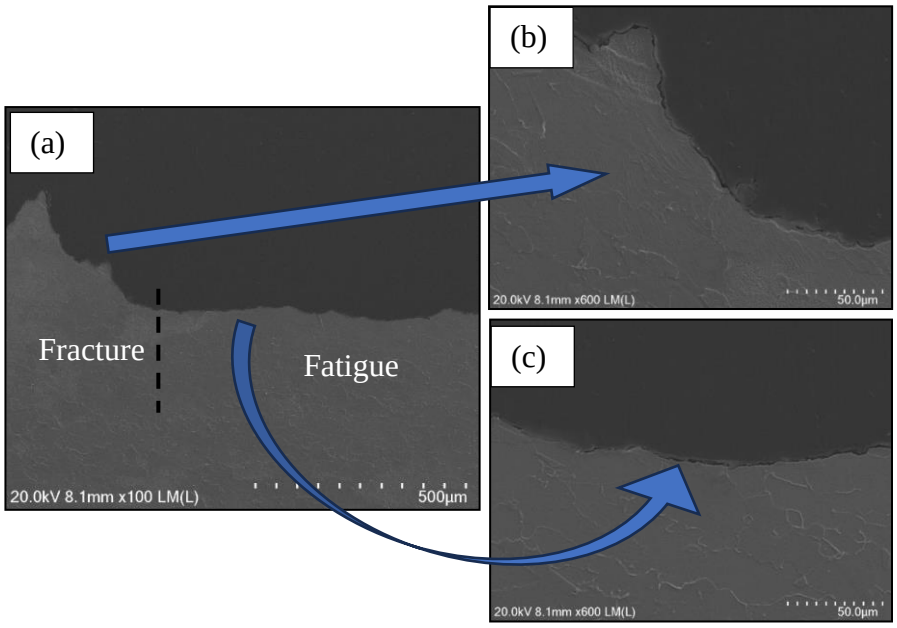

Figure 94: SEM image shows (a) the complete crack path, (b) the crack path in fracture and (c) the crack path in fatigue of specimen FT-1.

The examination of the broken FT-6 specimen unveils a ductile failure, as illustrated in Figure 95. Microscopic analysis indicates the formation of micro voids, with void coalescence aiding in crack propagation perpendicular to the applied axial force refer to Figure 95 (b). Furthermore, the fatigue fracture surface exhibits distinct striation marks as depicted in Figure 95 (c). The fracture process entails a combination of linear elastic and elastic-plastic crack growth mechanisms, although linear elastic crack growth prevails. This dominance is attributed to the presence of relatively smaller dimples and the fine austenitic grain microstructure within the material.

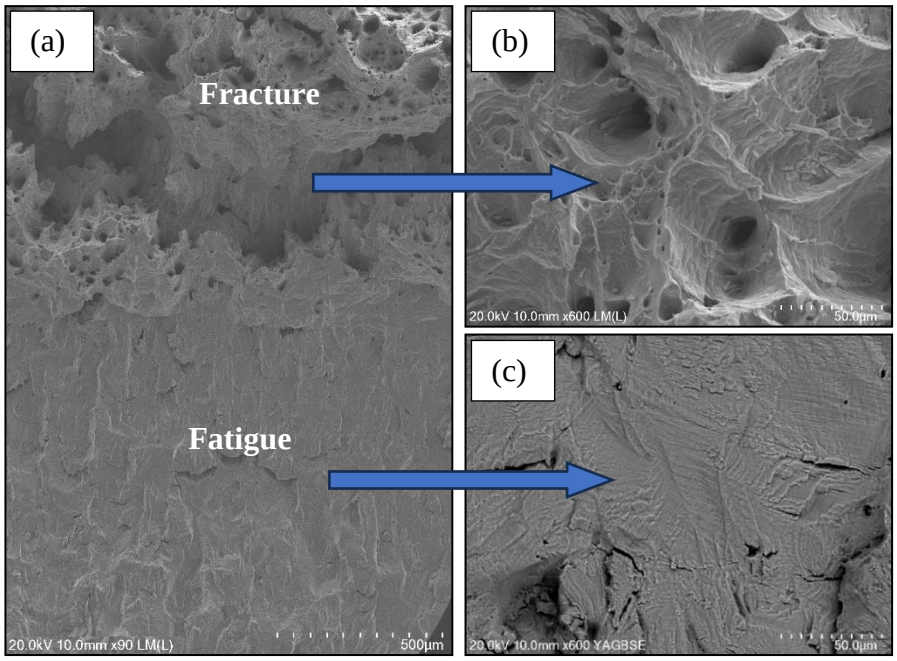

Figure 95: SEM image shows (a) the complete failure surface, (b) the fracture surface and (c) back scattered electron image of fatigue surface of specimen FT-6.

Crack path study discloses that crack propagates through transgranular path in both fatigue and fracture mechanism as depicted in Figure 96.

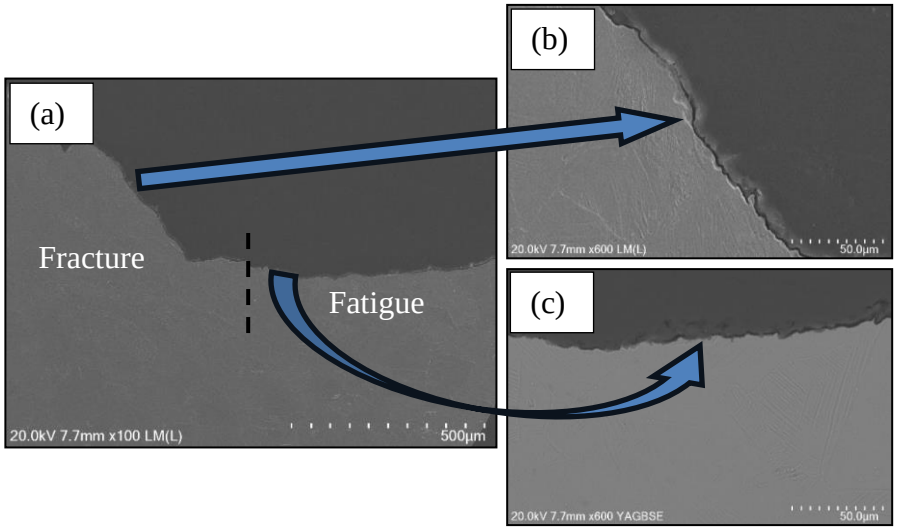

Figure 96: SEM image shows (a) the complete crack path, (b) crack path in fracture and (c) back scattered electron image of crack path in fatigue of specimen FT-6.

Upon microscopic examination of the fractured surface of the FT-7 specimen, a fully ductile failure is evident, as depicted in Figure 97. Microscopic voids emerge, facilitating crack propagation perpendicular to the axial force (Figure 97 (b). Additionally, the fatigue fracture surface displays distinct striation marks (Figure

97 (c). The fracture process encompasses both linear elastic and elastic-plastic crack growth mechanisms, with linear elastic crack growth prevailing. This dominance is attributed to the presence of fine dimples on the fracture surface and the refined ferrite-pearlite microstructure within the material.

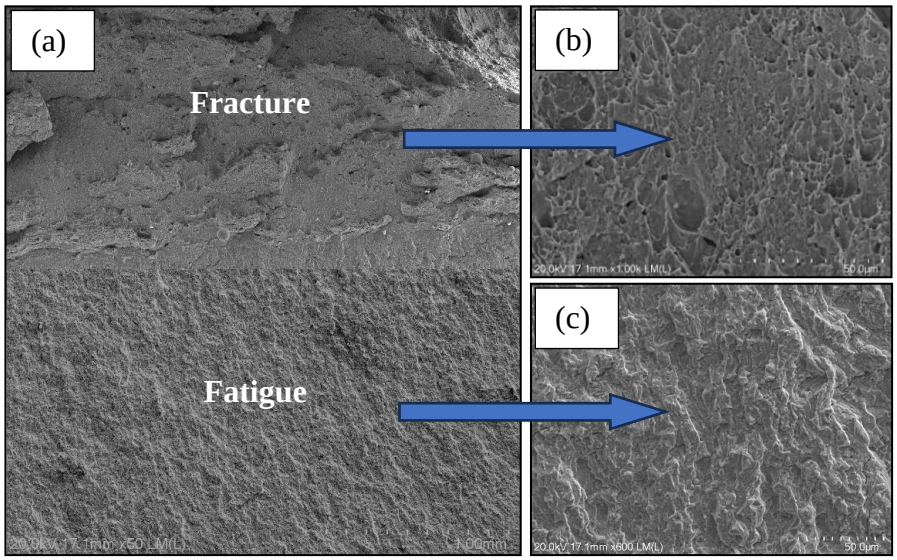

Figure 97: SEM image shows (a) the complete failure surface, (b) the fracture surface and (c) the fatigue surface of specimen FT-7.

Crack path study discloses that crack propagates through transgranular path in both fatigue and fracture mechanism as illustrated in Figure 98.

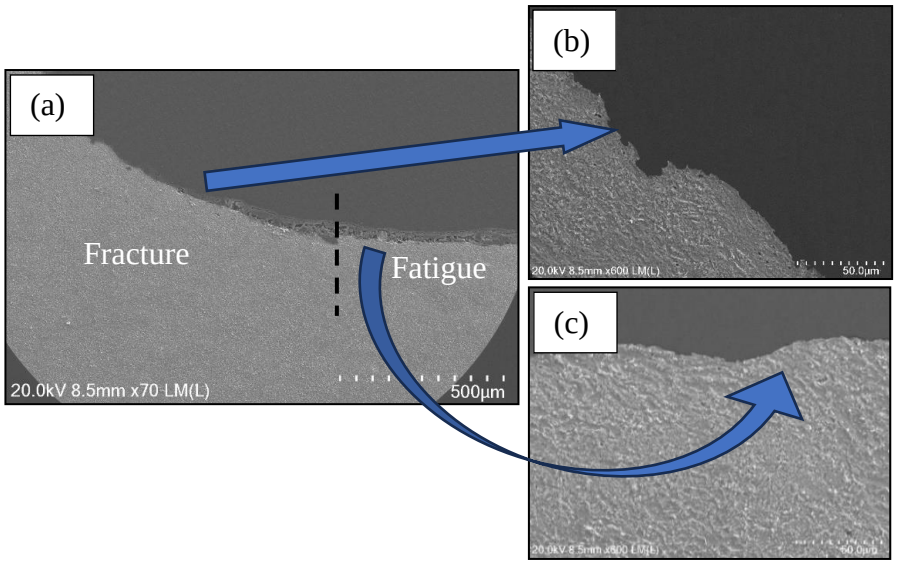

Figure 98: SEM image shows (a) the complete crack path, (b) the crack path in fracture and (c) the crack path in fatigue of specimen FT-7.

The analysis of the fracture surface of the broken FT-9 specimen clearly identifies it as a cleavage fracture, as depicted in Figure 99. Notably, a glossy and flat surface is observed in fracture surface and there is a notable absence of void coalescence, indicating a predominantly cleavage fracture mode as illustrated in Figure 99 (b). Furthermore, the fatigue fracture surface displays distinct striation marks, as depicted in Figure 99 (c). The fracture process predominantly involves linear elastic crack growth mechanisms. This behaviour can be attributed to the deposition of chromium carbide along the grain boundaries of columnar austenite, in conjunction with the presence of δ-ferrite, as elucidated in Figure 79. Understanding these characteristics sheds light on the fracture behaviour of the material, facilitating insights into its mechanical properties and failure mechanisms.

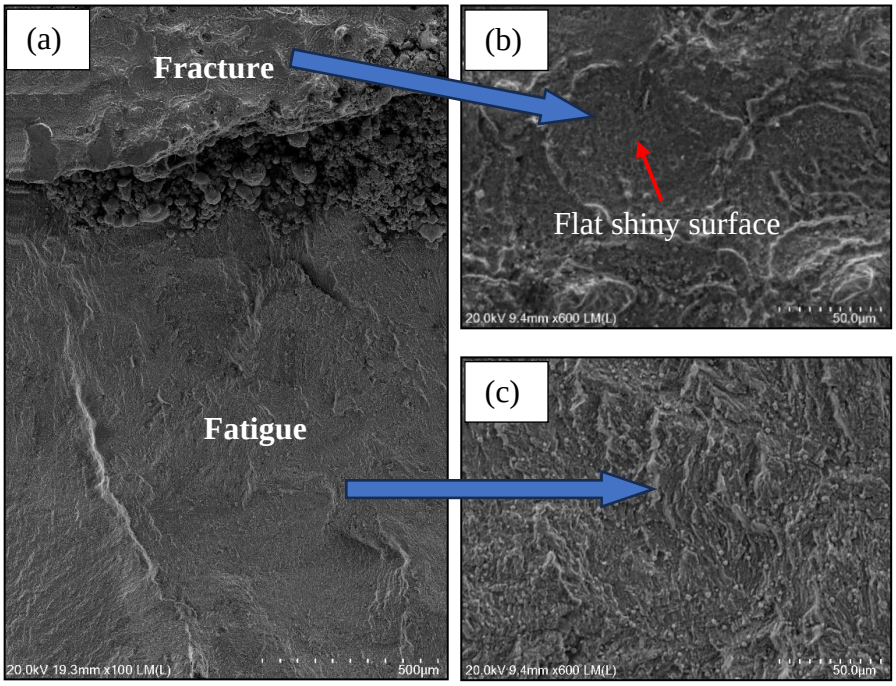

Figure 99: SEM image shows (a) the complete failure surface, (b) the fracture surface and (c) the fatigue surface of specimen FT-9.

Crack path study discloses that crack propagates through transgranular path in both fatigue and fracture mechanism as shown in Figure 100.

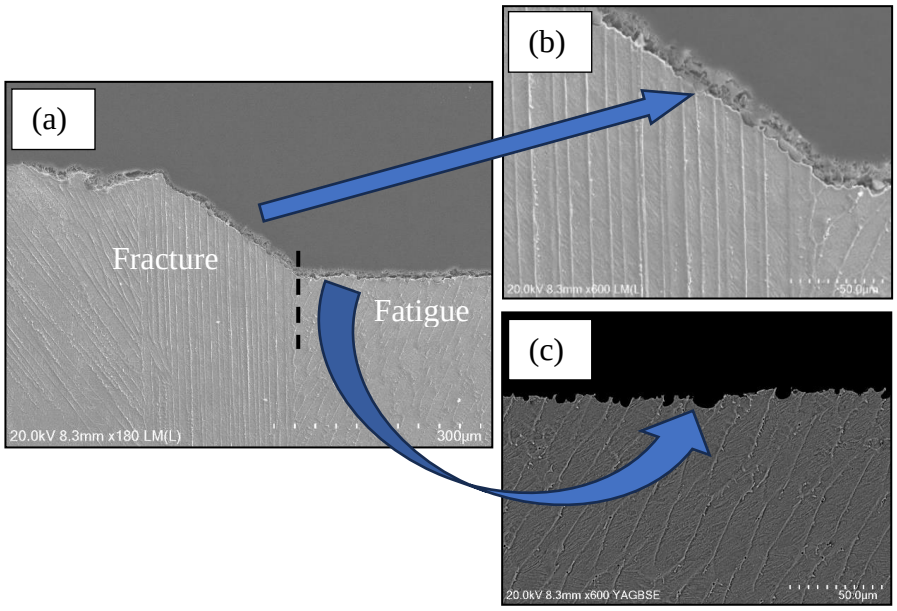

Figure 100: SEM image shows (a) the complete crack path, (b) the crack path in fracture and (c) the back scattered electron image of crack path in fatigue of specimen FT-9.

The examination of the microstructure on the broken surface of the FT-5 specimen distinctly indicates a ductile failure mode, as depicted in Figure 101.

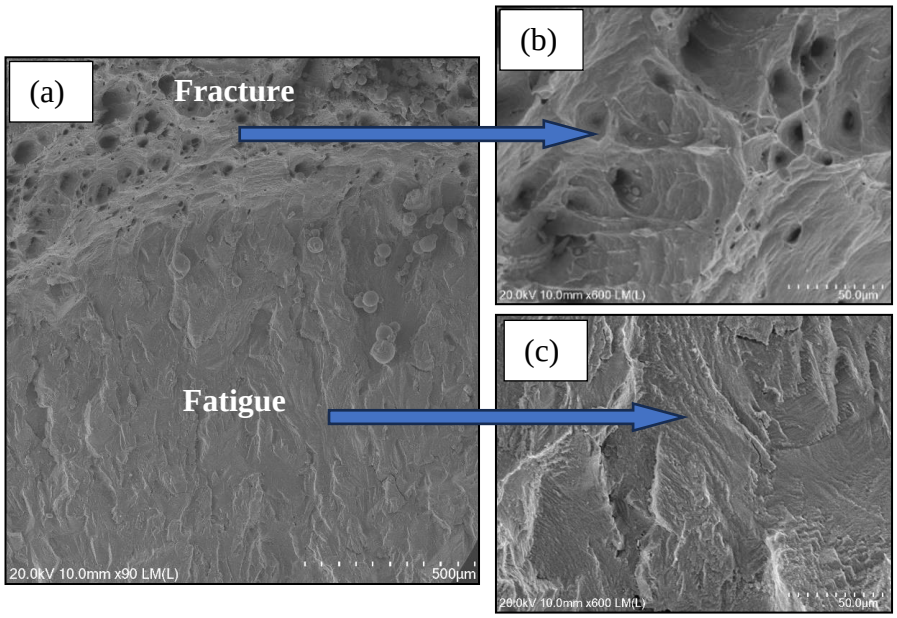

Figure 101: SEM image shows (a) the complete failure surface, (b) the fracture surface and (c) the fatigue surface of specimen FT-5.

Microscopic voids are discernible, with void coalescence facilitating crack propagation perpendicular to the axial force, as illustrated in Figure 101 (b).

Moreover, the fatigue fracture surface exhibits distinct striation marks, as shown in Figure 101 (c). The fracture process encompasses both linear elastic and elastic-plastic crack growth mechanisms. However, the dominance of elastic-plastic crack growth is evident in crack propagation. This dominance can be attributed to the presence of large dimples on the fracture surface, indicating significant plastic deformation during the fracture process.

Crack path study discloses that crack propagates through transgranular path in both fatigue and fracture mechanism as depicted in Figure 102.

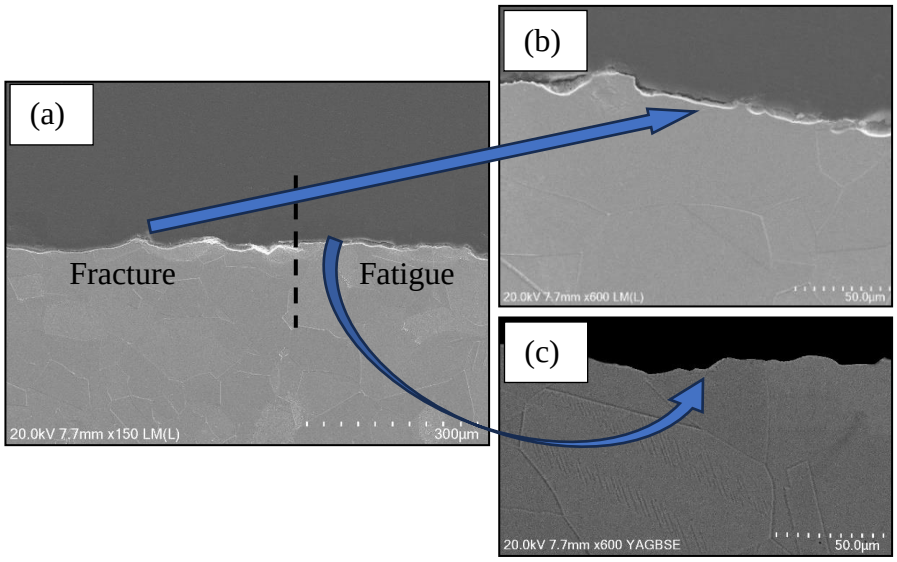

Figure 102: SEM image shows (a) the complete crack path, (b) the crack path in fracture and (c) back scattered electron image of the crack path in fatigue of specimen FT-5.

The examination of the microstructure on the broken surface of the FT-8 specimen confirms a ductile failure mode, as evidenced in Figure 103. Microscopic voids are evident, with void coalescence facilitating crack propagation transverse to the axial force, as depicted in Figure 103 (b). Additionally, the fatigue fracture surface displays discernible striation marks, as shown in Figure 103 (c). The fracture process involves both linear elastic and elastic-plastic crack growth mechanisms. However, the dominance of linear elastic crack growth is notable in crack propagation. This dominance is attributed to the presence of martensitic and ferrite-pearlite microstructures within the material.

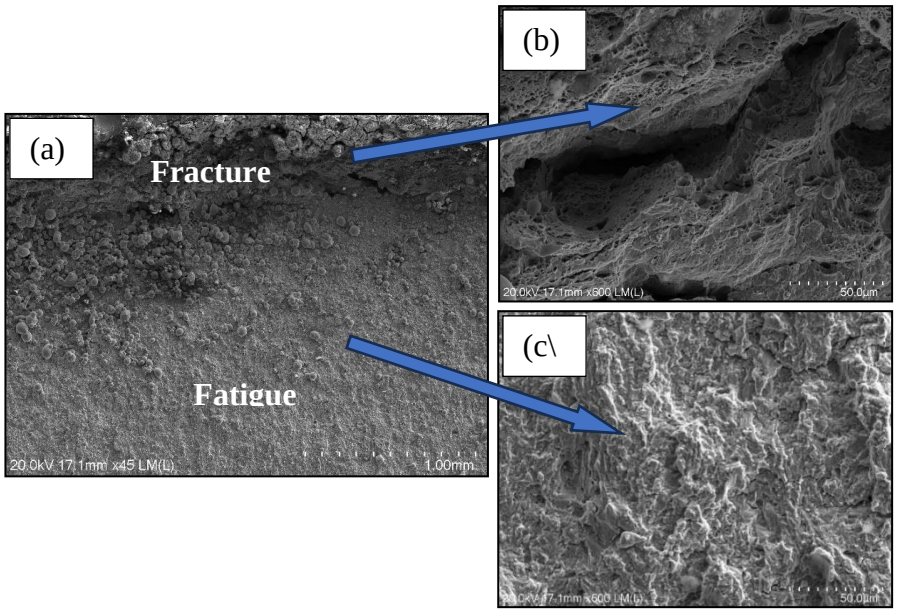

Figure 103: SEM image shows (a) the complete failure surface, (b) the fracture surface and (c) the fatigue surface of specimen FT-8.

Crack path study discloses that crack propagates through transgranular path in both fatigue and fracture mechanism as illustrated in Figure 104.

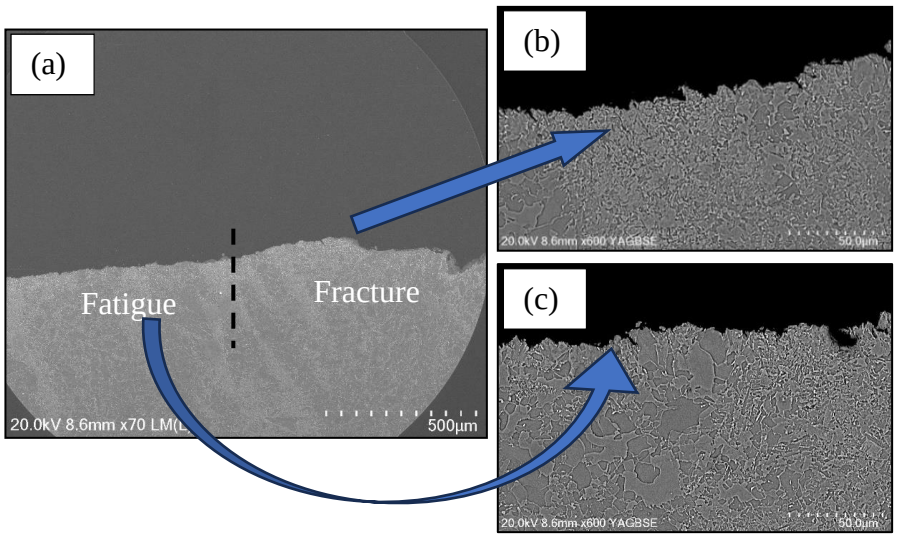

Figure 104: SEM image shows (a) the complete crack path, (b) back scattered electron image of the crack path in fracture and (c) the crack path in fatigue of specimen FT-8.

4.3 Dissimilar weld between Ti64 and Ti1023

4.3.1 Macroscopic examination

Macroscopic examination of the RFW joint between Ti-64 and Ti-1023, as illustrated in Figure 105 (a & b), reveals the joint formed as a result of RFW process. Notably, a clearly defined fusion line describes the bond between the two dissimilar alloys. The seamless integration of components, evidenced by the presence of weld centre line or fusion line, features a robust welding process. A distinct HAZ is apparent on both parent metals, extending approximately 2.0 mm distance from the fusion line. The presence of such a HAZ confirms the influence of heat generated during the welding process. Importantly, careful observations confirmed the absence of common weld flaws such as lack of side wall fusion, porosity, or cold lap.

(a) (b)

Figure 105: (a) Macro recorded using optical microscopy showing the welded joint achieved by RFW between Ti-64 and Ti-1023 alloys. and (b) schematic illustrating the different zones developed in the joint during RFW process.

4.3.2 Microstructure analysis

Figure 106 presents a montage of optical microscope image showcasing a complete RFW dissimilar joint between Ti-64 and Ti-1023. The weld is divided into six zones to facilitate a comprehensive examination of microstructural alterations across distinct regions of the weld joint. Zones A and D provide a glimpse into the microstructure of the parent metal, offering valuable insights into its original material characteristics. Meanwhile, Zones B and E delineate the HAZ, capturing segments affected by thermal changes during the welding process. Zones C and F encapsulate the TMAZ, where the material undergoes changes due to both heat and

forging pressure, resulting in distinctive microstructural modifications. This systematic division enables a detailed analysis of microstructural changes within different zones of the weld joint, providing valuable information for understanding the welding process and its impact on mechanical properties.

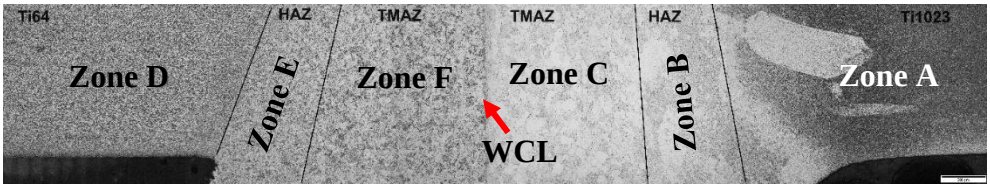

Zone A – Ti-1023 parent metal, Zone B – HAZ of Ti-1023, Zone C – TMAZ of Ti-1023, Zone D – Ti-64 parent metal, Zone E – HAZ of Ti-64 and Zone F – TMAZ of Ti-64.

Figure 106: Macro from optical microscopy showing different zones of RFW joint made between of Ti-64 and Ti-alloys.

Microstructural characteristics of parent metal Ti-1023 (Zone A)

Figure 107 illustrates SEM microstructure observations of Zone A. At low magnification as depicted in Figure 107 (a), the microstructure reveals a relatively homogeneous distribution of primary alpha (α_p) within the β matrix. Upon closer examination at high magnification as displayed in Figure 107 (b), very fine acicular secondary alpha (α_s) is observed to grow inside the β matrix (which is called as transformed β). Ageing produces very fine acicular secondary alpha (α_s) to grow inside the β matrix [103]. This microstructural composition, characterized by the homogeneous distribution of primary alpha (α_p) and the presence of β matrix with secondary alpha (α_s), matches with the findings reported by Utama, et al. [104]. Their investigation into electron beam welding between Ti-64 and Ti-1023 identified this similar microstructure characteristics. This consistency underscores the reproducibility and reliability of the observed microstructural features across different studies.

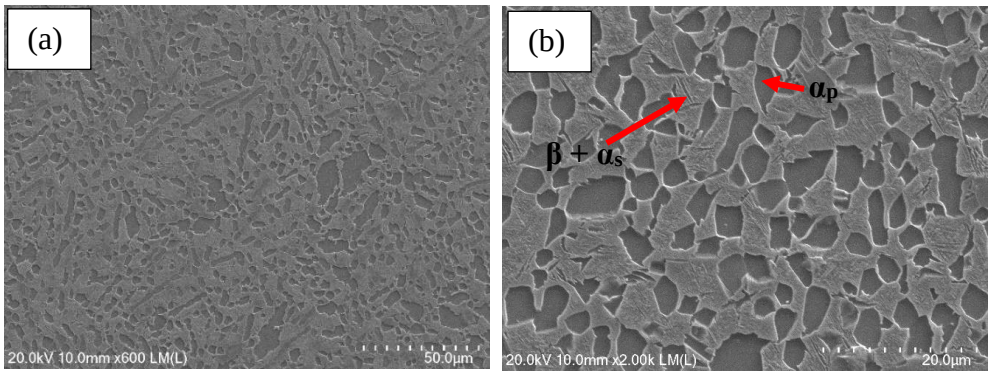

Figure 107: SEM images showing the microstructural characteristics of Zone A in the RFW joint between Ti-64 and Ti-1023 (a) at low and (b) at higher magnification.

Microstructural characteristics of HAZ of Ti-1023 (Zone B)

Zone B exhibits distinct characteristics indicative of a partially deformed zone. A noticeable alteration in the shape of primary alpha (α_p) grains compared to Zone A is observed, with the formation of elongated α_p grains. Additionally, large β grains are formed along with the α_p grain boundary. Notably, secondary alpha (α_s) begins to grow from the grain boundary towards the interior of the grain, as illustrated in Figure 109. During welding, HAZ experiences raising temperatures. Studies, such as those conducted by Jedrasiak, et al. [105], have indicated that the HAZ encounters temperatures ranging from 400°C to 500°C during thermal modelling of linear friction welding, as depicted in Figure 108. As these temperatures remain below the transus temperature of Ti-1023 (as illustrated in Figure 10), thereby inducing microstructural changes in the solid state. Furthermore, the slower cooling rate less than 20°C/sec in this zone [106], attributed to the lower thermal conductivity of Ti-1023, facilitates aging effects. This aging effect results microstructural changes in this zone. Notably, similar microstructural changes also reported in the case of Ti-1023 due to aging at 400°C to 600°C by Leyens and Peters [34] in their study. They also found that a coarsening of the α_p as well as a change from globular to acicular α_p leads to a reduction in ductility of Ti-1023 alloy.

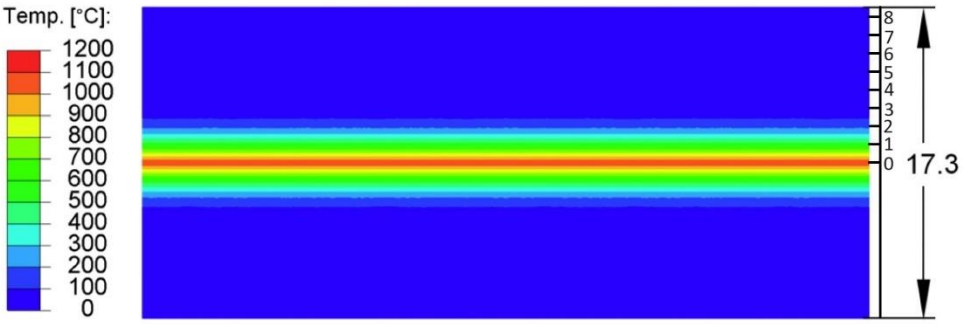

Figure 108: Temperature field across the weld at the end of equilibrium stage, with the length of the model workpieces indicated (dimensions in mm) [105].

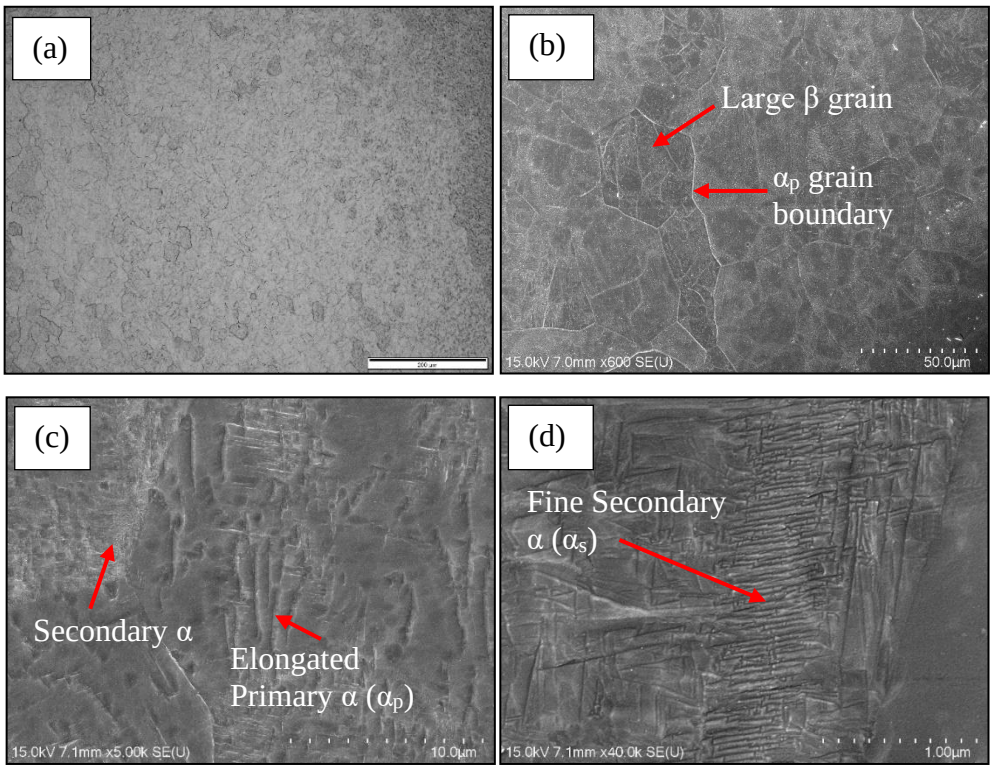

Figure 109: (a) Optical image shows coarse equiaxed β grains and SEM image (b) at low magnification shows large β grains, (c) at higher magnification shows lamellar primary α and secondary α laths and (d) at high magnification shows nanoscale secondary α grow into the β grain in Zone B of the RFW joint between Ti-64 and Ti-1023.

Microstructural characteristics of TMAZ of Ti-1023 (Zone C)

Figure 110 reveals the intricate microstructure of Zone C, characterized by large β grains, primary alpha (α_p) grain boundaries, and orthorhombic α′′ martensite phases. This zone experiences a confluence of thermal and pressure effects, initiating substantial dynamic recrystallization driven by the heat generated from friction and the strain imposed by forging pressure [106]. In the realm of thermal modelling for linear friction welding, studies by Jedrasiak, et al. [105] have reported that Zone C experiences a temperature of 1000°C, as depicted in Figure 108. Fundamentally, this temperature surpasses the β-transus temperature of Ti-1023 (refer to Figure 10), facilitating the transformation of α_p grains into β grains. Furthermore, Zone C contends with significant strains and strain rates, reaching up to 2500/sec during welding, fostering dynamic recrystallization of the high-temperature β-phase. The exposure to elevated temperatures, along with a rapid cooling rate of approximately 410°C/second and welding-induced pressure, foster the formation of stress induced α′′ martensite and thick film of α_p along the grain boundaries of β grains formed within Zone C. Similar microstructural changes have reported in the Ti-1023 due to stress application by Niessen, et al. [107] and in their studies on the effect of applied stress state on transformation from β to α'' martensite in metastable β Titanium.

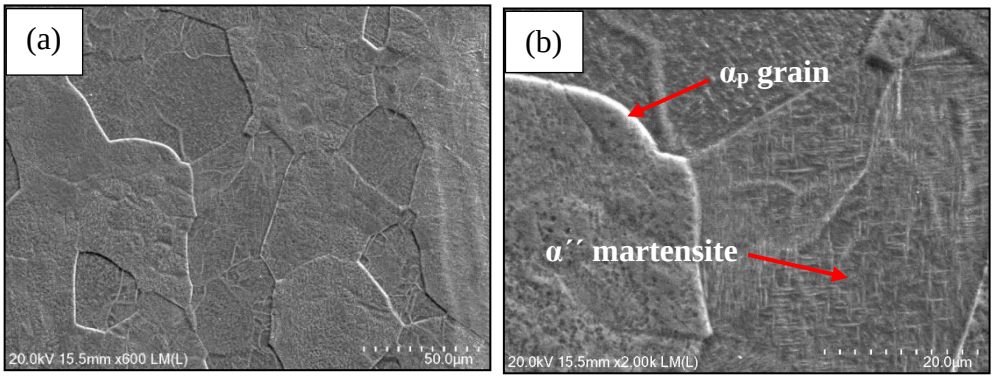

Figure 110: SEM images of the microstructure of Zone C in the RFW joint at two different magnification (a) 600X and (b) 2000X.

Microstructural characteristics of parent metal Ti-64 (Zone D)

The SEM micrographs of Zone D show coarse equiaxed microstructures consist of intergranular brighter β phase in darker α matrix as shown in Figure 111. Equiaxed microstructures are the result of a recrystallization process. Initially alloy is highly

deformed in the α + β field to introduce enough cold work into the material. Upon subsequent solution heat treatment at a temperature in the two-phase field (refer Figure 9), a recrystallized and equiaxed microstructure is generated and extended annealing coarsens the equiaxed microstructure. The chemical compositions of the α and β phases change in the two-phase field with decreasing temperature under equilibrium conditions (refer Figure 9). Vanadium strongly enriches β and thus stabilizes this phase at lower temperatures. Hence, the microstructure shows β as a small seam around the coarse dark coloured α grins [34].

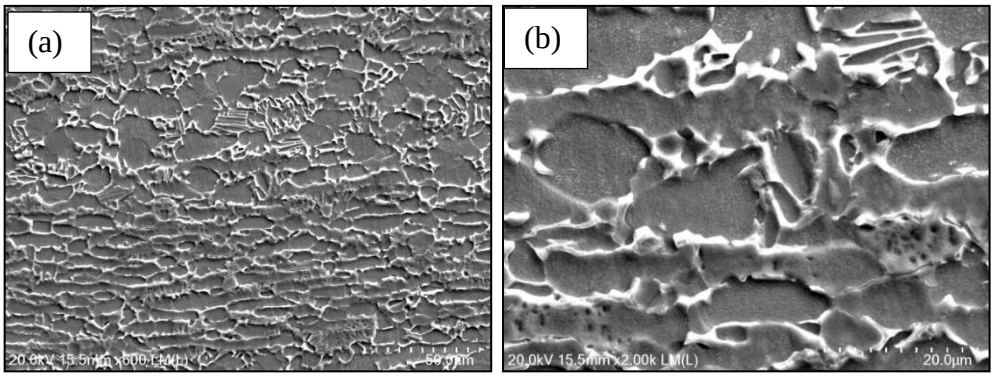

Figure 111: SEM image of the microstructure of Zone D in the RFW joint between Ti-64 and Ti-1023 at two different magnifications showing the presence of coarse equiaxed primary α and thin β in the matrix (a) 600X and (b) 2000X.

Microstructural characteristics of HAZ of Ti-64 (Zone E)

Zone E exhibits characteristics of a partially deformed zone, where both α grains and the β phase along grain boundaries elongate in the direction of heat flow refer to Figure 112. While microstructural phase changes compared to Zone D are not pronounced, the HAZ undergoes temperature variations during welding. Studies, such as those conducted by Jedrasiak, et al. [105], have observed that the HAZ experiences temperatures of 400°C – 500°C during thermal modelling of linear friction welding as illustrated in Figure 108. Since this temperature remains below the transus temperature of Ti-64 (refer to Figure 9), microstructural changes occur in the solid state. Furthermore, temperatures of 400°C – 500°C and the slower cooling rate less than 20°C/sec in this zone [106], attributed to the lower thermal conductivity of Ti-64, facilitates aging effects. This aging effect results microstructural changes in this zone. Notably, similar microstructural changes in the HAZ were reported by McAndrew, et al. [106] in their review study of linear

friction welding of Ti-64. These observations underscore the complex interplay between temperature, cooling rate, and microstructural evolution in the HAZ of Ti64.

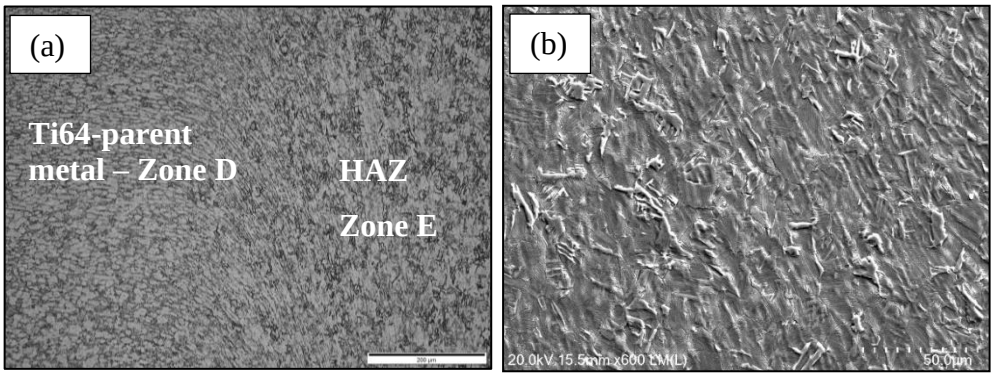

Figure 112: Microstructure of Zone E in the RFW joint between Ti-64 and Ti-1023 showing the evidence for formation lamellar α in the matrix (a) Optical image and (b) SEM image.

Microstructural characteristics of TMAZ of Ti-64 (Zone F)

Zone F exhibits a microstructure characterized by hexagonal α′ martensite and a secondary α (α_s) morphology grows from existing β grain boundaries, as depicted in Figure 113. This zone undergoes the combined effects of thermal and pressure, enabling significant dynamic recrystallization resulting from the heat generated by friction and the strain induced by forging pressure [106]. Studies, such as those conducted by Jedrasiak, et al. [105], have noted that Zone F experiences temperatures reaching 1000^{o}C during thermal modelling of linear friction welding, as illustrated in Figure 108. Importantly, this temperature surpasses the β-transus temperature of Ti-64 (refer to Figure 9), facilitating the transformation of primary α grains into β grains. Additionally, Zone F encounters substantial strains and strain rates, reaching up to 2500/sec during welding, leading to significant dynamic recrystallization of the high-temperature β-phase. The exposure to high temperatures, coupled with a rapid cooling rate of about 410°C/second, fosters the generation of α′ martensite and α morphology near the existing β grain boundary within Zone F. The volume fraction of this α morphology progressively nucleates with decreasing cooling rates along prior β boundaries, highlighting the intricate microstructural evolution within the zone. Studies, such as those conducted by

McAndrew, et al. [106] and Ahmed and Rack [108] have observed similar microstructural changes in TMAZ during linear friction welding of Ti-64.

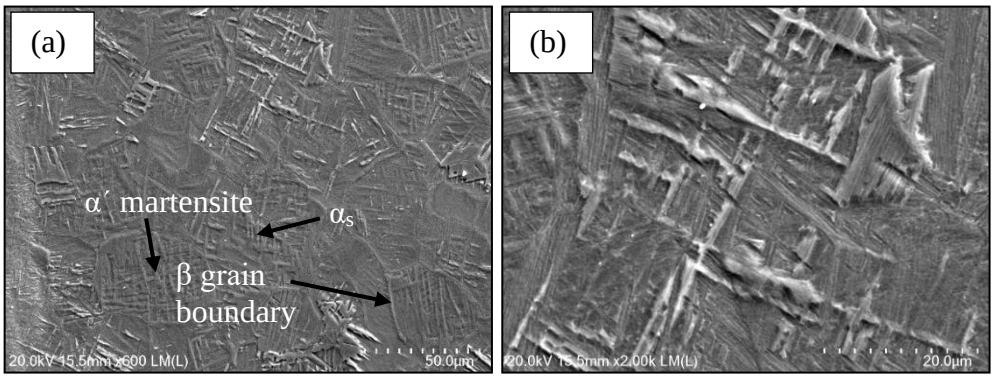

Figure 113: SEM image of the microstructure of Zone F showing the evidence for α′ martensite, well growth laths of α from β grain boundary in the RFW joint between Ti-64 and Ti-1023 at (a) low and (b) high magnification.

Microstructural characteristics of weld interface

The microstructure analysis of the weld interface in RFW joints between Ti-64 and Ti-1023 unveils a fascinating mixing zone. This zone exhibits a blend of Ti-64, characterized by α′ martensite and a secondary α (α_s) morphology grows from pre-existing β grain boundaries, and Ti-1023, which showcases α″ martensite and α_p grain boundaries blended with the β grain, as depicted in Figure 114. Within this metal mixing zone, distinct islands of Ti-64 and Ti-1023 are discernible. Notably, the diffusion of alloying elements between these phases in the solid state contributes significantly to the joint's enhanced strength. This phenomenon confirms findings from previous studies, such as those conducted by Boyat, et al. [109] exploring RFW joints between Ti-17 and Ti-6242. The welding interface undergoes severe plastic deformation [106] and intense heating during the welding process as depicted in Figure 108, leading to the formation of islands, and facilitating mixing, thereby establishing a robust interlock between the materials. The application of axial force resulting from the forge pressure induces excessive deformation, compelling the materials to intermix. Prior research has indicated that the angular velocity during the friction [93] prompts the softened metals to disperse from the centre. However, certain materials remain at the centre and blend with the opposing metal, resulting in the creation of an intermixing zone at the joint, as also evident in the present investigation.

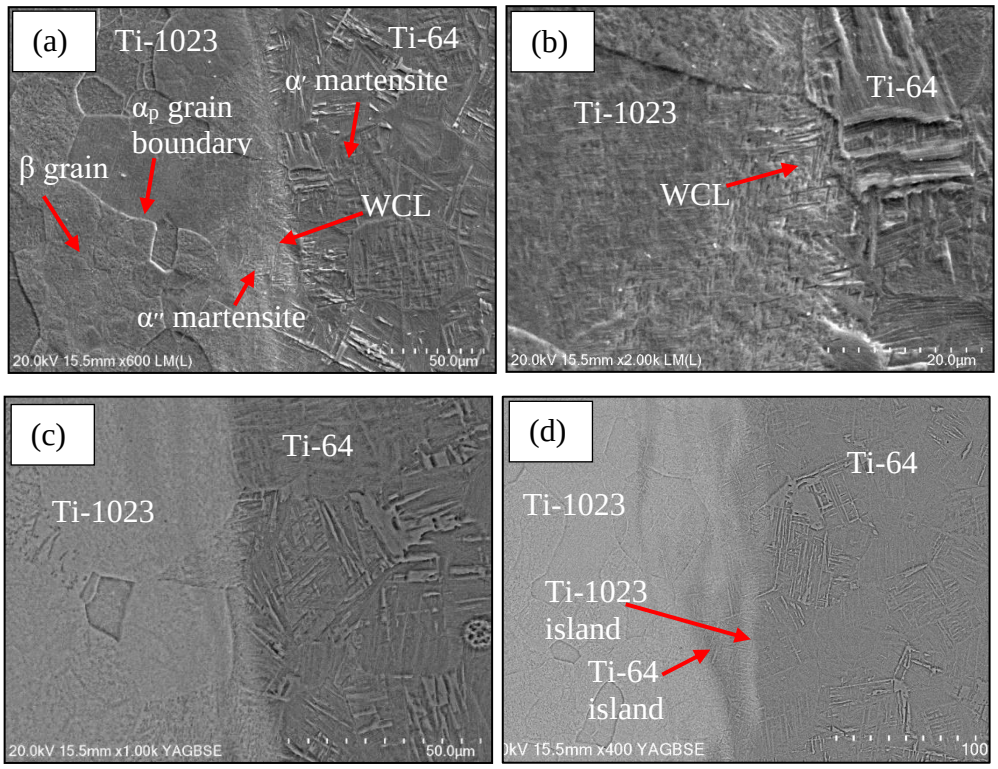

Figure 114: Images of the microstructure of the weld interface in the RFW joint between Ti-64 and Ti-1023 at (a) low, and (b) high magnification under SEM, and at (c) high, and (d) low magnification under back scattered electron mode.

An in-depth area analysis employing EDS technique is conducted across the weld interface, as illustrated in Figure 115. The EDS spectrum unveils the dominant elemental composition of the both Ti-64 and Ti-1023 base metal, featuring Ti, V, Al and Fe. Notably, the EDS analysis proves elemental diffusion occurring between Ti-64 and Ti-1023 within this interface region. The EDS examination elucidates the migration of vanadium and iron from Ti-1023 (Spectrum 29) to the Ti-64 Island (Spectrum 25), while conversely, Aluminium migrates from Ti-64 (Spectrum 30) to the Ti-1023 Island (Spectrum 28) forms at the weld interface, as depicted in Figure 116. This observation resonates with the findings reported by Chander, et al. [94], which documented the migration of Cr and Ni from AISI 304 to AISI 4140 SS within the welding zone. The occurrence of high shear forces and localized heating due to friction significantly contributes to elemental diffusion and metallurgical bonding between Ti-64 and Ti-1023, thereby culminating in the formation of a robust weld joint.

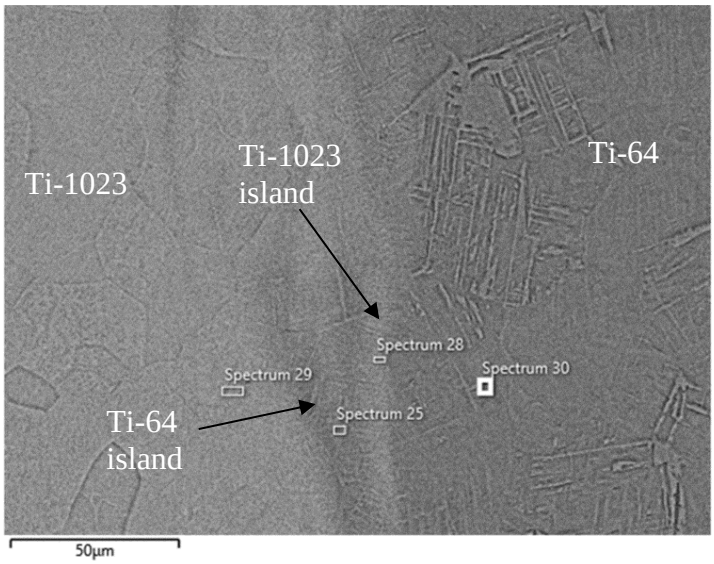

Figure 115: Back scattered electron mode image of the weld interface in the RFW joint showing four different areas used for the EDS analysis.

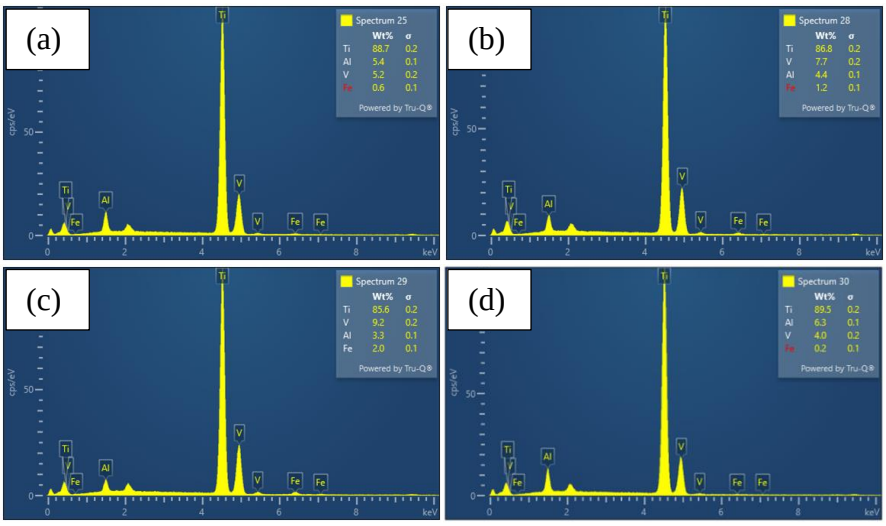

Figure 116: Results of the EDS area analysis conducted (a) at Ti-64 Island (Spectrum 25), (b) at Ti-1023 Island (Spectrum 28), (c) at Ti-1023 parent metal (Spectrum 29), and (d) at Ti-64 parent metal (Spectrum 30) of the RFW joint.

An enhanced line analysis employing the EDS technique is conducted across the weld interface of RFW joint between Ti-64 and Ti-1023, as illustrated in Figure 117. The EDS line analysis reveals significant variations in vanadium and aluminium concentrations across the weld, as detailed in Figure 118. In Ti-1023, the vanadium concentration is showing the highest levels before gradually decreasing within the Ti-64 Island. However, it shows another increase within the

Ti-1023 Island before declining once more within the Ti-64 region. Notably, the vanadium concentration within the Ti-64 Island exceeds that of the parent Ti-64, while it registers lower levels within the Ti-1023 Island compared to parent Ti-1023. These observations strongly support the inference of vanadium diffusion from Ti-1023 to the Ti-64 Island. Similar trends are observed in aluminium concentration, reinforcing the parallel phenomena observed for vanadium.

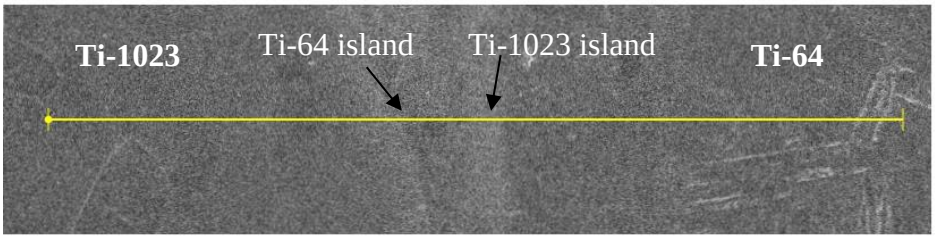

Figure 117: SEM image of the weld interface in the RFW joint between Ti-64 and Ti-1023 reflecting EDS line analysis.

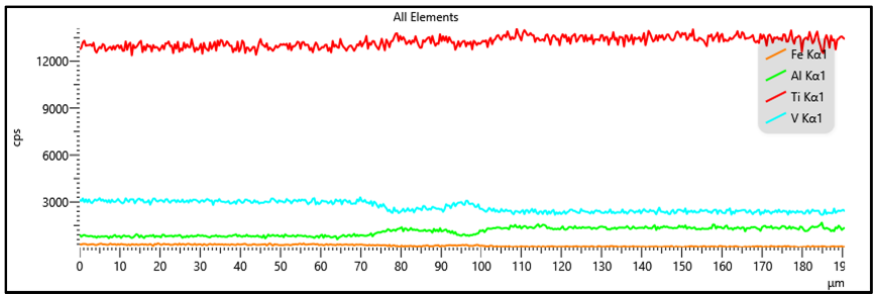

Figure 118: Results of the EDS line analysis across the weld interface in the RFW joint between Ti-64 and Ti-1023.

4.3.3 Hardness study

Hardness assessment is pivotal for understanding material mechanics, evaluating resistance to deformation, indentation, and wear, and providing insights into material performance and microstructural characteristics.

Figure 119 illustrates the variation in Vickers micro-indentation hardness test results across different zones of RFW weld joint between Ti-64 and Ti-1023. The average hardness of Zone A measures 281 HV1. This finding consistent with Vickers hardness test results of Ti-1023 ageing at 600°C and 650°C reported by Li, et al. [110]. Conversely, Zone D demonstrates average hardness values, with

measurements of 304 HV1, findings consistent with hardness test results of Ti-64 in annealed condition reported in ATI technical data sheet [111].

Zone B (i.e., the hardness indentation line at 1.6 mm from the WCL towards Ti-1023 side) exhibit an average hardness of 321 HV1. The distinct variation in hardness between Zone A and Zone B is attributed to changes in microstructural phases. Zone B is characterized by the precipitation of the secondary alpha (α_s) phase and the transformation of the primary alpha (α_p) from globular to elongated as depicted in Figure 109. Similar findings were observed by Leyens and Peters [34] .

Zone C (i.e., the hardness indentation line at 0.6 mm from WCL towards Ti-1023 side) exhibit an average hardness of 338 HV1. In compared to Zona A and B, this hardness is much higher. This is due to the formation of stress induced α″ martensite phase as illustrated in Figure 110. Haghighi, et al. [112] reported an increase in microhardness after precipitation of the α″ martensite in β titanium alloys.

Conversely, Zone E, the hardness indentation line situates 1.6 mm from the WCL towards the Ti-64 side, exhibits an average hardness of 318 HV1. This is attributed to the redistribution of β grain boundaries within the α matrix and the formation of elongated grains, as depicted in Figure 112.

Zone F (i.e. the hardness indentation line at 0.6 mm from WCL towards Ti-64 side) exhibits an average hardness of 321 HV1, comparatively higher than Zone D. This is due to the formation of α′ martensitic structure in Zone F as shown in Figure 113. The similar hardness incremental trend was observed by Utama, et al. [104] in their study.

WCL of RFW joint shows an average hardness of 342HV1 due to presence of blend of Ti-64, characterized by α′ martensite and a secondary α (α_s) morphology grows from pre-existing β grain boundaries, and Ti-1023, which showcases α″ martensite and α_p grain boundaries blended with the β grain as displayed in Figure 114.

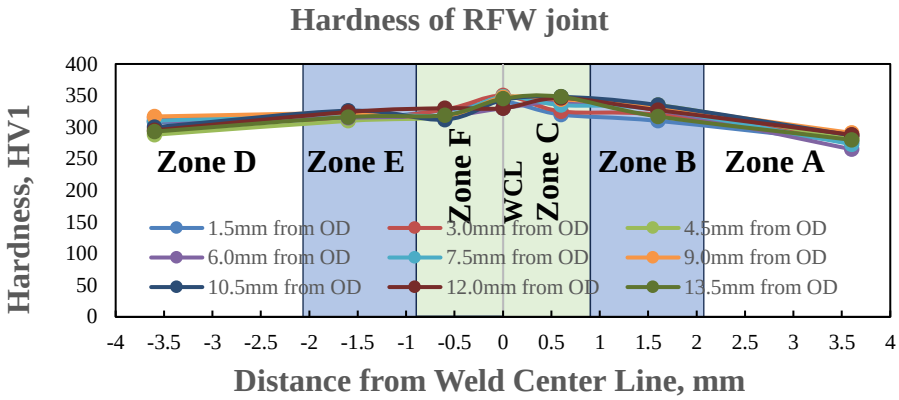

Figure 119: Graphical presentation of the result from the micro-hardness analysis showing on the variation in the hardness values across different zones associated with the RFW joint between Ti-64 and Ti-1023.

4.3.4 Tensile behaviour

Tensile properties refer to the behaviour of materials under tensile loading, revealing their ability to withstand the tensile forces before experiencing deformation or failure.

The tensile test results obtained from the RFW dissimilar welded joint between Ti-64 and Ti-1023 at room temperature are summarized in Table 15. Remarkably, the average ultimate tensile strength of the RFW joint is an impressive, measuring 826 MPa, almost matching that of the Ti-64 parent metal (828 MPa) [87] but slightly lower than the UTS of the Ti-1023 parent metal (965 MPa) [88]. Moreover, the average yield strength (YS) of the RFW joint (792 MPa) surpasses that of the Ti-64 parent metal (759 MPa) [87] but falls short of the YS of the Ti-1023 parent metal (896 MPa) [88]. This observation underscores the superior quality of the weld joint, as its strength outperforms that of any one parent metal. Additionally, the average elongation of the RFW joint is notably impressive (7%) as depicted in Figure 120, slightly lower than that of Ti-64 (10%) but surpassing the elongation of Ti-1023 (6%) [87]. This phenomenon arises from the establishment of a robust weld joint facilitated by elemental diffusion, which fosters metallurgical bonding between Ti-64 and Ti-1023. Notably, each tensile specimen exhibits varying strain to failure due to differences in their cross-sectional areas. It is observed that specimens with larger cross-sectional areas tend to manifest comparatively higher strain at failure.

Similar conclusions were drawn by Kumar, et al. [98] in their study assessing tensile properties through the utilization of miniature tensile specimens.

Table 15: Summary of tensile properties of RFW joint between Ti-64 and Ti-1023.

Specimen ID	$YS_{0.2\%}$	UTS	Young's Modulus	Strain at Fracture	True UTS	Strain Hardening Exponent	Strength coefficient
	(MPa)	(MPa)	(GPa)		(MPa)		(MPa)
RFW Specimen 1	808	833	87.991	0.054	854	0.275	2226
RFW Specimen 2	802	841	95.013	0.071	867	0.298	2362
RFW Specimen 3	766	804	88.867	0.085	831	0.219	1622
Average of RFW	**792**	**826**	**90.624**	**0.070**	**851**	**0.264**	**2070**

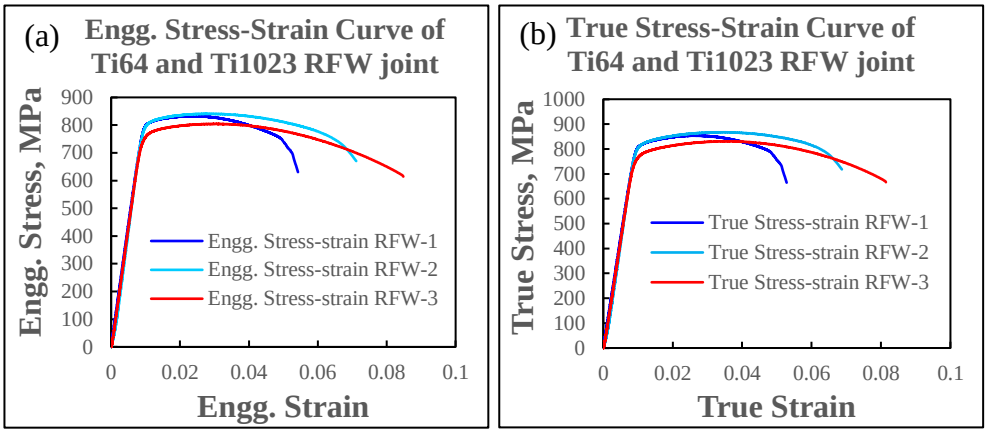

Figure 120: (a) Engineering and (b) true stress strain curve of RFW joint between Ti-64 and Ti-1023.

Fracture behaviour of tensile specimen: The failure analysis of all cross-weld tensile specimens of weld joints reveal that fractures predominantly occur on the Ti-1023 parent metal side. This incidence is attributed to the lower ductility of Ti-1023 (6%) compared to Ti-64 (10%). The fracture surfaces of broken tensile specimen of the RFW joints reveal ductile failure characteristics. These characteristics include the presence of cup and cone features with shear lips as illustrates in Figure 121.

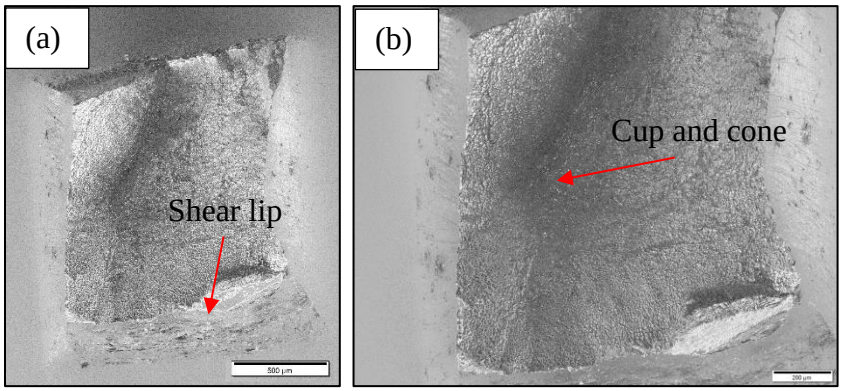

Figure 121: Optical microscopy image of the fracture surface at (a) low magnification and, (b) at high magnification of tensile specimen RFW-1.

4.4 High cycle fatigue

Results of HCF tests enhance our understanding of material behaviour under cyclic loading conditions. Through meticulous experimentation and analysis, it is aimed to elucidate the fatigue limit and endurance characteristics of the tested materials. Incorporation high-cycle fatigue test results contribute valuable insights into the mechanical performance and durability of the materials under consideration.

Determining the fatigue limit in HCF tests involves subjecting a material specimen to cyclic loading under controlled load or stress conditions. Typically, the test specimen undergoes progressively increasing cyclic stress amplitudes until failure occurs. For high cycle fatigue tests, the maximum number of cycles is typically restricted to 10^7 to determine the fatigue limit.

The selection of initial stress levels is pivotal. These levels are meticulously chosen by considering the minimum fatigue limit of either parent metal, which ranges from 450 to 500 MPa for Ti-64 [113] in this case. The testing sequence begins with loading the first specimen at a maximum stress of 500 MPa under cyclic loading, monitoring its performance up to 10^7 cycles. If the specimen remains intact, subsequent tests are conducted at 50 MPa increments until failure occurs within the 10^7-cycle limit. Each stress amplitude and its corresponding number of cycles to failure are recorded, forming an S-N curve (stress versus number of cycles) for the material.

After testing at 500 MPa, another specimen is loaded at 550 MPa, and it remains intact. Finally, the first specimen to fail under 10^7 cycles is the one loaded at a

maximum stress of 600 MPa. To confirm the fatigue limit, a repeatability test is conducted at a maximum stress of 550 MPa, extended up to 1.2 x 10^7 cycles and found the specimen remaining intact.

Upon completing the test, the fatigue life curve, or S-N curve, is formed, as illustrated in Figure 122. The fatigue limit, also known as the endurance limit, is then determined as the stress amplitude below which the material can endure an infinite number of cycles (i.e. 10^7) without failure. This is typically identified by analysing the S-N curve, where a horizontal plateau region emerges, indicating a constant stress amplitude corresponding to infinite fatigue life.

From Figure 122, the fatigue limit of the RFW joint between Ti-64 and Ti-1023 is identified as 550 MPa. This value surpasses the fatigue strength of the Ti-64 parent metal (450 - 500 MPa) as recorded by Janeček, et al. [113] but falls short of the fatigue strength of Ti-1023 (700 - 800 MPa) [88]. Understanding this fatigue limit is crucial for designing components subjected to cyclic loading, ensuring their reliability and longevity in service.

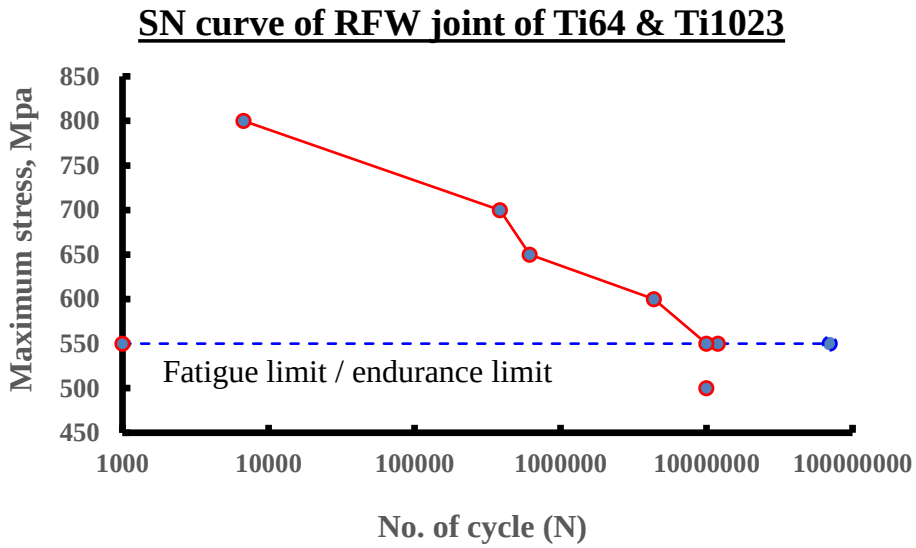

Figure 122: S-N curve of RFW joint between Ti-64 and Ti-1023

4.4.1 Fractography study

Failure of the fatigue specimens of dissimilar weld between Ti-64 and Ti-1023 occurs exclusively in the parent metal. However, in case of the HCF test conducted at the higher maximum stress (i.e. 800 MPa), fracture occurs on the Ti-1023 side,

while, in the lower maximum stress regime (i.e. 600 MPa), it is on the Ti-64 side. The failure occurs at roughly 3 ± 1 mm away from the weld centre line for both the stress conditions. Similar observation was noticed by Rajan, et al. [10] in their study.

For the analysis of the fracture surface of the broken fatigue specimen, only two specimens are chosen out of all tested samples: one subjected to a maximum load of 800 MPa and another to a maximum load of 600 MPa.

HCF specimen subjected to 800 MPa: Figure 123 depicts the fracture surface of the broken HCF specimen, tested at a maximum load of 800 MPa. The fracture surface examination reveals that the crack initiation point is at the surface of the Ti-1023 side of the specimen, as indicated in Figure 123 (a). Subsequently, the crack propagates rapidly through a small crack propagation area characterized by coarse striation marks as illustrated in Figure 123 (b). Eventually, the specimen fails under tensile overloading conditions, as evidenced by the presence of dimples (micro voids) in the high-magnification image of the fracture surface in Figure 123 (c). Evidence of dimples justifies ductile failure. Despite Ti-1023 possessing a higher fatigue limit compared to Ti-64, fatigue failure still occurs on the Ti-1023 side. This occurrence is attributed to tensile failure. At higher stress levels (800 MPa), tensile loading conditions become dominant over dynamic loading conditions. Since Ti-1023 exhibits lower ductility compared to Ti-64, failure manifests on the Ti-1023 side under tensile loading. Furthermore, the HAZ of Ti-1023 exhibits elongated primary alpha and secondary alpha deposition within beta grains, as depicted in Figure 109. The presence of these phases contributes to a further reduction in the ductility of Ti-1023. Consequently, crack initiation occurs at the HAZ of Ti-1023, leading to specimen failure under tensile loading conditions. Similar phenomena were observed by Rajan, et al. [10] in their study of HCF and LCF test of dissimilar weld between Ti-64 and Ti-6242.

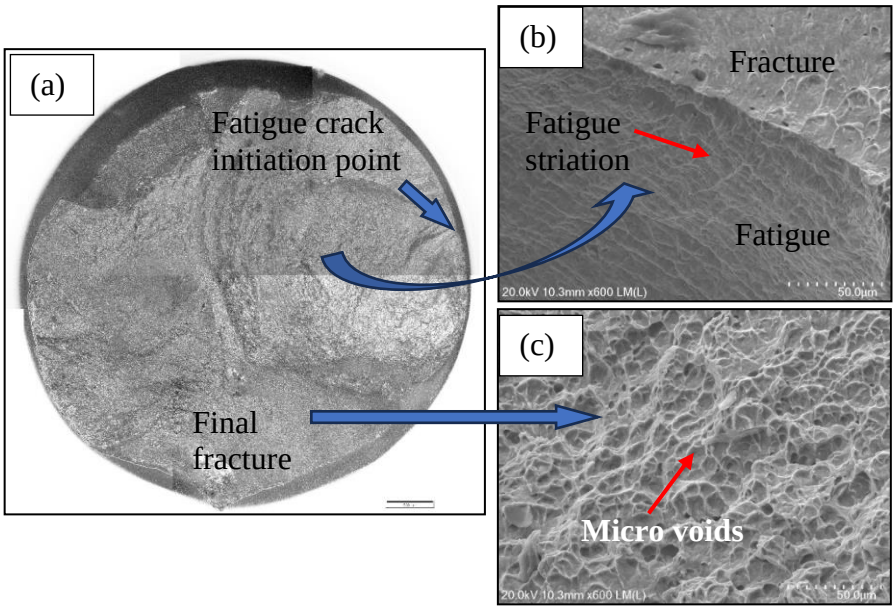

Figure 123: (a) Optical image shows the complete failure surface, (b) SEM image of crack propagation and (c) SEM image of final failure of HCF specimen 4/3 of the RFW joint between Ti-64 and Ti-1023, loaded at max. stress 800 MPa.

Crack path study discloses that crack propagates through transgranular path in both fatigue crack propagation and final fracture as illustrated in Figure 124.

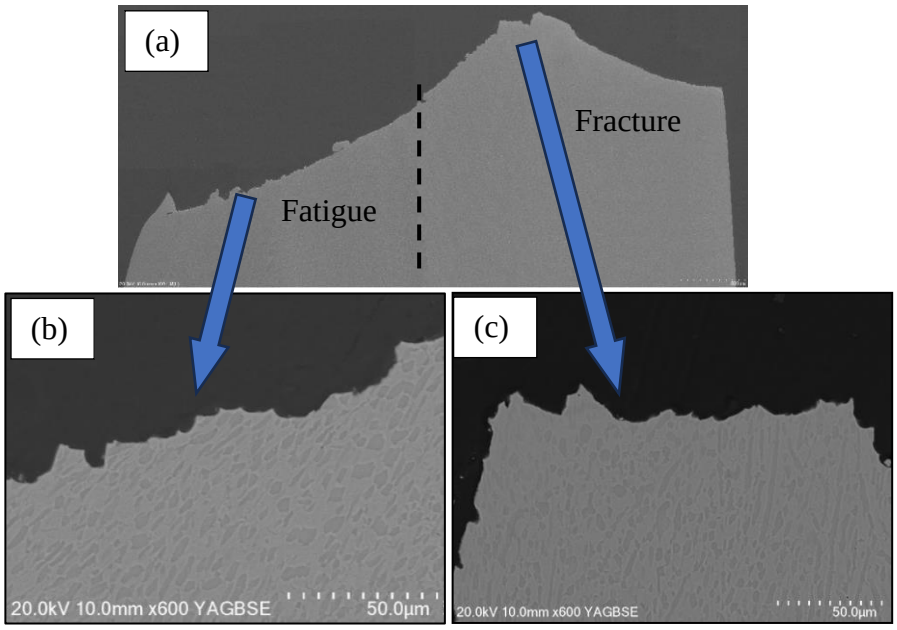

Figure 124: (a) SEM image shows the complete crack path, and back scattered electron image shows (b) the crack path in fatigue crack propagation zone and (c) the crack path in final fracture zone of HCF specimen 4/3 of RFW joint between Ti-64 and Ti-1023, loaded at max. stress 800 MPa.

HCF specimen subjected to 600 MPa: The fracture surface of the broken HCF specimen, tested at a maximum load of 600 MPa, is depicted in Figure 125. Upon examination, it is observed that the crack initiation point resides at the surface of the Ti-64 side of the specimen, as depicted in Figure 125 (a). Subsequently, the crack propagates slowly through a wide crack propagation area characterized by quasi-cleavage facets, accompanied by very fine fatigue striations, as illustrated in Figure 125 (b). Ultimately, the specimen fails under tensile loading conditions, evidenced by the presence of dimples (micro voids) in the high-magnification image of the fracture surface in Figure 125 (c). The dominant governing factor of the failure is attributed to the crack propagation region, as depicted in Figure 125 (a). The presence of dimples justifies ductile failure. As Ti-64 possesses a lower fatigue limit compared to Ti-1023, fatigue failure occurs on the Ti-64 side. This occurrence is attributed to fatigue failure, as the applied stress levels (600 MPa) surpass the fatigue limit of Ti-64. The specimen is exposed to a high number of fatigue cycles, indicating dynamic loading conditions prevailing over tensile loading. Consequently, crack initiation occurs at the Ti-64 side, leading to specimen failure under dynamic loading conditions. These findings are consistent with similar observations made by Rajan, et al. [10] in their study on fatigue behaviour of dissimilar weld between Ti-64 and Ti-6242.

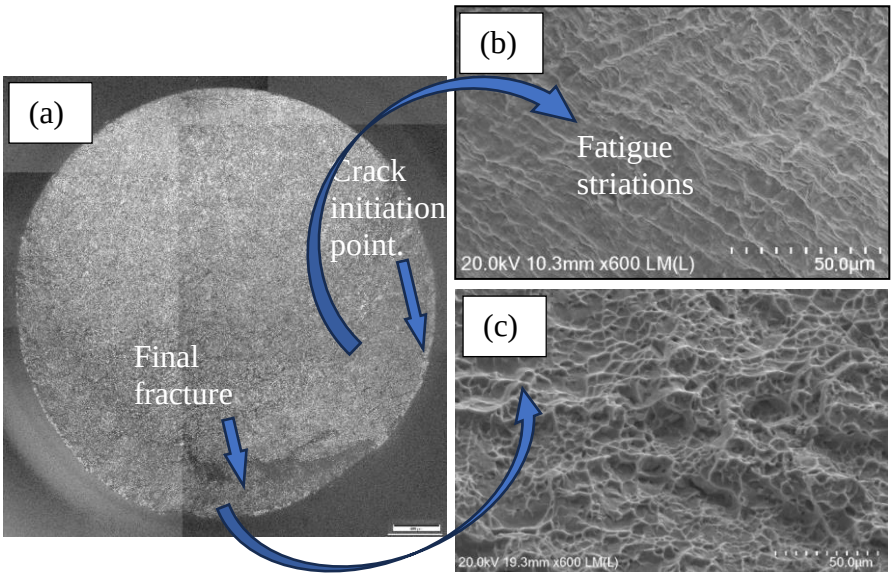

Figure 125: (a) Optical image shows the complete failure surface, (b) SEM image of fatigue surface of the crack propagation and (c) SEM image of the fracture surface of final failure of HCF specimen -3/3 of RFW joint between Ti-64 and Ti-1023, loaded at max. stress 600 MPa.

Crack path study discloses that crack propagates through transgranular path in both fatigue crack propagation and final fracture as illustrated in Figure 126.

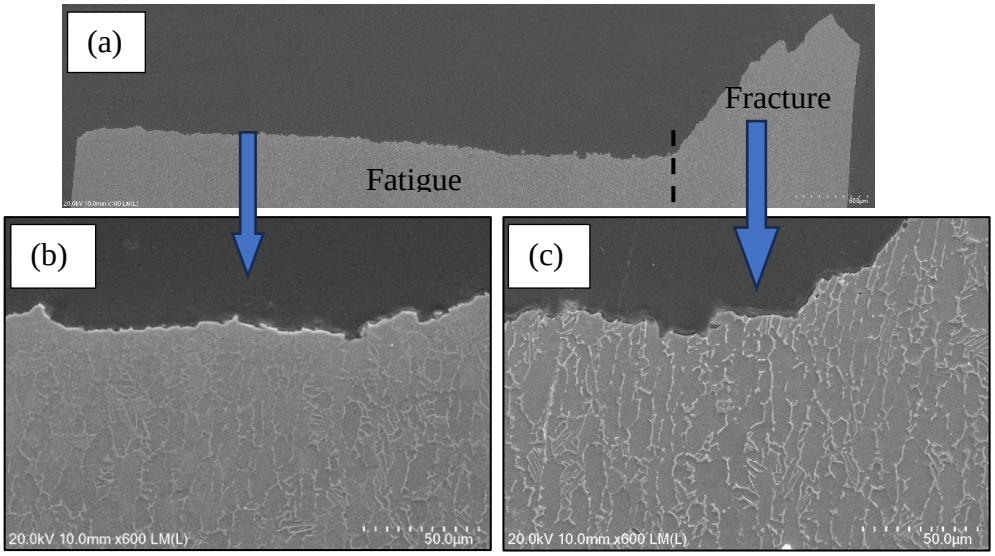

Figure 126: (a) SEM image shows the complete crack path, and back scattered electron image shows (b) the crack path in fatigue crack propagation zone and (c) the crack path in final fracture zone of HCF specimen 3/3 of RFW joint between Ti-64 and Ti-1023, loaded at max. stress 600 MPa.

Chapter 5

5 Conclusions and Future work

The current study is designed to delve into two crucial areas. Firstly, it aims to investigate the influence of welding process parameters on both the microstructural characteristics and mechanical properties, particularly fracture toughness, to establish a durable dissimilar welding connection between S355J2 and SS316L using RFW process. Simultaneously a comparative analysis with a dissimilar weld produced using the TIG welding process enriches the study, providing valuable insights into the efficacy of different welding methods. Secondly, the study endeavours to examine the effects of welding process parameters on microstructural characteristics and mechanical properties, specifically fatigue, to fabricate a robust dissimilar welding bond between Ti-64 and Ti-1023 alloys, employing the RFW process.

The key findings of this study, which are computed below, are expected to shed light on optimizing welding parameters, enhancing the understanding of dissimilar welding processes, and advancing the reliability and performance of welded joints across diverse industrial applications.

5.1 Key findings on dissimilar weld between S355J2 and SS 316L

Microstructure: The compositional gradient between S355J2 and SS316L induces significant microstructural variations in both welding processes. In RFW, bainite and austenite microstructures are prominent at the WCL, accompanied by S355J2 and SS316L islands. Additionally, bainite forms in the TMAZ, while ferrite-pearlite structures emerge in the HAZ of S355J2, with austenite prevailing in SS316L. Conversely, the TIG weld exhibits chromium carbide precipitation, delta ferrite in the WM, hard martensite in the S355J2 HAZ, carbon diffusion from the S355J2 HAZ to the WM, and without distinct microstructural changes on the SS316L side. The high welding interpass temperature is implicated in these microstructural alterations in TIG welding.

Hardness: In addition to microstructural variations, noticeable changes in hardness are observed across the weld. In RFW, the highest hardness of 208 HV1 is found in the TMAZ of S355J2, with 206 HV1 at the WCL. Conversely, in the TIG weld, the WCL exhibits the highest hardness of 419 HV1 due to chromium carbide

precipitation, while the HAZ of S355J2 displays a hardness of 284 HV1 attributed to martensite formation, and the HAZ of SS316L shows a hardness of 172 HV1.

Tensile properties: Both welds demonstrate superior tensile properties, including UTS and YS, compared to the parent metal. In the RFW weld, UTS reaches 540 MPa, with an YS of 367 MPa, while the TIG weld exhibits UTS of 526 MPa and YS of 300 MPa. Tensile failures predominantly occur on the S355J2 side, displaying a ductile feature. Furthermore, the RFW weld exhibits enhanced elongation at 21%, surpassing the TIG weld's 16%. These findings underscore the robust mechanical performance of the welds.

Fracture toughness: Both welds exhibit nearly identical K_Q values, closely matching those of the parent metal. The RFW-WCL displays a K_Q value of 40.9 MPa√m, while the TIG-WCL shows a slightly higher value of 42.1 MPa√m. However, these K_Q values do not qualify as K_{1C} due to specimen size limitations. Regarding CTOD, the RFW-WCL demonstrates superior performance with a CTOD of 0.35 mm compared to the TIG-WCL's 0.31 mm. Notably, the HAZ of S355J2 in the TIG weld exhibits the lowest CTOD of 0.31 mm. These findings underscore the importance of CTOD in evaluating weld integrity and fracture toughness.

Fractography: All specimens exhibit ductile failure characterized by the presence of micro voids and void coalescence, except for the TIG WCL, which displays cleavage fracture featuring a flat shiny surface without void coalescence.

Based on the findings of the current study, it can be concluded that the RFW process outperforms the TIG process in the preparation of dissimilar weld joints between S355J2 and SS316L.

5.2 Key findings on dissimilar weld between Ti-64 and Ti-1023

Microstructure: The compositional gradient between Ti-64 and Ti-1023 significantly influences microstructural variations during the RFW process. At the WCL, α′ martensite, α″ martensite, and the growth of secondary alpha (α_s) inside β grains, alongside primary alpha (α_p) at grain boundaries, are notable, with Ti-64 and Ti-1023 islands. Moreover, α′ martensite forms in the TMAZ of Ti-64, α″ martensite in the TMAZ of Ti-1023, while secondary alpha (α_s) and elongated primary alpha (α_p) emerge in the HAZ of Ti-1023, and redistributed α-β structure

prevails in HAZ of Ti-64, attributed to temperature rise from friction and forging pressure during RFW.

Hardness: Alongside microstructural variations, significant changes in hardness manifest across the weld. The highest hardness of 342 HV1 occurs at the WCL, gradually diminishing on either side of the weld. Notable values include 321 HV1 in the TMAZ of Ti-64, 338 HV1 in the TMAZ of Ti-1023, 318 HV1 in the HAZ of Ti-64, and 328 HV1 in the HAZ of Ti-1023. The elevated hardness at the WCL and TMAZ regions can be attributed to α' and α'' martensite formation and the growth of secondary alpha (α_s) phases.

Tensile properties: The RFW weld exhibits remarkable tensile properties, surpassing those of the parent metal. With a UTS of 826 MPa and an YS of 792 MPa, the weld showcases superior strength. Tensile failures primarily manifest on the Ti-1023 side, demonstrating ductile characteristics. Moreover, the weld displays an enhanced elongation of 7%, emphasizing its robust mechanical performance.

Fatigue strength: The HCF test, conducted at a frequency of 40 Hz with an R value of 0.1, reveals a fatigue strength of the weld is 550 MPa, surpassing that of the Ti-64 parent metal. This result highlights the robust integrity of the weld, affirming its exceptional performance under cyclic loading conditions.

Fractography: In all specimens, crack initiation points occur at the surface. Those tested under higher stress display a narrow crack propagation area characterized by coarse fatigue striation marks, indicating dominant tensile overloading. Conversely, specimens tested under lower stress reveal a wider crack propagation area with quasi-cleavage facets and very fine fatigue striations. These distinctions highlight the varying fracture characteristics under different stress levels, offering insights into fatigue behaviour.

The findings of the current study firmly establish that the RFW process yields a robust weld joint between Ti-64 and Ti-1023.

5.3 Future works

While the current project effectively achieves its objectives, acknowledging the limitations encountered during its execution opens avenues for further exploration to bolster the validity of test results. Additionally, the findings of this project pave the way for diverse directions of future research. By considering these limitations

and cultivating confidence in industrial applications, forthcoming studies can delve into untapped areas for deeper understanding and broader applicability.

(i) Find out plane-strain fracture toughness properties of dissimilar RFW joints between S355J2 and SS316L for application in engineering design.

(ii) Explore HCF and LCF properties of dissimilar RFW joints between S355J2 and SS316L.

(iii) Characterize stress corrosion cracking properties of dissimilar RFW joints between S355J2 and SS316L. It helps to use this welding process in manufacturing various components that are intended to be used in sour environment.

(iv) Explore high temperature tensile properties or creep resistance properties of RFW joints between S355J2 and SS316L.

(v) Current project scope of work can be repeated on the post weld heat treated (PWHT) RFW joints between Ti-64 and Ti-1023.

(vi) Find out plane-strain fracture toughness properties of dissimilar RFW joints between Ti-64 and Ti-1023.

(vii) Characterise corrosion properties of dissimilar RFW joints between Ti-64 and Ti-1023.

6 References

[1] D. H. Phillips, *Welding Engineering An Introduction*, 2016 ed. United Kingdom: John Wiley & Sons, Ltd (in English), 2016, p. 275.

[2] C. Weisman and W. Kearns, *Welding Handbook: Metals and their weldability*. American Welding Society, 1976.

[3] P. Kah, M. Shrestha, and J. Martikainen, "Trends in joining dissimilar metals by welding," *Applied Mechanics and Materials,* vol. 440, pp. 269-276, 2014.

[4] S. Yang, J. Zhang, J. Lian, and Y. Lei, "Welding of aluminum alloy to zinc coated steel by cold metal transfer," *Materials & Design,* vol. 49, pp. 602-612, 2013.

[5] Y. Kusuda, "Honda develops robotized FSW technology to weld steel and aluminum and applied it to a mass-production vehicle," *Industrial Robot: An International Journal,* vol. 40, no. 3, pp. 208-212, 2013.

[6] V. Patel, S. Bhole, and D. Chen, "Improving weld strength of magnesium to aluminium dissimilar joints via tin interlayer during ultrasonic spot welding," *Science and Technology of Welding and Joining,* vol. 17, no. 5, pp. 342-347, 2012.

[7] C. Thomy and F. Vollertsen, "Laser-MIG hybrid welding of aluminium to steel—effect of process parameters on joint properties," *Welding in the World,* vol. 56, pp. 124-132, 2012.

[8] H. Hanninen *et al.*, "Dissimilar metal weld joints and their performance in nuclear power plant and oil refinery conditions," *VTT TIEDOTTEITA,* vol. 2347, p. 208, 2006.

[9] H. Wang, G. Wang, F. Xuan, and S. Tu, "Fracture mechanism of a dissimilar metal welded joint in nuclear power plant," *Engineering Failure Analysis,* vol. 28, pp. 134-148, 2013.

[10] S. Rajan, P. Wanjara, J. Gholipour, and A. S. Kabir, "Fatigue behavior of linear friction welded Ti-6Al-4V and Ti-6Al-2Sn-4Zr-2Mo-0.1 Si dissimilar welds," *Materials,* vol. 14, no. 11, p. 3136, 2021.

[11] *ASM Handbook, Volume 1, Properties and Selection: Irons, Steels, and High Performance Alloys*, 2005.

[12] V. Igwemezie, P. Dirisu, and A. Mehmanparast, "Critical assessment of the fatigue crack growth rate sensitivity to material microstructure in ferrite-pearlite steels in air and marine environment," *Materials Science and Engineering: A,* vol. 754, pp. 750-765, 2019.

[13] *Hot rolled products of structural steels - Part 2,* EN 10025-2: 2019, 31 August 2019 2019.

[14] "STEEL NAVIGATOR – find the right steel for your needs." Ovako. https://steelnavigator.ovako.com/ (accessed.

[15] F. Bozkurt and E. Schmidová, "Fracture toughness evaluation of S355 steel using circumferentially notched round bars," *Periodica Polytechnica Transportation Engineering,* vol. 47, no. 2, pp. 91-95, 2019.

[16] R.-b. Song, J.-y. Xiang, and D.-p. Hou, "Characteristics of mechanical properties and microstructure for 316L austenitic stainless steel," *Journal of iron and steel research international,* vol. 18, no. 11, pp. 53-59, 2011.

[17] M. Nastac and R. L. A. Klein, "Microstructure and mechanical properties comparison of 316L parts produced by different additive manufacturing processes," in *2017 International Solid Freeform Fabrication Symposium*, 2017: University of Texas at Austin.

[18] *ASTM A312/A312M-22a-Standard Specification for Seamless, Welded, and Heavily Cold Worked Austenitic Stainless Steel Pipes*, ASTM A312/A312M-22a, ASTM, 2022.
[19] "Stainless steel grade 316." AZO Materials. https://www.azom.com/properties.aspx?ArticleID=863 (accessed.
[20] N. T. Le, K. M. Pham, H. M. Le, and N. D. Nguyen, "The relationship between continuous cooling rate and microstructure in the heat affected zone (HAZ) of the dissimilar weld between carbon steel and austenitic stainless steel," *Acta Metallurgica Slovaca,* vol. 23, no. 4, pp. 363-370, 2017.
[21] M. Hathesh, "A Review on Welding Related Problems and Remedy of Austenitic Stainless Steels," *International Research Journal of Engineering and Technology (IRJET),* 2020.
[22] B.-S. Huang, J. Yang, D.-H. Lu, and W.-J. Bin, "Study on the microstructure, mechanical properties and corrosion behaviour of S355JR/316L dissimilar welded joint prepared by gas tungsten arc welding multi-pass welding process," *Science and Technology of Welding and Joining,* vol. 21, no. 5, pp. 381-388, 2016.
[23] H. Lalvani, P. Mandal, A. Yaghi, P. Santos, and B. Baufeld, "A solid-state joining approach to manufacture of transition joints for high integrity applications," *Journal of Manufacturing Processes,* vol. 73, pp. 90-111, 2022.
[24] G. Lütjering, J. Williams, and A. Gysler, "Microstructure and mechanical properties of titanium alloys," in *Microstructure And Properties Of Materials: (Volume 2)*, 2000, pp. 1-77.
[25] M. J. Donachie, *Titanium: A Technical Guide, 2nd Edition*. ASM International, 2000.
[26] K. Moussaoui, M. Mousseigne, J. Senatore, R. Chieragatti, and P. Lamesle, "Influence of milling on the fatigue lifetime of a Ti6Al4V titanium alloy," *Metals,* vol. 5, no. 3, pp. 1148-1162, 2015.
[27] S. Liu and Y. C. Shin, "Additive manufacturing of Ti6Al4V alloy: A review," *Materials & Design,* vol. 164, p. 107552, 2019.
[28] "MatWeb-Material Property Data." https://www.matweb.com/search/DataSheet.aspx?MatGUID=10d463eb3d3d4ff48fc57e0ad1037434 (accessed.
[29] C. Veiga, J. P. Davim, and A. Loureiro, "Properties and applications of titanium alloys: a brief review," *Rev. Adv. Mater. Sci,* vol. 32, no. 2, pp. 133-148, 2012.
[30] J. D. Cotton *et al.*, "State of the art in beta titanium alloys for airframe applications," *Jom,* vol. 67, no. 6, pp. 1281-1303, 2015.
[31] L. Xu, "Metastable beta titanium alloys: tuning the beta phase stability and low-temperature martensitic transformation of metastable beta titanium alloys," 2015.
[32] A. Chamanfar, M.-F. Huang, T. Pasang, M. Tsukamoto, and W. Z. Misiolek, "Microstructure and mechanical properties of laser welded Ti–10V–2Fe–3Al (Ti1023) titanium alloy," *Journal of Materials Research and Technology,* vol. 9, no. 4, pp. 7721-7731, 2020.
[33] G. Srinivasu, Y. Natraj, A. Bhattacharjee, T. Nandy, and G. N. Rao, "Tensile and fracture toughness of high strength β Titanium alloy, Ti–10V–2Fe–3Al, as a function of rolling and solution treatment temperatures," *Materials & Design,* vol. 47, pp. 323-330, 2013.

[34] C. Leyens and M. Peters, *Titanium and titanium alloys: fundamentals and applications*. Wiley Online Library, 2006.
[35] E. Dalgaard, P. Wanjara, J. Gholipour, X. Cao, and J. Jonas, "Linear friction welding of a near-β titanium alloy," *Acta Materialia*, vol. 60, no. 2, pp. 770-780, 2012.
[36] C. Mukundhan, P. Sivaraj, V. Balasubramanian, T. Sonar, V. Petley, and S. Verma, "Effect of friction pressure on microstructure and tensile properties of linear friction welded Ti–6Al–4V alloy joints," *International Journal of Lightweight Materials and Manufacture*, vol. 6, no. 4, pp. 483-493, 2023.
[37] A. I. H. Committee, *ASM Handbook Vol 6 - Welding, Brazing and Soldering* (no. v. 6). ASM International, 1990.
[38] F. Elshawesh and A. Elhoud, "Role of heat tint on pitting corrosion of 304 austenitic stainless steel in chloride environment," 2004.
[39] A. W. Society, *AWS D18.2:2020, Guide to Weld Discoloration Levels on Inside of Austenitic Stainless Steel Tube*. American Welding Society, 2020.
[40] F. C. Campbell, *Fatigue and fracture: understanding the basics*. ASM International, 2012.
[41] C.-J. Li, "Effects of temperature and loading rate on fracture toughness of structural steels," *Materials & Design*, vol. 21, no. 1, pp. 27-30, 1999.
[42] M. Srinivas and S. Kamat, "Effect of strain rate on fracture toughness of mild steel," *Materials science and technology*, vol. 17, no. 5, pp. 529-535, 2001.
[43] C. Wiesner and H. MacGillivray, "Loading rate effects on tensile properties and fracture toughness of steel," in *Fracture, Plastic Flow and Structural Integrity in the Nuclear Industry*: CRC Press, 2019, pp. 149-174.
[44] W. J. Mills, *Fracture toughness of stainless steel welds*. ASTM International, 1988.
[45] K. Samuel, O. Gossmann, and H. Huthmann, "Temperature dependence of fracture toughness (J–R-curves) of a modified type 316L austenitic stainless steel," *International journal of pressure vessels and piping*, vol. 41, no. 1, pp. 59-74, 1990.
[46] S. Ghosh *et al.*, "Deterioration in fracture toughness of 304LN austenitic stainless steel due to sensitization," *Metallurgical and materials transactions A*, vol. 40, pp. 2938-2949, 2009.
[47] S. Kumar, R. P. Kale, P. K. Singh, M. Ghosh, and J. Chattopadhyay, "Fracture toughness behavior of dissimilar metal (SA508 Gr. 3 Class 1 and SA312 Type 304LN) weld joint: With and without stress relieving treatment," *Fatigue & Fracture of Engineering Materials & Structures*, vol. 44, no. 9, pp. 2462-2474, 2021.
[48] G. E. Dieter, *Mechanical Metallurgy*, SI Metric Edition ed. UK: McGraw-Hill Book Company, 1988.
[49] Y.-L. Lee, *Fatigue testing and analysis: theory and practice*. Butterworth-Heinemann, 2005.
[50] S. Wang, J. Liu, and D. Chen, "Strain-controlled fatigue properties of dissimilar welded joints between Ti–6Al–4V and Ti17 alloys," *Materials & Design*, vol. 49, pp. 716-727, 2013.
[51] J. Yang, J. Li, J. Xiong, J. Liao, and F. Jin, "Effect of welding parameters on microstructure characteristics and fatigue properties of dissimilar joints prepared by linear friction welding on TC11 and TC17 titanium alloys," *Welding in the World*, vol. 64, pp. 683-695, 2020.
[52] G. Wen, T. Ma, W. Li, S. Wang, H. Guo, and D. Chen, "Strain-controlled fatigue properties of linear friction welded dissimilar joints between Ti–

6Al–4V and Ti–6.5 Al–3.5 Mo–1.5 Zr–0.3 Si alloys," *Materials Science and Engineering: A*, vol. 612, pp. 80-88, 2014.
[53] W. Li, A. Vairis, M. Preuss, and T. Ma, "Linear and rotary friction welding review," *International Materials Reviews*, vol. 61, no. 2, pp. 71-100, 2016.
[54] W. contributors, "Rotary friction welding," in *Rotary friction welding*, ed: Wikipedia, The Free Encyclopedia., Retrieved 03:18, May 28, 2023.
[55] S. Kou, *Welding Metallurgy* John Wiley & Sons, Inc., 2002, p. 461.
[56] R. Selvaraj, K. Shanmugam, P. Selvaraj, and V. Balasubramanian, "Optimization of process parameters of rotary friction welding of low alloy steel tubes using response surface methodology," *Forces in Mechanics*, vol. 10, p. 100175, 2023.
[57] S. A. S. Alghazalah and S. M. J. M. Ali, "Effect of Friction Time on Mechanical Properties of Two Dissimilar Welded Joints of Austenitic Stainless Steel AISI304 and Low Carbon Steel ST-37 Using Rotary Friction Welding Techniques," *International Research Journal of Innovations in Engineering and Technology*, vol. 6, no. 9, p. 121, 2022.
[58] S. A. S. Alghazalah and S. M. J. M. Ali, "Effect of Forging Pressure on Mechanical Properties of Two Dissimilar Welded Joints of Austenitic Stainless Steel AISI304 and Low Carbon Steel ST-37 Using Rotary Friction Welding Techniques," *Universal Journal of Mechanical Engineering*, vol. 11, no. 1, p. 12, 2023, doi: 10.13189/ujme.2023.110101.
[59] S. Egerland, "A contribution to arc length discussion," *Soldagem & Inspeção*, vol. 20, pp. 367-380, 2015.
[60] G. Dak and C. Pandey, "A critical review on dissimilar welds joint between martensitic and austenitic steel for power plant application," *Journal of Manufacturing Processes*, vol. 58, pp. 377-406, 2020.
[61] C. Lundin, "Dissimilar metal welds-transition joints literature review," *Welding Journal*, vol. 61, no. 2, pp. 58-63, 1982.
[62] L. Osoba, I. Ekpe, and R. Elemuren, "Analysis of dissimilar welding of austenitic stainless steel to low carbon steel by TIG welding process," *Int. J. Metall. Mater. Eng*, vol. 5, pp. 1-12, 2015.
[63] "AVOIDING DISSIMILAR METAL WELD FAILURES WITH GRADED TRANSITION JOINTS," in *Lehigh Energy Update*, 2007, vol. 25, p. 3.
[64] K.-Y. Jhang, C. Chung, L. Yang, and C. Kim, "Nonlinear Ultrasonic Technique for Evaluating Degradation of Dissimilar metal welds in Nuclear Facilities," 2012.
[65] D. K. Singh, G. Sahoo, R. Basu, V. Sharma, and M. Mohtadi-Bonab, "Investigation on the microstructure—mechanical property correlation in dissimilar steel welds of stainless steel SS 304 and medium carbon steel EN 8," *Journal of Manufacturing Processes*, vol. 36, pp. 281-292, 2018.
[66] D. K. Singh, V. Sharma, R. Basu, and M. Eskandari, "Understanding the effect of weld parameters on the microstructures and mechanical properties in dissimilar steel welds," *Procedia Manufacturing*, vol. 35, pp. 986-991, 2019.
[67] A. R. Sayed, Y. V. Kumbhare, N. G. Ingole, P. T. Dhengale, and N. R. Dhanorkar, "A review study of dissimilar metal welds of stainless steel and mild steel by TIG welding process," *Int. J. Res. Appl. Sci. Eng. Technol*, vol. 7, pp. 370-373, 2019.
[68] K. Touileb *et al.*, "Comparative Microstructural, Mechanical and Corrosion Study between Dissimilar ATIG and Conventional TIG Weldments of 316L Stainless Steel and Mild Steel," *Metals*, vol. 12, no. 4, p. 635, 2022.

[69] K. Krishnaprasad and R. V. Prakash, "Fatigue crack growth behavior in dissimilar metal weldment of stainless steel and carbon steel," *World Academy of Science, Engineering and Technology*, vol. 56, no. 158, pp. 873-879, 2009.
[70] V. Satyanarayana, G. M. Reddy, and T. Mohandas, "Dissimilar metal friction welding of austenitic–ferritic stainless steels," *Journal of Materials Processing Technology*, vol. 160, no. 2, pp. 128-137, 2005.
[71] T. Y. Sunay, M. Sahin, and S. Altintas, "The effects of casting and forging processes on joint properties in friction-welded AISI 1050 and AISI 304 steels," *The International Journal of Advanced Manufacturing Technology*, vol. 44, pp. 68-79, 2009.
[72] N. Özdemir, "Investigation of the mechanical properties of friction-welded joints between AISI 304L and AISI 4340 steel as a function rotational speed," *Materials letters*, vol. 59, no. 19-20, pp. 2504-2509, 2005.
[73] D. Ananthapadmanaban, V. S. Rao, N. Abraham, and K. P. Rao, "A study of mechanical properties of friction welded mild steel to stainless steel joints," *Materials & Design*, vol. 30, no. 7, pp. 2642-2646, 2009.
[74] H. Firmanto, S. Candra, M. A. Hadiyat, Y. P. Triastomo, and I. Wirawan, "Tensile Strength and Microstructure of Rotary-Friction-Welded Carbon-Steel and Stainless-Steel Joints," *Journal of Manufacturing and Materials Processing*, vol. 7, no. 1, p. 7, 2022.
[75] H. Ma, G. Qin, P. Geng, F. Li, B. Fu, and X. Meng, "Microstructure characterization and properties of carbon steel to stainless steel dissimilar metal joint made by friction welding," *Materials & Design*, vol. 86, pp. 587-597, 2015.
[76] N. Arivazhagan, S. Singh, S. Prakash, and G. Reddy, "Investigation on AISI 304 austenitic stainless steel to AISI 4140 low alloy steel dissimilar joints by gas tungsten arc, electron beam and friction welding," *Materials & Design*, vol. 32, no. 5, pp. 3036-3050, 2011.
[77] T. Saju and M. Velu, "Fracture toughness and fatigue crack growth rate studies on rotary friction weldments of nickel-based superalloys," *Materials Letters*, vol. 327, p. 133027, 2022.
[78] H. Firmanto, S. Candra, M. A. Hadiyat, Y. P. Triastomo, and I. Wirawan, "Tensile Strength and Microstructure of Rotary Friction-Welded Carbon Steel and Stainless Steel Joints," *Journal of Manufacturing and Materials Processing*, vol. 7, no. 1, p. 7, 2022.
[79] G. I. Khidhir and S. A. Baban, "Efficiency of dissimilar friction welded 1045 medium carbon steel and 316L austenitic stainless steel joints," *Journal of Materials Research and Technology*, vol. 8, no. 2, pp. 1926-1932, 2019.
[80] J. M. García, V. Esin, and T. F. Morgeneyer, "Strength, fatigue strength and toughness of dissimilar Ti17–Ti64 linear friction welded joints: Effect of soft surface contamination and depletion of α precipitates," *Materials Science and Engineering: A*, vol. 799, p. 139989, 2021.
[81] M. I. Utama, N. Park, and E. R. Baek, "Microstructure and mechanical features of electron beam welded dissimilar titanium alloys: Ti–10V–2Fe–3Al and Ti–6Al–4V," *Metals and Materials International*, vol. 25, pp. 439-448, 2019.
[82] J. Luijan, K. Eidhed, and P. Surin, "Weldability and Joining of Dissimilar Metal Welding between Low Carbon Steel and Ferritic Stainless Steel," *Key Engineering Materials*, vol. 973, pp. 87-92, 2024.
[83] D. N. V. AS, "Submarine pipeline systems," *Det Norske Veritas*, 2007.

[84] *E1820 - Standard Test Method for Measurement of Fracture Toughness*, E1820, A. International, 2011.
[85] *ASTM E399-22*, ASTM, 2023.
[86] O. I. d. Normalización, *ISO 12135: Metallic Materials - Unified Method of Test for the Determination of Quasistatic Fracture Toughness*. ISO, 2016.
[87] "TIMETAL 6-4." TIMET. https://www.timet.com/documents/datasheets/alpha-and-beta-alloys/timetal-6-4.pdf (accessed.
[88] "TIMETAL 10-2-3." TIMET. https://www.timet.com/documents/datasheets/metastable-beta-alloys/timetal-10-2-3.pdf (accessed.
[89] A. Nagode *et al.*, "The development of a banded microstructure in S355J2 steel bar," *Kovove Materialy-Metallic Materials,* vol. 55, no. 01, pp. 51-56, 2017.
[90] P. Geng, G. Qin, and J. Zhou, "Numerical and experimental investigation on friction welding of austenite stainless steel and middle carbon steel," *Journal of Manufacturing Processes,* vol. 47, pp. 83-97, 2019.
[91] A. Hasçalik, E. Ünal, and N. Özdemir, "Fatigue behaviour of AISI 304 steel to AISI 4340 steel welded by friction welding," *Journal of materials science,* vol. 41, pp. 3233-3239, 2006.
[92] H. Purwanto, "Interface Structure in Friction Welded Joints between Stainless Steel 304 and Mild Carbon Steel," *Journal of Chemical Process and Material Technology,* vol. 1, no. 1, pp. 8-14, 2022.
[93] V. C. Kantumuchu and M. M. Cheepu, "The Influence of Friction Time on the Joint Interface and Mechanical Properties in Dissimilar Friction Welds," *Journal of Metallic Material Research,* vol. 5, no. 1, pp. 1-7, 2022.
[94] G. S. Chander, G. M. Reddy, and G. Tagore, "Influence of process parameters on impact toughness and hardness of dissimilar AISI 4140 and AISI 304 continuous drive friction welds," *The International Journal of Advanced Manufacturing Technology,* vol. 64, pp. 1445-1457, 2013.
[95] W. Wu, S. Hu, and J. Shen, "Microstructure, mechanical properties and corrosion behavior of laser welded dissimilar joints between ferritic stainless steel and carbon steel," *Materials & Design (1980-2015),* vol. 65, pp. 855-861, 2015.
[96] L. Zhang, W. Harrison, M. A. Yar, S. G. Brown, and N. P. Lavery, "The development of miniature tensile specimens with non-standard aspect and slimness ratios for rapid alloy prototyping processes," *journal of materials research and technology,* vol. 15, pp. 1830-1843, 2021.
[97] P. Zheng *et al.*, "On the standards and practices for miniaturized tensile test–a review," *Fusion Engineering and Design,* vol. 161, p. 112006, 2020.
[98] K. Kumar *et al.*, "Optimisation of thickness of miniature tensile specimens for evaluation of mechanical properties," *Materials Science and Engineering: A,* vol. 675, pp. 32-43, 2016.
[99] A. Bannister and S. Trail, "Structural Integrity assessment procedures for European industry," *British steel plc,* 1996.
[100] T. Senthil, S. R. Babu, and M. Puviyarasan, "Mechanical, microstructural and fracture studies on inconel 825–SS316L functionally graded wall fabricated by wire arc additive manufacturing," *Scientific Reports,* vol. 13, no. 1, p. 5321, 2023.
[101] W. Khor, P. Moore, H. Pisarski, M. Haslett, and C. Brown, "Measurement and prediction of CTOD in austenitic stainless steel," *Fatigue & Fracture*

of Engineering Materials & Structures, vol. 39, no. 11, pp. 1433-1442, 2016.
[102] J. Li *et al.*, "Effects of geometric dimension and grain size on impact properties of 316L stainless steel," *Materials Letters*, vol. 284, p. 128908, 2021.
[103] R. R. Rashid, M. Bermingham, S. Sun, G. Wang, and M. Dargusch, "The response of the high strength Ti–10V–2Fe–3Al beta titanium alloy to laser assisted cutting," *Precision Engineering*, vol. 37, no. 2, pp. 461-472, 2013.
[104] M. I. Utama, J. A. Nugroho, A. A. Ammar, N. Park, and E. R. Baek, "Different Ratios of Electron Beam Welding of Dissimilar Titanium Alloys: Ti-10V-2Fe-3Al and Ti-6Al-4V," in *MATEC Web of Conferences*, 2019, vol. 269: EDP Sciences, p. 01003.
[105] P. Jedrasiak, H. Shercliff, A. McAndrew, and P. A. Colegrove, "Thermal modelling of linear friction welding," *Materials & Design*, vol. 156, pp. 362-369, 2018.
[106] A. R. McAndrew, P. A. Colegrove, C. Bühr, B. C. Flipo, and A. Vairis, "A literature review of Ti-6Al-4V linear friction welding," *Progress in Materials Science*, vol. 92, pp. 225-257, 2018.
[107] F. Niessen, E. V. Pereloma, and A. A. Saleh, "Predicting the available work from deformation-induced α″ martensite formation in metastable β Ti alloys," *Journal of Applied Crystallography*, vol. 53, no. 4, pp. 1015-1028, 2020.
[108] T. Ahmed and H. Rack, "Phase transformations during cooling in α+ β titanium alloys," *Materials Science and Engineering: A*, vol. 243, no. 1-2, pp. 206-211, 1998.
[109] X. Boyat *et al.*, "Interfacial characteristics and cohesion mechanisms of linear friction welded dissimilar titanium alloys: Ti–5Al–2Sn–2Zr–4Mo–4Cr (Ti17) and Ti–6Al–2Sn–4Zr–2Mo (Ti6242)," *Materials Characterization*, vol. 158, p. 109942, 2019.
[110] P. Li *et al.*, "Secondary hardening behavior in Ti alloy," *Materials Science and Engineering: A*, vol. 759, pp. 640-647, 2019.
[111] "Ti-64." ATI. https://www.atimaterials.com/Products/Documents/datasheets/titanium/alloyed/ati_6-4_tds_en_v1.pdf (accessed.
[112] S. E. Haghighi, H. Lu, G. Jian, G. Cao, D. Habibi, and L. Zhang, "Effect of α ″martensite on the microstructure and mechanical properties of beta-type Ti–Fe–Ta alloys," *Materials & Design*, vol. 76, pp. 47-54, 2015.
[113] M. Janeček *et al.*, "The very high cycle fatigue behaviour of Ti-6Al-4V alloy," *Acta Physica Polonica A*, vol. 128, no. 4, pp. 497-502, 2015.

7 Appendix

A.1 Fracture toughness calculation

Sample calculation of fracture toughness

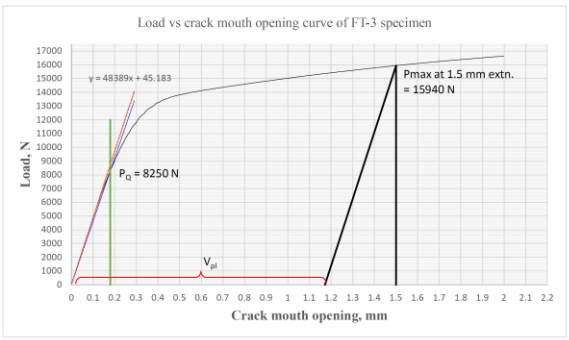

P_Q	8250	N
Crack mouth opening at 1.5 mm extension	1.5	mm
Pmax at 1.5 mm, N	15940	N
Elastic component of crack mouth opening at Pmax., mm	0.328479964	mm
Plastic component, v_{pl} , mm=	1.171520036	mm

Equation used:

$$K = \frac{Pf(a/W)}{(BB_N W)^{1/2}} \qquad f(a/W) = \left(\frac{\xi}{\zeta}\right)[C_0 + C_1(a/W) + C_2(a/W)^2 + C_3(a/W)^3 + C_4(a/W)^4]$$

$$\delta_{(i)} = \frac{K_{(i)}^2(1-\nu^2)}{2\sigma_{YS}E} + \frac{[r_p(W-a_o)]\,v_{pl(i)}}{[r_p(W-a_o)+a_o+z]}$$

where:
a_o = original crack length,
K = stress intensity factor as defined in A2.4.1 with $a = a_o$,
ν = Poisson's ratio,
σ_{YS} = yield or 0.2 % offset yield strength at the temperature of interest,
E = elastic modulus at the test temperature,
v_{pl} = plastic component of clip gage opening displacement at the point of evaluation on the load-displacement curve, v_p, v_{pl}, or v_{pm},
z = distance of knife-edge measurement point from the load-line on the $C(T)$ specimen, and
r_p = plastic rotation factor = 0.4 (1 + α),
where:

$$\alpha = -2\left[\left(\frac{a_o}{b_o}\right)^2 + \frac{a_o}{b_o} + \frac{1}{2}\right]^{1/2} - 2\left(\frac{a_o}{b_o} + \frac{1}{2}\right) \qquad \text{(A2.17)}$$

	Specimens
	C(T)
ξ	$2 + a/W$
ζ	$(1 - a/W)^{3/2}$
C_0	0.886
C_1	4.64
C_2	−13.32
C_3	14.72
C_4	−5.6
Limits	$0.2 \le a/W \le 1$ $H/W = 0.6$
Refs	(10), (11)

Specimen ID			FT-1	FT-3	FT-4	FT-5	FT-6	FT-7	FT-8	FT-9
Notch location			RFW-WCL	BM-CS	BM-SS	TIG-HAZ-SS	RFW-HAZ-SS	RFW-HAZ-CS	TIG-HAZ-CS	TIG-WCL
Wall thickness	B=	mm	11.93	11.94	12.02	11.95	11.88	11.92	11.95	11.95
B_N= B	B_N=	mm	11.93	11.94	12.02	11.95	11.88	11.92	11.95	11.95
Width of specimen	W=	mm	24.08	24.09	23.98	24.05	23.97	23.96	23.95	23.92
Yield Stress	σ_{YS}=	MPa	367.0	376.0	255.0	255.0	255.0	376.0	376.0	300.0
Ultimate Tensile stress	σ_{TS}=	MPa	540.0	522.0	536.0	536.0	536.0	522.0	522.0	526.0
Machined crack length	a_i=	mm	10.35	10.31	10.29	10.28	10.33	10.33	10.19	10.35
Fatigue precrack length	a_f=	mm	0.66	0.95	0.53	1.38	1.53	1.72	1.67	1.66
Final crack length (a_i + a_f)	a_o=	mm	11.01	11.26	10.82	11.66	11.86	12.05	11.86	12.01
			12.17	11.82	11.52	12.62	13.06	12.38	12.20	12.18
Uncracked ligament before fatigue precrack (W-a_i)	b_i=	mm	13.73	13.78	13.69	13.77	13.64	13.63	13.76	13.57
Uncracked ligament after fatigue precrack (W-a_o)	b_o=	mm	13.07	12.83	13.16	12.39	12.11	11.91	12.09	11.91
			11.91	12.27	12.46	11.43	10.91	11.58	11.75	11.74
Distance of knife edge measurement point from load line	z=	mm	5.94	5.92	6	5.95	6.03	6.04	6.02	6.05
Plastic component of clip gage opening displacement at point of evaluation (max. load up to 1.5 mm extension)	**$V_{pl\,at\,1.5mm}$=**	**mm**	**1.174**	**1.1715**	**1.2575**	**1.212**	**1.155**	**1.215**	**1.133**	**1.165**
Young modulus	E=	MPa	185754	201869	169309	169309	169309	201869	201869	191448
Poisson ratio	v=		0.3	0.3	0.265	0.265	0.265	0.3	0.3	0.3
α	α=		0.180188709	0.1758588	0.1827109	0.168483011	0.164440936	0.161045726	0.16425331	0.161420355
	α1=		0.160056281	0.1661867	0.1704018	0.15223642	0.14417801	0.155437032	0.158396283	0.15844779
r_p	r_p=		0.472075484	0.4703435	0.4730844	0.467393204	0.465776375	0.46441829	0.465701324	0.464568142
	r_{p1}=		0.464022513	0.4664747	0.4681607	0.460894568	0.457671204	0.462174813	0.463358513	0.463379116
	Part1=	(mm)	0.033697683	0.0340667	0.0290527	0.039879971	0.046452653	0.039767788	0.039089045	0.044383722
	Part2=	(mm)	0.313304622	0.3045262	0.3396113	0.299807231	0.276896325	0.284447661	0.271334474	0.273214549
	$P_{Q\,at\,1.5\,mm\,extension}$=	N	15454	15940	11550	12220	12710	15415	15690	14230
CTOD	**δm=**	**(mm)**	**0.35**	**0.34**	**0.37**	**0.34**	**0.32**	**0.32**	**0.31**	**0.32**
	K_Q=	$MPam^{-1/2}$	71.1	75.4	51.9	60.9	65.7	81.4	80.8	74.9
	a/W=		0.457225914	0.4674139	0.4513344	0.484989605	0.494743429	0.503005008	0.49519833	0.502090301
	f(a/W)=		8.511855092	8.764408	8.370989	9.229280226	9.50487357	9.749108203	9.518056797	9.721556392
	ξ =		2.457225914	2.4674139	2.4513344	2.484989605	2.494743429	2.503005008	2.49519833	2.502090301
	ζ =		0.399879055	0.3886734	0.4064073	0.369593217	0.359143454	0.350370892	0.358658539	0.35133861
	C_0=		0.886	0.886	0.886	0.886	0.886	0.886	0.886	0.886
	C_1=		4.64	4.64	4.64	4.64	4.64	4.64	4.64	4.64
	C_2=		-13.32	-13.32	-13.32	-13.32	-13.32	-13.32	-13.32	-13.32
	C_3=		14.72	14.72	14.72	14.72	14.72	14.72	14.72	14.72
	C_4=		-5.6	-5.6	-5.6	-5.6	-5.6	-5.6	-5.6	-5.6
	$P_{q\,initial}$=	N	7710	8250	6370	6530	6830	7774	7430	7825
Fracture toughness	**K_Q =**	$MPam^{-1/2}$	**40.9**	**41.8**	**31.2**	**36.8**	**41.5**	**42.9**	**40.0**	**42.1**
	a/W_{final}=		0.505424626	0.4905199	0.4803899	0.524742723	0.545025031	0.516793614	0.509496347	0.509369774
	f(a/W)=		9.82262008	9.3838995	9.1038272	10.44447423	11.17244903	10.18078607	9.948433899	9.944482363
	ξ =		2.505424626	2.4905199	2.4803899	2.524742723	2.545025031	2.516793614	2.509496347	2.509369774
	ζ =		0.34781534	0.363656	0.3745557	0.327637167	0.306888953	0.335891487	0.343528972	0.34366195
	C_0=		0.886	0.886	0.886	0.886	0.886	0.886	0.886	0.886
	C_1=		4.64	4.64	4.64	4.64	4.64	4.64	4.64	4.64
	C_2=		-13.32	-13.32	-13.32	-13.32	-13.32	-13.32	-13.32	-13.32
	C_3=		14.72	14.72	14.72	14.72	14.72	14.72	14.72	14.72
	C_4=		-5.6	-5.6	-5.6	-5.6	-5.6	-5.6	-5.6	-5.6

Figure 127: Typical fracture toughness calculation.

Figure 127 illustrates sample calculation of K_Q and CTOD. For the calculation of both fracture toughness (K_Q) and CTOD, the YS and YM for specimen FT1 (RFW-WCL) and FT-9 (TIG-WCL) are determined by averaging the YS and YM values obtained from the cross-weld tensile tests performed for their respective welds, as indicated in Table 13.

For specimens extracted from the HAZ of S355J2 (FT-7 and FT-8) and the S355J2 parent metal (FT-3), the YS and YM are derived from the average values obtained from the tensile tests of the S355J2 parent metal. This approach is employed because the HAZ is considered an integral part of the parent metal, in accordance with the requirements outlined in the international standard ISO 15653.

A similar methodology is applied to specimens extracted from the HAZ of SS (FT-5 & FT-6) and SS parent metal (FT-4).

A.2 Fracture toughness test validation

To validate the test, initial and final crack length as illustrated in Figure 46 and Figure 47 were measured. The measured crack length of specimen FT-7 are displayed in Table 16. Subsequently the average crack size is calculated using Equation 16, yielding a value of 12.382 mm. Notably, all nine measurements (S1, S2, P1, …P7) fell within ±5% of 12.382 mm (i.e., 11.763 mm – 13.001 mm). Similar calculations were conducted for all specimens, and it was determined that their measurements also fell within 5% of the average value. This phenomenon concludes that test is a valid test.

Table 16: Crack length of fracture specimen FT-7

SL No.	1	2	3	4	5	6	7	8	9	10
ID#	S1	S2	P1	P2	P3	P4	P5	P6	P7	P8 = (S1+S2)/2
Crack length, mm	12.078	12.116	12.33	12.374	12.417	12.439	12.482	12.46	12.46	12.097
Average crack length i.e. avg. (P1+….+P8), mm	= 12.382									
Min. average crack length, i.e. (-)5% of average crack length	= 11.763									
Max. average crack length, (+)5% of average crack length	= 13.001									